

Mechanical resonators with high dissipation dilution in precision and quantum measurements

Présentée le 8 janvier 2021

à la Faculté des sciences et techniques de l'ingénieur
Laboratoire de photonique et mesures quantiques (STI/SB)
Programme doctoral en physique

pour l'obtention du grade de Docteur ès Sciences

par

Sergey FEDOROV

Acceptée sur proposition du jury

Prof. C. Hébert, présidente du jury
Prof. T. Kippenberg, directeur de thèse
Prof. A. Schliesser, rapporteur
Prof. A. Heidmann, rapporteur
Prof. C. Galland, rapporteur

Acknowledgements

I would like to express my gratitude to numerous people who directly or indirectly contributed to this thesis.

First of all, to my advisor, Prof. Tobias Kippenberg, who gave me an opportunity to be a part of his group. For his dedication to the lab, attentiveness to details, enthusiasm, and the promotion of open science.

To Dal Wilson, Hendrik Schütz, Vivishek Sudhir, and Ryan Schilling, for introducing me to various aspects of quantum optomechanics. I am separately grateful to Dal for teaching me to strive for simplicity, and Vivishek for teaching me to appreciate a certain level of abstraction.

To Nils Engelsen, Alberto Beccari, and Mohammad Bereyhi, whom I was privileged to work with for most of my PhD, I owe a special thank. Nils to me has been both an inexhaustible source of the finest hands-on knowledge and a regular company to discuss the most involved theory. His patience and carefulness inspired me, and even his mere presence in the lab made me more efficient. I am separately thankful to him for the careful reading of the thesis and for the enormous number of suggestions that greatly improved it. Alberto and Mohammad mastered the noble art of suspending fragile nanostructures and are the people who should be truly credited for many of our experimental results. Designs of the most complex membrane resonators immensely benefited from discussions with Alberto.

To my junior colleagues, Guanhao Huang, Robin Groth, and Amirali Arabmoheghi, whose fresh insights I am certain will lead them to great success; To Amir Ghadimi; To Alexey Feofanov, who taught me everything I know about cryogenics; To Alexandre Tagantsev for illuminating theoretical discussions; To Itay Shomroni, Liu Qiu and Clément Javerzac-Galy for the friendly atmosphere of the office; To Philippe Roelli, especially for translating the abstract of this thesis into French; To my neighbors Dmitrii, Maria, Ivan, and Nikolai, for the lively environment they created.

My gratitude to my parents, my brother Kirill and my wife Elena for their ever-continuing support is beyond any measure.

Abstract

Position measurements of mechanical oscillators underpin experiments spanning from applied nanoscale sensing to endeavors aiming to resolve open fundamental problems of modern physics. Sufficiently precise position measurements are also used for engineering quantum states. Because of the coupling to the thermal environment, mechanical oscillators undergo Brownian motion, which sets the lowest measurement error when an oscillator is used as a probe and puts an upper bound on the decoherence time of mechanical quantum states. The thermal noise from the environment that drives the Brownian motion is proportional to the energy dissipation rate, and for this reason, mechanical resonators with low dissipation are the subject of broad and long-standing interest.

The dissipation of vibrational modes in mechanical resonators is ultimately limited by intrinsic losses, which appear to be unavoidable as the acoustic strain creating them is also the source of potential energy for the vibrational modes. Intrinsic dissipation is nearly constant for different modes of bulk resonators. In striking contrast, the flexural modes of high aspect-ratio resonators subjected to static stress can experience very small, “diluted”, intrinsic dissipation. Understanding and engineering dissipation dilution led to remarkable progress in the development of low-loss mechanical resonators, which is in part covered in this thesis. Presently, chip-scale MHz-frequency mechanical resonators made of stoichiometric silicon nitride films are among the highest quality factor resonators that exist, reaching quality factors close to one billion at room temperature. The demonstration of these devices paves the way for force measurements with unprecedented resolution and the generation of long-lived quantum states of macroscopic objects.

This thesis explores dissipation dilution in thin-film mechanical resonators and experimental position measurements performed on such resonators integrated into optomechanical cavities. Using an on-chip integrated optomechanical transducer, we implement the variational measurement strategy and demonstrate quantum correlations arising between the quadratures of meter light as a result of quantum measurement backaction. In our experiments at cryogenic temperature, these correlations lead to ponderomotive squeezing of light.

The potential of the recently emerged record low-loss mechanical devices is particularly enticing at room temperature, as dissipation dilution is one of the few means to counteract the high thermal occupation of the bath modes. The large amplitudes of Brownian motion at room temperature, however, put a stringent limitation on the

linearity range of the detector. As shown in this thesis, the interferometric nonlinearity inherent to optical measurements can easily become the dominant source of extrinsic thermal noise in detection.

Keywords: dissipation dilution, high-stress resonators, quantum measurements, cavity optomechanics, nonlinear transduction.

Résumé

Les mesures de position des oscillateurs mécaniques sont au cœur d'expériences allant d'applications usant de la détection à l'échelle nanométrique aux efforts visant à résoudre certains problèmes fondamentaux de la physique moderne. Des mesures de position suffisamment précises sont également utilisées pour contrôler des états quantiques. En raison du couplage à l'environnement thermique, les oscillateurs mécaniques subissent un mouvement brownien qui détermine l'erreur de mesure la plus faible, lorsqu'un oscillateur est utilisé comme sonde, et fixe une limite supérieure au temps de décohérence des états quantiques de systèmes mécaniques. Le bruit thermique de l'environnement, qui entraîne le mouvement brownien, est proportionnel au taux de dissipation d'énergie et, pour cette raison, les résonateurs mécaniques à faible dissipation font l'objet d'un intérêt généralisé et de persistant.

La dissipation des modes vibrationnels dans les résonateurs mécaniques est en définitive limitée par des pertes intrinsèques qui semblent inévitables du fait que la contrainte acoustique qui les crée est également la source d'énergie potentielle des modes vibrationnels. La dissipation intrinsèque est presque constante pour les différents modes de résonateurs volumineux. En revanche, les modes de flexion de résonateurs à fort rapport d'aspect et soumis à une contrainte statique peuvent présenter une dissipation intrinsèque très faible, "diluée". La compréhension et l'ingénierie de la dilution de la dissipation ont conduit à des progrès remarquables dans le développement de résonateurs mécaniques à faibles pertes, qui sont en partie couverts dans cette thèse. Actuellement, les résonateurs mécaniques de fréquence MHz à l'échelle d'une puce, constitués de films stoechiométriques de nitrure de silicium, sont parmi les résonateurs de facteur de qualité le plus élevé qui existent, atteignant des facteurs proches d'un milliard à température ambiante. La démonstration de tels dispositifs ouvre la voie à des mesures de force d'une résolution sans précédent et à la génération d'états quantiques d'objets macroscopiques de longue durée de vie.

Cette thèse explore la dilution de la dissipation dans les résonateurs mécaniques à couche mince et les mesures expérimentales de position effectuées sur de tels résonateurs, intégrés dans des cavités optomécaniques. En utilisant un transducteur optomécanique intégré sur puce, nous mettons en œuvre la stratégie de mesure variationnelle et démontrons les corrélations quantiques qui se produisent entre les quadratures de la lumière de mesure des suites de la rétroaction de la mesure quantique. Dans nos expériences à température cryogénique, ces corrélations conduisent à une compression ponderomotrice de la lumière.

Le potentiel des dispositifs mécaniques pertes faibles, qui ont récemment fait leur apparition, est particulièrement intéressant à température ambiante car la dilution de la dissipation est l'un des rares moyens de contrecarrer la forte occupation thermique des modes du bain. Les grandes amplitudes du mouvement brownien à température ambiante limitent cependant fortement la plage de linéarité du détecteur. Comme le montre cette thèse, la non-linéarité interférométrique inhérente aux mesures optiques peut facilement devenir la source dominante de bruit thermique extrinsèque lors de la détection.

Mots-clés : dilution de la dissipation, résonateurs à fortes contraintes, mesures quantiques, optomécanique, transduction nonlinéaire.

Contents

Acknowledgements	iii
Abstract	v
Résumé	vii
Contents	ix
1 Overview	1
2 Dissipation dilution in mechanical resonators	7
2.1 Introduction	7
2.2 Toy models	11
2.2.1 A mass on a lossy spring	11
2.2.2 Quality factors and dissipation dilution	12
2.2.3 The lossless motion of a mass on lossy tensioned springs	14
2.2.4 Suspended pendula	17
2.3 General theory of dissipation dilution	18
2.3.1 Deformations, stress and strain in elastic bodies	19
2.3.2 Geometrically nonlinear strain and local rotations	20
2.3.3 Acoustic vibrations	22
2.3.4 Intrinsic mechanical dissipation	25
2.3.5 Loss angle in a continuous medium	27
2.3.6 Dissipation dilution by static stress	29
2.3.7 A continuous toy model with infinite dilution	30
2.3.8 A numerical example	32
2.4 Resonators with reduced dimensionality	35
2.4.1 2D—membranes	37
2.4.2 Effective material loss angle in thin films	42
2.4.3 Clamping curvature	44
2.4.4 1D—beams with arbitrary cross section	45
2.4.5 Thin-film beams	48
2.4.6 Distributed and boundary losses in thin-film beams	49
2.4.7 The ultimate limit for dissipation dilution in thin films	54
2.4.8 Torsional lossy energy	55

CONTENTS

2.4.9	Dissipation dilution and frequency noise	56
2.5	High-stress phononic crystals	57
2.5.1	Soft clamping in PnC nanobeams	60
2.5.2	Elastic strain engineering	64
2.5.3	Comparison between one- and three-dimensional simulations	70
2.5.4	PnC membranes with low effective mass localized modes	72
2.5.5	Global stress concentration in 2D	75
2.6	Fractal-like resonators	76
2.6.1	Soft clamping of a fundamental mode	77
2.6.2	Fractional spectral dimensionality	83
2.6.3	Trampolines with branching tethers	84
2.6.4	A pendulum with a self-similar suspension	86
2.7	Experimental characterization of high- Q mechanical resonators	88
3	Quantum correlations in position measurements	93
3.1	Introduction	93
3.2	Linear continuous measurements	96
3.2.1	Spectral densities of quantum operators and measurement records	97
3.2.2	Photodetection	99
3.2.3	The mechanical oscillator	100
3.2.4	General aspects of linear position measurements	102
3.2.5	On the physical significance of SQL	107
3.2.6	An optomechanical cavity as a parametric position detector	108
3.3	Quantum correlations in variational homodyne measurements	112
3.3.1	Variational measurements	114
3.3.2	Narrowband external force detection	118
3.3.3	Ponderomotive squeezing	119
3.3.4	Main experimental limitations	121
3.4	Experiments with near-field optomechanical cavities	122
3.4.1	Setup for the detection of measurement backaction-imprecision correlations at room temperature	124
3.4.2	Broadband correlations	127
4	Nonlinear measurements and thermal intermodulation noise	131
4.1	Introduction	131
4.2	Thermal intermodulation noise in a membrane in the middle cavity	136
4.2.1	Membrane in the middle cavity	136
4.2.2	Theory of thermal intermodulation noise	140
4.2.3	Quadratic transduction and quadratic coupling in MIM system	143
4.3	Experimental observation and characterization of TIN	144
4.3.1	Setup, cavity assembly and alignment	144
4.3.2	Square membranes	149
4.3.3	PnC membranes with soft-clamped modes	151

5 Summary and outlook	157
A Appendices	159
A.1 Elastic energy and dissipation in a geometrically nonlinear body	160
A.2 FEM simulation of dissipation dilution in patterned membranes	164
A.3 Buckling of thin-film structures	166
A.4 Closed-cycle low-vibration cryogenic setup	169
A.5 Scalable data acquisition framework	171
Bibliography	175
Curriculum Vitae	191
List of publications	193

CONTENTS

Overview

Mechanical resonators, thermal noise and quantum measurements

The way measurements act in the quantum world has been a source of uneasiness for physicists since the inception of quantum mechanics. At the operational level, there hardly seems to be a problem presently. Beginning with Von Neumann's postulate that measurement is a "collapse" of the wavefunction to one of the eigenstates, a general and elaborated measurement theory was developed [1, 2, 3], which has been faultless in describing the outcomes of even the most sophisticated experiments performed with quantum objects to date. And yet, a conceptual incompleteness remains [4]—there is no mechanism by which a wavefunction can collapse within the quantum theory itself. According to the Copenhagen interpretation, quantum objects need to interact with classical ones in order to be measured. At the same time the location of classical-to-quantum boundary remains unclear, and the question of whether there is any fundamental mechanism that can collapse the wavefunction (e.g. related to gravity) is open [5, 6, 7, 8]. Hypotheses related to these problems are difficult to test because tests would require the observation of quantum behavior of macroscopic (in some sense) objects. Such experiments are also difficult for purely technical and non-fundamental reasons, since quantum superpositions become increasingly fragile and sensitive to perturbations as the system size is increased [9, 3].

An act of measurement prepares the quantum object in a certain state and provides the observer with an outcome identifying this state. Contrary to our experience with classical unknowns described by probability distributions, measurements of two different quantum observables are not necessarily compatible and can not always be done simultaneously. When incompatible measurements are performed sequentially, the state prepared by one always leaves the outcome of the other uncertain. In this way the second measurement senses the backaction of the first. The projective effect of measurement was not of much relevance in early experiments. For example, in the famous Stern-Gerlach experiment, particle spins were inferred from the positions at which the particles collided with the screen after deflection by magnets. Measurement outcomes

provided information about the spins, but it could not be verified what happened to the particle state after the measurement, since the particles were lost on the screen. Experimental observation of state projection by measurements requires a non-destructive method of monitoring quantum objects. It can be implemented by coupling an object to an intermediary party as, for example, propagating optical field, and performing destructive measurement on this party. Experimental methods of such measurements were developed in the second half of the 20th century. A prominent early achievement was the observation of quantum jumps between two electronic states of a laser-cooled ion in an electromagnetic trap [10, 11]. Even more recently, in the 2000s, jumps between Fock states of a harmonic oscillator were observed for the first time [12, 13] for an electromagnetic field in microwave cavities. These experiments directly evidenced the quantum state projection and validated the textbook picture of quantum measurements.

Interest in quantum measurements is also driven by very practical considerations—in precision experiments, it is desirable to reduce the measurement error down to the fundamental minimum allowed by quantum uncertainties. The mechanical oscillator is one physical system for which the problem of quantum error arises naturally. Various physical phenomena manifest as forces acting on mechanical oscillators, which can be inferred with high sensitivity by measuring the oscillator displacement. At the quantum level, displacements of an oscillator at different times, unless these times are judiciously chosen [14], is a canonical example of observables that cannot simultaneously have zero uncertainty. Hence, the quantum backaction of measurements enters the problem.

Historically, it was largely the analysis of fundamental limitations on the precision of force measurements in gravitational wave detectors which motivated the early theoretical research on continuous quantum measurements [15, 16]. In 2015 gravitational waves were detected for the first time in Laser Interferometer Gravitational-wave Observatory (LIGO) [17] by measuring the displacements of suspended test masses. Signatures of measurement backaction were observed in present-day LIGO using correlation techniques [18], but the backaction is not yet a major sensitivity limitation. The theoretical results obtained within the gravitational wave detection community, however, apply to various physical settings, in the first place to smaller but conceptually very similar interferometric position transducers—optomechanical cavities [19]. In such cavities the backaction in position measurements of an oscillator was observed for the first time in 2013 [20].

In parallel to optomechanics, the interest in quantum limits of measurements was renewed in the end of the 1990s with the emergence of mesoscale solid-state devices [21]—tunneling junctions and single electron transistors—which are highly sensitive transducers of charge. Despite their sensitivity, attaining the minimum backaction-to-sensing error product in tunneling devices is not a trivial task [22, 23]. Related works clarified the requirements that the measurement apparatus need to satisfy in order to be capable of reaching the minimum quantum error. A rigorous definition of a quantum-limited detector [22] was introduced, based on the fact that there should be no information about the measured system in the measurement apparatus that is not available to the end observer.

Aside from their relation to quantum measurements, the exploration of the classical-to-quantum border and precision experiments have one more aspect in common—they are limited by the intrinsic dissipation of quantum objects and their thermal decoherence. The phenomenon of decoherence poses a similar conceptual challenge to quantum theory as measurements do. There is a fundamental duality between the two—decoherence can be interpreted as measurements performed by the environment where the outcomes remain unknown to the observer [9, 3, 24]. Since interactions between quantum objects are reversible, an external entity—a thermal reservoir—is introduced as a source of the energy gain or loss and random thermal perturbations that realistic objects experience. Unlike measurements, to which classical and quantum objects react differently, dissipation acts on both in a similar way. Thermalized quantum states are not very different from classical states [3] and quantum superpositions decay at the thermal decoherence rate [9]. Quantum effects of measurements can only be observed if the measurement-induced collapse of the wavefunction happens faster than the thermal decoherence. In order to satisfy this condition in experiments two strategies can be pursued—reducing the coupling of the system to the environment and increasing (highly selectively) the coupling to the measurement apparatus.

In the second half of the 20th century research in precision measurements (again, gravitational wave detection among them) resulted in the development of macroscopic mechanical resonators with unprecedentedly low levels of dissipation [25], which remain state of the art till now. By utilizing high-purity materials and elaborated ways of resonator mounting, quality factors as high as $5 \cdot 10^{10}$ at cryogenic temperature [25] and $2 \cdot 10^8$ at room temperature [26] were demonstrated. Understanding what limited these record numbers has always been a challenge. The main reasons for this are the wide variety of mechanisms that can potentially contribute to dissipation, the limited means that an experimentalist has to differentiate between them, and the general lack of information about microscopic details of structural imperfections. There are two phenomenological trends which help to unify the results, although seemingly without an underlying fundamental reason. The first trend is that the intrinsic relaxation of energy usually happens locally, e.g. due to local two-level defects in amorphous solids [27]. The second is that the frequency dispersion of internal friction in solids is strikingly different from that in liquids [28], where it follows the viscous law. These observations can be summarized by a model [29, 30], in which material losses are characterized by a single frequency-independent internal friction angle, equal to the fractional energy lost per radian of acoustic vibration. As this model does not suggest a route to reduce the level of intrinsic losses, it predicts that the loss should be the same for any vibrational mode with a bulk body made of a given material.

While there has been a limited progress in reducing mechanical dissipation in large resonators, over the last few years nanoscale devices reached and exceeded their performance [31, 32]. These devices are still macroscopic in a sense that they contain between 10^{10} and 10^{15} atoms, and their masses are in the range from picogram to nanogram. In many aspects the development of low-loss nanomechanical resonators is following the route of their bigger analogues, but there are also important differences. The reduction

of resonator size, on the one hand, increases the surface-to-volume ratio, thus increasing the importance of the contribution from the lossy surface layer. On the other hand, modern nanofabrication techniques offer a high level of control over the resonator geometry, which can ease the elimination of extrinsic sources of loss. Also the small size of the devices and the ability to produce them in large numbers simplifies their characterization and improves the measurement statistics. At cryogenic temperatures, the lowest level of dissipation in nanoresonators to date [31] was achieved by relying on the low intrinsic loss of crystalline materials. However, the resonators that have the lowest loss at room temperature [32] are made of an amorphous material with moderate intrinsic quality factor—stoichiometric silicon nitride. In this case the losses of vibrational modes were reduced by the factor of up to $\sim 10^6$ by dissipation dilution.

Dissipation dilution for solid state resonators refers to the reduction of dissipation in presence of static stress and geometric nonlinearity of deformations [33, 34], typical for flexural modes of high-aspect ratio structures. Same as almost anything related to low-loss mechanical resonators, the concept comes from the community of gravitational wave detection, where it was presented for the first time in 1994 [33]. Its path from macroscopic to microscopic resonators was not entirely straight, and dilution was recognized in microscopic devices only around 2010 [35]. Given the general lack of control over intrinsic mechanical losses, dissipation dilution appears as a promising material-independent approach towards engineering mechanical modes with the lowest dissipation. The latest developments have also showed that the high level of control over the resonator geometry offered by microfabrication techniques is an invaluable tool for improving the dilution. The complex interplay between the vibrational mode shapes and the distribution of static stress in tensile structures creates a wide space for optimization. Various concepts proved useful in this task, including the localization of vibrational modes in phononic crystals [36], engineering stress concentration [32, 37, 38], and self-similar resonator design [39].

From the perspective of an experimentalist who set out to observe quantum aspects of measurements, the decoherence of states is only one way how the thermal environment manifests. Indirect observation requires an intermediary apparatus, which is also at finite temperature and experiences thermal fluctuations. Measurements of mechanical oscillators are commonly done by coupling them to electromagnetic field in the optical or RF domain—such an interferometric readout is one of the most sensitive known techniques. Optical cavities are often used to further enhance sensitivity by making the probe field interact with the oscillator multiple times. While the optical field has high frequency and its thermal occupation is negligible even at room temperature, fundamental thermodynamic fluctuations of optical cavities can parametrically modulate it in a way similar to the oscillator position, and be essentially inseparable from the signal. Common mechanisms by which thermodynamic fluctuations transduce into the optical field include the Brownian motion of mirror surfaces, fluctuations of the refractive index or thermoelastic effect [40, 41, 42]. In the present-day interferometric gravitational wave detectors, which are among the most sensitive instruments ever built, thermal fluctuations of cavity mirrors are a key challenge to further sensitivity improvements [43]. The

absolute magnitude of thermal fluctuations increases upon the reduction of cavity size, which makes them more pronounced in table-top Fabry-Perot resonators and even more so in optical microresonators.

In position measurements performed on a mode of a nanomechanical resonator, a significant fraction of error can also come from the thermally excited motion of other resonator modes. If the measurement is linear, the observer can separate the signal of one mode from the contributions of other modes in the spectral domain, to a degree permitted by the mechanical quality factors and mode density. Linearity is important, as quite typically without spectral separation multiple mechanical modes coupled to the measurement apparatus make measurements to be dominated by classical errors. At the same time, interferometric measurements inherently have some amount of nonlinearity, which is not so surprising since the optical phase is a periodic variable. Interferometric nonlinearity leads to cross-mixing of spectral components of thermal noise, which we refer to as thermal intermodulation [44], and becomes a challenge of a new kind in experiments with low-loss mechanical resonators at room temperature. This effect, while presently seen as undesirable in our experiments, can potentially become useful for implementing nonlinear measurements and creating non-Gaussian mechanical states.

This thesis

The thesis consists of three parts, which address different aspects of cavity-based measurements and thermal noises, and which are united by the motivation of bringing the error of measurements down to the quantum minimum.

The first part concerns the quality factors of stressed mechanical resonators. The theory of dissipation dilution is presented, starting from toy models that illustrate the concept and ending with the general case of arbitrary solid-state resonators. This part has an extended number of details, since the impact of stress on mechanical dissipation has only recently been recognized, and a comprehensive theoretical overview of dissipation dilution has not appeared in the literature so far. In particular, this applies to thin-film resonators, which are of great practical importance. An effort is made to clearly separate common assumptions and approximations made when analyzing dissipation in mechanical resonators, and discuss the physical roots of these assumptions. A particular emphasis is made on quasi one-dimensional resonators (beams), for which a number of analytic results is derived, and on fractal-like binary tree resonators. Experimental results, presented in this section, corroborate theoretical predictions and feature nanobeam mechanical resonators with quality factors up to $8 \cdot 10^8$ at room temperature and $1.6 \cdot 10^9$ at 6 Kelvin.

In the second part, experiments are presented that demonstrate manifestations of quantum measurement backaction in position measurements of mechanical oscillators near-field coupled to optical microcavities. Measurement backaction manifests as correlations between the quadratures of optical field, which constitute an essential ingredient of the variational measurement strategy that can have sensitivity better than the stan-

standard quantum limit. At cryogenic temperature, the backaction-induced correlations are strong enough to produce the quadrature squeezing of light. The observation of these correlations at room temperature, though in a weaker form, was one of the very first demonstrations of measurement backaction on a room temperature mechanical oscillator. In the same section, measurements of broadband thermal noise of a silicon nitride mechanical resonator are presented, and it is shown that the frequency dispersion of oscillator loss angle follows the frequency independent damping model.

In the last part, measurements made using a different optomechanical platform, membrane-in-the-middle, are presented. It is shown that the high optical finesse achievable in such cavities leads to high nonlinearity of measurements. In combination with a large number of modes that membrane resonators possess, the transduction nonlinearity of the optical cavity results in additional thermal noise in detection, which is coined thermal intermodulation noise.

Dissipation dilution in mechanical resonators

2.1 Introduction

The utility of a mechanical oscillator as a probe body is limited by its thermal fluctuations. The degree of thermal agitation is quantified by the magnitude of random force exerted on the oscillator by its environment¹. The two-sided spectral density of thermal force noise, S_{FF}^{th} , is determined by the fluctuation-dissipation theorem [45],

$$S_{FF}^{\text{th}} = 2k_B T m \Gamma. \quad (2.1)$$

Here k_B is the Boltzmann constant, T is the temperature, m is the oscillator mass, Γ is the dissipation rate (the inverse of the acoustic energy decay time). A reduction of thermal noise, therefore, requires lowering the temperature, the oscillator mass, its dissipation, or all of the above. The reduction of dissipation is usually particularly desirable and challenging to realize [46].

Understanding experimentally observed levels of mechanical dissipation from first principles can be difficult, and improving upon them is even more so. While frequencies and displacement profiles of mechanical modes depend on a small number of material parameters and are typically weakly perturbed by imperfections of the real structure and by the ambient environment, the situation is completely different for dissipation. It is not uncommon that a few independent loss mechanisms contribute to dissipation at the same time, making it vary drastically with system parameters and be sensitive to the resonator imperfections and the environment. Moreover, while some mechanisms that can limit dissipation are theoretically well understood (for some examples see Refs [29, 25, 47] for review), or can be simulated by means of molecular dynamics [48, 49], in a

¹From some perspective it might appear counterintuitive that the oscillator dissipation affects the measurement error, as the total variances of oscillator position in thermal equilibrium is independent of dissipation and is simply given by the equipartition, $\langle x^2 \rangle = k_B T / (m \Omega^2)$. In realistic experiments, however, interactions that one sets out to detect do not produce fixed displacements of the oscillator, but rather exert forces on it. These forces need to be above the thermal noise level (Eq. (2.1)) in order to be detectable.

wide range of practically important cases the details of physical processes responsible for dissipation are still obscure.

Mechanical dissipation can be separated as *intrinsic* and *extrinsic*. Although such a separation is not always unambiguous, generally dissipation originating from the interaction of the resonator with its surroundings is considered extrinsic, and dissipation that occurs due to the coupling of strain field to internal degrees of freedom inside the resonator itself is considered intrinsic. Extrinsic mechanisms include damping due to the interaction with surrounding gas [50, 51, 52], the radiation of acoustic energy [53, 54], and the attachment of the resonator to a support (“clamping loss”) [55, 56, 57]. Typically extrinsic loss mechanisms can be eliminated in a carefully designed experiment, although this is not always straightforward. Intrinsic mechanical losses are more fundamental, they occur due to the coupling of strain to internal degrees of freedom in the material [29], like local temperature, the configuration of structural defects, or other phononic modes. In the presence of such a coupling, strain responds to stress not instantaneously but with a delay, equal to the time that it takes for the internal degrees of freedom to relax to a new equilibrium state. In the process of this relaxation some energy is dissipated. Intrinsic damping is also referred to as “internal friction”, as it arises due to inherent material properties, like the nonlinearity of crystalline lattice potential (thermoelastic [58] and Akhiezer [59, 60] damping), or due to structural defects [27, 29, 49]. Note that while the structural defects in crystalline materials can be regarded as imperfections, in amorphous materials some density of them is always present [27].

Mechanical dissipation due to the resonator surface deserves a separate comment. Since the early days of macroscopic resonators, mechanical and chemical surface treatments are known to affect the resonator damping [25], leading to the conclusion that the material in the surface layer has higher mechanical loss than in the bulk. This excess loss is commonly explained by the microscopic complexity of the surface layer [25, 31], which can host an increased number of structural defects, absorb molecules of gas and water, or be covered by oxide in resonators made of reactive elements. The problem of surface loss is particularly relevant to nanomechanical resonators in which the surface-to-volume ratio is high. A lot of data on dissipation in nano- and microscale resonators seems to hint that mechanical losses generally increase with the reduction of resonator size [61]. In some cases, for example in crystalline silicon resonators, the extra loss in the surface layer predominantly comes from the native oxide, and can be reduced by chemical treatment [62, 63]. Mechanical resonators employed in the experiments in this thesis are made of stoichiometric silicon nitride Si_3N_4 . Dissipation in Si_3N_4 films thinner than 100 nm is limited by surface loss, which was reported to have the same order of magnitude in numerous works from several laboratories [64]. It is still a subject of debate what physical mechanism is responsible for the surface loss in Si_3N_4 films, and no way of reducing this loss has been reported to date.

Despite surface losses mechanical dissipation in microscopic resonators can be on par with, or even lower than, that of big macroscopic devices. This, at least in part, is a result of the high degree of control offered by modern nanofabrication techniques, which

makes the elimination of extrinsic losses easier than in the case of macroscopic devices. Recently, quality factors as high as 5×10^{10} at GHz frequencies were demonstrated in silicon resonators [31], enabled by the reduction of mechanical losses at millikelvin temperatures and a carefully designed phononic crystal shield that prevented acoustic radiation. An alternative way of achieving low loss in microscopic mechanical resonators is dissipation dilution by stress, which is a subject of this thesis and is treated in detail in the following. With the help of this technique, we were able to demonstrate nanomechanical resonators with quality factors as high as 8×10^8 at room temperature [32], where the material loss is high.

Whereas systematic studies of mechanical dissipation in solids have a history which is more than a hundred years long, the effect of static stress received little attention until the 1990s. The term “dissipation dilution” appeared for the first time in 1994 in Ref. [33], although the notion of this effect existed earlier in a narrow community [30]. In the 1990s it was known that violin and pendulum modes of suspended masses have higher quality factors when the mass suspensions are under high tension. Since the tension was created by the gravitational potential, an intuitive explanation was proposed [30, 65, 66] that the energy stored in the lossless gravitational potential “dilutes” the internal friction in the strings. Quality factors of mechanical modes were (and still are) commonly simulated using finite-element methods and the loss angle model to describe the material loss. If properly applied, this approach correctly predicts the magnitude of dilution, so the physical interpretation of this effect was of secondary interest for a while.

Later, in 2000s, anomalously high quality factors were observed in nanometric strings and membranes made of highly-strained materials (most notably, silicon nitride [67, 68, 35]). This was as well explained by dissipation dilution [35, 69], without any lossless potential being involved, which motivated revisiting the concept and reformulating it in geometric terms [35, 34]. Dilution at the nanoscale was first recognized in doubly-clamped beam resonators around 2010; Ref. [35] appears to be the first work which applied this concept in a context different than the suspensions of macroscopic pendula. The recognition of dilution in membranes by Yu et.al. [69] followed soon. In these works the mechanical losses of flexural modes of uniform beams [35] and membranes [69] was calculated from a structural mechanics perspective and shown to be much lower than the bulk material loss—in excellent agreement with experiments [35, 64, 69, 54]. These results had partially demystified the effect, but its fully general description was introduced only more recently in our work [34].

A key concept to explain dissipation dilution is the geometric nonlinearity of deformations. When a continuous body is deformed, distances between its points (and hence strains) in general depend nonlinearly on the displacement vectors of these points, which is purely a property of our Euclidean space. Flexural deformations of high aspect-ratio structures have an especially high ratio of nonlinear and linear strains [70]. In high aspect-ratio structures, geometric nonlinearity dominates the Duffing nonlinearity of strongly driven mechanic modes [71], it can give rise to static mechanical nonreciprocity [72], and, in the presence of tensile stress, it creates dissipation dilution [34]. Qualitatively, the dilution mechanism can be explained as follows: The combination of tensile

stress and strong geometric nonlinearity creates a situation where most of the energy is stored by strains that are of the second order of smallness in the mechanical displacements. Because of their small amplitude, such strains couple negligibly to the internal degrees of freedom and do not give rise to intrinsic mechanical losses. Therefore, the elastic energy stored by geometrically nonlinear deformations can be seen in a way as a lossless potential.

By now it is firmly established that dilution by stress is a highly practical tool for the reduction of intrinsic mechanical dissipation irrespective of the microscopic origin of losses. Whereas suspended pendula in which dilution was originally observed are bulky and specialized instruments for fundamental research, on-chip nanoresonators made of suspended high-stress thin films have a much broader range of applications. Thin-film mechanical resonators have a long history, as such geometries are natural for nanofabricated devices, where materials are commonly produced layer-by-layer on a substrate. Initially the development of thin-film resonators was spurred by the need for miniaturization of electromechanical components, including oscillators and filters [73]. Mechanical elements are essential in these devices, as high acoustic quality factors are not easily matched by purely electrical circuits. Electromechanical components, although, do not often require particularly thin films to be free-standing, which makes their acoustic modes similar to those of bulk devices. Low-frequency (kHz to MHz range) free-standing mechanical microresonators, since their early days, were recognized as sensitive probes for small forces and employed in nanoscale sensing. A prominent example is atomic force microscopy [74], others include the detection of magnetic field [75], added mass [76], acceleration [77] and Casimir force [78]. Mechanical resonators employed in Magnetic Resonance Force Microscopy enable the detection of electronic and nuclear magnetic moments with nanometer spatial resolution, and in this way imaging morphologies of complex molecules and simple biological samples [46]. In sensing applications, the cantilever is a common resonator geometry, but membrane and double-clamped beam resonators are also employed. While bringing additional geometrical constraints, they have advantages such as robustness and high quality factors [79, 80], usually related to the fact that they can be subjected to static tension.

Stress is not uncommon in films used for microresonator fabrication, it can be produced by lattice mismatch [81] between the film and substrate or by mismatch in their thermal expansion coefficients [82]. One material which is widely available in the form of high-stress films is silicon nitride. Produced by chemical vapor deposition on silicon substrate, silicon nitride has tensile stress varying from hundreds of MPa in silicon-rich films to ≈ 1.3 GPa in stoichiometric Si_3N_4 films. The combination of high stress and existing techniques for the fabrication of cm-long free-standing structures makes silicon nitride popular in high- Q nanomechanics. Interestingly, sub-100 nm thick free-standing silicon nitride membranes have been commercially available for more than a decade as windows for transmission electron and X-ray microscopy, recognized for their transparency and the ability to sustain differential pressure of more than one atmosphere. Commercial silicon nitride membranes were among the first resonators in which anomalously high quality factors were reported [68, 83], later explained by dissipation dilution. Because

of the combination of low optical absorption and high mechanical quality factors, they were also employed in cavity optomechanics experiments [84, 85].

Practical interest in dissipation dilution has been growing since its discovery in microresonators. Very recently, dilution enabled nanomechanical resonators in the form of patterned membranes and beams to achieve exceptionally high quality factors [36, 32]. By localizing a beam mode away from its supports with a phononic crystal (the “soft clamping” approach introduced by Tsaturyan et al. [36]) and using geometric strain engineering [86] to enhance strain in the beam constriction, we demonstrated quality factors as high as 8×10^8 at room temperature [32]—surpassing even the highest values measured in macroscopic sapphire bars [25]. As time progresses, new and unexpected resonator geometries with enhanced dissipation dilution are being found. We theoretically showed recently [39] that systems of tensioned strings in the shape of self-similar binary trees can have fundamental modes which are effectively soft clamped, and are predicted to have unprecedented quality factors. The concept of soft clamping by string branching proved very generic and has been applied to trampoline membrane resonators in a work that is ongoing in our lab. During the time of writing this thesis, first devices have been fabricated which demonstrate this concept and which levels of dissipation dilution are in a good agreement with theoretical expectations.

2.2 Toy models

2.2.1 A mass on a lossy spring

Before embarking on the general analysis of dissipation in solid-state resonators subjected to stress, it is useful to illustrate the main concepts with the help of toy models.

Every mode of a solid-state resonator behaves as a harmonic oscillator. The simplest model of a conservative oscillator is a mass M mounted on a spring, characterized by the rigidity k , which responds to the deformation x with the force $F = -kx$ (see Figure 2.1A). Intrinsic loss can be introduced in this model by adding a dashpot in parallel to the spring, as shown in Figure 2.1B. The composite structure of a lossless spring and a dashpot will be referred to as a “lossy spring”. If the dashpot is filled with a viscous medium, the force-displacement relation of the lossy spring is given by

$$F = -kx - \eta\dot{x}, \quad (2.2)$$

where η is the viscous damping coefficient and dot stands for time derivative. In the frequency domain², Eq. (2.2) becomes

$$F[\omega] = -(k - ik')x[\omega], \quad (2.3)$$

where $k' = \omega\eta$. Given the form of Eq. (2.3), it is customary to regard $(k - ik')$ as a complex spring constant and express it in terms of magnitude and phase,

$$(k - ik') = |k - ik'|e^{-i\phi}. \quad (2.4)$$

²With Fourier transform given by $x(t) = \int_{-\infty}^{\infty} x[\omega]e^{-i\omega t}d\omega$

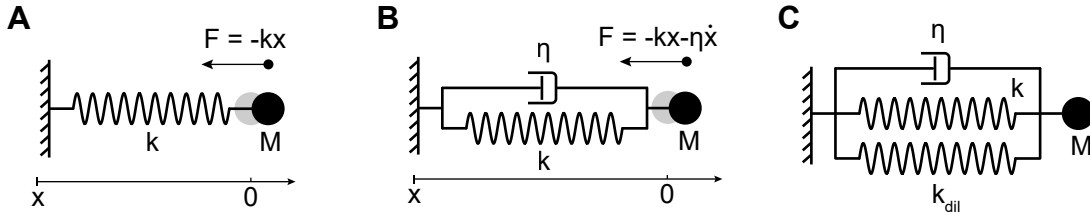


Figure 2.1: (Simple spring pendula. A) A mass on a spring—model of a conservative oscillator. The gray circle indicates the position of the mass at rest. B) Voigt damping model of intrinsic friction in the spring. C) An oscillator with a lossy spring and an extra one, with rigidity k_{dil} , connected in parallel.

The phase ϕ is referred to as “loss angle” for the reason that it characterizes dissipation. In what follows only the case of small dissipation, $\phi \ll 1$, will be considered, in which $|k - ik'| \approx k$.

The viscous damper exerting force proportional to the velocity of the mass is a special case that can be generalized by ascribing frequency dependence to η and k . It can be shown that in this way an arbitrary response function can be constructed that satisfies the requirements of a) being linear in applied force and b) bringing the system to an equilibrium after a steady force has been acting for a sufficiently long time. The frequency domain relation between $F[\omega]$ and $x[\omega]$ in the general case is given by

$$F[\omega] = -k[\omega]e^{-i\phi[\omega]}x[\omega]. \quad (2.5)$$

In the time domain, Eq. (2.5) translates into a relation between the force and the displacement that is more complex than Eq. (2.2) and involves time integration. The general relation between time and frequency domain responses is not discussed in details here, this subject is well presented the literature, for example in Ref. [29]. Note only that the frequency dispersion of the spring and the loss angle need to satisfy

$$k[\omega] = k[-\omega], \quad (2.6)$$

$$\phi[\omega] = -\phi[-\omega], \quad (2.7)$$

in order for the Fourier transform of the force susceptibility, $x[\omega]/F[\omega]$, to be real. The constraint given by Eq. (2.7) needs to be kept in mind when considering the frequency-independent loss angle model—frequency-independence here can only apply to positive frequencies ($\omega > 0$), while at $\omega = 0$ the loss angle is always zero.

2.2.2 Quality factors and dissipation dilution

The dissipation of a mechanical oscillator can be characterized by its quality factor Q , which is defined as the ratio of total stored energy, W , to the average energy lost per radian of free vibration, $\Delta W/(2\pi)$,

$$Q = 2\pi \frac{W}{\Delta W}. \quad (2.8)$$

In order to calculate the Q of a low-loss oscillator, it is convenient to adopt a perturbative approach, in which both W and the energy decrement ΔW are found assuming that the oscillator follows an undamped (conservative) trajectory. For the spring pendula shown in Figure 2.1, the trajectory of lossless motion is given by

$$x(t) = a \cos(\Omega t), \quad (2.9)$$

where $\Omega = \sqrt{k/M}$ is the resonance frequency and a is the vibration amplitude. The stored energy, W , is a constant of conservative motion. It is related to the kinetic energy, $W^{(\text{kin})}$, according to the virial theorem,

$$W = 2\langle W^{(\text{kin})} \rangle, \quad (2.10)$$

where $\langle \dots \rangle$ denotes time averaging over the lossless trajectory given by Eq. (2.9). When dissipation is accounted, the energy ΔW lost per oscillation cycle is found by evaluating the work done by the non-conservative part of the force, $F^{(\text{diss})}$, as

$$\Delta W = - \int_0^T F^{(\text{diss})}(t) \dot{l}(t) dt, \quad (2.11)$$

where T is the oscillation period, and $\delta l(t)$ is the elongation of the spring due to the mechanical displacement³. In the case of our simple pendulum, $\delta l(t) = x(t)$. For $\phi \ll 1$ the dissipative force is found using Eq. (2.9) and Eq. (2.5) to be

$$F^{(\text{diss})}(t) = -k' \frac{\dot{\delta l}(t)}{\Omega}. \quad (2.12)$$

In the case if the loss angle ϕ is frequency dependent, it need to be evaluated at the resonance frequency Ω . Explicitly, the energy decrement is found as

$$\Delta W = 2\pi k' \frac{\langle \dot{\delta l}^2 \rangle}{\Omega^2}, \quad (2.13)$$

and the quality factor as

$$Q = \frac{\Omega^2}{k'} \frac{2\langle W^{(\text{kin})} \rangle}{\langle \dot{\delta l}^2 \rangle}. \quad (2.14)$$

For the simple pendulum in Figure 2.1B, the kinetic energy is $\langle W^{(\text{kin})} \rangle = M\langle \dot{x}^2 \rangle/2$ and the quality factor evaluates to

$$Q = \frac{1}{\phi[\Omega]}. \quad (2.15)$$

The term “dissipation dilution” (aka “loss dilution” or “ Q dilution”) was coined to describe a situation in which the mechanical quality factor is increased by the addition

³If the mass could move in more than one dimension, it would be more precise to say that F is the projection of force on the spring axis. An idealized spring, however, always exerts forces directed along its axis, so even in this case, there would be no need for vector notations.

of a lossless potential to the original lossy spring [65]. Indeed, suppose that a lossless spring with the rigidity k_{dil} is added in parallel to the lossy one with the rigidity k and the loss angle ϕ , as shown in Figure 2.1C. Then the new resonance frequency Ω' and the new quality factor Q' are given by

$$\Omega' = \sqrt{(k + k_{\text{dil}})/M}, \quad (2.16)$$

$$Q' = \left(1 + \frac{k_{\text{dil}}}{k}\right) \frac{1}{\phi[\Omega']}. \quad (2.17)$$

The ratio $D_Q = Q'/Q$ is called dilution coefficient [34]. Examples of settings in which dissipation dilution occurs include a mechanically compliant mirror trapped by an optical potential [87, 88], metallic membrane pinned by the Casimir force [89], or solid-state resonators under tension.

2.2.3 The lossless motion of a mass on lossy tensioned springs

Somewhat counterintuitively, a mechanical structure made of springs, all of which are lossy, can still host vibrational modes free from dissipation. A minimalistic model that demonstrates this is a stretched double-spring pendulum [90] shown in Figure 2.2A. The pendulum consists of the mass M , which can move in the xy plane, and which is connected to two identical springs with the rigidity k and the equilibrium length l . The positions of the other ends of the springs are fixed, in such a way that the springs at rest are elongated by Δl . All springs in Figure 2.2 are lossy in the sense defined in the previous section, but the dashpots are not explicitly shown for the sake of space saving.

To find quality factors, same as in the previous section, we first find the conservative dynamics and then perturbatively include intrinsic losses. For a system involving multiple springs, the quality factor is given by (generalizing Eq. (2.14))

$$Q = \Omega^2 \frac{2\langle W^{(\text{kin})} \rangle}{\sum_i k'_i \langle \dot{\delta} l_i^2 \rangle}, \quad (2.18)$$

where the sum is conducted over all the springs.

The conservative dynamics of the double-spring pendulum can be derived from its classical Hamiltonian, equal to the sum of the kinetic and elastic energies. In equilibrium, the mass is at the coordinate origin, and its displacement by (x, y) from the origin creates the extra elongations δl_1 and δl_2 in the springs one and two, respectively. These elongations are related to the mass displacement as

$$\delta l_{1,2} = \sqrt{(l + \Delta l \pm x)^2 + y^2} - (l + \Delta l) \approx \pm x + \frac{y^2}{2l}. \quad (2.19)$$

The instantaneous elastic energy is given by Hooke's law,

$$W^{(\text{el})} = k \frac{(\Delta l + \delta l_1)^2 + (\Delta l + \delta l_2)^2}{2} = k \left(x^2 + \frac{y^4}{4l^2} + (\epsilon l)^2 + \epsilon y^2 \right), \quad (2.20)$$

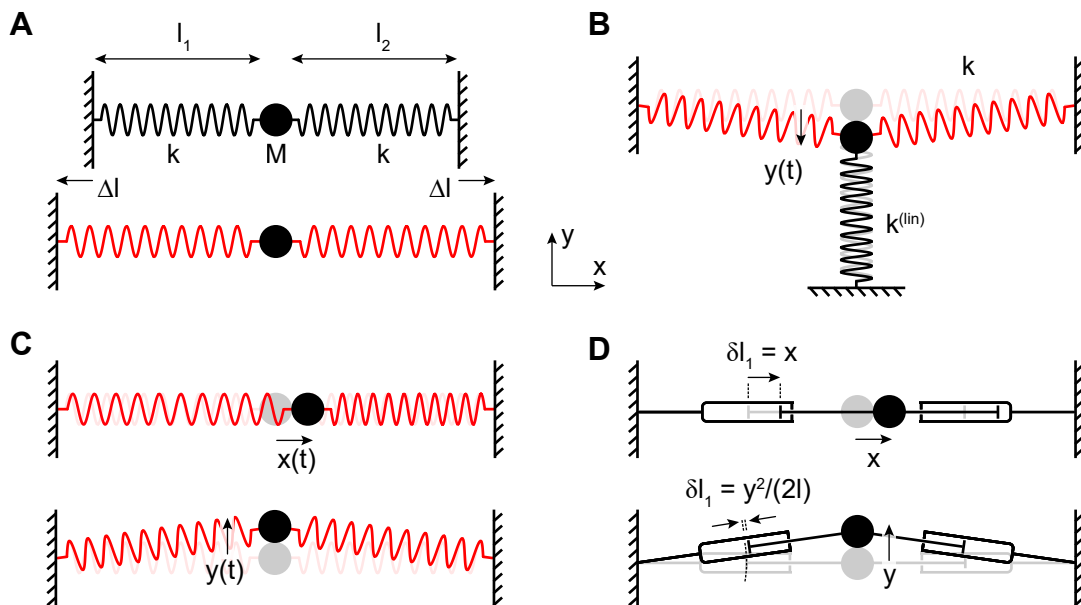


Figure 2.2: Spring models with modes experiencing dissipation dilution. Springs undeformed in equilibrium are shown as black, and springs with static elongation are shown as red. In the panels showing deformations, undeformed geometries are drawn in pale colors. A) A double-spring pendulum with unstretched (top) and stretched (bottom) springs. In equilibrium $l_1 = l_2 = l$. B) T-pendulum, the y mode of which experiences finite dilution. C) The displacements corresponding to the two normal modes of a mass on stretched springs, x mode (top) and y mode (bottom). D) The motions of the effective spring dampers over the vibrations along x (top) and y (bottom) directions.

where $\epsilon = \Delta l/l$ is the static strain. Dropping the static term $(\epsilon l)^2$ and the high-order term $\propto y^4$, the Hamiltonian is found as

$$H = \frac{M(\dot{x}^2 + \dot{y}^2)}{2} + k(x^2 + \epsilon y^2). \quad (2.21)$$

This Hamiltonian has two normal modes, which displacements are oriented along the x and y directions (as shown in Figure 2.2C) and which resonance frequencies are $\Omega_x = \sqrt{2k/M}$ and $\Omega_y = \sqrt{2\epsilon k/M}$, respectively.

The intrinsic losses of the springs have a qualitatively different effect on the x and y modes of the double-spring pendulum. For the x mode, $2\langle W^{(\text{kin})} \rangle = M\langle \dot{x}^2 \rangle$, and $\langle \delta \dot{l}_1^2 \rangle = \langle \delta \dot{l}_2^2 \rangle = \langle \dot{x}^2 \rangle$. After the evaluation of Eq. (2.18) we get the same quality factor as for a simple mass on an unstrained spring,

$$Q_x = \frac{1}{\phi}. \quad (2.22)$$

(We assumed that both springs have the same loss angle ϕ .) The kinetic energy of the y mode is given by $2\langle W^{(\text{kin})} \rangle = M\langle \dot{y}^2 \rangle$, which looks similar to the x mode. However, the

spring elongations in this case are quadratic in displacement,

$$\delta l_1(t) = \delta l_2(t) = \frac{y_0^2}{4l}(1 + \cos(2\Omega_y t)), \quad (2.23)$$

where y_0 is the motional amplitude of the mode. Since $\langle \delta l_1^2 \rangle = O(y_0^4)$ and $\langle W^{(\text{kin})} \rangle = O(y_0^2)$, using Eq. (2.18) we can conclude that the quality factor of the y mode diverges,

$$Q_y \rightarrow \infty, \quad (2.24)$$

as the motional amplitude goes to zero, $y_0 \rightarrow 0$. This result can be explained with the help of Figure 2.2D, in which the deformations of effective spring dampers are shown for the x and the y mode. Infinitesimal displacements of the mass perpendicular to the springs do not elongate them and cause no internal friction loss, in contrast to displacements along the x axis.

The result, on the face of it, appears paradoxical—however lossy the spring material may be, the y mode of the double pendulum never experiences dissipation. This is made possible by the combination of two ingredients: the quadratic, “geometrically nonlinear”, dependence of the spring elongation on the displacement of the mass, and the static stress in the springs. The fact that the geometrically nonlinear dependence of the elongation on the displacement is essential for the mode to be lossless is already apparent from the derivation above. The role of the static stress is to supply a finite trapping potential to the y mode. In the absence of stress, the y mode is “soft”, i.e. its confining potential is higher order than two in displacement. The elastic energy created by the tension in a way acts as a lossless potential, although it is not physically different from the elastic energy in a linearly deformed spring.

The role of tension in dissipation dilution can be made more clear if the quality factor is directly expressed in terms of elastic energies, as

$$Q = \frac{\sum_i k_i (2\Delta l_i \langle \delta l_i \rangle + \langle \delta l_i^2 \rangle)}{\sum_i k'_i \langle \delta l_i^2 \rangle}. \quad (2.25)$$

Obtaining this result from Eq. (2.18) requires the use of the virial theorem, and also the fact that $\dot{\delta l}_i(t) = \Omega \delta l_i(t)$, which is valid since the anharmonic terms are higher-order in the oscillation amplitude. If non of the springs are elongated in equilibrium ($\Delta l_i = 0$), and all of them have the same loss angle $\phi = k'/k$, then, according to Eq. (2.25), the quality factor of any mode is equal to $1/\phi$. If static elongations are present in the system, they can supply additional energy $\propto \Delta l \langle \delta l \rangle$ and lead to an increase in the quality factor. The extra energy is non-zero only if $\langle \delta l \rangle \neq 0$, which, same as the absence of friction loss, also requires geometric nonlinearity of spring deformations.

The double pendulum in Figure 2.2C-D is an extreme example where dilution leads to infinite Q . Mechanical modes in real resonators always store some elastic energy in linear strain and their intrinsic-loss limited Q is finite. The effectively lossless elastic energy, however, results in dissipation dilution for vibrational modes, which is formally analogous to the dilution in the simple model of Sec. 2.2.2. It is not difficult to construct

a spring pendulum that experiences finite dilution, an example of such is the T-shaped pendulum shown in Figure 2.2B. By applying Eq. (2.25), the quality factor of its y mode depicted in the figure is found as

$$Q_{T,y} = \left(1 + \frac{k^{(\text{nl})}}{k^{(\text{lin})}}\right) \frac{1}{\phi}, \quad (2.26)$$

where $k^{(\text{lin})}$ is the rigidity of the vertical spring, and we also introduced the notation $k^{(\text{nl})} = 2\epsilon k$, corresponding to the effective spring constant created by the nonlinearly deformed elements in the presence of stress.

Note, finally, that although the y mode of the double pendulum in Figure 2.2C-D is not affected by intrinsic dissipation, it would be affected by extrinsic losses. For example, if the mass was immersed in a viscous medium that created drag force $-\eta\dot{y}$, the quality factor of the y mode would $Q = M\Omega_y/\eta$.

2.2.4 Suspended pendula

As was mentioned earlier, dissipation dilution by stress was first recognized in vibrational modes of suspended test masses in 1990s. In their seminal work, Gonzalez and Saulson [33] experimentally characterized and theoretically calculated the quality factors of a mass hanging on a thin wire. According to their results, quality factors were increased by the stress in the wire. Around the same time, it was experimentally verified by Huang and Saulson [91] that stress does not affect the intrinsic material loss, so that the increased quality factors observed previously were indeed fully consistent with the dilution model. To provide physical intuition on the origin of dilution, it was argued that the vibrational modes of tensioned strings store the majority of their potential energy as gravitational energy, and not as the elastic energy of deformation. Due to the success of Gonzalez and Saulson's dissipation dilution model, this explanation is widely used to date [65, 66, 92, 93].

In view of recent developments, however, we propose to have a fresh look at the problem and argue that dissipation dilution is related to the geometry of the pendulum motion (and that of the violin modes) rather than to the lossless nature of the gravitational potential. A simple suspended pendulum is depicted in Figure 2.3A-B, it has modes which

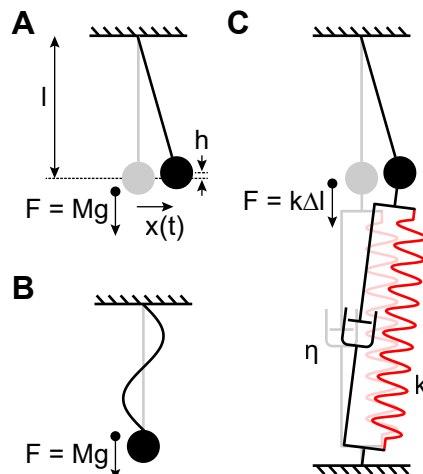


Figure 2.3: Suspended pendulum. A) The pendulum mode of a mass on a wire in the gravitational field. B) A violin mode of the pendulum suspension. C) The pendulum mode of a mass for which the restoring force is created by a tensioned lossy spring.

correspond to the pendulum motion of the mass (Figure 2.3A) and violin standing waves in the wire (Figure 2.3B). The dissipation properties of these modes are very similar, but the pendulum mode is easier to analyze, which we will do next. The gravitational energy $W^{(g)}$ of the mass M at height h is given by,

$$W^{(g)} = Mgh, \quad (2.27)$$

where g is the free fall acceleration. The gravitational potential itself is linear in the elevation h , and hence a mechanical constraint is required to create a quadratic potential suitable for the confinement of mechanical motion. This constraint is the fixed length of the pendulum suspension, which relates the height change to the horizontal mass displacement x as

$$h = x^2/2l. \quad (2.28)$$

The Hamiltonian is given by

$$H = \frac{M\dot{x}^2}{2} + \frac{Mgx^2}{2l}. \quad (2.29)$$

It describes a familiar textbook pendulum with resonance frequency $\Omega = \sqrt{g/l}$.

By the construction of our problem so far, the pendulum mode experiences no dissipation. Indeed, the gravitational potential is lossless, the mass suspension cannot contribute any friction as it does not deform, and the attachments are assumed to be free from any friction as well. One item on this list, however, is not essential to the overall conclusion, which is the lossless nature of the gravitational potential. If we replace the gravitational force acting on the mass by an equal force from a lossy spring-dashpot system, the pendulum mode will remain lossless. The new setting is shown in Figure 2.3C, where the spring is assumed to be much longer than the suspension length l . If the spring elongated in equilibrium by Δl such that

$$k\Delta l = Mg, \quad (2.30)$$

the Hamiltonian of the mode in Figure 2.3C is the same as of the pendulum mode in Figure 2.3A (which is given by Eq. (2.29)). Using the result of the previous section that small displacements of a mass perpendicular to a lossy spring are not affected by the intrinsic loss in the spring, we conclude that the pendulum in Figure 2.3C is also lossless.

The same kind of equivalence applies to the violin modes of the mass suspension. They experience dissipation dilution similar to that of the pendulum mode, and the nature of force producing the tension is unimportant. In the next section 2.4.4, we will analyze flexural modes of strings, and the results will apply equally well to strings tensioned by macroscopic suspended masses and to pre-stressed doubly-clamped nano-mechanical resonators.

2.3 General theory of dissipation dilution

In this section the structural mechanics theory of dissipation dilution is formulated under quite general assumptions. Despite the fact that the majority (if not all) of practical

problems can be solved using simpler 2D and 1D approaches, the 3D formulation is useful in case of doubts, when a careful examination of the validity of underlying simplifications is required. The general formulation also helps developing some physical intuition, and to find out what kind of physical dissipation mechanisms are amenable to dilution.

2.3.1 Deformations, stress and strain in elastic bodies

The mechanics of deformations of continuous solid-state media is described by the theory of elasticity⁴. The position of a body point prior to deformation is parametrized by a radius-vector \mathbf{r} with components x_i . In this section, i and other Latin indices run over the dimensions of the problem, in 3D $i = x, y, z$. The mechanical deformation is defined by mapping

$$\mathbf{r} \rightarrow \mathbf{r}', \quad (2.31)$$

which assigns to every point in the undeformed body a new position \mathbf{r}' with components x'_i . This mapping can be interpreted as a transformation from the material (Lagrangian) coordinates x_i , which deform with the body, to the spatial (Eulerian) coordinates x'_i . A Cartesian system can always be chosen to parametrize the space and the undeformed body, but the material coordinate system of the deformed body is generally curvilinear. The deviation of the material system from Cartesian is negligible if the deformations are small, and we restrict our attention to this case in the following. For a more general consideration and a discussion of validity of this approximation see Appendix A.1.

Small deformations are convenient to characterize using a displacement field \mathbf{u} , defined as

$$\mathbf{u} = \mathbf{r}' - \mathbf{r}. \quad (2.32)$$

The distance between two closely spaced points in the deformed body is related to their coordinate difference dx_i in the absence of deformation as

$$(dx'_i)^2 = dx_i^2 + 2\epsilon_{ij}dx_idx_j, \quad (2.33)$$

where summation over repeated indices is assumed (Einstein convention) and the components ϵ_{ij} of the Green strain tensor are given by [70]

$$\epsilon_{ij} = \frac{1}{2} \left(\frac{\partial u_i}{\partial x_j} + \frac{\partial u_j}{\partial x_i} + \frac{\partial u_k}{\partial x_i} \frac{\partial u_k}{\partial x_j} \right). \quad (2.34)$$

In the theory of large deformations, Eq. (2.33) defines metrics in the material coordinates.

The strain tensor consists of two types of terms, which are, respectively, linear and quadratic in the deformation gradients. If the deformation gradients are small, the

⁴The theory of elasticity is the subject of many textbooks. For example, the reader can refer to the book of Landau and Lifshitz [70] for a pedagogical introduction, and to the book of Berdichevsky [94] for a more detailed exposition, in particular of nonlinear problems.

quadratic part of the strain tensor may be negligible, in which case the deformations are called *geometrically linear* [94], and the strain tensor is given by

$$\epsilon_{ij}^{(\text{lin})} = \frac{1}{2} \left(\frac{\partial u_i}{\partial x_j} + \frac{\partial u_j}{\partial x_i} \right). \quad (2.35)$$

In this case the spatial and material coordinates coincide and the theory simplifies significantly. In the following, however, effects quadratic in deformation gradients will be of key interest, and the *geometrically nonlinear* definition of strain, given by Eq. (2.34), is retained. For our purposes, the material frame differs from the spatial frame by a local rotation at an angle of the order of $\partial u_i/\partial x_j$.

Reversible deformations store elastic energy, which is a key quantity in the formulation of physical laws of mechanical statics and dynamics. In the material coordinates the volumetric density of elastic energy, $w(\mathbf{r})$, is invariant under deformations that do not change distances between body points, i.e. under rotations and translations of the body as a whole. Therefore the elastic energy can depend on the deformation gradients $\partial u_i/\partial x_j$ only via the strain tensor ϵ_{ij} . To the lowest order in the strain, w is given by

$$w = C_{ijkl} \epsilon_{ij} \epsilon_{kl}, \quad (2.36)$$

where C_{ijkl} is a rank-4 tensor of elastic constants specific to the material. Elastic forces inside the body are characterized by the stress tensor σ_{ij} , related to the energy density as

$$\sigma_{ij} = \frac{\partial w}{\partial \epsilon_{ij}}. \quad (2.37)$$

The stress tensor is symmetric, $\sigma_{ij} = \sigma_{ji}$. If energy density is given by Eq. (2.36) the stress is a linear function of strain, and the material is called *physically linear*. The elastic energy in this case can be expressed as

$$w = \frac{1}{2} \sigma_{ij} \epsilon_{ij}. \quad (2.38)$$

In isotropic materials there are only two independent elastic constants, and the stress tensor is related to strain by the generalized Hooke's law

$$\sigma_{ij} = \frac{E}{1+\nu} \left(\epsilon_{ij} + \frac{\nu}{1-2\nu} \epsilon_{kk} \delta_{ij} \right), \quad (2.39)$$

where E is the Young's modulus and ν is the Poisson's ratio. A less formal introduction of the elastic energy as the work performed by elastic forces requires the use of the theory of large deformations and is given in Appendix A.1.

2.3.2 Geometrically nonlinear strain and local rotations

The strain tensor is a sum of linear and nonlinear parts, given, respectively, by

$$\epsilon_{ij}^{(\text{lin})} = \frac{1}{2} \left(\frac{\partial u_i}{\partial x_j} + \frac{\partial u_j}{\partial x_i} \right), \quad \epsilon_{ij}^{(\text{nl})} = \frac{1}{2} \frac{\partial u_k}{\partial x_i} \frac{\partial u_k}{\partial x_j}. \quad (2.40)$$

The nonlinear part, which is quadratic in the displacement gradients $\partial u_i/\partial x_j$, is a continuous counterpart of the quadratic spring elongation that appeared in Sec. 2.2.3 and has the same geometrical origin.

In many problems, the geometrically nonlinear strain is negligible unless deformations are large. Consider, for example, a uniform elongation in x direction, which displacement field is given by

$$u_x = \varepsilon x, \quad u_y = u_z = 0. \quad (2.41)$$

In this case the only non-zero component of strain is $\epsilon_{xx} = \varepsilon + \varepsilon^2/2$, and the geometrically nonlinear contribution is negligible compared to the linear one as far as $\varepsilon \ll 1$. Most conventional solid materials experience fracture or plasticity at strains above percent level [95, 96]. Two-dimensional materials like graphene and MoS₂ can survive strains up to about 10% [97, 98], but yet larger values are truly rare.

A situation when $\epsilon_{ij}^{(nl)}$ is not negligible occurs when the deformations produce zero linear strain, namely if

$$\frac{\partial u_i}{\partial x_j} = -\frac{\partial u_j}{\partial x_i}. \quad (2.42)$$

Let us examine first the local structure of a deformation that satisfies Eq. (2.42) at a given point, which we are free to choose as the coordinate origin. Around this point $a_{ij} = \partial u_i/\partial x_j$ is a constant anti-symmetric matrix, and therefore the coordinate transformation that this displacement field corresponds to is an infinitesimal rotation. Such a transformation is convenient to describe by the vector $\delta\boldsymbol{\varphi} = \delta\varphi \mathbf{n}$, where the unit vector \mathbf{n} and magnitude $\delta\varphi$ (such that $|\delta\varphi| \ll 1$) define the rotation axis and angle, respectively. The components of $\delta\boldsymbol{\varphi}$ are related to a_{ij} as

$$a_{ij} = e_{ikj} \delta\varphi_k, \quad (2.43)$$

where e_{ikj} is the Levi-Civita symbol. With this notation, the local displacement field is given by a constant plus the vector product of $\delta\boldsymbol{\varphi}$ and the radius-vector,

$$\mathbf{u}(\mathbf{r}) = \mathbf{u}(0) + \delta\boldsymbol{\varphi} \times \mathbf{r}. \quad (2.44)$$

The strain tensor produced by this deformation is given by

$$\epsilon_{ij} = \frac{\delta\varphi^2}{2} (\delta_{ij} - n_i n_j). \quad (2.45)$$

It turns out that the displacement field of the form given by Eq. (2.44), which is a linear function of coordinates, is the only solution of Eq. (2.42) in a finite volume (see the end of this section for a proof). Such linear deformations are of limited practical interest, although we will return to them in the following Sec. 2.3.7.

What is important, however, is that the condition of zero linear strain given by Eq. (2.42) can be non-trivially satisfied on a set of points of reduced dimensionality, i.e. a surface or a line. For this reason, geometrically nonlinear strain plays a prominent

role in the theory of shells and beams [70]. Consider, for example, a deformation in the xz plane (i.e. $u_y = 0$) for which the displacement in the z direction, u_z , is an arbitrary function of the x -coordinate only. With the corresponding x -displacement u_x given by

$$u_x(x, z) = -z \frac{\partial u_z(x)}{\partial x}, \quad (2.46)$$

and all other displacements being zero, it can be verified that the linear strain is zero at $z = 0$ for arbitrary x . If the entire structure is “thin” in the z direction, Eq. (2.42) is therefore approximately satisfied in all volume.

Proof that the linear strain can zero everywhere only for a displacement field which a linear function of coordinates. Consider the second derivatives of the displacement field. Assuming that the condition for linear strain to be zero, $\partial u_i / \partial x_j = -\partial u_j / \partial x_i$, is fulfilled everywhere we find

$$\frac{\partial}{\partial x_k} \frac{\partial u_i}{\partial x_j} = -\frac{\partial}{\partial x_k} \frac{\partial u_j}{\partial x_i} = -\frac{\partial}{\partial x_i} \frac{\partial u_j}{\partial x_k} = \frac{\partial}{\partial x_i} \frac{\partial u_k}{\partial x_j} = \frac{\partial}{\partial x_j} \frac{\partial u_k}{\partial x_i} = -\frac{\partial}{\partial x_j} \frac{\partial u_i}{\partial x_k} = -\frac{\partial}{\partial x_k} \frac{\partial u_i}{\partial x_j}. \quad (2.47)$$

The conclusion is that $\partial^2 u_i / \partial x_k \partial x_j = -\partial^2 u_i / \partial x_k \partial x_j$ and therefore for all indices

$$\frac{\partial^2 u_i}{\partial x_j \partial x_k} = 0. \quad (2.48)$$

The solution of Eq. (2.48) is a linear function of coordinates, $u_i = a_{ij} x_j$, where a_i is an arbitrary constant matrix. Inserting this solution into the original constraints, $\partial u_i / \partial x_j = -\partial u_j / \partial x_i$, we find that they are satisfied whenever a_{ij} is antisymmetric. This proves that the coordinate transformation is an infinitesimal rotation, for which $\delta\varphi$ can be found with the help of Eq. (2.43).

2.3.3 Acoustic vibrations

We are interested in the dynamics of acoustic vibrations in the presence of static deformation and static stress. From now on, we will denote by $\bar{x}'_i(\mathbf{r})$ the static deformation and $u_i(\mathbf{r}, t)$ will refer only to the time-dependent displacement field created by acoustic vibrations. The total deformation is thus given by

$$x'_i(\mathbf{r}, t) = \bar{x}'_i(\mathbf{r}) + u_i(\mathbf{r}, t). \quad (2.49)$$

The strain, stress and elastic energy density contain static terms, denoted by bars, and time-dependent terms, produced by the acoustic field and denoted by capital deltas (Δ),

$$\epsilon_{ij}(\mathbf{r}, t) = \bar{\epsilon}_{ij}(\mathbf{r}) + \Delta\epsilon_{ij}(\mathbf{r}, t), \quad (2.50)$$

$$\sigma_{ij}(\mathbf{r}, t) = \bar{\sigma}_{ij}(\mathbf{r}) + \Delta\sigma_{ij}(\mathbf{r}, t), \quad (2.51)$$

$$w(\mathbf{r}, t) = \bar{w}(\mathbf{r}) + \Delta w(\mathbf{r}, t). \quad (2.52)$$

The static and dynamic parts of the energy density are given by

$$\bar{w} = \frac{1}{2} \bar{\sigma}_{ij} \bar{\epsilon}_{ij}, \quad (2.53)$$

$$\Delta w(\mathbf{r}, t) = \bar{\sigma}_{ij} \Delta \epsilon_{ij} + \frac{1}{2} \Delta \sigma_{ij} \Delta \epsilon_{ij}, \quad (2.54)$$

where the last expression is obtained using the identity $\bar{\sigma}_{ij} \Delta \epsilon_{ij} = \bar{\epsilon}_{ij} \Delta \sigma_{ij}$. The equations describing the dynamics of acoustic vibrations can be obtained with the help of the least action principle [94]. If a Lagrangian functional \mathcal{L} is specified in terms of the static strain and the spatial and temporal derivatives of the displacement field, then the action \mathcal{I} is given by

$$\mathcal{I} = \int_{t_0}^{t_1} \int_V \mathcal{L}(x_i, \bar{\epsilon}_{ij}, u_{i,j}, \dot{u}_i) dV dt, \quad (2.55)$$

where the comma-separated subscript is a shorthand notation for partial derivative,

$$u_{i,j} = \partial u_i / \partial x_j. \quad (2.56)$$

Within the required precision, the integration can be done in the Cartesian coordinates of the undeformed material. For elastic bodies in the absence of external volumetric forces the Lagrangian functional is given by the difference of the kinetic and elastic energy densities,

$$\mathcal{L} = \rho \frac{\dot{u}_i^2}{2} - \Delta w. \quad (2.57)$$

We are interested in small vibrations and for the dynamic energy, we only keep terms up to quadratic order in $u_{i,j}$. Within this approximation Δw is given by

$$\Delta w = \bar{\sigma}_{ij} \Delta \epsilon_{ij}^{(nl)} + \frac{1}{2} \Delta \sigma_{ij}^{(lin)} \Delta \epsilon_{ij}^{(lin)}. \quad (2.58)$$

The term $\bar{\sigma}_{ij} \Delta \epsilon_{ij}^{(nl)}$ is not present in Eq. (2.58), since this term is zero if $\bar{x}'_i(\mathbf{r})$ represents an equilibrium deformation field. For the following it is useful to express the total energy as a sum of two contributions containing, respectively, the geometrically linear and nonlinear strain and given by

$$\Delta w^{(nl)} = \bar{\sigma}_{ij} \Delta \epsilon_{ij}^{(nl)}, \quad \Delta w^{(lin)} = \Delta \sigma_{ij}^{(lin)} \Delta \epsilon_{ij}^{(lin)} / 2. \quad (2.59)$$

The term $\Delta w^{(lin)}$ mirrors the generic material elastic energy (as in Eq. (2.38)), whereas $\Delta w^{(nl)}$ is nonzero only in the presence of static stress and geometric nonlinearity of deformations. The expression for Δw can be evaluated explicitly with known material stress-strain relations, but for the following it is sufficient to note that within quadratic approximation the following identity holds

$$\frac{\partial \Delta w}{\partial u_{i,j}} u_{i,j} = 2 \Delta w. \quad (2.60)$$

The variation of action⁵ results in the following dynamical equations

$$\left(\rho \frac{\partial^2}{\partial t^2} + \widehat{O}\right) u_i = 0, \quad (2.61)$$

where \widehat{O} is a linear positive definite self-adjoint operator, which action on u_i is defined by

$$\widehat{O}u_i = -\frac{\partial}{\partial x_j} \left(\frac{\partial \Delta w}{\partial u_{i,j}} \right). \quad (2.62)$$

The solution of Eq. (2.61) for a resonator of finite size is a discrete set of acoustic modes. The displacement field of every mode is the product of a real spatial envelope U_i and a time-dependent amplitude $q(t)$,

$$u_i(\mathbf{r}, t) = U_i(\mathbf{r})q(t), \quad (2.63)$$

where the spatial envelope U_i is an eigenfunction of \widehat{O} , normalized as

$$\int U_i^2 dV = 1. \quad (2.64)$$

After plugging $u_i(\mathbf{r}, t)$ from Eq. (2.63) in Eq. (2.61), multiplying by U_i and integrating over the resonator volume, it is found that $q(t)$ obeys a harmonic oscillator equation,

$$\rho \ddot{q}(t) = -kq(t), \quad (2.65)$$

with the effective spring constant k determined by the elastic energy stored by the spatial envelope of the mode

$$k = \int U_i \widehat{O}U_i dV = 2 \int \Delta w(U_{i,j}) dV. \quad (2.66)$$

The transformation here is made using Eq. (2.60). Next, denoting the spatial envelope of the linear strain produced by the acoustic mode as

$$\mathcal{E}_{ij}(\mathbf{r}) = \frac{1}{2} (U_{i,j} + U_{j,i}), \quad (2.67)$$

and the corresponding stress as

$$\mathcal{S}_{ij}(\mathbf{r}) = C_{ijkl} \mathcal{E}_{kl}, \quad (2.68)$$

the effective spring constant is explicitly found as

$$k = \int (\bar{\sigma}_{ij} U_{k,i} U_{k,j} + \mathcal{S}_{ij} \mathcal{E}_{ij}) dV. \quad (2.69)$$

In a similar way to the elastic energy, k consists of contributions produced by the geometrically linear and nonlinear strains.

⁵For the details of this procedure, which is quite common, see e.g. [94].

2.3.4 Intrinsic mechanical dissipation

Mechanical dissipation is introduced by adding to the elastic stress σ_{ij} an irreversible component, $\sigma_{ij}^{(\text{diss})}$, which is related to strain by a linear response with a finite memory time. This approach dates back to the works of Boltzmann [99] and Zener [100], but its application in our case has one subtlety—it needs to be ensured that the geometrically nonlinear strain is *not* neglected from the beginning. As a starting point, we take the power of energy dissipation $P^{(\text{diss})}$, which is related to the stress and strain as

$$P^{(\text{diss})}(t) = - \int \sigma_{ij}^{(\text{diss})}(\mathbf{r}, t) \frac{\partial}{\partial t} \epsilon_{ij}(\mathbf{r}, t) dV. \quad (2.70)$$

This expression directly follows from the definition of work done by the intrinsic body forces in the material frame and thus so far includes the geometrically nonlinear strain (as shown in detail in Appendix A.1). The most general linear relation between the dissipative stress and strain is given by

$$\sigma_{ij}^{(\text{diss})}(\mathbf{r}, t) = - \int_{V_1} \int_{-\infty}^t \eta_{ijkl}(\mathbf{r}, \mathbf{r}_1, t - t_1) \epsilon_{kl}(\mathbf{r}_1, t_1) dt_1 dV_1, \quad (2.71)$$

where the dissipative susceptibility η_{ijkl} is nonlocal in both time and space. The time dependence of η is responsible for the energy loss and the frequency dispersion of elastic constants. Nonlocality in space also arises naturally in many problems. For example, in thermoelastic damping the strain at \mathbf{r}_1 creates a local elevation of temperature, which affects stresses at all neighboring points \mathbf{r} to which the heat can diffuse within the oscillation period.

In the absence of plastic deformation, the irreversible stress is zero when the body is in a steady state⁶. This assumption is what defines an “anelastic body” [29], and physically means that irreversibility arises due to nonequilibrium dynamical relaxation processes, while quasi-static deformations are reversible. In this case the susceptibility η_{ijkl} has the property

$$\int_0^\infty \eta_{ijkl}(\mathbf{r}, \mathbf{r}_1, \tau) d\tau = 0, \quad (2.72)$$

and in Eq. (2.71) the strain tensor ϵ_{ij} can be replaced by its time-dependent part, $\Delta\epsilon_{ij}$. The rate of the strain change also depends on $\Delta\epsilon_{ij}$ only. Therefore, to the lowest (quadratic) order in displacement gradients only linear stress contributes to dissipation, and the dissipation power is given by

$$P^{(\text{diss})}(t) = \int_V \int_{V_1} \int_{-\infty}^t \eta_{ijkl}(\mathbf{r}, \mathbf{r}_1, t - t_1) \Delta\epsilon_{kl}^{(\text{lin})}(\mathbf{r}_1, t_1) \frac{\partial}{\partial t} \Delta\epsilon_{ij}^{(\text{lin})}(\mathbf{r}, t) dt_1 dV_1 dV. \quad (2.73)$$

Next we suppose that the irreversible stress is much smaller than the elastic stress, $\sigma_{ij}^{(\text{diss})} \ll \sigma_{ij}$, and perturbatively find the power dissipated by an acoustic mode. The

⁶Also, if it so happened that the stress given by Eq. (2.71) caused any static response, it could be eliminated by redefining elastic constants.

linear strain can be factorized in the spatial and temporal parts as $\Delta\epsilon_{ij}^{(\text{lin})} = \mathcal{E}_{ij}(\mathbf{r})q(t)$, where the spatial envelope is evaluated for the acoustic mode in the absence of dissipation and is therefore real. In this case the dissipated power can be expressed as

$$P^{(\text{diss})}(t) = \dot{q}(t) \int_{-\infty}^t \eta(t-t_1)q(t_1)dt_1, \quad (2.74)$$

where

$$\eta(\tau) = \int_V \int_{V_1} \eta_{ijkl}(\mathbf{r}, \mathbf{r}_1, \tau) \mathcal{E}_{ij}(\mathbf{r}) \mathcal{E}_{kl}(\mathbf{r}_1) dV dV_1. \quad (2.75)$$

The generalized dissipative force acting on $q(t)$ can be extracted from Eq. (2.74) using the fact that $P^{(\text{diss})} = -\dot{q}F$. After adding this force, the equation of motion for the vibrational mode amplitude is given by

$$\rho \ddot{q}(t) = -kq(t) - \int_{-\infty}^t \eta(t-t_1)q(t_1)dt_1, \quad (2.76)$$

which describes a damped harmonic oscillator. The rate Γ at which the energy of free oscillations decays is given by

$$\Gamma = -\frac{\text{Im}(\eta[\Omega])}{\rho\Omega}, \quad (2.77)$$

where $\Omega = \sqrt{k/\rho}$ is the oscillator resonance frequency⁷ and $\eta[\omega]$ is the Fourier transform of the dissipative susceptibility,

$$\eta[\omega] = \int_0^\infty \eta(\tau)e^{i\omega\tau} d\tau. \quad (2.78)$$

The presented approach to mechanical dissipation is very generic, and is suitable for the description of quantum damping mechanisms as well as classical. In the quantum picture, the mechanical dissipation rate is the rate of phonon scattering (absorption can be seen as inelastic scattering). Scattering can occur, for example, due to the interaction of phonons with structural defects in amorphous materials, commonly modeled by two-level systems [27], or due to phonon-phonon interaction mediated by the anharmonicity of the atomic lattice potential [101, 31], which is particularly important for phonons at GHz and higher frequencies. The lattice anharmonicity is also responsible for Akhiezer damping [59]. Scattering matrix elements are generally proportional to the phonon strain field $\mathcal{E}_{ij}(\mathbf{r})$ times a spatial function $\mathcal{A}_{ij}(\mathbf{r})$ characteristic to the system to which the acoustic energy is lost. This can be the mean field of other phonons or a delta-function in the case of interaction with localized defects [27]. The rate of scattering Γ_{scat} is found using the Fermi's golden rule as

$$\Gamma_{\text{scat}} = \frac{2\pi}{\hbar} \sum_s \left| \int \mathcal{A}_{ij}^{(s)}(\mathbf{r}) \mathcal{E}_{ij}(\mathbf{r}) dV \right|^2, \quad (2.79)$$

⁷To be more precise, one can put $\Omega = \sqrt{(k + \text{Re}(\eta[\Omega]))/\rho}$, but with the assumption of small η such a correction would be small and unimportant.

where s designates different scattering channels. This expression is equivalent to Eq. (2.77) with the dissipative susceptibility given by

$$\eta_{ijkl}(\mathbf{r}, \mathbf{r}_1, \omega) = -\frac{i\rho\omega}{2} \sum_s \left(\mathcal{A}_{ij}^{(s)}(\mathbf{r}) \mathcal{A}_{kl}^{(s)*}(\mathbf{r}_1) + \mathcal{A}_{ij}^{(s)*}(\mathbf{r}) \mathcal{A}_{kl}^{(s)}(\mathbf{r}_1) \right), \quad (2.80)$$

which shows that scattering can be described within our linear response approach.

2.3.5 Loss angle in a continuous medium

The analysis of mechanical dissipation is significantly simplified if the material is homogeneous, isotropic and the energy in it is dissipated *locally*. Then, same as in the case of elastic constants, there are only two parameters that can enter the dissipative stress-strain relation [102]. Denoting these parameters by $\eta^{(1)}$ and $\eta^{(2)}$, we obtain

$$\sigma_{ij}^{(\text{diss})}(\mathbf{r}, t) = \int_{-\infty}^t \left(\eta^{(1)}(t-t_1) \epsilon_{ij}(\mathbf{r}, t_1) + \eta^{(2)}(t-t_1) \epsilon_{kk}(\mathbf{r}, t_1) \delta_{ij} \right) dt_1. \quad (2.81)$$

A further simplification can be made on the phenomenological basis. Suppose that $\eta^{(1)}$ and $\eta^{(2)}$ are not independent but related in a way so that Eq. (2.81) resembles Hooke's law. Then the dissipative stress is characterized by a single response function $\eta^{(E)}$ and given by

$$\sigma_{ij}^{(\text{diss})}(\mathbf{r}, t) = \int_{-\infty}^t \frac{\eta^{(E)}(t-t_1)}{1+\nu} \left(\epsilon_{ij}(\mathbf{r}, t_1) + \frac{\nu}{1-2\nu} \epsilon_{kk}(\mathbf{r}, t_1) \delta_{ij} \right) dt_1, \quad (2.82)$$

where ν is the Poisson's ratio. It is suggestive to interpret $\eta^{(E)}$ as a dynamic contribution to the Young's modulus, hence the notation. This analogy is especially apparent in the frequency domain. Omitting the tensor indices for brevity⁸, the total (elastic plus irreversible) stress is related to strain as

$$\sigma[\omega] + \sigma^{(\text{diss})}[\omega] = E e^{-i\phi_{\text{mat}}} \epsilon[\omega], \quad (2.83)$$

where $\phi_{\text{mat}}[\omega] = -\text{Im}(\eta^{(E)}[\omega])/E \ll 1$ is the loss angle ascribed to the material⁹, and the Fourier transform is defined in the same way as in Eq. (2.78).

In a medium which dissipation is described by the loss angle model, and which is not subjected to static stress, all mechanical modes dissipate the same fraction of their energy per oscillation period [66]. In fact, the frequency-dependent loss angle of any mechanical mode ϕ is equal to the material loss angle,

$$\phi[\omega] = \phi_{\text{mat}}[\omega]. \quad (2.84)$$

This result can be seen as a mere consequence the construction of the model, by which the dissipative stress is proportional to the elastic stress in the frequency domain. It can

⁸This is equivalent to assuming that all stress components except one, for example σ_{xx} , are zero.

⁹Again, the difference between $|E + \eta[\omega]|$ and E is neglected

be rigorously obtained e.g. by evaluating Eq. (2.75) for the dissipative susceptibility of the loss-angle medium,

$$\eta_{ijkl}(\mathbf{r}, \mathbf{r}_1, \tau) = \frac{\eta^{(E)}(\tau)}{1 + \nu} \left(\delta_{ik} \delta_{jl} + \frac{\nu}{1 - 2\nu} \delta_{ij} \delta_{kl} \right) \delta(\mathbf{r} - \mathbf{r}_1). \quad (2.85)$$

The material loss angle is a less fundamental concept than the loss angle of a spring introduced in Sec. 2.2. Every vibrational mode is dynamically equivalent to a mass on a spring, and can be assigned a loss angle which characterizes the rate of energy dissipation and the response to driving force. Loss angles of different modes are not necessarily identical, as the modes can be affected by different intrinsic dissipation mechanisms. For example, thermoelastic damping affects longitudinal but not shear bulk acoustic waves [70] and flexural but not torsional modes of suspended pendula¹⁰. There is, however, one ubiquitous source of mechanical dissipation which is local and isotropic. This is damping due to structural defects [27], described as tunneling two-level systems (TLS). It is believed to be the dominant source of intrinsic losses in many amorphous materials, which makes the material loss angle model to be particularly suitable in this case. Damping due to two-level systems has also been reported in crystalline materials as silicon [103], although here the physical nature of the defects (if they are structural or electronic [104]) remained debatable. Another use of the material loss angle model is to provide a simplified aggregated description, which may be convenient given the large number of processes that can contribute to dissipation. Even if the model is not exactly applicable, an effective material loss angle can be introduced for broad families of modes. This may be useful as in experiments one is typically restricted to produce mechanical deformations of a certain type, which is specific to the measurement apparatus. For example, in the seminal work in Ref. [28] in order to extract mechanical losses the authors applied bending deformations to rotating bars. In this scheme, loss angles could be measured as the angles of steady-state deflection of the bar ends with respect to the vertical direction. As another example, in the following Sec. 2.4.2, effective loss angle will be introduced for flexural modes in free-standing thin films.

Historically, since at least the 1920s, the loss angle has been a widely used figure of merit for the characterization of dissipative processes in solids [105, 29, 66], including such properties as energy decay rates of acoustic resonances and the attenuation of sound waves. A part of the reason for the popularity of loss angle could be the frequency dependence of losses. Since the work of Kimball and Lovell in 1927 [28], it is known that the typical frequency dependence of intrinsic mechanical losses in solids is quite different from the case of liquids. Whereas in typical liquids the acoustic attenuation coefficient is proportional to frequency, consistent with viscous damping, in solids the attenuation coefficient is usually weakly dependent on frequency and is better describes by a frequency-independent loss angle ϕ . Despite the lack of first-principle explanation, this trend has been ubiquitously seen in experiments with different materials, including metals, dielectrics, and even complex composites like stone and wood [105]. In particular,

¹⁰As torsional modes create no volumetric strain

according to Ref. [27, 106], all amorphous material known to date have almost frequency-independent mechanical losses.

2.3.6 Dissipation dilution by static stress

In solid-state resonators, dissipation dilution emerges in the same way as in the toy models considered in Sec. 2.2.3, where the geometrically nonlinear elongations of tensioned springs supplied extra rigidity for some modes without contributing to their dissipation. After the necessary preliminaries, we are now in a position to introduce this concept in a more general way.

Using the results of the previous sections, the quality factor of an acoustic mode is found as

$$Q = \frac{\Omega}{\Gamma} = -\frac{k}{\text{Im}(\eta[\Omega])}. \quad (2.86)$$

Here the effective spring constant k is given by Eq. (2.69) and $\eta[\omega]$ found from the combination of Eq. (2.75) and Eq. (2.78). From Sec. 2.3.4 it follows that the damping factor η is not expected to explicitly depend on static deformations (there are rare exceptions from this rule, see e.g. [107]). In contrast, the spring constant k incorporates a term directly proportional to the static stress. Thus, by applying tensile stress to the material the quality factor of the acoustic mode can be increased. (It should be noted that η can implicitly depend on stress as the stress affects vibrational mode shapes, but this fact does not qualitatively change the final conclusion.)

The quality factor increase can be interpreted as being due to a diluting potential, created by the elastic energy of geometrically nonlinear strain in the presence of static stress. To make the analogy formal, we can decompose the effective spring constant as

$$k = k^{(\text{lin})} + k^{(\text{nl})}, \quad (2.87)$$

where $k^{(\text{lin})}$ and $k^{(\text{nl})}$ are the parts contributed by the geometrically linear and nonlinear dynamic strains, respectively, which are given by

$$k^{(\text{lin})} = \int \mathcal{S}_{ij} \mathcal{E}_{ij} dV, \quad k^{(\text{nl})} = \int \bar{\sigma}_{ij} U_{k,i} U_{k,j} dV. \quad (2.88)$$

The quality factor can be expressed as a product of the “intrinsic” value Q_{int} and a dilution factor D_Q ,

$$Q = D_Q Q_{\text{int}}, \quad (2.89)$$

where the dilution factor is given by

$$D_Q = 1 + \frac{k^{(\text{nl})}}{k^{(\text{lin})}}, \quad (2.90)$$

and the “intrinsic” value of the quality factor is

$$Q_{\text{int}} = -\frac{k^{(\text{lin})}}{\text{Im}(\eta[\Omega])}. \quad (2.91)$$

The term “intrinsic” here should be used with caution (hence the quotes) as Q_{int} is not necessarily completely independent of static stress. Indeed, static stress affects the vibrational mode shape $U_i(\mathbf{r})$, and therefore the envelopes $\mathcal{S}_{ij}(\mathbf{r})$ and $\mathcal{E}_{ij}(\mathbf{r})$ on which $k^{(\text{lin})}$ and η are dependent. It is, however, natural to expect that the variation of Q_{int} with stress is much weaker than that of D_Q (for the experimental validation of this see e.g. [108], while Ref. [107] presents a rather exotic counterexample). Theoretically, Q_{int} is expected to be completely independent of mode shape when the intrinsic loss is described by the material loss angle ϕ_{mat} . In this case [66],

$$Q_{\text{int}} = 1/\phi_{\text{mat}}. \quad (2.92)$$

In all situations of practical interest in the following Q_{int} can be assumed to be constant.

There are two alternative formulas for the dilution coefficient that are useful in practical calculations. The first one relates the total spring constant to the kinetic energy, so that the dilution factor is given by

$$D_Q = \frac{\rho\Omega^2}{k^{(\text{lin})}}. \quad (2.93)$$

This is obtained using the fact that $(k^{(\text{lin})} + k^{(\text{nl})})\langle q(t)^2 \rangle = \rho\langle \dot{q}(t)^2 \rangle$, where $q(t)$ is the temporal part of the vibrational mode and $\langle \dots \rangle$ means time averaging over one period of harmonic oscillations. Alternatively, if one works with unnormalized mode profiles, the dilution can be expressed as the ratio of time-averaged energies $\langle W^{(\text{lin})} \rangle$ and $\langle W^{(\text{nl})} \rangle$ stored by the mode,

$$D_Q = 1 + \frac{\langle W^{(\text{nl})} \rangle}{\langle W^{(\text{lin})} \rangle}. \quad (2.94)$$

The energies are only different from the corresponding spring constants by the same constant factor.

Before concluding, we would like to make one remark. Whereas it was shown that static *tensile* stress can add an effectively lossless potential to mechanical modes, *compressive* stress has the opposite effect and can reduce quality factors [109]. Compressive stress creates a negative $k^{(\text{nl})}$, to the point that the total spring rigidity can become zero and an instability can occur (known as “buckling instability” [70] in the theory of elastic beams). Mechanical elements with stiffness reduced by compressive stress (so called “spring-antispring” systems) are useful for designing vibrational isolators, as the isolation level is inversely proportional to the resonance frequency. In this case the tradeoff between the reduction of the resonance frequency and the increase in thermal noise must be considered [109].

2.3.7 A continuous toy model with infinite dilution

There is no fundamental limitation on how high dissipation dilution of a vibrational mode can be, even when restricted to resonators of given size or frequency. In this section we provide an example of a continuous structure which has a mechanical mode

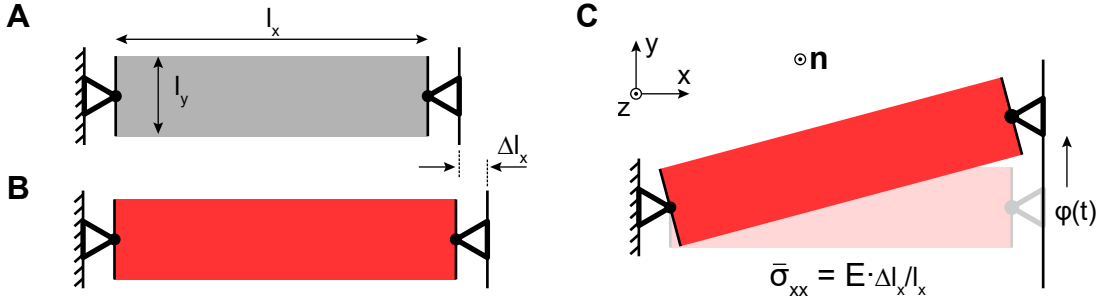


Figure 2.4: A setting in which a block of lossy material possesses a lossless vibrational mode. The block is fixed between two walls by prisms, in a way that it is free to pivot on the prism connections. The left prism is rigidly fixed, and right prism is free to slide up and down with no orientation change. All elements that are colored black are assumed to have infinite rigidity. A) Dimensions of the block. B) Static elongation. C) A geometrical transformation that is free of linear strain. In the presence of static stress, it corresponds to the spatial displacement profile of a lossless vibrational mode.

with infinite D_Q , i.e. for which the dissipation is zero in the presence of material loss. Unfortunately, implementing such a structure would require a combination of boundary conditions that is rather uncommon in reality, and therefore the model mostly serves the purpose of concept demonstration.

A mechanical mode is not affected by material loss if its displacement field does not produce geometrically linear strain. In Sec. 2.3.2, it was shown that this can only happen if the displacement field is a sum of a constant vector, which corresponds to the motion of the body as a whole and therefore is uninteresting, and an infinitesimal rotation (see Eq. (2.44)). The displacement field of the rotation part is given by

$$\mathbf{u}(\mathbf{r}) = (\mathbf{n} \times \mathbf{r})\varphi, \quad (2.95)$$

where \mathbf{n} is a constant unit-norm vector and φ is the rotation angle. This transformation is an actual rotation only in the linear approximation, so in fact it stretches the material quadratically in φ , hence producing geometrically nonlinear strain.

In order to visualize this deformation, consider it applied to a rectangular block of material with dimensions $l_x \times l_y \times l_z$ shown in Figure 2.4A. The aspect ratio of the block plays no role, so all dimensions are assumed to be of the same order of magnitude. Figure 2.4C shows the deformation, $\mathbf{r} \rightarrow \mathbf{r}'$, corresponding to Eq. (2.95) with \mathbf{n} directed along z axis. In coordinate notations, the deformation is given by

$$\begin{bmatrix} x' \\ y' \end{bmatrix} = \begin{bmatrix} 1 & -\varphi \\ \varphi & 1 \end{bmatrix} \begin{bmatrix} x \\ y \end{bmatrix}. \quad (2.96)$$

The setup in Figure 2.4 is a continuous analog of the lossless spring oscillator considered previously in Sec. 2.2.3. Similar to the spring oscillator, static stress is required in order for the nonlinear strain to store elastic energy quadratic in deflection. With static

elongation added along x axis as shown in Figure 2.4B, the deformation in Figure 2.4C produces elastic energy density

$$\Delta w^{(\text{nl})} = \bar{\sigma}_{xx} \varphi^2 / 2, \quad \Delta w^{(\text{lin})} = 0, \quad (2.97)$$

(found using Eq. (2.45)), thus creating harmonic oscillator potential for φ . The resonance frequency of motion in this potential is found as

$$\Omega = \sqrt{\frac{12}{l_y^2 + 4l_x^2} \frac{\bar{\sigma}_{xx}}{\rho}}. \quad (2.98)$$

This mechanical mode is free of linear strain and is therefore not affected by the intrinsic material dissipation. It has infinite Q , if the constraints that enforce the boundary conditions are ideal. In reality, a direct attempt to implement the structure in Figure 2.4 would face the problem of extrinsic losses—rotation and sliding friction in the attachment points could easily overwhelm the reduction of intrinsic loss.

The structure in Figure 2.4, similar to any real mechanical resonator, has an infinite number of modes. While its fundamental mode is not affected by intrinsic losses, the high order modes are. In general, it appears unlikely that in any structure all modes can experience high dissipation dilution at the same time. In all practical cases known so far, dissipation dilution is only important for a selected family of modes below a certain frequency. At high frequencies the acoustic wavelength inevitably gets short compared to the resonator size and the modes become reminiscent of bulk waves, for which the geometrically nonlinear contribution to strain is small (see Ref. [54] for related experimental results). The high-order modes of the resonator shown in Figure 2.4 include standing waves with frequencies above $\Omega \sim (\sqrt{E/\rho})/l$

Hamiltonian of the mode in Figure 2.4C. The zero linear strain field given by Eq. (2.95), strictly speaking, is a *quasi-static* deformation, which means that it satisfies Eq. (2.61) with no time dependence. Such a deformation can correspond to a vibrational mode which frequency is far below all other acoustic resonances of the structure, which is naturally fulfilled when the static stress is small, $\bar{\sigma}_{xx} \ll E$. With this, the Hamiltonian for $\varphi(t)$ is given by

$$H = I \frac{\dot{\varphi}^2}{2} + V \bar{\sigma}_{xx} \frac{\varphi^2}{2}, \quad (2.99)$$

where

$$I = \frac{M}{12}(l_y^2 + 4l_x^2), \quad M = V\rho, \quad V = l_x l_y l_z, \quad (2.100)$$

are the block moment of inertia, mass and volume, respectively.

2.3.8 A numerical example

To conclude the general discussion, we consider a more realistic example of mechanical resonator, which shape is shown in Figure 2.5A. Section 2.3.6 provides a recipe for

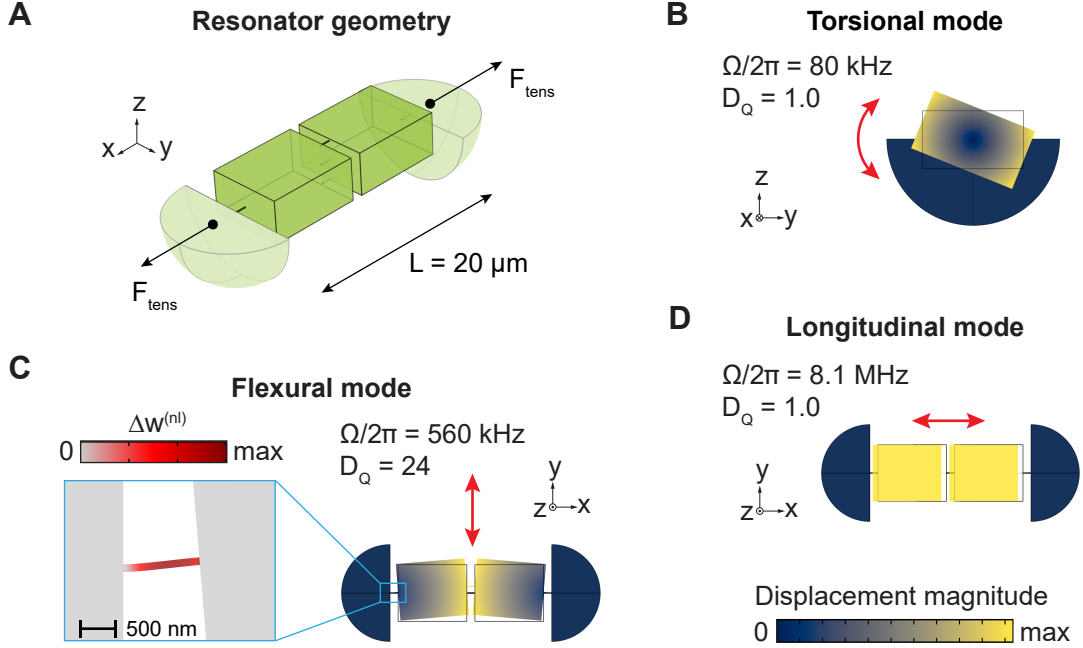


Figure 2.5: A) Resonator geometry. Each block has a size of $7 \times 4 \times 8.5 \mu\text{m}$, the blocks are separated by $1 \mu\text{m}$ -long 100 nm -diameter bridges and clamped to the fixed quarter-square parts (shown in pale green). B) Torsional mode. C) Flexural mode and the spatial distribution of lossless elastic energy $\Delta w^{(nl)}$. D) Longitudinal mode.

the numerical calculation of dissipation dilution of arbitrary vibrational modes. We apply this recipe to a few representative modes from different families, which resonance frequencies and displacement profiles are found with the help of finite element simulation.

The resonator in question has micro- to nano- scale features, it consists of two blocks, each $7 \times 4 \times 8.5 \mu\text{m}$ in size, separated by $1 \mu\text{m}$ -long 100 nm -diameter bridges. The structure is suspended between two fixed pads, to which it is clamped by bridges of the same size. The resonator is assumed to be made of silicon nitride ($E = 250 \text{ GPa}$, $\nu = 0.23$, $\rho = 3100 \text{ kg/m}^3$). The static tension is introduced by initially adding an isotropic pre-stress in the material equal to 1.1 GPa , and then letting it relax to an equilibrium configuration. This physical scenario is typical for MEMS resonators, where stresses are produced during material synthesis. However, once the static stress distribution is known, the way it was created does not matter, so we could equally assume that the structure is tensioned by external forces applied to the pads as shown in Figure 2.5A.

The simulation results show that the low-frequency modes of the resonator in Figure 2.5 can generally be classified as flexural, torsional or longitudinal. The fundamental modes of each family are shown in Figure 2.5B-C, together with their frequencies and D_Q factors. Among the modes shown, only the flexural one experiences dissipation dilution, whereas the torsional and longitudinal modes do not. This observation provides a warning: although dissipation dilution is also known as “stress dilution” in

nanomechanics, it would not correct to assume that the mere presence of tensile stress increases vibrational quality factors. This fact seems to be quietly known in the community of gravitational wave detection, at least statements that the losses of torsional and longitudinal modes of the same structure that has high- Q flexural modes are not diluted by the gravitational potential sporadically appear in the discussions of test mass suspensions ([110] mentions dilational and [93] torsional modes). Now we can give a physical explanation to this observation—the displacement profiles of non-flexural modes create elastic energies dominated by geometrically linear strains. For longitudinal modes, the nonlinear contribution to energy compares to the linear¹¹ as $\bar{\sigma}/E \ll 1$. The absence of geometrically nonlinear energy for torsional modes may not be so obvious in view of the relation of geometric nonlinearity to rotations, but here there is no static deformation perpendicular to the rotation axis, which is required for lossless elastic energy to emerge.

So far the total lossless elastic energy has been discussed. A visualization of its spatial density, $\Delta w^{(nl)}(\mathbf{r})$, for the flexural mode in Figure 2.5C shows that the lossless energy is distributed highly inhomogeneously—it is entirely concentrated in the thin bridges. This is mostly explained by the concentration of static stress in constrictions, which will be extensively discussed further for the 1D case in Sec. 2.5.2.

It does not seem straightforward to come up with a general-purpose recipe how to optimize dissipation dilution, in the first place because the optimum depends on experimental constraints. As was shown in Sec. 2.3.7, there is no fundamental limit on how high the dilution can be. The optimum under constraints specific to thin-film nanomechanical resonators will be discussed separately in the following sections. Nevertheless, two trends of general relevance can be clearly identified. First of all, since the nonlinear part of strain tensor is only non-negligible when the linear part is small, dissipation dilution favors flexural modes of high aspect ratio structures. This is widely known since the strong dilution was first identified in pendulum suspensions [33] and nano- beams and membranes [68, 35]. Dilution does not typically take place for modes in which the directions of deformation and dynamic strain coincide. Secondly, a mechanical resonator of strongly non-uniform shape has a strongly inhomogeneous strain distribution with peak values greatly exceeding the average [34]. This limits the acceptable average stress (and hence the average dilution) as the peak needs to stay below the material yield value. Therefore, unless the vibrational mode is confined inside a region of locally high stress, an overly strong inhomogeneity of the resonator shape is likely to be disadvantageous. In the case where the resonator is patterned from a material with fixed pre-stress, highly non-uniform shapes also reduce the average stress that remains in the structure after the relaxation.

¹¹Correspondingly, the frequency of the fundamental longitudinal mode is higher than that of the fundamental flexural mode by a factor of $\sim \sqrt{E/\bar{\sigma}}$

2.4 Resonators with reduced dimensionality

Resonators with reduced dimensionality are natural (and so far the only practically realized) structures in which high dissipation dilution can emerge. Chip-scale quasi two-dimensional membrane and one-dimensional beam resonators are now routinely produced by patterning and suspending high-stress material films. Dilution factors D_Q as high as 6×10^5 have been experimentally realized [32], and theoretical values realistically accessible using existing fabrication techniques seem even higher.

In this section we present the theory of dissipation dilution in resonators with reduced dimensionality, concentrating on the case of microfabricated devices. Such devices have a few common constraints, the main of which are the following.

1. Constant resonator thickness. The variation of thickness is usually less straightforward to implement than the variation of in-plane shape, which can be controlled by lithographic patterning.
2. Hard-clamped boundary conditions (will be rigorously defined later).
3. Static stress patterns, consistent with the relaxation of originally homogeneous pre-stress in a film upon its suspension. A key aspect of this process is that the stress is reduced on average but is locally enhanced in constrictions [86, 111, 112].

These constraints will be generally respected in the following, although some results will also be presented in more general forms, wherever it is possible to do so without adding too much complexity.

The reduction of dimensionality will be introduced progressively. The two dimensional case is still quite complex, but the resulting equations are practically useful for FEM simulations. In the one-dimensional case, a number of analytical results will be obtained, which also give qualitative insights in the behavior of more complex two-dimensional structures.

Before turning to the rigorous analysis of high aspect ratio structures under stress, it is instructive to consider the spring models of a beam shown in Figure 2.6, which illustrate several key features of flexural deformations. Typical flexural modes of high-aspect ratio resonators under stress are standing waves, which for a uniform doubly-clamped beam have sinusoidal displacement profiles with zeros at the clamping points. Such standing waves can be reproduced in a simple model shown in Figure 2.6A, which consists of a chain of identical point masses connected by identical springs. The chain is a direct extension of the lossless oscillator geometry presented in Sec. 2.2.3, it has finite flexural rigidity only in the presence of tensile stress, and its flexural modes have no intrinsic dissipation because all the strain they produce is geometrically nonlinear. The elastic energy stored by a flexural mode is parametrically proportional to the static stress, for which reason this energy is referred to as “tension energy”.

The strain produced by the deformation shown in Figure 2.6A is fully geometrically nonlinear only as far as the structure is infinitely thin. A more realistic beam model is shown in Figure 2.6B. It consists of two spring chains and has finite thickness, which means that the constituent springs experience geometrically linear deformation

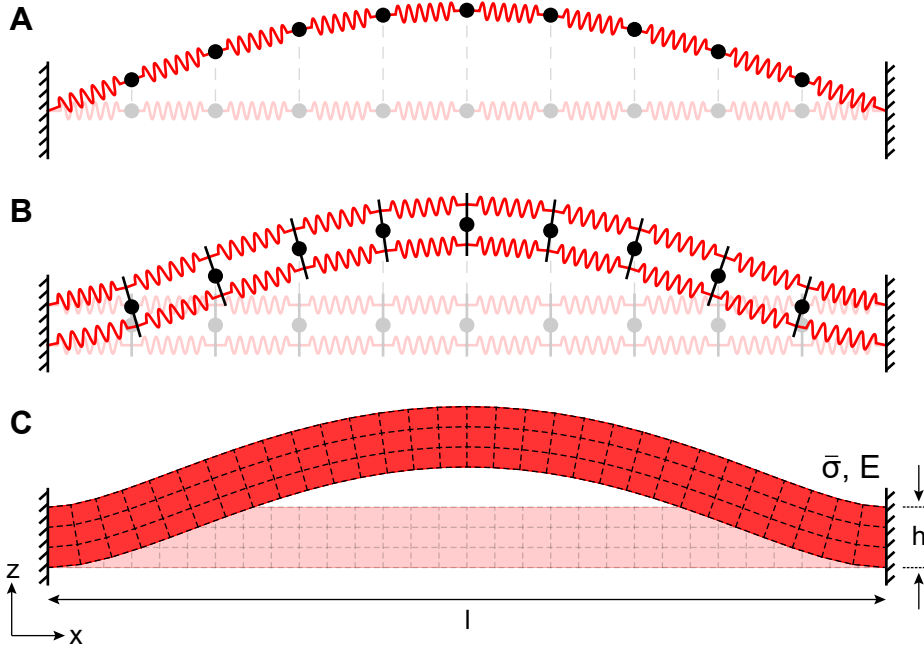


Figure 2.6: Flexural deformations, corresponding to the fundamental mode of a beam and its spring-mass models. The structures in saturated colors are deformed according to the mode profiles, semi-transparent undeformed geometries are also shown for comparison. (A) Single chain of springs—no bending rigidity, model for a beam with $\lambda = 0$. (B) Double-layer spring chain—finite bending rigidity, $\lambda = 0.07$. (C) Deformation of a continuous beam, $\lambda = 0.07$.

and their intrinsic loss contributes to the resonator dissipation. The magnitude of geometrically linear strain is determined by how fast the mode gradient changes, and thus is proportional to the bending curvature of the mode. For this reason, the linear part of elastic energy is called “bending” energy. As illustrated in Figure 2.7, the deformation of each segment in Figure 2.6B can be decomposed into the superposition of an infinitesimal rotation, which only produces geometrically nonlinear strain, and bending, which only produces linear strain. The elastic energies of two deformations add up as if they were applied independently (this fact follows from the general argument that led to Eq. (2.58)).

The relative importance of tension and bending energies in a uniform beam or a membrane is quantified by the strain parameter λ [69, 64], defined as

$$\lambda = \frac{h}{l} \sqrt{\frac{1}{12\bar{\epsilon}}}, \quad (2.101)$$

where h , l and $\bar{\epsilon}$ are the structure thickness, lateral size and static strain, respectively (see Figure 2.6C). In resonators with $\lambda \ll 1$ the tension energy dominates and their flexural modes have high dissipation dilution. The frequencies and shapes of low-frequency

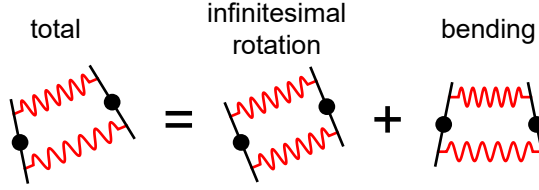


Figure 2.7: Deformation decomposition of a segment of the structure in Figure 2.6B.

modes¹² in this case are well described even when the bending is completely neglected. The structure in Figure 2.6A has $\lambda = 0$ (since its thickness is zero), in Figure 2.6B and C the mode shapes are plotted assuming $\lambda = 0.07$.

It is noticeable in Figure 2.6B and C, which show displacement profiles of actual vibrational modes of a beam, that the bending is the largest near the resonator clamps. It turns out in fact, that the total geometrically linear contribution to the elastic energy is commonly dominated by the small region around the clamps. Devising ways to avoid this “clamp-bending” contribution is crucial to design resonators with enhanced dissipation dilution.

2.4.1 2D—membranes

In order to describe dissipation dilution in what is called membrane resonators in nanomechanics, they are modeled as “plates”, according to the terminology of structural mechanics. A plate is a flat structure where the size in one direction is much smaller than in the other two, but the bending rigidity is not negligible. We choose to follow experiment-oriented language and refer to membrane resonators as membranes, which should not lead to confusion.

We consider a membrane with uniform thickness h which in equilibrium is aligned along the xy plane so that its center is at $z = 0$. The instantaneous state of stress in a thin membrane is fully characterized by four components of the stress tensor belonging to the xy plane. The remaining stresses are zero,

$$\sigma_{xz} = \sigma_{yz} = \sigma_{zz} = 0. \quad (2.102)$$

The non-zero stresses form a two-dimensional tensor σ_{ij} , in which the indices run over only two values, x and y . Accounting for the constraints given by Eq. (2.102), we can find the in-plane stress-strain relations as

$$\sigma_{ij} = \frac{E}{1 + \nu} \left(\epsilon_{ij} + \frac{\nu}{1 - \nu} \epsilon_{kk} \delta_{ij} \right), \quad (2.103)$$

where $i, j = \{x, y\}$. The strain components containing z among their indices are depen-

¹²For high frequency modes the effective λ is obtained by substituting the acoustic wavelength for the resonator length.

dent on the in-plane strains and are given by

$$\epsilon_{zz} = -\frac{\nu}{1-\nu}(\epsilon_{xx} + \epsilon_{yy}), \quad \epsilon_{xz} = \epsilon_{yz} = 0. \quad (2.104)$$

While the vertical stress σ_{zz} is zero, the vertical strain ϵ_{zz} is not due to Poisson's effect.

In-plane stresses can be produced by static in-plane deformations and by dynamical deflections of membrane along z direction. The equilibrium distribution of static stress, $\bar{\sigma}_{ij}(x, y)$, satisfies the force balance condition,

$$\frac{\partial \bar{\sigma}_{ij}}{\partial x_j} = 0. \quad (2.105)$$

The geometrically linear approximation is typically appropriate for the description of static deformations, in which case $\bar{\sigma}_{ij}$ can be found in terms of biharmonic functions using Airy's method [113] or complex potentials [114]. Solutions yielded by analytic methods, however, are complicated, and their practical utility in problems involving dissipation dilution has not been apparent so far. Finite-element numerical simulation is usually a more practical way of solving Eq. (2.105) and obtaining the equilibrium stress distribution.

In the following, the way the distribution of static stress is created makes no difference, and we assume that $\bar{\sigma}_{ij}$ is known. The specific case, however, which is relevant to our experiments is that of nanomechanical membranes. Here the stress distribution is a result of relaxation of homogeneous and isotropic pre-stress σ_{film} in the film. The components of initial stress and strain in the film are given by

$$\sigma_{ij}^{(\text{init})} = \begin{bmatrix} \sigma_{\text{film}} & 0 \\ 0 & \sigma_{\text{film}} \end{bmatrix}, \quad \text{and} \quad \epsilon_{ij}^{(\text{init})} = \begin{bmatrix} \epsilon_{\text{film}} & 0 \\ 0 & \epsilon_{\text{film}} \end{bmatrix}, \quad (2.106)$$

where $\epsilon_{\text{film}} = \sigma_{\text{film}}(1 - \nu)/E$ according to Eq. (2.103). If the membrane has holes, the uniform stress distribution is not an equilibrium one, as the boundary condition of zero normal force is not satisfied at the edges of holes. The stress assumes a new configuration after the membrane is released. In our experience, finite element simulations provided reliable information regarding the distribution of static stress, judging by the agreement of experimental resonator quality factors with theory. Interestingly, as was demonstrated by Capelle et al. [112], the full anisotropic pattern of relaxed stress can be experimentally characterized by analyzing the polarization of light, transmitted through the sample. The spatial resolution of this technique (not implemented in our lab) was on the order of 10 μm .

We are concerned with flexural acoustic modes in a statically stressed membrane. The three-dimensional deformation field produced by membrane flexure is fully characterized by the displacement of the membrane center ($z = 0$) in the z direction. We denote the function characterizing this displacement as $u(x, y, t)$ without subscripts, so that by definition

$$u(x, y, t) \equiv u_z(x, y, 0, t). \quad (2.107)$$

The plane $z = 0$ is known as the neutral plane, as distances between its points do not change upon small flexural deformations. Conditions of zero stress (Eq. (2.102)) constrain the three-dimensional deformation field in such a way that its x and y components are given by [70]

$$u_x(x, y, z, t) = -z \frac{\partial u(x, y, t)}{\partial x}, \quad u_y(x, y, z, t) = -z \frac{\partial u(x, y, t)}{\partial y}, \quad (2.108)$$

and with sufficient precision $u_z \approx u$, which means there is no variation of u_z along z . The in-plane components of dynamic strain $\Delta\epsilon_{ij}$ are found by inserting this parametrization of the displacement field in the general three-dimensional expression [70],

$$\Delta\epsilon_{ij} = -zu_{,ij} + \frac{1}{2}u_{,i}u_{,j}. \quad (2.109)$$

For the sake of brevity, we introduced a shorthand notation for spatial derivatives by using comma-separated indices,

$$u_{,i} \equiv \frac{\partial u}{\partial x_i}, \quad u_{,ij} \equiv \frac{\partial^2 u}{\partial x_i \partial x_j}, \quad (2.110)$$

where, again, $i, j = \{x, y\}$. Strain components other than those in Eq. (2.109), although they might be non-zero, do not contribute to the elastic energy.

With the help of Eq. (2.109), the dynamic parts of the elastic energy are found in terms of the derivatives of u as

$$\Delta w^{(\text{lin})} = \frac{E}{2(1-\nu^2)} z^2 \left((u_{,ii})^2 + (1-\nu)(u_{,ij}u_{,ij} - (u_{,ii})^2) \right), \quad (2.111)$$

$$\Delta w^{(\text{nl})} = \frac{1}{2} \bar{\sigma}_{ij} u_{,i} u_{,j}. \quad (2.112)$$

These are volumetric energy densities, which can be integrated over z and in this way related to unit area. Next, by integrating over the entire membrane area, the total elastic energy $W \equiv \int \Delta w \, dz dS$ is obtained,

$$W^{(\text{lin})} = \frac{h\mathcal{D}}{2} \int \left((u_{,ii})^2 + (1-\nu)(u_{,ij}u_{,ij} - (u_{,ii})^2) \right) dS, \quad (2.113)$$

$$W^{(\text{nl})} = \frac{h}{2} \int \bar{\sigma}_{ij} u_{,i} u_{,j} dS. \quad (2.114)$$

Here \mathcal{D} is the bending rigidity, defined as

$$\mathcal{D} = \frac{Eh^2}{12(1-\nu^2)}. \quad (2.115)$$

Note that above $\mathcal{D} \propto h^2$, whereas according to a common alternative definition $\mathcal{D} \propto h^3$. The linear parts of strain (Eq. (2.109)) and energy (Eq. (2.113)) are related to the *curvature* of the displaced neutral plane, while their nonlinear parts (Eq. (2.109) and Eq. (2.114)) are related to the *gradient*.

The expressions for the elastic energy allow us to obtain the dynamical equation of motion for $u(x, y, t)$ using the least action principle (the action is given by Eq. (2.55)). The variation of simplified action is a more straightforward route than directly simplifying the 3D dynamical equations of motion. One aspect of the variational problem that is different in the case of a membrane is that here the order of the dynamical equations is higher than in 3D (four versus two). This is not a paradox, as $u(x, y, t)$ that parametrizes the membrane deformation is not the actual deformation field but rather a proxy for its description. Consistent with the differential order, for every edge of the membrane there are two boundary conditions to be satisfied by u . If the membrane edge is clamped, the boundary conditions are

$$u = 0, \quad \partial u / \partial \mathbf{n} = 0, \quad (2.116)$$

where \mathbf{n} is a unit vector in the xy plane oriented normal to the edge. When a membrane edge is free, the boundary conditions are more cumbersome (they are explicitly given, for example, in [70]).

The dynamical equation for $u(x, y, t)$ obtained from the least action principle is

$$\mathcal{D} u_{,iijj} - \bar{\sigma}_{ij} u_{,ij} + \rho \frac{\partial^2 u}{\partial t^2} = 0. \quad (2.117)$$

The case of a uniform square membrane with no holes and isotropic stress distribution was analytically treated by Yu et al. in the SI of Ref. [69]. Generally, Eq. (2.117) can be solved numerically in the usual way by first expressing the deflection field as a product of a spatial envelope and a time-dependent oscillating factor, and then finding eigenfunctions $U(x, y)$ and eigenfrequencies Ω of the resulting problem,

$$\mathcal{D} U_{,iijj} - \bar{\sigma}_{ij} U_{,ij} = \Omega^2 \rho U, \quad (2.118)$$

using finite-element modeling. Once the vibrational modes are found, the effective linear and non-linear spring constants can be determined from their spatial envelopes $U(x, y)$ (assumed to be normalized so that $\int U^2 dS dz = 1$, consistent with the 3D case) as

$$k^{(\text{lin})} = h \mathcal{D} \int ((1 - \nu) U_{,ij} U_{,ij} + \nu (U_{,ii})^2) dS, \quad (2.119)$$

$$k^{(\text{nl})} = h \int \bar{\sigma}_{ij} U_{,i} U_{,j} dS. \quad (2.120)$$

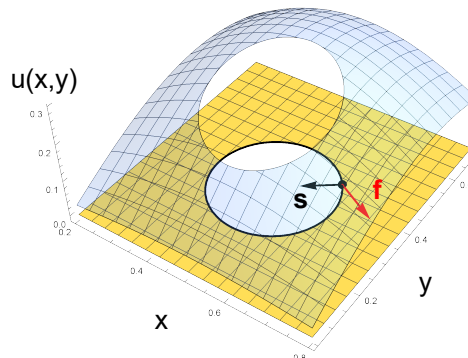


Figure 2.8: Out of plane deformation, $u(x, y)$, of a membrane with a hole. For one point on the hole edge, the red arrow shows the vector \mathbf{f} (Eq. (2.126)), and the black arrow shows the unit normal vector \mathbf{s} .

The dissipation dilution coefficient of the mode is obtained using the general recipe, $D_Q = 1 + k^{(\text{nl})}/k^{(\text{lin})}$.

While the above information is already sufficient for numeric simulations of mode spectra and dissipation dilution in planar structures, there is an interesting interpretation of bending elastic energy in geometric terms. Any surface is locally determined up to a rotation by two parameters, the mean curvature H and the Gaussian curvature K [115]. For the weakly deformed neutral plane of a membrane, these curvatures are given by

$$H = \frac{1}{2}u_{,ii} = \frac{1}{2} \left(\frac{\partial^2 u}{\partial x^2} + \frac{\partial^2 u}{\partial y^2} \right), \quad (2.121)$$

and

$$K = \frac{1}{2}((u_{,ii})^2 - u_{,ij}u_{,ij}) = \frac{\partial^2 u}{\partial x^2} \frac{\partial^2 u}{\partial y^2} - \left(\frac{\partial^2 u}{\partial x \partial y} \right)^2. \quad (2.122)$$

The bending energy of an isotropic uniform surface is completely determined by these parameters. Indeed, bending energy given by Eq. (2.113) can be expressed in terms of the curvatures as

$$W^{(\text{lin})} = h\mathcal{D} \int (2H^2 - (1 - \nu)K) dS. \quad (2.123)$$

While the contribution of the mean curvature to the energy is genuinely local, the contribution of the Gaussian term is related to the geodesic curvature k_g of membrane edges by the Gauss-Bonnet theorem, [115, 116]

$$\int K dS = \left(2\pi - \oint_{\partial S_{\text{out}}} k_g dl \right) - \sum_n \left(2\pi - \oint_{\partial S_{\text{hole},n}} k_g dl \right). \quad (2.124)$$

The boundary contributions here come from all simple loops forming the edge of the deformed membrane. This includes the outer edge, ∂S_{out} , which is typically clamped, and the free edges of holes, $\partial S_{\text{hole},n}$, indexed by n . For a weakly deformed membrane, the Gauss-Bonnet theorem is expressed as,

$$\int K dS = \int_{\partial S} f_i ds_i, \quad (2.125)$$

where the components of vector \mathbf{f} are given by

$$f_i = (u_{,i}u_{,jj} - u_{,j}u_{,ij})/2, \quad (2.126)$$

and $d\mathbf{s}$ is a vector which is everywhere oriented perpendicular to the membrane edges and which norm is equal to the length of the arc element (see Figure 2.8). Eq. (2.125) is easy to verify, since the divergence of \mathbf{f} is equal to the Gaussian curvature, $\partial f_i / \partial x_i = K$. There is one subtle difference between Eq. (2.124) and Eq. (2.125)—whereas the integration dl in Eq. (2.124) is conducted over the edges of the deformed membrane, the integration ds_i is defined in the xy plane.

The boundary contribution of hard-clamped edges on the right hand side of Eq. (2.124) is always zero, since the membrane around hard-clamped edges is locally flat and for any

loop on a flat plane $\oint k_g dl = 2\pi$. This in particular means that Gaussian curvature does not manifest in any way in vibrations of a simple uniform membrane hard-clamped on all sides, as was first pointed out in [69]. For a membrane with holes, or in a hypothetical case when the boundary conditions on the outer edge are different from hard-clamped, the energy produced by Gaussian curvature is generally not negligible [117, 118]. It is remarkable that this energy is not distributed over the surface, but stored as excess geodesic curvature at the membrane edges.

2.4.2 Effective material loss angle in thin films

In thin-film resonators, a material loss angle can be introduced not as a local volumetric property, but as a local property of the surface, averaged over the strain energy profile in the z direction. This makes the loss angle model applicable to a wider range of practical situations compared to the bulk case.

As was discussed previously, intrinsic mechanical dissipation occurs because of the coupling of the dynamic strain field created by an acoustic mode to internal material degrees of freedom. The material loss angle model can be appropriate if the acoustic energy is dissipated locally. In thin films, the spatial relaxation of internal degrees of freedom (e.g. the equilibration of temperature) happens much faster in the direction perpendicular to the film than that parallel to the film, to the extent that the parallel relaxation is often completely negligible. This makes some damping mechanisms that are non-local in general act effectively locally in thin films. Examples of such mechanisms are thermoelastic [58] and Akhiezer [59] dampings.

Another circumstance (likely the most important one, in fact) that favors the loss-angle description of energy relaxation in thin films is that in sub-micron films surface losses are significant. It is generally believed that surfaces of nanofabricated devices host an increased number of two-level systems (TLS), which commonly dominate mechanical damping. Experimental evidence in support of this has been reported for devices made of both amorphous [119] and crystalline [120, 121, 31] materials. The microscopic origin of two-level systems on the surface is not necessarily clear, and is probably different in different cases. This is supported by the fact that estimates of the thicknesses of the surface layer vary drastically, ranging from nanometers [31] to hundreds of microns [122]. In any case, surface losses dissipate acoustic energy locally and uniformly in space, with respect to the dimensions parallel to the film.

In order to put the ideas above into mathematical form, we can derive the dissipative response of vibrational mode in the same way it was done in three dimensions (Eq. (2.75)). For flexural modes all the components of linear strain are proportional to the second derivatives of the mode shape, $U(\mathbf{r})$, and have the same z -dependence, given by Eq. (2.109)-2.104. Therefore, dissipative susceptibility integral runs over the surface rather than the volume and is given by

$$\eta(\tau) = h \int_S \int_{S_1} \tilde{\eta}_{ijkl}(\mathbf{r}, \mathbf{r}_1, \tau) \frac{\partial^2 U}{\partial x_i \partial x_j}(\mathbf{r}) \frac{\partial^2 U}{\partial x_k \partial x_l}(\mathbf{r}_1) dS dS_1, \quad (2.127)$$

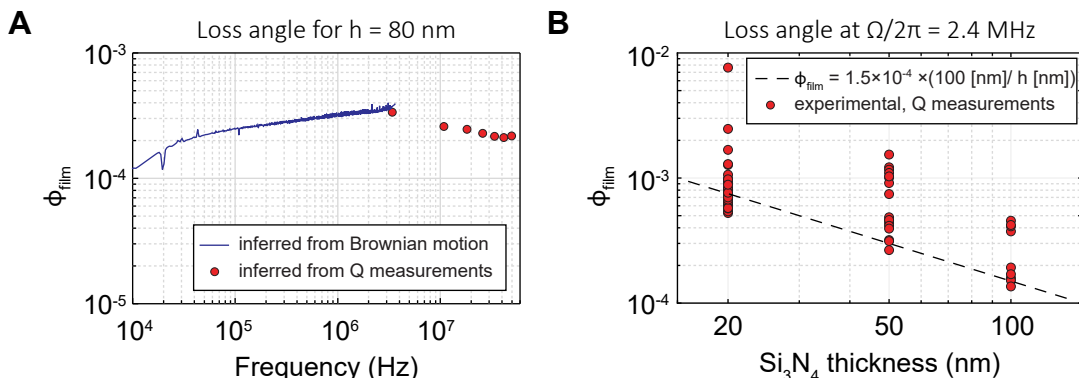


Figure 2.9: Loss angle in silicon nitride films produced at the CMI. A) Loss angle as a function of frequency for $h = 80$ nm. Measured for a nanobeam integrated with a microdisk optical cavity [123]. B) Loss angle as a function of film thickness, inferred from the measurements of quality factors of soft-clamped modes in PnC nanobeams at frequencies in the 2.2-2.6 MHz range [32].

where indices run over x and y , $\mathbf{r} = (x, y)$, and $\tilde{\eta}_{ijkl}$ is linearly related to its three dimensional counterpart in Eq. (2.75) (as shown in the end of the section). The loss angle description, same as in three dimensions, is obtained by assuming that $\tilde{\eta}_{ijkl}$ has the form of Hooke's law (Eq. (2.103)) with delayed response. The loss angle of a film is equivalent to the thickness average of the material loss angle,

$$\phi_{\text{film}} = \frac{12}{h^3} \int_{-h/2}^{h/2} \phi_{\text{mat}}(z) z^2 dz. \quad (2.128)$$

A common phenomenological model of surface loss assumes that the material is characterized by the bulk loss angle ϕ_{bulk} , in addition to which there is an infinitely thin layer on the surface that makes finite contribution to the dissipation. In which case Eq. (2.128) simplifies to

$$\phi_{\text{film}} = \phi_{\text{bulk}} + a_{\text{surf}}/h. \quad (2.129)$$

As was mentioned already, all flexural modes have the same distribution of stress in the z direction, so the aggregated loss angle ϕ_{film} is the same for all out-of-plane flexural modes. However, other mode families, e.g. in-plane modes, do not have the same z -distribution of stress. Therefore, they might have a somewhat different loss angle, although it is not easy to imagine a situation in which this difference would be large.

Compelling experimental evidence in favor of the surface loss model given by Eq. (2.129) exists for silicon nitride films produced by PECVD and LPCVD deposition. This trend was first pointed out in a metastudy made by Villanueva and Schmid [64], and later the inverse scaling of loss angle with film thickness was directly confirmed in Ref. [36] and in our work [32]. According to the average data from [64], for silicon nitride films

$$\phi_{\text{film}} = 3.6 \times 10^{-5} + 1.7 \times 10^{-4} \frac{100 \text{ [nm]}}{h \text{ [nm]}}. \quad (2.130)$$

The corresponding bulk material quality factor is $Q_{\text{bulk}} = 2.8 \times 10^4$, and the surface loss-limited $Q_{\text{surf}} = 6 \times 10^3$ for $h = 100$ nm.

Despite the overall consistency found by [64], the loss angles of films produced in different cleanrooms can still show spread by more than a factor of two. Numbers for films of different thicknesses deposited in the same facility are in a much better agreement. Experimental results presented in this thesis were obtained with films from 20 nm to 100 nm thick, which were produced by LPCVD deposition at the CMi¹³. The bulk contribution to the loss angle of such thin films is negligible, and the experimentally measured resonator quality factors [32, 37] are consistent with the surface-dominated loss angle given by

$$\phi_{\text{film}} = 1.5 \times 10^{-4} \frac{100 \text{ [nm]}}{h \text{ [nm]}}. \quad (2.131)$$

This corresponds to intrinsic quality factor $Q = 6900$ at 100 nm. The experimental characterization of frequency dependence and scaling with thickness of the loss angle in our Si_3N_4 films is summarized in Figure 2.9.

Relation between three dimensional and film damping susceptibilities. The damping susceptibility of the film, $\tilde{\eta}_{ijkl}$, can be found by explicitly separating the terms in Eq. (2.75) which contain z among their indices. Then, expressing the strains $\Delta\epsilon_{xz}$, $\Delta\epsilon_{yz}$ and $\Delta\epsilon_{zz}$ as functions of the derivatives of $U(\mathbf{r})$ with the help of 2.104, one obtains

$$\begin{aligned} \tilde{\eta}_{ijkl}(\mathbf{r}, \mathbf{r}_1, \tau) = & \frac{1}{h} \int_{-h/2}^{h/2} \int_{-h/2}^{h/2} \left(\eta_{ijkl}(\mathbf{r}, \mathbf{r}_1, z, z_1, \tau) - \frac{\nu}{1-\nu} (\eta_{zzkl}(\mathbf{r}, \mathbf{r}_1, z, z_1, \tau) \delta_{ij} + \right. \\ & \left. \eta_{ijzz}(\mathbf{r}, \mathbf{r}_1, z, z_1, \tau) \delta_{kl}) + \frac{\nu^2}{(1-\nu)^2} \eta_{zzzz}(\mathbf{r}, \mathbf{r}_1, z, z_1, \tau) \delta_{ij} \delta_{kl} \right) z z_1 dz dz_1. \end{aligned} \quad (2.132)$$

Here the indices i, j, k, l run over x and y only, and $\mathbf{r} = (x, y)$. The normalization by $1/h$ is a matter of convention.

2.4.3 Clamping curvature

Flexural modes in high stress and high aspect ratio structures are generally well described even neglecting the bending term in Eq. (2.117), which makes the dynamic equation wave-like,

$$-\bar{\sigma}_{ij} u_{,ij} + \rho \frac{\partial^2 u}{\partial t^2} = 0. \quad (2.133)$$

This approximate equation, however, has lower differential order than the original one and its solution cannot satisfy all the original boundary conditions. In the clamped case, only the condition $u = 0$ is satisfied by the solution of Eq. (2.133), while $\partial u / \partial \mathbf{n}$ is not. Even a coincidental satisfaction of the second constraint is not possible. For a second order equation, the definition of a solution value and its first derivatives in one

¹³EPFL Center of MicroNanoTechnology

place determines the function everywhere, and hence the only solution of Eq. (2.133) fully compatible with hard-clamped boundary conditions (Eq. (2.116)) is zero. It is well known since the works in Ref. [35, 69] that the boundary condition incompatibility has profound consequences for dissipation dilution, giving rise to clamping curvature. The satisfaction of both hard-clamped boundary conditions requires that there is a region near the membrane edge where the bending term in Eq. (2.117) dominates, which is only possible at the expense of large high-order derivatives and hence large mode curvature.

A naive estimation based on the expression for the spring constants in Eq. (2.119) and Eq. (2.120) suggests that the magnitude of dissipation dilution when $k^{(\text{nl})} \gg k^{(\text{lin})}$ is given by

$$D_Q \approx k^{(\text{nl})}/k^{(\text{lin})} \sim 12\sigma l_a^2/(Eh^2), \quad (2.134)$$

where l_a is acoustic wavelength, so that $\partial u/\partial x \sim u/l_a$. Clamping curvature, however, changes this scaling. In reality the dilution is more typically estimated as the square root of the above value,

$$D_Q \sim \sqrt{12\sigma l_a^2/(Eh^2)}, \quad (2.135)$$

which is much lower. In the following Sec. 2.4.6 the effect of clamping curvature will be analyzed in great detail for quasi one-dimensional beams. The case of membranes is more complex in general, although effects and trends that exist for beams generally have direct analogs here.

2.4.4 1D—beams with arbitrary cross section

Beams are effectively one-dimensional structures in which both transverse dimensions, the width and the height, are much smaller than their length. The problem of flexural vibrations in this case is much simpler than in the case of membranes, in particular the static stress configuration can be found in a closed form. As a consequence, a number of analytical results can be obtained in one dimension [34].

In the following, we will first give the expression for dissipation dilution of beams under no specific assumptions about the cross-section shape. Next we will consider in more details the case which is particularly relevant to nanomechanical resonators—out-of-plane vibrations of thin-film structures, characterized by rectangular cross-section of uniform thickness. The generic treatment comes at a small cost and is useful for at least two reasons. First, it is applicable to macroscopic strings, which typically have a circular cross-section, often of non-uniform diameter [110, 122, 124]. Although finite-element modeling of dissipation dilution in non-uniform macroscopic strings used as suspensions of test masses has been reported, e.g. in Ref. [92, 92], these works do not provide explicit expressions for D_Q and use terminology specific to the situation when tension is created by the gravitational field. Second, the general expressions we will develop are applicable to in-plane vibrational modes of thin-film resonators. Although in-plane modes generally have lower dilution than out-of-plane modes, they are still useful in applications involving geometrical constraints. For example, in-plane modes of phononic crystal nanobeam resonators have recently been employed in near-field coupled optomechanical devices [125].

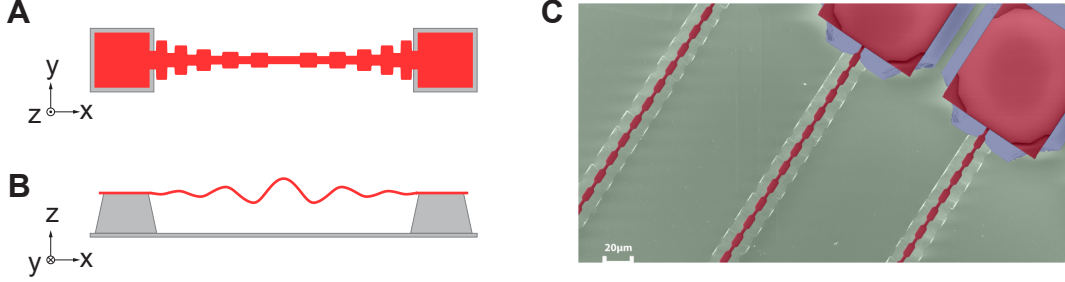


Figure 2.10: Example beams with non-uniform cross section. A) Profile sketch of a tapered phononic crystal beam, shown to illustrate the orientation with respect to coordinate axes. B) Localized vibrational mode of the beam in (A). C) False-colored scanning electron microscope image of an array of nanofabricated phononic crystal beams. Green and blue—silicon substrate, red—silicon nitride.

The assumed orientation of the beam with respect to coordinate axes is shown in Figure 2.10A-B, where the structure is aligned along the x axis and the vibrational mode displacement is along z . In a beam oriented this way, stress and strain are fully characterized by their xx components. While the remaining components of stress tensor are zero, the same is not true for strain because of the Poisson's effect. Instead, ϵ_{yy} and ϵ_{zz} are proportional to ϵ_{xx} . It turns out that the static deformation in the transverse direction has no effect on the vibrational modes, whereas the dynamic part $\Delta\epsilon_{yy}$ contributes to the linear (lossy) elastic energy. Zero stress in the y direction implies that there is always transverse bending curvature $u_{,yy}$ for the vibrating mode, given by

$$u_{,yy} = -\nu u_{,xx}. \quad (2.136)$$

In order to describe the static stress and strain distributions we define

$$\bar{\sigma} \equiv \bar{\sigma}_{xx}, \quad \bar{\epsilon} \equiv \bar{\epsilon}_{xx}. \quad (2.137)$$

Similar to the transition from three to two dimensions, the equation describing the vibrations of a beam is easier to obtain from the variation of action, rather than from simplifying Eq. (2.117) for a two dimensional plate. The composition of action requires knowledge of elastic energies, which can be found by further reducing the two dimensional expressions in Eq. (2.111)-2.112. The geometrically linear (bending) energy density is given by

$$\Delta w^{(\text{lin})}(x, y, z) = \frac{E}{2(1-\nu^2)} z^2 \left((1-\nu)(u_{,xx}^2 + u_{,yy}^2 + 2u_{,xy}^2) + \nu(u_{,xx} + u_{,yy})^2 \right), \quad (2.138)$$

which has to be simplified using the quasi-one dimensionality assumptions, $u_{,xy} = 0$ and $u_{,yy} = -\nu u_{,xx}$ (Eq. (2.136)). The simplification of the geometrically nonlinear (tension) term for the one-dimensional case is done by setting $u_{,y} = 0$. Overall, the result is

$$\Delta w^{(\text{lin})}(x, y, z) = E z^2 (u_{,xx})^2 / 2, \quad (2.139)$$

$$\Delta w^{(\text{nl})}(x, y, z) = \bar{\sigma} (u_{,x})^2 / 2. \quad (2.140)$$

The integration over cross section, and then over the beam length yields total elastic energies,

$$W^{(\text{lin})} = \int_l \frac{E}{2} I(x) (u_{,xx})^2 dx, \quad (2.141)$$

$$W^{(\text{nl})} = \frac{\mathcal{T}}{2} \int_l (u_{,x})^2 dx, \quad (2.142)$$

where \mathcal{T} is the tension force along the beam and $I(x)$ is the cross section geometric moment of inertia. Finally, the kinetic energy is given by

$$W^{(\text{kin})} = \int_l \frac{\rho_l}{2} (\dot{u})^2 dx, \quad (2.143)$$

where ρ_l is the linear mass density. I and ρ_l are given, respectively, by

$$I = \int z^2 dy dz, \quad \text{and} \quad \rho_l = \int \rho dy dz, \quad (2.144)$$

where the integrations are conducted over the beam cross section.

In a beam, the variation of displacement field, $u(x, t)$, is negligible over the cross section, so it is only a function of x and time. Correspondingly, the spatial profile $U(x)$ of a vibrational mode is a function of single variable, and we denote its derivative by U' ,

$$U'(x) \equiv U_{,x}(x). \quad (2.145)$$

Unlike the cases of higher dimensions where the distribution of stress entered non-trivially in the elastic energy, in one dimension it is characterized by a single value of the tension force $\mathcal{T} = \bar{\sigma}(x)A(x)$, where $A(x)$ is the cross section area. The fact that the tension is constant along the structure is required by the simple law of force equilibrium, therefore the fact that it can be taken out of the integral in Eq. (2.142) is quite fundamental.

The variation of action, composed of the energies from Eq. (2.141)-2.143, yields the well-known Euler-Bernoulli equation [70]

$$\frac{d^2}{dx^2} \left(EI(x) \frac{d^2 U(x)}{dx^2} \right) - \mathcal{T} \frac{d^2 U(x)}{dx^2} - \rho_l(x) \Omega^2 U(x) = 0. \quad (2.146)$$

the solution of which gives eigenfrequencies Ω and vibrational mode shapes $U(x)$. For a doubly clamped structure, the boundary conditions are

$$U(0) = U(l) = 0, \quad U'(0) = U'(l) = 0. \quad (2.147)$$

The effective spring constants are obtained from Eq. (2.141)-2.142 by formal substitution $u(x, t) \rightarrow U(x)$ as

$$k^{(\text{lin})} = \int_l EI(x) (U_{,xx})^2 dx, \quad (2.148)$$

$$k^{(\text{nl})} = \mathcal{T} \int_l (U_{,x})^2 dx, \quad (2.149)$$

and the dissipation dilution is found using the general recipe, $D_Q = 1 + k^{(\text{nl})}/k^{(\text{lin})}$. These expressions for spring constants are valid for beams and strings with arbitrary cross sections, the only assumption (which has been implicit so far) is that the structure is symmetric with respect to xz and xy planes so that it supports z -polarized flexural modes.

2.4.5 Thin-film beams

Next we consider more closely beams patterned from thin films. Such structures have a rectangular cross section in the yz plane with the second moment of area given by

$$I(x) = w(x)h^3/12, \quad (2.150)$$

where w is the width in y -direction and h is the thickness in the direction of deformation, z . While the thickness is constant, the width is, generally, x -dependent. We will first find the distribution of static stress along the beam and then will derive the dimensionless form of Euler-Bernoulli equation, which is particularly well suited for theoretical analysis.

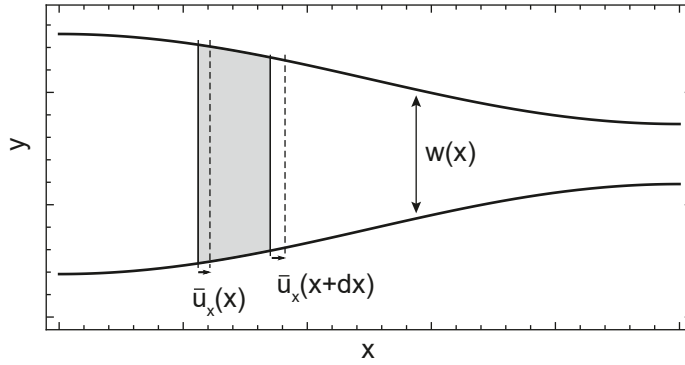


Figure 2.11: Beam profile and static deformation field

In a thin-film resonator the axial tension force, \mathcal{T} , originates from the pre-stress, σ_{film} , which exists in the film prior to suspension. In order to find how the tension force is related to σ_{film} , it is convenient to introduce the displacement field of static in-plane deformation in x direction, \bar{u}_x . This field is related to strain as usual,

$$\bar{\epsilon}(x) = \frac{d}{dx}\bar{u}_x(x). \quad (2.151)$$

In the process of stress relaxation \bar{u}_x is fixed in the beginning and in the end of the beam, because the material is clamped to the frame there, so that

$$\bar{u}_x(0) = 0, \quad \bar{u}_x(l) = \epsilon_{\text{film}}l, \quad (2.152)$$

where $\epsilon_{\text{film}} = \sigma_{\text{film}}(1 - \nu)/E$ is the uniform pre-strain of the film and ν is Poisson's ratio. The balance of tensile force requires $w(x)\bar{\sigma}(x) = \text{const}$, which is expressed in terms of

the displacement as

$$Eh w(x) \frac{d}{dx} \bar{u}_x(x) = \mathcal{T}. \quad (2.153)$$

The displacement field is found by integration,

$$\bar{u}_x(x) = \frac{\mathcal{T}}{hE} \int_0^x \frac{dx_1}{w(x_1)}, \quad (2.154)$$

and, using the boundary conditions from Eq. (2.152), the equilibrium tension is related to the film pre-stress as

$$\mathcal{T} = \sigma_{\text{film}}(1 - \nu)h \left(\frac{1}{l} \int_0^l \frac{dx}{w(x)} \right)^{-1}. \quad (2.155)$$

The balance of tensile force allows one to express the distribution of static stress along the beam in a suggestive form,

$$\bar{\sigma}(x) = \sigma_{\text{avg}}/v(x), \quad (2.156)$$

where $v(x) = w(x)/w_0$ is the variation of beam width relative to the mean value, w_0 , given by

$$w_0 = \frac{1}{l} \int_0^l w(x) dx, \quad (2.157)$$

and σ_{avg} is the stress, averaged over the beam volume,

$$\sigma_{\text{avg}} = \frac{1}{hw_0l} \int_0^l hw(x)\bar{\sigma}(x) dx = \frac{\mathcal{T}}{w_0h}. \quad (2.158)$$

It will be shown in the following Sec. 2.4.7 that the average stress satisfies $\sigma_{\text{avg}} \leq \sigma_{\text{film}}(1 - \nu)$.

The relation in Eq. (2.156) means that there is one-to-one correspondence between the bending moment of the beam (defined as EI , which is $\propto v(x)$) and local static stress. This can create some ambiguity of interpretation for the origin of dissipation dilution enhancement in non-uniform beams—whether it comes from the increase in local stress or from the reduction of bending moment. On the formal level, both views are equivalent. One physical interpretation may be more fruitful than the other in certain circumstances and, importantly, assuming a specific reference. When tension energy is enhanced compared to the reference, it is useful to speak about the effect of stress, and when the bending energy is reduced, it might be more transparently explained in terms of the bending moment.

2.4.6 Distributed and boundary losses in thin-film beams

In this section we elaborate on the dissipation dilution in thin-film beams, describe clamping curvature and obtain an expression for D_Q in which its scaling with the strain parameter λ is explicit.

The theoretical analysis of Euler-Bernoulli equation is facilitated by expressing this equation in dimensionless form. This approach also has the advantages of reducing the number of independent parameters in the problem to a minimum. The first step here is to introduce a normalized coordinate $s = x/l$, which takes values from 0 to 1. After this the Euler-Bernoulli equation (2.146) is transformed to

$$\lambda^2 \frac{d^2}{ds^2} \left(v(s) \frac{d^2 U(s)}{ds^2} \right) - \frac{d^2 U(s)}{ds^2} - \Lambda v(s) U(s) = 0. \quad (2.159)$$

Here Λ is the normalized eigenvalue related to the resonance frequency Ω as

$$\Lambda = \frac{\rho l^2 \Omega^2}{\sigma_{\text{avg}}}, \quad (2.160)$$

and λ is defined as

$$\lambda = \frac{h}{l} \sqrt{\frac{E}{12\sigma_{\text{avg}}}}, \quad (2.161)$$

generalizing Eq. (2.101) for non-uniform beams. It should be mentioned that there is some unavoidable arbitrariness in the definition of dimensionless parameters. Above, the mean width w_0 is assumed as the reference width and σ_{avg} as the reference stress. This is a convenient, but not the only possible choice.

The evaluation of Eq. (2.148)-2.149 results in the following expression for the dilution of a thin-film beam mode,

$$D_Q = 1 + \frac{1}{\lambda^2} \frac{\int_0^1 (U'(s))^2 ds}{\int_0^1 v(s) (U''(s))^2 ds}. \quad (2.162)$$

In the high-stress limit, when $\lambda \ll 1$ and $D_Q \gg 1$, the first term on the right hand side can be neglected. This regime is the most practically interesting, since it is a necessary prerequisite for attaining high D_Q . For practical use, we implemented the solution of Eq. (2.159) and the calculation of dissipation dilution according to Eq. (2.162) in a Mathematica notebook [126].

Since the bending term in the Euler-Bernoulli equation (Eq. (2.159)) is $\propto \lambda^2$, it is expected to be negligible when λ is small. Once bending is neglected, the Euler-Bernoulli equation becomes a wave equation,

$$-\frac{1}{v(s)} \frac{d^2}{ds^2} U_d(s) = \Lambda_d U_d(s). \quad (2.163)$$

For the future use mode shapes and eigenvalues that satisfy Eq. (2.163) are denoted as U_d and Λ_d , respectively, with the subscript meaning ‘‘distributed’’. Λ_d is different from Λ by only a small amount, on the order of $1/D_Q$. This difference will be discussed in the end of this section, but until then for all our practical purposes we can assume $\Lambda_d \approx \Lambda$.

The relation between $U_d(s)$ and the solution of the original Euler-Bernoulli equation, $U(s)$, is subtle. As λ goes to zero, the two solutions approach each other

$$\lim_{\lambda \rightarrow 0} U(s) = U_d(s), \quad (2.164)$$

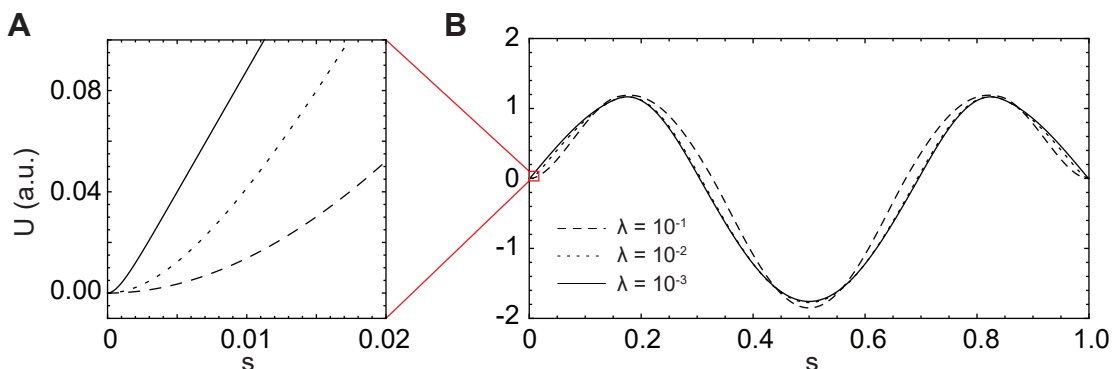


Figure 2.12: Displacement fields U of the third order flexural modes of beams with $\lambda = 10^{-1}, 10^{-2}, 10^{-3}$. A) The displacement fields in the clamping region, illustrating an increase in mode curvature around the clamp with the reduction of λ . B) Overall shapes of the flexural modes, which show convergence as λ is reduced.

for all s . The same is not true for their derivatives if the beam is hard-clamped at $s = 0$ and $s = 1$, in this case

$$\lim_{\lambda \rightarrow 0} U'(0) \neq U'_d(0). \quad (2.165)$$

Indeed, since Eq. (2.163) is second order in spatial derivatives, the theory of ordinary differential equations tells us that if $U_d = 0$ and $U'_d = 0$ at one point, then U_d is zero for all s . Therefore the solution of wave equation only satisfies the boundary conditions $U(0) = U(1) = 0$ (the violation of which would incur higher energy cost), but not $U'(0) = U'(1) = 0$.

Since $U(s)$ does converge to $U_d(s)$ as λ gets small, an approximate mode shape that satisfies all boundary conditions can be obtained by locally correcting $U_d(s)$ around the clamps. We write such corrected function as

$$U(s) = U_d(s) + U_{cl,l}(s) + U_{cl,r}(s), \quad (2.166)$$

where $U_{cl,l}$ and $U_{cl,r}$ are the corrections, respectively, around the left and right clamps. Now one already can qualitatively predict the impact of stress or aspect ratio encoded into the λ parameter on the mode shape $U(s)$. The distributed part of the mode, $U_d(s)$, is independent of λ . The amplitudes of clamping contributions U_{cl} reduce to zero as $\lambda \rightarrow 0$, in accordance with Eq. (2.164), but because the derivative change stays finite their curvatures increase indefinitely. In order to visualize these trends, we plot in Figure 2.12 the vibrational mode shapes obtained by solving the Euler-Bernoulli equation for a beam with the same transverse profile at different λ . Physically, this corresponds to the evolution of flexural mode shape as the tension force \mathcal{T} is increased, since $\lambda \propto 1/\sqrt{\mathcal{T}}$.

In the high-stress limit, the clamping contributions $U_{cl,l}$ and $U_{cl,r}$ can be found to a very good approximation under quite general assumptions. We will do this for the left clamp ($s = 0$), and for simplicity assume that the beam is symmetric so that the

mode around the right clamp behaves in the same way. As was qualitatively argued above and as will be rigorously verified in the following, the region of s over which $U_{\text{cl},l}$ contributes substantially to the mode shape (“clamping region”) reduces to zero as $\lambda \rightarrow 0$. Therefore, we can assume that the beam width and the static stress are approximately constant in the clamping region,

$$v(s) \approx v(0), \quad \bar{\sigma}(s) \approx \bar{\sigma}(0). \quad (2.167)$$

A “local” value of λ , renormalized by the clamping stress, is denoted by λ_{cl} and given by

$$\lambda_{\text{cl}} \equiv \frac{h}{l} \sqrt{\frac{E}{12\bar{\sigma}(0)}} = \lambda \sqrt{v(0)}. \quad (2.168)$$

Around $s = 0$, U is close to zero, so that the inertia term in the Euler-Bernoulli equation (ΛU term) is negligible, while the bending term is not, as the mode curvature U'' is anomalously high. The Euler-Bernoulli equation in the vicinity of the clamp simplifies to

$$\lambda_{\text{cl}}^2 U''''(s) - U''(s) = 0. \quad (2.169)$$

The general solution of Eq. (2.169) is

$$U(s) = C_1 + C_2 s + C_3 e^{-s/\lambda_{\text{cl}}} + C_4 e^{s/\lambda_{\text{cl}}}, \quad (2.170)$$

where the constants C_{1-4} are found from the boundary conditions

$$U(0) = 0, \quad U'(0) = 0, \quad \text{and} \quad U'(s \gg \lambda_{\text{cl}}) = U'_d(0). \quad (2.171)$$

The overall result for the solution is

$$U(s) = U'_d(0) \left(s + \lambda_{\text{cl}} \left(e^{-s/\lambda_{\text{cl}}} - 1 \right) \right), \quad (2.172)$$

By comparing it to Eq. (2.166) we identify the clamping contribution as

$$U_{\text{cl},l}(s) = U'_d(0) \lambda_{\text{cl}} \left(e^{-s/\lambda_{\text{cl}}} - 1 \right). \quad (2.173)$$

The displacement field around the other clamp, $U_{\text{cl},r}$, is found in an analogous way. Note, that the length of the clamping region in physical units is given by $\Delta x_{\text{cl}} = \lambda_{\text{cl}} l$, which is much smaller than the beam length. This validates the assumption made in the beginning that the clamping correction is localized.

It is instructive to estimate the length of the clamping region Δx_{cl} in real structures. For uniform Si_3N_4 beams, assuming material parameters typical for LPCVD silicon nitride at the CMi [127], we obtain

$$\Delta x_{\text{cl}} = h \sqrt{E/12\bar{\sigma}} \approx 5h, \quad (2.174)$$

i.e. that the clamping length is about 5 times the beam thickness. Thicknesses relevant to the devices in this thesis vary between 20 and 100 nm, which gives Δx_{cl} in the range of 100 – 500 nm.

Next, we use the obtained insight into the mode shapes to evaluate dissipation dilution and transparently expose its dependence on beam dimensions, stress, and the transverse shape. We take as a starting point D_Q given by the ratio of gradient and curvature integrals in Eq. (2.162), and evaluate it for $U = U_d + U_{cl}$, where U_{cl} depends on λ and U_d does not. The contribution of U_{cl} to the tension energy can be neglected, while its contribution to the bending energy is sizable or even dominant. Using the shape of $U_{cl,1}$ found previously, the bending energy stored by the clamping curvature around the left clamp is found as

$$\int_0^\infty v(s) (U''_{cl,1}(s))^2 ds = \frac{1}{2\lambda} \sqrt{v(0)} [U'_d(0)]^2, \quad (2.175)$$

where we returned to the original stress parameter, $\lambda = \lambda_{cl}/\sqrt{v(0)}$. The contribution of the right clamp can be found analogously, for simplicity it is assumed to be equal to that of the left clamp. Because of the delta-function nature of the clamping curvature, and because $U''_d = 0$ at the clamping point, the cross terms $\propto U''_d U''_{cl,1}$ does not contribute to the bending energy.

The dilution factor D_Q is found by combining the boundary and the distributed contributions as

$$D_Q = \frac{1}{\alpha\lambda + \beta\lambda^2}. \quad (2.176)$$

Here α and β are the boundary and distributed loss coefficients, respectively, given by

$$\alpha = \sqrt{v(0)} [U'_d(0)]^2 \Big/ \int_0^1 (U'_d(s))^2 ds, \quad (2.177)$$

$$\beta = \int_0^1 v(s) (U''_d(s))^2 ds \Big/ \int_0^1 (U'_d(s))^2 ds. \quad (2.178)$$

Both loss coefficients are expressed as functions of the solution of wave equation, U_d , and therefore one can be sure that they do not have any further implicit dependence on λ . Solving the full Euler-Bernoulli equation is, strictly speaking, unnecessary for the calculation of quality factors.

Interestingly, corrections to mode frequencies due to the bending energy, i.e. the difference between Λ and Λ_d , can also be expressed using the same coefficients α and β . It can be checked using perturbation theory that if $D_Q \gg 1$ then the eigenvalue of Euler-Bernoulli equation Λ is related to the eigenvalue of the simplified wave equation, Λ_d as

$$\Lambda \approx \Lambda_d(1 + 2\alpha\lambda + \beta\lambda^2). \quad (2.179)$$

Expressions in Eq. (2.176) and Eq. (2.179), when applied to a uniform beam, reproduce the result from [33, 64]. For a uniform rectangular beam $v(s) = 1$, and the distributed mode shapes are sinusoidal,

$$U_d(s) = \sqrt{2} \sin(\pi n s), \quad (2.180)$$

where $n = 1, 2, \dots$ is the mode index. The corresponding eigenvalues are $\Lambda = (\pi n)^2$, the loss coefficients are

$$\alpha = 2, \quad \beta = (\pi n)^2. \quad (2.181)$$

and overall [35, 64],

$$D_Q^{(\text{u.b.})} = \frac{1}{2\lambda + (n\pi)^2\lambda^2}, \quad (2.182)$$

The beam frequencies, including the bending correction, are given by

$$\Omega^{(\text{u.b.})} = \frac{\pi n}{l} \sqrt{\frac{\sigma}{\rho}} \left(1 + 2\lambda + \frac{(\pi n)^2}{2} \lambda^2 \right). \quad (2.183)$$

Eq. (2.182) and Eq. (2.183) were first derived and experimentally verified for macroscopic strings with circular cross-sections in the pioneering work on dissipation dilution [33].

In non-uniform beams dissipation dilution can be higher than that predicted by Eq. (2.182). With the help of Eq. (2.176)-2.178, an optimization of D_Q can be conducted over different shapes $v(s)$. In the high-stress limit, when $\lambda \ll 1$, the value of D_Q is limited by the boundary curvature term $\alpha\lambda$. If α is engineered to be close to zero, D_Q is strongly enhanced, techniques of achieving this are known as *soft clamping*. First introduced for phononic crystal membranes by Tsaturyan et al. [36], in our works soft clamping was applied to beams [32] and then extended to non-bandgap structures [39]. Once the boundary contribution to the mode curvature is eliminated, dissipation dilution is limited by the distributed contribution [32]. In this case the local enhancement of stress can improve it further, up to the point when it is limited by the breaking stress of the material.

2.4.7 The ultimate limit for dissipation dilution in thin films

The usual, if not the only, practical goal of control over mechanical losses is to reduce them to the lowest possible level. Optimizing dissipation dilution within given constraints for the resonator configuration is one way towards this goal. In our works [32, 37, 39] we developed and explored a number of strategies for optimizing dilution, and before considering them more closely, it is useful to present a general argument showing the ultimate limitation of this approach.

Dissipation dilution increases with the reduction of the strain parameter λ , and therefore it is clear from the start that high-aspect ratio structures with high tensile stress are favorable. The maximum stress that material can sustain is known as yield strength, σ_{yield} . For stoichiometric silicon nitride this value is around 6.8 ± 0.8 GPa [128, 37], and the corresponding strain ϵ_{yield} is around 3%. Exceeding the yield stress value in any part of the mechanical resonator leads to its collapse. Therefore, dissipation dilution of a mode in a uniform beam can never exceed the value for a structure tensioned to the yield strain,

$$D_Q \leq \frac{12E\epsilon_{\text{yield}}^2}{\rho h^2 \Omega^2}. \quad (2.184)$$

The expression on the right hand side is obtained from Eq. (2.182) by neglecting the boundary loss contribution and relating the mode number to frequency. It turns out that Eq. (2.184) is a rigorous bound that applies to any non-uniform thin-film beam, which is proven in the end of this section. There is little doubt that the same limit qualitatively applies to two-dimensional modes in membranes, although this is less straightforward to rigorously prove.

For the following use, we also introduce the “soft-clamping limit”, given by substituting the yield strain in Eq. (2.184) with the film pre-strain,

$$D_Q^{(\text{soft.clamp.})} = \frac{12E\epsilon_{\text{film}}^2}{\rho h^2 \Omega^2}. \quad (2.185)$$

This is not a rigorous limit for any kind of resonators, but it is a useful benchmark value, approaching which means that the boundary curvature contribution to intrinsic loss is well suppressed.

Proof of the yield stress limit. We start from the simple fact that neglecting boundary losses does not decrease the dilution,

$$D_Q = \frac{1}{\alpha\lambda + \beta\lambda^2} \leq \frac{1}{\beta\lambda^2}, \quad (2.186)$$

and find a lower bound for the distributed loss coefficient β . Noting that the normalized beam profile $v(s)$ is related to the axial stress,

$$v(s) = \sigma_{\text{avg}}/\bar{\sigma}(s) \geq \sigma_{\text{avg}}/\bar{\sigma}_{\text{peak}} \geq \sigma_{\text{avg}}/\bar{\sigma}_{\text{yield}}, \quad (2.187)$$

we use this fact to evaluate the curvature integral in the definition of β (Eq. (2.178)) using Eq. (2.163),

$$\begin{aligned} \int_0^1 v(s) (U_d''(s))^2 ds &= \Lambda_d \int_0^1 v(s)^2 (-U_d(s)U_d''(s)) ds \geq \\ &\Lambda_d \left(\frac{\sigma_{\text{avg}}}{\sigma_{\text{yield}}} \right)^2 \int_0^1 (-U_d(s)U_d''(s)) ds = \Lambda_d \left(\frac{\sigma_{\text{avg}}}{\sigma_{\text{yield}}} \right)^2 \int_0^1 (U_d'(s))^2 ds. \end{aligned} \quad (2.188)$$

Therefore, the distributed loss coefficient is lower-bound as $\beta \geq \Lambda_d (\sigma_{\text{avg}}/\sigma_{\text{yield}})^2$, and overall

$$D_Q \leq \frac{1}{\Lambda_d \lambda^2} \left(\frac{\sigma_{\text{yield}}}{\sigma_{\text{avg}}} \right)^2 = \frac{12E\epsilon_{\text{yield}}^2}{\rho h^2 \Omega^2}, \quad (2.189)$$

which proves the point. Here $\sigma_{\text{yield}} = E\epsilon_{\text{yield}}$.

2.4.8 Torsional lossy energy

A different kind of deformation than flexure which is supported by beams is torsion. It corresponds to twisting the beam cross-section about the beam axis over a variable

angle $\tau(x, t)$. Here we again consider a high aspect-ratio beam aligned along x axis and evaluate the energy of its torsional deformation. For simplicity, we consider a thin-film beam, and find the energy by regarding it as a membrane strip. Despite this fact, we find it useful to consider torsional energy as a separate concept, as it is generalizable to strings with non-rectangular cross section for which there is no direct relation to membranes.

For small τ , with sufficient precision the two-dimensional deformation field produced by beam torsion is given by

$$u(x, y, t) = \tau(x, t)y. \quad (2.190)$$

As we are interested in thin beams which extent in y direction is small, strains which are $O(y)$ are neglected. In this approximation, torsion produces no nonlinear strain and therefore no tension energy. In contrast, the linear elastic energy is finite. The two-dimensional curvature terms are found as

$$u_{,xx} = 0, \quad u_{,xy} = \tau_{,x}, \quad u_{,yy} = 0. \quad (2.191)$$

The lossy energy is found according to the general membrane formula,

$$W^{(\text{lin})} = \frac{h\mathcal{D}}{2} \int 2(1 - \nu)u_{,xy}^2 dx dy = \frac{Eh^3}{12(1 + \nu)} \int_l w(x)\tau_{,x}(x, t)^2 dx. \quad (2.192)$$

It should be noted that the torsional deformation of a beam has different symmetry with respect to y axis as compared to the out-of-plane bending. Therefore the two kinds of deformations do not couple—their cross-energy term is zero, and their energies can be computed independently.

For a uniform beam ($w = \text{const}$) that is uniformly twisted ($\tau' = \text{const}$) between $\tau = \tau_0$ at $x = 0$ and $\tau = 0$ at the end of the beam, $x = l$, the torsion energy is given by

$$W^{(\text{lin,tors})} = \frac{Ewh^3}{12(1 + \nu)} \frac{\tau_0^2}{l}. \quad (2.193)$$

This energy is of the same order as the distributed part of the bending energy of a flexural beam mode for which $du/dx(0) = \tau_0$.

2.4.9 Dissipation dilution and frequency noise

The quality factor of a mechanical resonator determines the uncertainty in frequency and force measurements due to the resonator's Brownian motion [30, 129, 130]. Therefore dissipation dilution directly improves these fundamental sensitivity limits. In the case of force measurements, a nanobeam is a particularly advantageous kind of resonator due to its low mass. For the highest- Q nanobeams that were experimentally demonstrated at room temperature [32], with a Q of $8 \cdot 10^8$ at 1.3 MHz (in agreement with the theory presented here within 30%) and effective mass of 11 pg, the thermal noise limit is

$$\delta F_{\text{th}} = \sqrt{4k_B T m \Gamma_n} = 1.4 \text{ aN}/\sqrt{\text{Hz}} \quad (2.194)$$

at $T = 300$ K. Here $\Gamma_n = \omega_n/Q$ is the resonance linewidth.

The thermal noise limit for an oscillator frequency is more ambiguous to define in absolute terms, since here the resolution in general depends on the amplitude of the drive [129, 131] which is typically limited by the onset of nonlinearity. For flexural modes of thin beams and membranes the dominant source of nonlinearity at large amplitudes is not material but geometric nonlinearity [71], the same which creates dissipation dilution. Therefore we can estimate the contribution of Brownian motion to oscillator frequency noise by assuming that the amplitude of driven motion is such that the nonlinear part of the energy is of the same order of magnitude as the linear part. This is equivalent to the condition that the average kinetic energy approaches the static elastic energy, $\langle W^{(\text{kin})} \rangle = W^{(\text{el.stat.})}$,

$$m_{\text{eff}}\Omega^2\langle X_{\text{osc}}^2 \rangle \simeq V_{\text{eff}}\epsilon_{\text{avg}}^2/E. \quad (2.195)$$

Here m_{eff} and $V_{\text{eff}} = m_{\text{eff}}/\rho$ are the effective resonator mass and volume, respectively, X is the oscillator position and $\langle X_{\text{osc}}^2 \rangle$ is the magnitude of driven motion. The frequency noise spectrum due to Brownian motion is given by [131]

$$S_{\omega\omega}[\omega] = 2\frac{\langle X_{\text{th}}^2 \rangle}{\langle X_{\text{osc}}^2 \rangle}\Gamma\frac{\omega^2}{\omega^2 + (\Gamma/2)^2}, \quad (2.196)$$

where $\langle X_{\text{th}}^2 \rangle$ is the magnitude of the thermal position fluctuations. Using Eq. (2.195), we estimate the minimum frequency noise (at $\omega \gg \Gamma$) as

$$S_{\omega\omega} \simeq \frac{k_B T}{W^{(\text{el.stat.})}}\Gamma. \quad (2.197)$$

From Eq. (2.197), we see that static strain reduces Brownian frequency noise in two ways—by reducing the resonator linewidth and by increasing the driving amplitude threshold at which nonlinearity comes into play. Plugging in numbers from above we find that the highest- Q soft-clamped mode has minimum frequency noise $\sqrt{S_{\omega\omega}}/(2\pi) \simeq 3 \cdot 10^{-7}$ Hz/ $\sqrt{\text{Hz}}$. If converted to phase noise, this is equivalent to -230 dBc/Hz at 20 kHz offset, which is an extremely low level.

Practically, other factors than Brownian motion almost always limit the frequency stability of mechanical resonators, in particular of silicon nitride nanobeams [71]. On the other hand, in nanobeams extraneous frequency noises of different modes are highly correlated, which made it possible to demonstrate Brownian-noise limited frequency measurements with moderate- Q resonators using feedback [131]. Therefore the attainability of the Brownian noise limit in frequency measurements using ultra-high Q beams remains an open question.

2.5 High-stress phononic crystals

A periodic modulation of medium properties (e.g. as shown in Figure 2.13) gives rise to acoustic bandgaps—spectral regions in which the propagation of elastic waves is

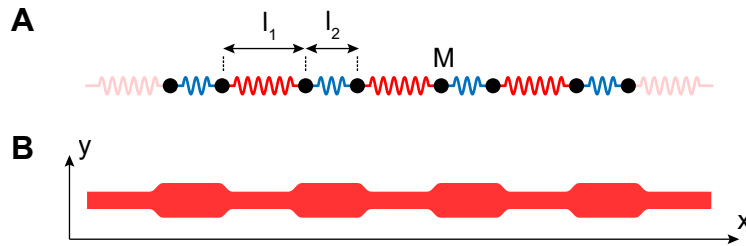


Figure 2.13: One-dimensional phononic crystals. A) Model of a tensioned phononic-crystal beam—system of masses joined by springs with alternating lengths. B) Corrugation profile a PnC beam, that can be patterned from a thin film.

forbidden. Such media are known as phononic crystals (PnCs). Acoustic bandgaps are easily observed in macroscopic structures [132]. At the microscale, enabled by rapid developments in microfabrication techniques over the last two decades, phononic crystals became an indispensable tool for the manipulation of acoustic waves [133]. One of the key applications of phononic crystals is the isolation of mechanical modes with high frequencies (MHz-GHz range) and low masses, which is not easy to accomplish by other means. Modes localized in PnC's can have long coherence time and strongly couple to optical [134] and microwave fields [135], as well as superconducting qubits [136], which makes them a promising building block for quantum circuits. In recent years there has been an increasing research interest in topological aspects of phononic crystals. Although the time-reversal symmetry commonly found in acoustic systems precludes the existence of chiral edge states, other manifestations of topological order have been predicted and observed (see e.g. [137] and references therein, also [138, 139]).

Phononic crystals have a lot in common with their electromagnetic counterparts, photonic crystals, which historically appeared first and supplied many ideas for the development of the acoustic platform. There is one important practical difference between the two, related to the fact that electromagnetic waves can propagate in vacuum while acoustic waves cannot. In photonic crystals the scattering of light into free space, be it due to fabrication imperfections or due to the tight localization of mode envelope, is a major problem [140]. In contrast, the energy of modes localized in phononic crystals can only escape by tunneling through the crystal itself—either because of its finite size or, if the bandgap is not complete, by coupling to a mode family that can propagate freely [31]. The absence of radiation into the free space makes localized acoustic modes weakly sensitive to disorder and to the details of mode shape, in contrast to the optical case.

Phononic bandgaps in periodically patterned suspended high-stress films were demonstrated for the first time relatively recently [36, 54]. Originally, works in this direction aimed to reduce mechanical dissipation by preventing the coupling of acoustic modes to the resonator frame (a silicon chip) [57, 54]. Over the course of research it was found (in Ref. [36]) that modes localized in stressed PnCs can also have dramatically enhanced dissipation dilution due to the suppression of boundary contribution to the linear strain.

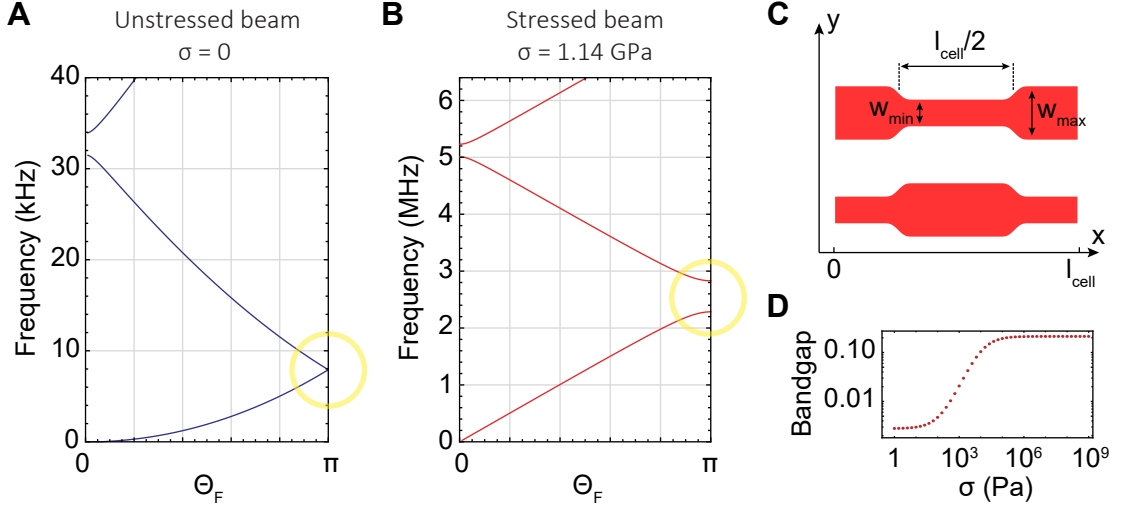


Figure 2.14: Acoustic dispersion of phononic crystals with $h = 20$ nm, $l_{\text{cell}} = 100$ μm . Here $\theta_F = kl_{\text{cell}}$ is the Floquet phase. A) Phononic band diagram for the pattern shown in C) and in Figure 2.13B in the absence of stress. B) Band diagram for the same unit cell in the presence of stress. C) The two choices of inversion-symmetric unit cell. D) Dependence of the relative size of the first phononic bandgap (bandgap/midgap) on the material prestress σ_{film} .

Static stress affects phononic crystals in several ways. First of all, it controls the dispersion of flexural modes. Low-frequency flexural modes of an unstressed beam or membrane have the dispersion relation $\omega \propto k^2$, where k is the wavevector and ω is the mode frequency, while in presence of stress the dispersion changes to $\omega \propto k$. This is clearly visible in Figure 2.14, which shows two dispersion relations calculated for one-dimensional PnC with and without tensile stress. The calculation is done for a beam patterned from Si_3N_4 film with $h = 20$ nm and unit cell length $l_{\text{cell}} = 100$ μm . A not entirely intuitive result shown in Figure 2.14 is that the periodic modulation of beam width creates odd-order phononic bandgaps for flexural modes only in the presence of tensile stress. In this work, we are exclusively interested in the first order bandgap. This bandgap exists for z (out-of-plane) and y (in-plane) polarized flexural modes, the dispersion relations of which are almost identical, while torsional and longitudinal modes can propagate freely.

Another practical implication of stress in phononic crystals is that the freedom of choice of the unit cell pattern is generally limited. We observed in finite element simulations that many geometries can lead to a strong reduction, or even a sign reversal of the equilibrium stress compared to the initial value σ_{film} , resulting in a strong reduction of dissipation dilution for all modes. The problem is aggravated by the fact that particularly low-frequency and high-dissipation modes can emerge in the regions of near-zero stress, like the free edges of the film, and these modes tend to strongly couple to the rest of the spectrum due to stress inhomogeneities. When the equilibrium stress becomes compressive upon relaxation in one of the principal directions, static buckling instabi-

lities can occur, in which case the resonator ceases to be flat. All these effects affect thinner films more, and thus they are particularly relevant for the design of high-aspect ratio resonators with high dissipation dilution. In two dimensions, the most successful phononic crystal pattern so far is the simple hexagonal arrangement of holes introduced in Ref. [36]. In one dimension (PnC beams), avoiding static instabilities and coupling to low- Q transverse modes requires the usage of outer corrugation and the overall width of the structure to be sufficiently small. In our experiments we did not observe any deviations from the idealized on-dimensional theory for mm-long PnC beams with $2\ \mu\text{m}$ maximum width while using films with thicknesses as low as 20 nm.

Static stress in phononic crystals also leads to the fact that local acoustic properties are not uniquely determined by the local geometry of unit cell. The band diagram of a crystal obtained by the periodic repetition of a selected unit cell depends on the distribution of stress within the cell, which is globally affected by the entire PnC resonator. In this way, for example, the bandgap of each unit cell is modified by a perturbation introduced in the crystal in order to create a localized mode. Although in simple cases the perturbation can be small, generally this effect complicates the introduction of inhomogeneities, such as boundaries between different PnC patterns. In one dimensional crystals, the total tension force uniquely characterizes the distribution of stress, while local stresses can be adjusted by the variation of unit cell width. The invariance of the phononic spectrum in the high-stress limit with respect to $\sqrt{\sigma}/l$ provides an opportunity to arbitrarily change the envelope of the stress profile while maintaining the same frequency dispersion for all unit cells within the beam. As a desirable stress profile is defined, the only requirement to match the bandgap frequencies in all unit cells is to adjust the unit cell lengths $l \propto \sqrt{\sigma}$. By using this property, we can create vibrational modes co-localized with regions of enhanced stress inside one-dimensional phononic crystals.

In the following section we present results of simulations and experimental characterization of mechanical modes in phononic crystal beams and briefly mention phononic crystal membranes. The spectra of thermal motion presented in this section are obtained using home-built lensed fiber or free-space homodyne interferometers, and mechanical quality factors were characterized using ringdown spectroscopy as described in Sec. 2.7. In all measurements samples remained in high vacuum ($< 10^{-6}$ mbar) sufficient to make the gas damping of mechanical motion negligible. Because of their extreme aspect ratios, the integration of record- Q nanobeam devices with optical cavities for near-field readout presently remains an outstanding challenge.

2.5.1 Soft clamping in PnC nanobeams

An experiment demonstrating soft-clamped modes in 1D nanomechanical resonators is presented in Figure 2.15. 2.6-mm-long devices with unit cells of length $L_{\text{cell}} = 100\ \mu\text{m}$ and width $w_{\text{min(max)}} = 0.5(1)\ \mu\text{m}$ were studied, as shown in Figure 2.15A. Mode frequencies inferred from thermal noise spectra (Figure 2.15C) were found to agree very well with a numerical solution to the 1D Euler-Bernoulli equation. Particularly striking is

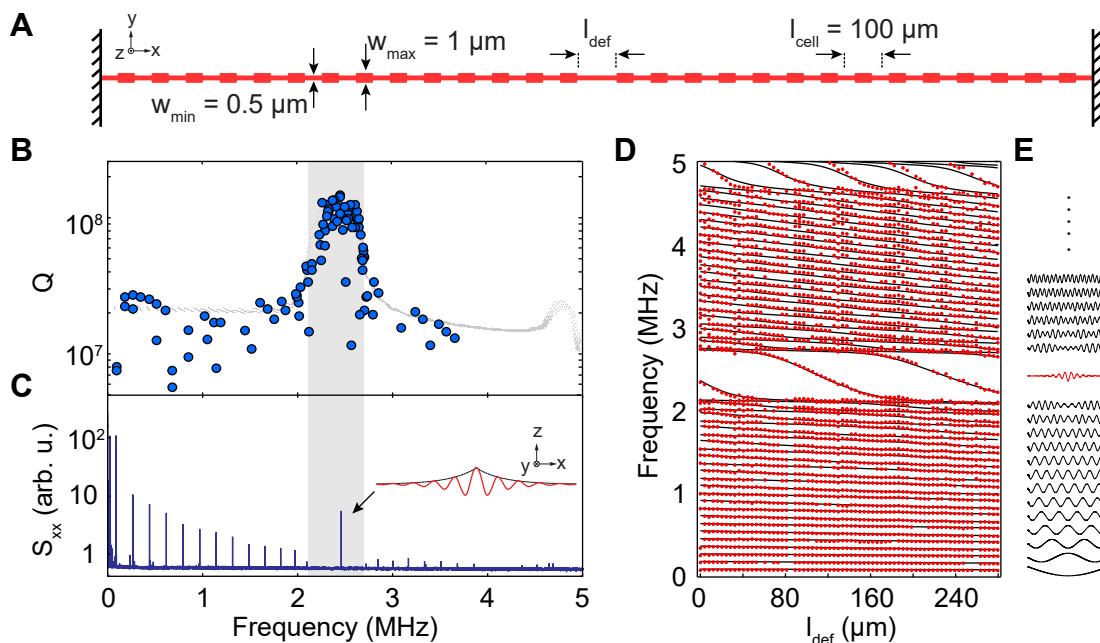


Figure 2.15: Experimental demonstration of soft clamping in one-dimensional phononic crystals. A) Geometry of the PnC beams and the definition of defect. B) Quality factors measured for the modes of beams in D. C) Experimental spectrum of position fluctuations, measured at the beam center. Inset: localized flexural mode shape $u(x)$ (blue) and its exponential envelope (orange). D) Frequencies of beam modes as the PnC defect length is swept. E) Displacement profiles of localized and distributed modes for one PnC beam, each mode is approximately positioned according to its frequency relative to the vertical axis of D.

the sparse mode spectrum inside the bandgap, visualized by compiling spectra of beams with different defects presented in Figure 2.15D. A single defect mode appears to move in and out of the bandgap as the defect length is varied. At every length of the defect, there is one and only one localized mode inside the bandgap, which is a consequence of the fact that the Bloch functions at the edges of the first and the second bands have different symmetries with respect to inversion. Localized modes have reduced effective masses. Comparing the area under thermal noise peaks and estimating the physical beam mass to be $m_0 = 100$ pg, we infer the effective mass of the localized mode to be ≈ 5 pg $\ll m_0$. This value is in good agreement with the value obtained from the theoretical mode profile, and is roughly two orders of magnitude smaller than that of an equivalent two-dimensional localized mode in a membrane.

We also observe a dramatic increase in the Q of localized modes. To visualize this enhancement, we compiled measurements of Q versus mode frequency for 40 beams of different defect length and presented them in Figure 2.15B. Outside the bandgap, we find that Q is consistent with that of a uniform beam, asymptoting at low mode order ($n \lesssim 20$) to $Q \approx 2 \times 10^7$. Inside the bandgap ($n \approx 26$), Q approaches that of an idealized clamp-free beam ($Q \approx Q_{\text{int}}/(\pi n \lambda)^2 \approx 10^8$). The highest quality factors were measured

for second-order (asymmetric with respect to the center) localized modes, realized for the devices with defect lengths in the range 160-280 μm in Figure 2.15D. The transition between the localized and distributed regimes agrees well with a full model (gray dots) based on the solution of Euler-Bernoulli equation, although the scatter is significantly greater for the quality factors than for the mode frequencies. The origin of this scatter has not been unambiguously identified, although potential contamination of the beams in the process of fabrication is a natural suspect.

Devices presented in Figure 2.15 use simple step-like corrugations to create a phononic bandgap, and a beam-like defect to break the periodicity and localize a mode. One might naturally wonder if the quality factors of localized modes can be further improved if another kind of corrugation is employed, or the same corrugation with different parameters, or if the defect is introduced differently. While according to our numerical simulations the answer is generally yes, the attainable improvement seems to be quite limited, not exceeding about a factor of two at a given frequency. This is not surprising given the fact that the practically realized devices already approach the performance of idealized clamp-free beams with their quality factors $Q \approx Q_{\text{int}}/(\pi n \lambda)^2$. According to our simulations, the clamp-free limit can be slightly surpassed with some PnC geometries, but never by much. A way to circumvent this limit is global strain engineering as will be discussed in the next section. Another reason for using simple structures in practice is that the optimum geometries tend to be sensitive to the optimization metric (e.g. quality factor or $Q \cdot f$ product) and the assumed constraints (e.g. fixed device length, or fixed mode frequency).

Concerning the problem of optimizing the shape of the PnC unit cell, the two main affected parameters here is the size of the phononic bandgap and the average stress within the structure. Deeper corrugation creates larger bandgaps which better isolate localized modes from the clamps. This is not necessarily advantageous for the quality factors of the localized modes, as deeper corrugation also leads to a lower average equilibrium stress in the structure assuming a fixed pre-stress σ_{film} . At the level of intuition, it was initially expected that an excessively strong localization can negatively affect quality factors due to an increase in the distributed curvature contributed by the steep exponential envelope of the mode. However, in simulations we did not observe this effect to be significant. This is not surprising taking into account that the dependence of average stress on corrugation is much more pronounced than the dependence of mode localization length. Also, it should be noted that extreme corrugation ratios are practically not accessible with the thinnest (20nm) nanobeams, as such structures would likely buckle in transverse direction upon fabrication, which destroys their quality factors entirely.

In order to illustrate the main limitations of quality factor enhancement by soft clamping in PnCs, we plot in Figure 2.16 theoretical D_Q s and Q s of localized modes versus frequency and beam length. We assume the same PnC pattern and the same definition of defect as in Figure 2.15. The film thickness is 20 nm, and the material parameters and film pre-stress are those of Si_3N_4 . In every PnC beam the length of the center defect is taken to be 1.2 of the unit cell length, which creates a soft clamped mode at the frequency approximately corresponding to the middle of the phononic bandgap. As

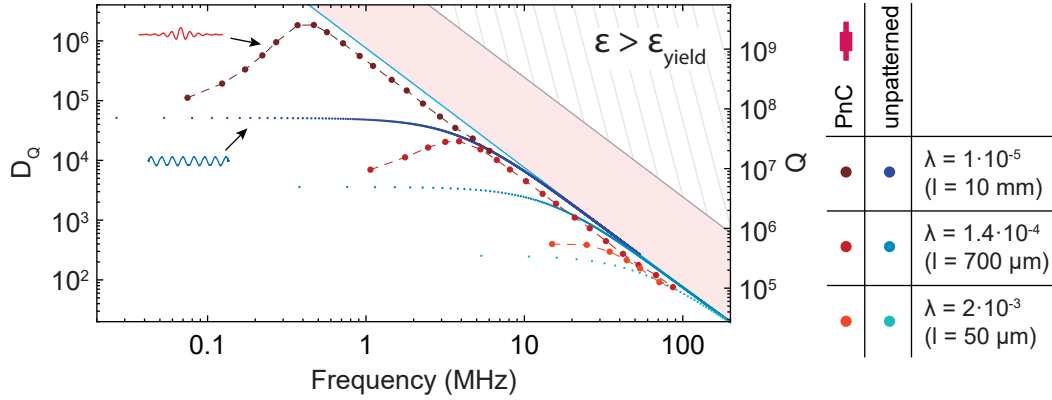


Figure 2.16: Theoretical variation of localized mode D_Q (shades of red) with frequency and beam length, and comparison to modes of uniform beams of the same lengths. Beam thickness here is $h = 20$ nm. Localized mode frequency is changed by the variation of the number of PnC unit cells within the beam (together with the unit cell length as the beam length is fixed) while keeping the ratio of the central defect to the unit cell length constant.

mentioned earlier, while such a fixed choice of PnC geometry leaves room for optimization, quality factors in such structures are not dramatically lower than the optimum and illustrate all qualitative trends.

In Figure 2.16, at every beam length ($l = 50 \mu\text{m}$, $l = 700 \mu\text{m}$ and $l = 10$ mm) the frequency of the localized mode is varied by changing the length of the PnC unit cell which determines the bandgap frequency. Mode frequencies cannot be varied continuously in this way, as an integer number of unit cells must fit into the beam, which results in discrete data points (red dots in Figure 2.16), joined by dashed lines as guides to the eye. Each curve of localized mode Q versus frequency obtained in this way has a peak, which can be understood as follows. When the localized mode frequency is low, its acoustic wavelength is comparable to the beam size and the mode is not fully shielded from the clamps. When the localized mode frequency is high, the increased ratio of film thickness to the acoustic wavelength results in a higher amount of energy stored in distributed bending.

A natural metric for the gain from PnC localization is how much the maximum quality factor attainable for a localized mode is higher than that of a distributed mode at the same frequency within a uniform beam of the same size (blue dots in Figure 2.16). This enhancement is controlled by the λ parameter, which in Figure 2.16 is different for different beam lengths (the stress and thickness are the same in all structures). Modes in longer beams can benefit more from soft clamping. It can be seen from Figure 2.15 that the localized modes of a 10-mm long devices can have quality factors more than an order of magnitude larger than the modes of a uniform beam, while the modes of a $50 \mu\text{m}$ long device can hardly experience an improvement beyond a factor of two.

Suspending structures with extreme aspect ratios is a major practical challenge in the implementation of devices with soft-clamped modes. The maximum length of beams in

our experiments was 7 mm (thickness $h = 20$ nm), while reliably high fabrication yield could only be obtained for devices not more than 4 mm-long. The primary limitation appeared to be the structure collapse due to perturbations in liquids at various stages of processing, in particular during the final stage of critical point drying. It was empirically found that the gap between the device and the chip has to be larger than $5 \mu\text{m}$ in order to suspend 3-mm long beams, which motivated the development of a two-stage etching process reported in [32, 37, 141].

Two other limitations of soft-clamping in PnCs can be inferred from Figure 2.16. The first one is that the acoustic wavelength of the localized mode must be much smaller than the size of the PnC in order to obtain a Q enhancement. This fact implies that the overall phonic crystal structure, which is hard-clamped and can be regarded as the total resonator, has a multitude of modes with frequencies lower than the frequency of the defect mode. Low-frequency modes are clearly visible in Figure 2.15C. Here, in fact, the overall magnitude of thermal fluctuations of the resonator central point is dominated by the low-frequency modes, and not by the localized soft-clamped mode. The second limitation is that the quality factors of the localized modes do not exceed those of a clamp-free uniform beam and never reach the ultimate limit set by the breaking stress. In Figure 2.16 this manifests in the fact that the red dots, representing the D_Q s of localized modes, never enter the shaded red area between the soft clamping limit (Eq. (2.185)) and the ultimate limit, defined by the inequalities

$$\frac{12E\epsilon_{\text{film}}^2}{\rho h^2 \Omega^2} < D_Q < \frac{12E\epsilon_{\text{yield}}^2}{\rho h^2 \Omega^2}. \quad (2.198)$$

The area forbidden by the breaking strain is hatched gray in Figure 2.16.

2.5.2 Elastic strain engineering

Elastic strain engineering (ESE) utilizes stress to realize unusual material properties [142]. For instance, stress can be used to enhance the electron mobility of a semiconductor, enabling more efficient solar cells [143] and smaller, faster transistors [144]. Dissipation dilution can be seen as a complementary strain engineering technique, where the affected material property is dissipation. Whereas ESE commonly relies on extreme inhomogeneous stresses produced by nanoscale deformation [145] (e.g. by lithographic patterning [86] or nano-indentation [146]), early studies of dissipation dilution have focused on materials under weak, uniform stress produced during material synthesis. The main challenge in bridging dissipation dilution and conventional ESE techniques is to identify strategies to colocalize stress and mechanical motion at the nanoscale. We proposed a strategy based on phononic crystal patterning, which is conceptually simple and entirely material independent. By weakly corrugating a prestressed nanobeam, we create a bandgap for localizing its flexural modes around a central defect. By tapering the beam, we colocalize these modes with a region of enhanced stress. Reduced motion near the supports results in higher dissipation dilution, while enhanced stress increases both dilution and mode frequency. Leveraging a multi-step release process, we implement our

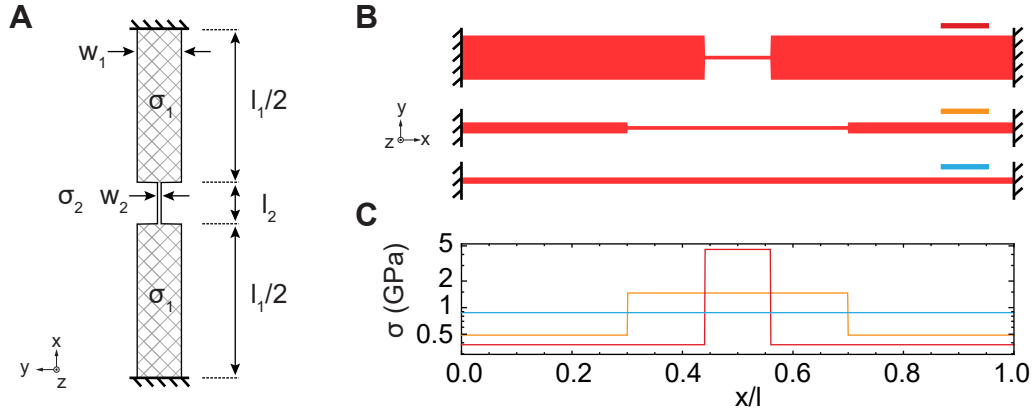


Figure 2.17: Stress concentration example. A) Geometry of a one-dimensional structure consisting of a narrow waist and two stressor pads (hatched regions). B) A few realizations of the geometry shown in (A). C) The distribution of axial stress along the structures in (B).

approach on extremely high aspect ratio tapered beams (as long as 7 mm and as thin as 20 nm) made of prestressed ($\sigma_{\text{film}} = 1.1$ GPa) Si_3N_4 , and achieve local stresses as high as 3.8 GPa.

ESE utilizes stress concentration in inhomogeneous films, which is a situation when stress distribution develops strong local maxima upon the film release. Stresses close to the yield value, beyond which the material breaks, can be realized in this way from a moderate homogeneous initial pre-stress. A strong enhancement of local stress, however, can only be attained over a small region—the smaller the region is compared to the total size of the suspended structure, the higher the enhancement can be. Qualitatively, this rule applies to both one-dimensional beams and two-dimensional membranes. A local enhancement of stress also necessarily requires that the stress elsewhere in the structure is reduced, which is why the phenomenon is referred to as “concentration”.

In Figure 2.17 we show an example of stress concentration in one-dimensional beams with narrow constrictions in the center. Each beam is a flat structure with constant thickness, rectangular cross section, and width profile shown in Figure 2.17A. It consists of a thin central part (“waist”), with length l_2 and width w_2 , and two wider pads on the sides, playing the role of stressors (cross-hatched regions in Figure 2.17A). Each of the two stressor pads have length $l_1/2$ and width w_1 . It is understood that the overall aspect ratio l/w is high enough so that the structures are effectively one-dimensional, which means that their aspect ratios are not shown to scale in the figure. Distributions of static axial stress for three different beams are plotted in Figure 2.17C, while the structures themselves are shown in Figure 2.17B. In agreement to what was mentioned above, larger pads result in larger peak stress, but smaller spatial extent of the high-stress region. A more quantitative and general conclusion can be made based on the analytic expression for the waist stress, $\bar{\sigma}_2$. The waist stress is found using the results

of Sec. 2.4.5,

$$\bar{\sigma}_2 = \sigma_{\text{film}}(1 - \nu) \left(\frac{l_2}{l} + \frac{l_1}{l} \frac{w_2}{w_1} \right)^{-1}, \quad (2.199)$$

where $l = l_1 + l_2$ is the total beam length. The value of $\bar{\sigma}_2$ in Eq. (2.199) is upper-bounded as

$$\frac{\bar{\sigma}_2}{\sigma_{\text{film}}} \leq \min \left(\frac{l}{l_2}, \frac{w_1}{w_2} \right), \quad (2.200)$$

which means that in order to enhance the stress in the waist by a factor of X with respect to the deposition value, the stressors need to be at least X times wider and X times longer than the waist.

Harnessing stress concentration to the enhancement of dissipation dilution is not a trivial task. While stress can be increased only locally, vibrational modes naturally tend to be distributed over the entire structure and be limited only by its hard-clamped boundaries. Only modes that stay entirely within the high-stress region can benefit from stress concentration, and even a small acoustic leakage into the stressor pads (which are low-stress per se) can drastically reduce dissipation dilution. While the simple structures considered in Figure 2.17 were sufficient to illustrate the idea of stress concentration, their modes would in fact have lower dilution than the modes of a regular uniform beam. This is true even despite the fact that a slight increase in stress can take place over a large part of the beam, as for the middle structure in Figure 2.17B. At the same time the opposite strategy—making the clamps narrow—would improve quality factors while slightly reducing the stress in the beam bulk[37].

Vibrational modes can be confined in high-stress regions with the help of phononic bandgaps. In this case, stress concentration can improve quality factors beyond the soft-clamping limit (Eq. (2.185)). Having established in Sec. 2.5.1 near-ideal soft-clamping for uniform PnC nanobeams, we next study the performance of strain-engineered (tapered) PnC nanobeams. These devices, which shapes are shown in Figure 2.18B, exploit adiabatic width tapering to locally enhance stress in the center. The tapering is implemented as follows. The width of the PnC is changed cell-wise according to

$$w_{\text{cell},i} \propto 1 - (1 - a) \exp(-i^2/i_0^2), \quad (2.201)$$

where $i = 0, 1 \dots$ is the cell index starting from the beam center, a and i_0 respectively define the transverse and longitudinal sizes of the waist region, which are chosen to optimize the Q at certain frequency. For each taper length the soft-clamped mode is engineered to be well localized inside the thin taper region by tuning the pitch of unit cells. Importantly, the PnC cell lengths must also be scaled proportional to $1/\sqrt{w_{\text{cell}}}$ in order to compensate for the bandgap frequency shift due to the non-uniform strain distribution.

A set of 4 and 7-mm-long tapered PnC nanobeams was fabricated with the length of the taper varied in order to tune the stress at the center of the beam $\bar{\sigma}(x_c)$ from 2 to 4 GPa. The measurements of spectra of thermal motion, presented in Figure 2.18A, allow us to extract bandgap frequencies, $\Omega_{\text{bg}}/(2\pi)$, and corroborate enhanced stress. This is

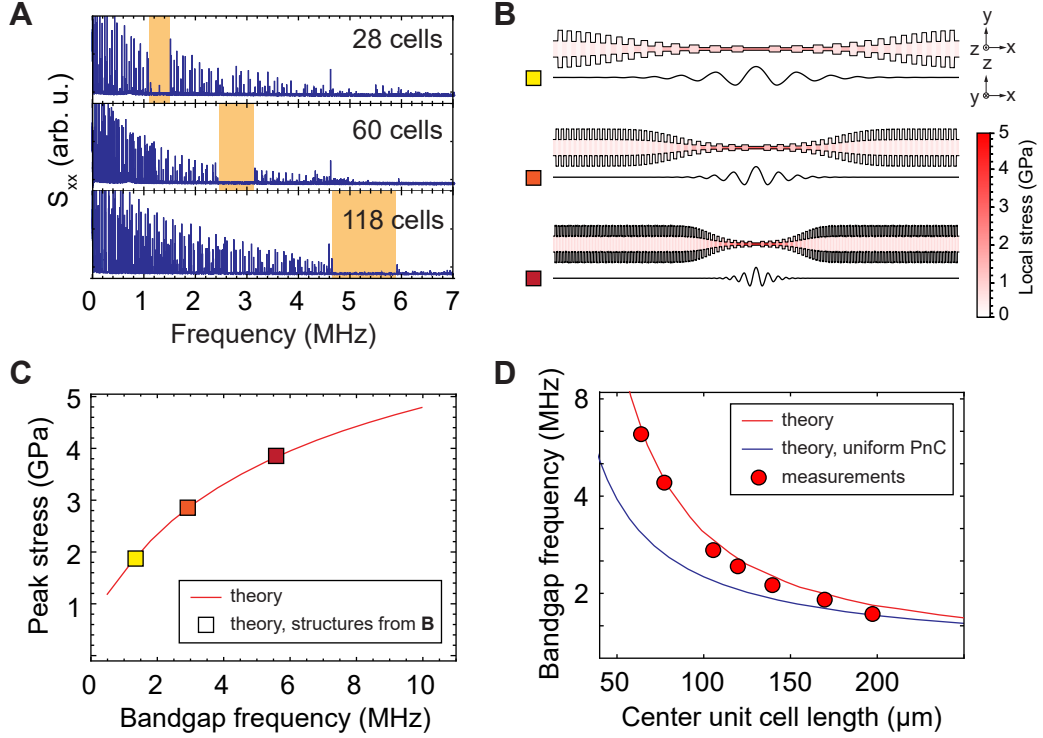


Figure 2.18: One-dimensional PnC beams utilizing strain engineering technique for Q enhancement. A) Thermal displacement spectrum of 4-mm-long devices with profiles shown in B). Bandgaps are highlighted in orange. (C) Simulation of peak stress versus bandgap frequency $\Omega_{\text{bg}}/(2\pi)$ for devices shown in (B). (D) Measurements of $\Omega_{\text{bg}}/(2\pi)$ versus length of the central unit cell. Red and blue lines are models with and without accounting for stress concentration, respectively.

done through analyzing the dependence of Ω_{bg} on the length of the central unit cell $l_{\text{cell},0}$. The theoretical trend is $\Omega_{\text{bg}} \propto \sqrt{\bar{\sigma}(x_c)}/l_{\text{cell},0}$, and therefore an enhancement of stress is expected to manifest as increased bandgap frequency for a fixed size of the unit cell. This expectation is in good agreement with the data presented in Figure 2.18C-D.

Measured quality factors of uniform and tapered PnC nanobeams are compared in Figure 2.19. Blue circles correspond to the measurements as shown in Figure 2.15B. Red circles are compiled for localized modes of 4-mm-long tapered beams with various peak stresses, corresponding to a bandgap frequency varied from $\Omega_{\text{bg}}/(2\pi) = 1 - 6$ MHz. Theoretically, $Q(\Omega_{\text{bg}})$ is predicted to trace out a line of constant $Q \times f \approx 10^{15}$ Hz, exceeding the soft-clamping limit (Eq. (2.185)) for sufficiently high frequency. We observe this behavior with an unexplained $\sim 30\%$ reduction, with Q factors exceeding the clamp-free model by a factor of up to three and reaching absolute values high as 3×10^8 . Though theoretically this Q should be accessible by soft-clamping alone at lower frequency, our strain-engineering strategy gives access to higher Q -frequency products ($Q \times f$), reaching a value as high as 8.1×10^{14} Hz for the 3.2 MHz mode of a 4-mm-long

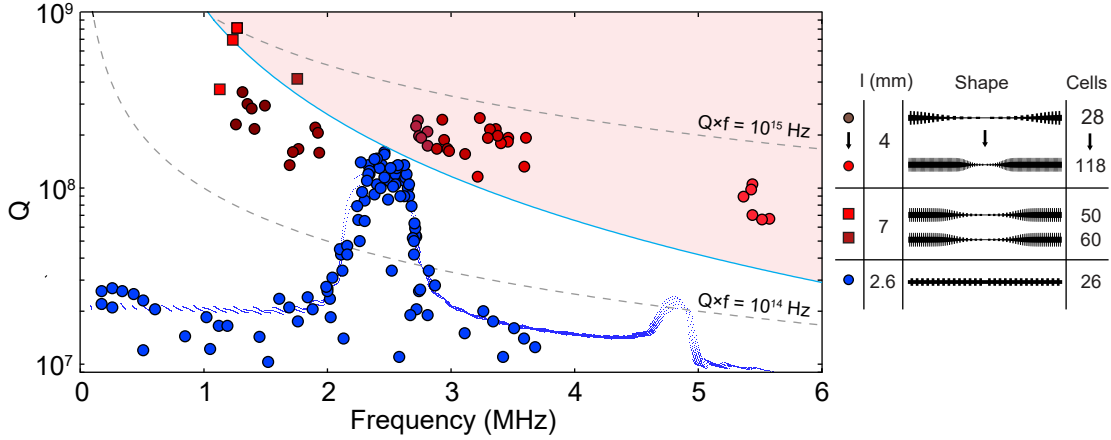


Figure 2.19: Quality factor versus mode frequency of PnC nanobeams with different geometries. Blue points correspond to modes of the uniform PnC nanobeam reproduced from Sec. 2.5.1 (large points are measurements and dots are numerical calculations). Red points correspond to defect modes of tapered beams, which Q s are enhanced by strain engineering techniques. Red color groups include the highest five Q factors recorded for each beam design. Q s in region shaded light red are above the soft-clamping limit, which is indicated by the blue line. The samples are fabricated by Amir Ghadimi and Mohammad Bereyhi.

device. Higher Q and $Q \times f$ factors were achieved using longer beams (red squares). For a 7-mm-long device we observed a 1.33 MHz defect mode, corresponding to $Q = 8.0 \times 10^8$ and $Q \times f = 1.1 \times 10^{15}$ Hz. We note that at this low damping rate ($\Gamma/(2\pi) \sim 1$ mHz), photothermal effects become important. Gated ringdowns confirm that photothermal damping is negligible (see Sec. 2.7 for experimental details).

The realization of $Q \times f \sim 10^{15}$ in a $m \sim \text{pg}$ mechanical oscillator has numerous intriguing implications. First, such an oscillator is an exquisite force sensor. The highest- Q mode among those characterized in Figure 2.19 is limited by thermal noise to a sensitivity of $\sqrt{4k_B T m \Gamma} \approx 1.4 \text{ aN}/\sqrt{\text{Hz}}$ at $T = 300$ K. This value is on par with a typical AFM cantilever operating at 100 times lower frequency and temperature [147], creating new opportunities for applications such as force microscopy with high spatial resolution [46, 80]. Of practical importance is that the reported devices also exhibit an exceptionally strong thermal displacement of $\sqrt{2k_B T \Gamma / (m \Omega^2)} \sim \text{nm}/\sqrt{\text{Hz}}$, accessible by rudimentary detection techniques such as deflectometry. Indeed, their zero-point motion $\sqrt{2\hbar Q / (m \Omega^2)} \sim \text{pm}/\sqrt{\text{Hz}}$ is orders of magnitude larger than the sensitivity of modern microcavity-based optical interferometers, offering possibilities in the field of quantum measurement and control [148]. A fascinating prospect is to use measurement-based feedback to cool such an oscillator to its ground state from room temperature. A basic requirement is that the oscillator undergo a single oscillation in the thermal decoherence time $\hbar Q / k_B T$. The devices reported are exceptional in this respect, capable of performing $2\pi Q \times f / (k_B T / \hbar) > 100$ coherent oscillations at room temperature.

Finally, in order to clearly illustrate the advantages and limitations of ESE techniques,

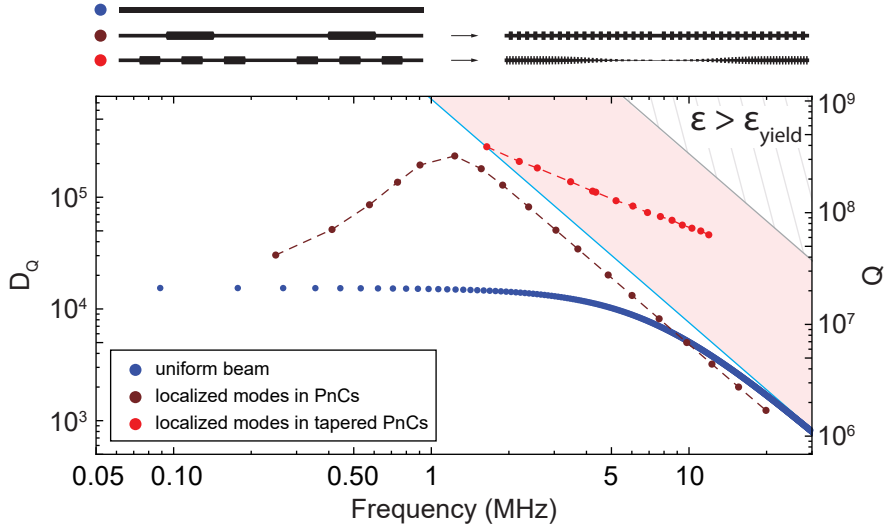


Figure 2.20: Theoretical dissipation dilution in PnC beams with and without tapering, assuming a fixed length $l = 3$ mm and thickness $h = 20$ nm. Points correspond to D_Q (left axis) and Q (right axis) for specific flexural modes, assuming $Q_{\text{int}} = 1.4 \times 10^3$. Blue points correspond to modes of a uniform beam. Dark red and red points correspond to localized modes of PnC beams and tapered PnC beams, respectively. Note that each localized mode corresponds to a different beam shape. Blue line: limit for a soft-clamped beam (Eq. (2.185)). Gray line: ultimate limit set by the breaking stress (Eq. (2.184)).

we compare in Figure 2.20 quality factors theoretically calculated for 3-mm-long and 20-nm-thick tapered and uniform Si_3N_4 PnC beams. The taper waist has been adjusted to match the wavelength of the localized mode. It can be seen that as the frequency increases, the dilution of modes in tapered PnC devices (red points) is progressively enhanced relative to conventional soft-clamped modes (dark red points). There are two other messages to take away. Firstly, the ultimate limit of dissipation dilution (Eq. (2.184)) is attainable with tapered PnC beam designs. Secondly, this limit can be only attained for high-order modes, which wavelength is short enough to significantly benefit from global stress concentration. This makes the practical implementation of devices particularly challenging, as even more extreme aspect ratios than those required for soft-clamping need to be realized.

Aside from the challenges related to fabrication yield, for the quality factors of the highest aspect ratio devices fabricated in this work we did not observe as good an agreement with theory as for the shorter ones. While the correspondence with theory was exceptionally good for the Q s of 2.6 mm-long beams presented in Sec. 2.5.1, for 4 mm beams the highest observed Q s were 30 % below the theoretical prediction. The measured quality factors of 7-mm beams were only marginally better than those of 4 mm ones, while theoretically an improvement by more than a factor of two was expected for longer devices. Thus what limited the highest quality factors observed in our work was not fully understood.

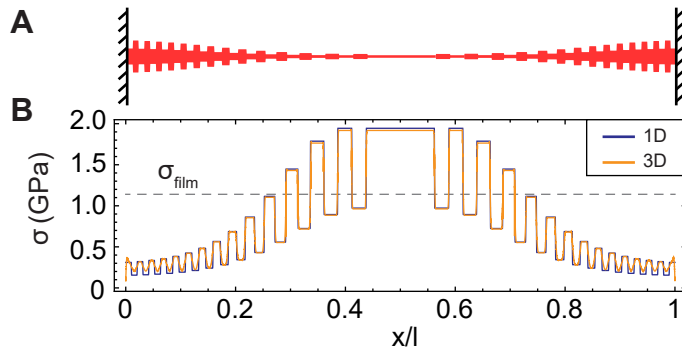


Figure 2.21: Equilibrium stress along the axis of a tapered PnC beam. A) Beam corrugation profile. B) Distribution of axial stress calculated with the 1D model (blue line) and simulated in 3D using COMSOL (orange line). The initial film deposition stress is marked by the dashed gray line.

2.5.3 Comparison between one- and three-dimensional simulations

The numerical solution of one-dimensional Euler-Bernoulli equation proved to be an efficient theory tool capable of rapidly providing insights into various aspects of nanobeam spectra and quality factors. We implemented a simple one-dimensional finite-element solver for the Euler-Bernoulli equation as a Mathematica notebook, which is openly available [126]. The solver can handle in-and out-of-plane flexural modes of doubly clamped beams as well as PnC unit cells under Floquet-periodic boundary conditions. The same notebook contains the beam geometries used in our works.

The results obtained using the one-dimensional model were extensively benchmarked against two- and three- dimensional finite-element simulations performed using COMSOL, which rely on fewer a priori assumptions, but which are also much more time-consuming. The agreement was found to be excellent within the validity range of the one-dimensional model, i.e. for structures with high-aspect ratios and purely flexural deformations. In Figure 2.21 and Figure 2.22 we present one example comparison between one- and three-dimensional simulations. The structure is a tapered PnC nanobeam with the overall length $l = 500 \mu\text{m}$, thickness $h = 100 \text{ nm}$, center width $w = 400 \text{ nm}$ and the widest part having $w = 5 \mu\text{m}$. The aspect ratio l/h is relatively moderate in this example, as we practically found that the results of three-dimensional simulation of mode shapes may not be reliable for higher aspect ratios (two-dimensional simulations using the COMSOL shell interface are free from this limitation).

Figure 2.21 shows the simulated distribution of axial stress along the beam. Stress engineering implemented by tapering results in the peak stress exceeding the initial value of the film deposition stress by a factor of two. According to the one-dimensional model (see Eq. (2.156) in Sec. 2.4.5), the equilibrium static stress is simply given by the inverse of the beam width times the average stress, $\sigma(x) = \sigma_{\text{avg}}/v(x)$. This is confirmed by the 3D FEM results, which somewhat deviate from the analytic formula only in the vicinity of the beam clamping points, where the width-to-length ratio for the unit cells

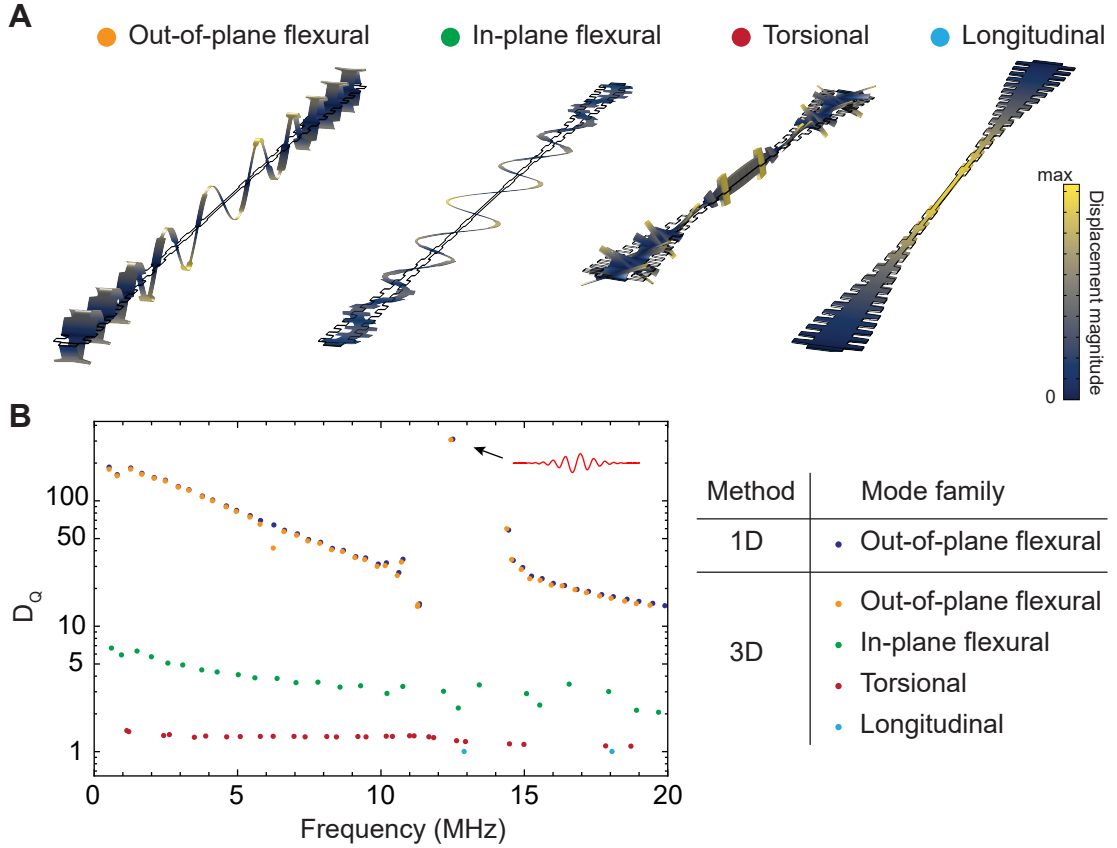


Figure 2.22: The full spectrum a doubly-clamped tapered PnC beam with length $l = 500 \mu\text{m}$, thickness $h = 100 \text{ nm}$, center width $w = 400 \text{ nm}$ and transverse profile shown in Figure 2.21. A) Example modes of different families. B) Dissipation dilution versus mode frequency calculated using 3D and 1D vibrational mode shapes. Orange, green, red and blue dots correspond to different mode families as explained in the caption. Calculations using the 1D model [126] are only presented for out-of-plane flexural modes (dark blue dots). The localized soft-clamped mode is denoted by the arrow.

is not very high ($l_{\text{cell}}/w_{\text{max}} = 20 \mu\text{m}/5 \mu\text{m}$), and the one-dimensional approximation is not expected to work particularly well.

We next simulate the full vibrational spectrum of the example tapered PnC nano-beam using COMSOL, which for frequencies up to 20 MHz consists of approximately one hundred modes. The results are presented in Figure 2.22. The low-frequency modes of the structure can be classified into four mode families: in- and out-of-plane flexural, torsional and longitudinal modes. The classification is not absolute, if two modes from different families happen to be around the same frequency, they form hybrid modes that do not belong to any of the classes. Also, modes at higher frequencies can have more complex displacement profiles.

Dilution factors found using the 3D FEM solutions for the mode shapes are presented

in Figure 2.22B. These factors are calculated using the generic expressions given by Eq. (2.87)—Eq. (2.90) from Sec. 2.3, which do not differentiate between mode families and take the full 3D deformation profile as an input. The calculations based on these formulas were implemented in MATLAB using its interface with COMSOL (the code is not yet published, it is available from the author upon request). Out-of-plane (z -polarized) flexural modes have been of our primary interest so far, as they exhibit the highest dissipation dilution and, correspondingly, the highest quality factors. In-plane flexural modes experience about an order of magnitude lower dilution than out-of-plane ones, consistent with the ratio of the beam width and thickness, w/h . Torsional modes experience marginal dissipation dilution because they are not perfectly well distinguished from flexural, and longitudinal modes experience no dilution.

While the 3D FEM simulation provides D_{QS} of all modes, the one-dimensional approximation that was used so far is only applicable to flexural modes (while other one-dimensional approximations can be derived for different mode families). For out-of-plane flexural modes, the predictions of our 1D model (also shown in Figure 2.22B) are in an excellent agreement with the orders-of-magnitude more time consuming full 3D simulations. The most prominent deviation between the 1D and 3D calculations takes place for the out-of-plane flexural mode with frequency around 6.2 MHz (the orange dot outlier in Figure 2.22B) that happened to hybridize with a low-dilution torsional mode and correspondingly has a reduced quality factor.

2.5.4 PnC membranes with low effective mass localized modes

The best experimentally demonstrated quality factors of nanobeam resonators, $Q = 1.6 \times 10^9$ at 6K and $Q = 8 \times 10^8$ at room temperature, are the highest among high-stress devices. Nanobeams also have very low masses, which together with their low dissipation translates into outstandingly low thermal force noise levels [32]. In order to take the full advantage of these properties, however, a high-sensitivity readout of resonator motion has to be implemented. While moderate-sized nanobeams have been successfully coupled to whispering gallery optical modes by means of near-field coupling [149], an analogous integration of mm-long beams hosting ultrahigh- Q mechanical modes remains an outstanding challenge.

In contrast to beams, membrane resonators can be relatively straightforwardly integrated with high-finesse optical cavities using the membrane-in-the-middle scheme. Not long after the soft clamping technique was pioneered by Tsaturyan et. al. [36], the first cavity optomechanics experiments with soft-clamped membrane modes followed [150, 151]. In this section, we discuss the designs of membranes with soft-clamped modes for our room temperature cavity optomechanics experiment, which will be presented in the following (see Chapter 4). The simulations of spectra and dissipation dilution in PnC membranes were performed using COMSOL as described in Appendix A.2.

The 2D phononic crystals in our work are formed by the hexagonal pattern of circular holes introduced in Ref. [36], which creates an almost isotropic bandgap for flexural modes. The hexagon pattern appears to be the simplest arrangement that has this

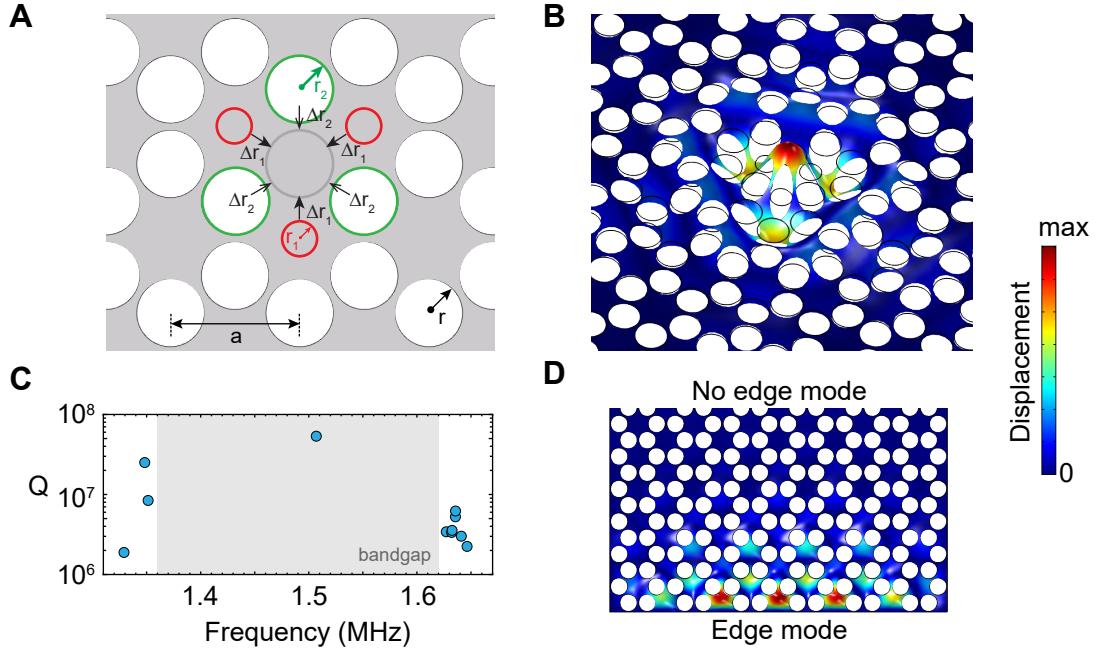


Figure 2.23: Simulations of a PnC membrane with a single low-mass soft-clamped mode. A) The definition of PnC defect. B) Displacement profile of the soft-clamped mode. C) Frequencies and quality factors of the localized mode and several other modes which are the closest to the phononic bandgap. D) Displacement profile of an edge mode localized around the bottom termination of the membrane. Terminating the membrane as shown on the top does not create edge modes.

property. In our trials, neither triangular nor rectangular arrays of circular holes produced acceptable bandgaps. Moreover, unlike unstressed phononic crystals, which can have unit cells of almost arbitrary shapes, introducing non-circular holes in thin stressed membranes is potentially problematic, and can easily result in locally compressive stress.

In perfectly periodic structures, no vibrational states exist within the phononic bandgap. If a defect is introduced, it can localize one or more modes, which do not reach the membrane edges if the overall PnC size is large enough. The sizes of defects used in [36, 150] are relatively large compared to the unit cell, and they localize more than one mode. At the same time, it is often desirable to selectively perform measurements on one mechanical mode, in which case the spectral overlap of this mode with all other modes needs to be minimized. This can be accomplished by engineering a membrane defect such that it localizes a single soft-clamped mode with frequency at the bandgap center. Single-mode defects also generally have a smaller size than multi-mode ones, which results in better mode confinement and, correspondingly, smaller effective masses.

Our approach to the formation of PnC defect is shown in Figure 2.23A. It consists of a) removing one hole (gray) from the membrane pattern, b) adding three holes in the centers of the adjacent cells (red), which have smaller radii, r_1 , and are displaced by Δr_1

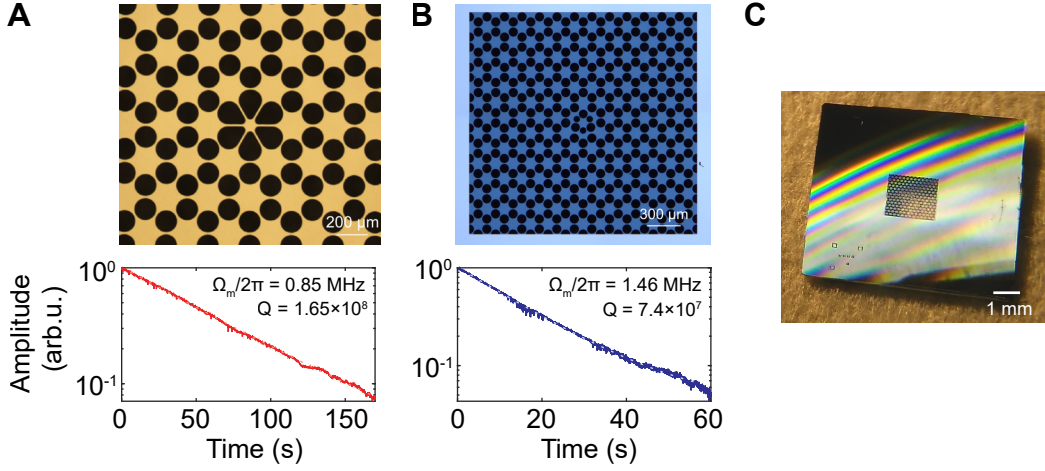


Figure 2.24: Microscope images of PnC membranes (top) and ringdowns of their soft-clamped, localized modes (bottom). A) $3.6\text{ mm} \times 3.3\text{ mm} \times 40\text{ nm}$, with a localized mode at 853 kHz. B) $2\text{ mm} \times 2\text{ mm} \times 20\text{ nm}$ membrane with a localized mode at 1.46 MHz. C) Camera photo of a chip with PnC membrane. The devices are fabricated by Alberto Beccari.

towards the center, c) rescaling the three nearest existing holes (green) and displacing them towards the center by Δr_2 . The precise parameter values (see their definition in Figure 2.23A) are the following: $r_1 = 0.7 \times r$, $r_2 = 0.95 \times r$, $\Delta r_1 = 0.15 \times a$, $\Delta r_2 = 0.07 \times a$, where a is the lattice constant. The displacement profile of the resulting soft-clamped mode is shown in Figure 2.23B, and the simulated frequencies and quality factors of this mode and a few other mechanical modes around the acoustic bandgap are shown in Figure 2.23C. Here the membrane thickness is 20 nm, the lattice constant $a = 160\ \mu\text{m}$ and the hole radius $r = 0.26 \times a$ [36]. The phononic bandgap spans the frequency range of 1.3 – 1.6 MHz. The effective mass of the localized mode in Figure 2.23B is 1.1 ng. This, according to our simulations, is approximately four times lower than the effective mass of the localized mode used in Ref. [150], if the PnC design is scaled to the same mode frequency. The quality factors of these modes are the same within a few percent according to our simulations.

Clamped membrane edges also break the periodicity of phononic crystal, and also can be a source of localized modes with frequencies within the phononic bandgap. Unlike soft-clamped modes, modes localized around the edges have low quality factors and their presence is undesirable. The presence or absence of these modes depends on the way the phononic crystal is terminated, as illustrated in Figure 2.23D. Termination on the bottom side, in which the edge crosses no holes, creates edge modes and therefore should be avoided. In contrast, the terminations on the top and on the lateral sides are free from edge modes, and we use them in practical membrane designs.

In Figure 2.24 we present realizations of Si_3N_4 PnC membranes with soft-clamped modes optimized for low effective mass and high Q . Figure 2.24B shows a $2\text{ mm} \times 2\text{ mm}$ phononic crystal membrane implementing the design from Figure 2.23, which creates a

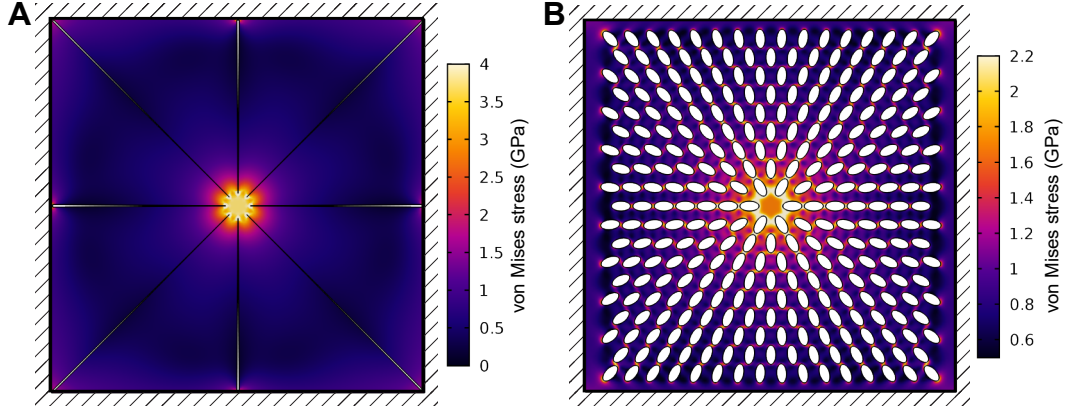


Figure 2.25: Simulation of stress concentration in patterned membranes. Hatching designates clamped boundaries. A) Stress enhancement in the center of a uniform membrane with radial cuts. B) Stress enhancement produced by a pattern of radially oriented elliptic holes.

single mode localized in the middle of the phononic bandgap. The displayed sample has $Q = 7.4 \times 10^7$ at 1.46 MHz and $m_{\text{eff}} = 1.1$ ng, corresponding to $S_{FF}^{\text{th}} = 34$ aN/ $\sqrt{\text{Hz}}$. Another approach towards clearing a low effective mass localized mode is introducing a trampoline defect, as shown Figure 2.24A. The device in the figure features $m_{\text{eff}} = 3.8$ ng and $Q = 1.65 \times 10^8$ at 0.853 MHz, corresponding to a thermal force noise $S_{FF}^{\text{th}} = 13$ aN/ $\sqrt{\text{Hz}}$. The main disadvantage of the design in Figure 2.24A, which is similar to the one reported in Ref. [152], is that its localized mode has frequency very close to the bandgap edge.

2.5.5 Global stress concentration in 2D

Techniques of local stress enhancement utilized for elastic stress engineering are not only applicable to beams but also to two-dimensional membranes. In Figure 2.25 we present two example membrane patternings that create localized areas of high stress. The plotted distributions of stress are obtained, as usual, by simulating the relaxation of originally uniform and isotropic film pre-stress ($\sigma_{\text{film}} = 1.14$ GPa) in membranes with fixed outer edges. There are no scale bars in the plots, as the stress profiles do not change under isotropic scaling of the geometries.

The membrane in Figure 2.25A presents an example in which the stress is enhanced close to the yield value. This geometry is based on the one utilized in Ref. [153]. It has a few radial cuts which split the membrane into several almost completely independent strips. Each strip is wider on the outer side and narrower in the center. In a qualitative agreement with the behavior of one-dimensional geometries, discussed in Sec. 2.5.2), the strips concentrate stress in their centers where they overlap with each other. A similar effect is produced by an array of elliptic holes oriented towards the membrane center, shown in Figure 2.25B.

Utilizing stress concentration to enhance dissipation dilution is even less trivial in

two dimensions than in one. Although the challenges in these cases are similar, to date no membrane geometry has been identified in which the concentration of stress would enhance quality factors. In particular, because of the inhomogeneous stress in the structure shown in Figure 2.25B, it does not have a phononic bandgap, and therefore cannot localize modes in the central region where the stress is enhanced. While in one dimension the variation of stress across the phononic crystal can be compensated by an appropriate variation of the unit cell length, this method is not directly transferable to two dimensions. The main challenge is that unlike one dimension, where the lengths and widths of PnC unit cells are independently adjustable, in two dimensions the unit cells need to fully cover the plane, and hence do not have similar transformation freedom.

Another key challenge for the application of stress concentration techniques in two dimensions is that the anisotropic stress distributions, commonly arising in stress-enhancing geometries, are prone to having locally compressive stress in one of the principal directions. Such a configuration leads to dissipation concentration rather than dilution for vibrational modes.

2.6 Fractal-like resonators

Self-similar structures can have surprising physical properties. Coast lines are a famous example—their length is loosely defined at geographic scale [154]. In the domain of optics, it was found that self-similar cavities can support modes with arbitrarily small mode volume [155] at a given wavelength. Meanwhile, hierarchical metamaterials can have improved stiffness per unit mass [156, 157] compared to natural materials. The acoustic vibrations of resonators are also known to be affected by structural self-similarity in a nontrivial way, both in terms of the vibrational mode density [158, 159] and damping [160]. The latter can aid the design of mechanical resonators with low dissipation.

In this section we theoretically study mechanical vibrations of systems of tensioned strings in the shape of self-similar binary trees, which are clamped at the tips in order to sustain tension (see Figure 2.26A). Dissipation dilution in such structures is found in a manner analogous to simple strings and membranes to be

$$D_Q = \frac{\langle W^{(\ln)} \rangle}{\langle W^{(\text{lin})} \rangle} = \frac{1}{\alpha\lambda + \beta\lambda^2}, \quad (2.202)$$

where λ is the stress parameter, and α and β are the boundary and distributed loss coefficients, respectively, which will be elaborated in the following. Low-frequency flexural modes in binary tree resonators have an unusual feature—their amplitude is reduced as they propagate from the trunk to the clamped tips of the branches. This can suppress the boundary loss coefficient, α , in a way analogous to mode localization in phononic crystals and thus implement soft clamping. A disadvantage of soft clamping by PnC localization is that it can only be applied to high order vibrational modes in the range from tens to hundreds. In contrast, suppression by propagation over string branchings does not require the structure to extend beyond one acoustic wavelength and therefore

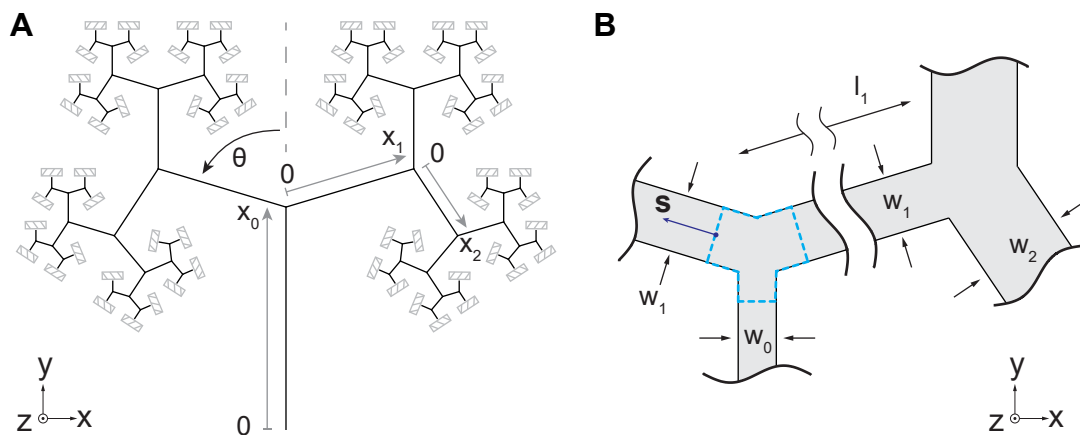


Figure 2.26: Binary tree resonator geometry. A) Binary tree with six branching levels, local x -coordinates are shown for the first three levels. One tree defines half a resonator, the complete structure is formed by adding its mirror reflection in the yz plane. B) Two branching points of a binary tree resonator with the definitions of the segment widths, w , and lengths, l . The blue contour is used to derive the transformation of the mode derivative.

can enhance the quality factor of the fundamental resonator mode, as well as of a multitude of other low-order modes at the same time. In particular, this method is applicable to the design of high- Q beam [67, 68] and tethered-membrane [161, 79] nanomechanical resonators.

The results, presented in this section, are relevant to areas ranging from sensing [78, 79] to cavity quantum optomechanics [19], which employ stressed, high- Q nanomechanical resonators [67, 68]. Moreover, because of the close relationship between the Q of the fundamental mode of a clamped tensioned structure and the Q of a pendulum [33], our results can be used for designing high- Q suspensions of test masses, akin to those employed in gravitational wave detectors and experiments on macroscopic optomechanics [162, 87, 163].

2.6.1 Soft clamping of a fundamental mode

The present section is based on the publication “Fractal-like mechanical resonators with soft-clamped fundamental modes” (Ref. [39]).

When a flexural mode propagates over a junction of three beams, its gradient is reduced, which can ultimately lead to the suppression of boundary loss according to the results of Sec. 2.4.6. In order how this reduction occurs, we consider a junction of beams with rectangular cross section, highlighted by the blue contour in Figure 2.26B. The dynamic equation for the two-dimensional profile of out-of-plane vibrations $u(x, y)$ is given by [70]

$$-\frac{\partial}{\partial x_i} \left(\sigma_{ij} \frac{\partial u}{\partial x_j} \right) = \omega^2 \rho u, \quad (2.203)$$

where as usual we assume summation over the repeating indices i and j , each of which runs over the two spatial coordinates, x and y . The components of the stress tensor σ_{ij} are functions of x and y . By integrating both sides of Eq. (2.203) over the infinitesimally small area of the blue contour in Figure 2.26B and transforming the divergence into a boundary integral we find

$$\oint ds_i \left(\sigma_{ij} \frac{\partial u}{\partial x_j} \right) = 2 w_2 \sigma_2 u'_2 - w_1 \sigma_1 u'_1 = 0, \quad (2.204)$$

where u'_1 and u'_2 are the amplitude gradients in the directions of axes x_1 and x_2 , respectively. By doubling the contribution of beam two we account for the assumption that the mode branches symmetrically. Next, the balance of static tensile forces requires

$$w_1 \sigma_1 = 2 w_2 \sigma_2 \cos(\theta). \quad (2.205)$$

Combining Eq. (2.204) and Eq. (2.205) we find

$$u'_2 = u'_1 \cos(\theta). \quad (2.206)$$

This shows that the mode gradient is reduced by a factor of $\cos(\theta)$ after propagating over a branch point. Although the reduction in principle can be arbitrarily large if θ is close to $\pi/2$, the improvement in dissipation dilution provided by a single branch point is fairly limited. The reason is an associated increase in the distributed part of the lossy energy caused by the torsional deformation of the beams.

Cascaded string branchings can be much more efficient in suppressing the boundary loss than a single one. When multiple branchings are combined, the totality of string segments forms a binary tree, as shown in Figure 2.26. After each branching the lengths of the string segments are reduced by the same ratio in order to prevent self-overlap. As realistic resonators have to be hard-clamped on all sides, we consider structures composed of two symmetric binary trees joined at the roots and clamped at the tips. We treat the case when all the strings are beams with rectangular cross section and the same thickness, a geometry that is amenable to nanofabrication. However, the main quantitative results are not contingent on this assumption. Since we are primarily interested in the properties of the fundamental resonator mode, in the following we consider the modes that split symmetrically at each branch point.

Binary tree resonators are convenient to analyze using a set of local axes, x_n , each directed along one segment, beginning at one branch point and ending at the next one as shown in Figure 2.26A. Considering one path from the resonator center to one of the clamps is sufficient for describing symmetrically splitting modes. We index the branching level by n , and the total number of branchings is denoted by N . The deformation of each segment as a function of the local coordinate is denoted by $u_n(x_n, t)$, and its spatial envelopes by $U_n(x_n)$. The segment lengths, l_n , and widths, w_n (shown in Figure 2.26B), are found using the ratios r_l and r_w as $l_n = l_0(r_l)^n$ and $w_n = w_0(r_w)^n$, respectively. Note that according to this definition the total length of the central resonator segment is $2l_0$, as it consists of two symmetric tree trunks.

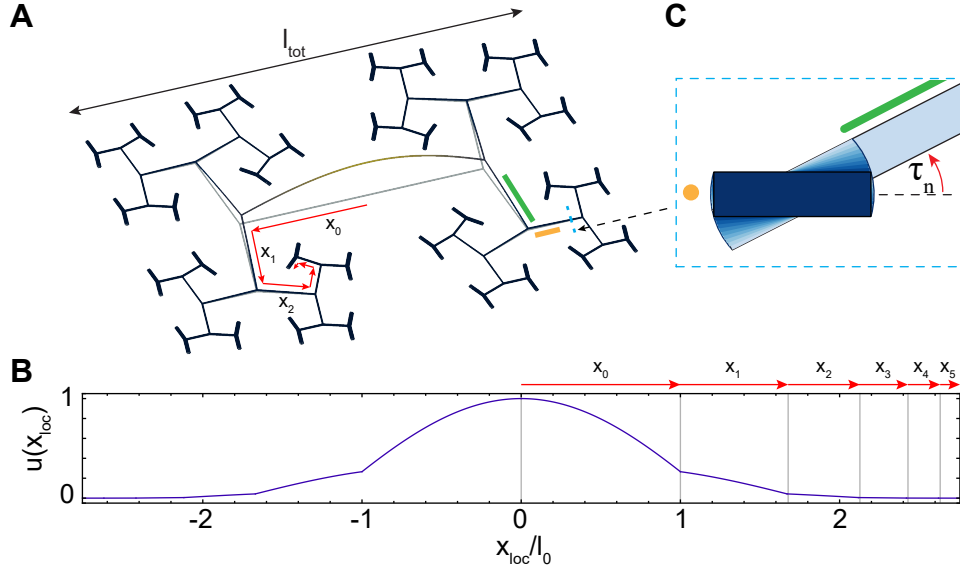


Figure 2.27: A) FEM simulation of the fundamental mode of a stress-preserving binary tree resonator with $r_l = 0.67$, $l_0 = 1$ mm ($l_{tot} = 3.7$ mm), $w_0 = 100$ nm, $h = 20$ nm, $\theta = 80$ deg, $N = 5$. The inset schematically shows a cut view of one segment (marked with orange) and illustrates the torsion created by the previous segment (marked with green). B) The displacement of the mode shown in A plotted over the local x coordinates following a path from one tip of the tree to another. C) Torsional deformation of a constituent beam segment.

Flexural modes and vibrational frequencies of tree resonators can be found by matching the mode envelopes $U_n(x_n)$ over different segments so that Eq. (2.206) is fulfilled, as well as the continuity condition $U_n(l_n) = U_{n+1}(0)$, and the boundary conditions $U_N(l_N) = 0$ and $U'_0(0) = 0$ (or $U_0(0) = 0$ for modes in which the two trees are deformed anti-symmetrically). With $U_n(x_n)$ in hand, one can compute the dissipation dilution factors, the Q s and the loss coefficients α and β of the modes.

Flexural deformations of a two-dimensional system of strings induce torsion of the segments. If the segments have high aspect ratios, the elastic energy stored in torsion has a negligible effect on the mode frequencies, but it profoundly impacts dissipation. Since torsion does not produce geometrically nonlinear strain in the direction of the string axis [34], it only contributes to the lossy elastic energy. Below it will be shown that the torsional contribution dominates the distributed loss coefficient of binary-tree resonators in the regime of strong boundary loss suppression.

The emergence of torsion in a tree segment is illustrated in Figure 2.27C. The equilibria of force moments at the junctions define the boundary conditions for the torsion angles. At the beginning of the segment, the angle is set by the previous segment as $\tau_n = u'_{n-1}(l_{n-1}) \sin(\theta)$. At the end of the segment the angle is zero. The torsional energy

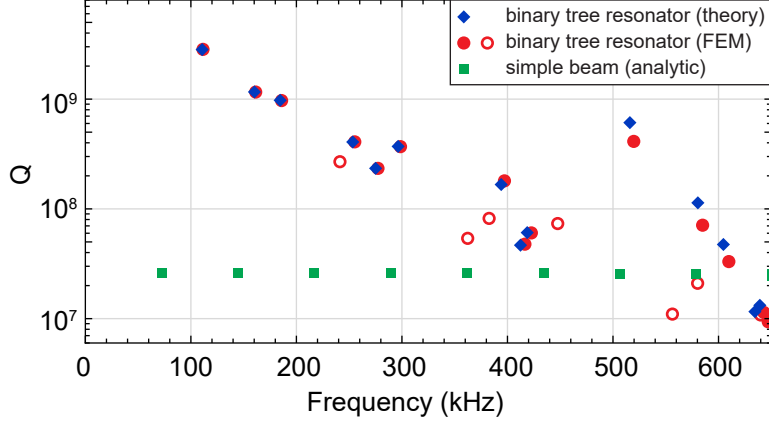


Figure 2.28: Quality factors and frequencies of out-of-plane modes of the resonator shown in Figure 2.27 with $l_{\text{tot}} = 3.7$ mm. Blue dots correspond to the theory presented in this work, red dots to the result of FEM simulation. Filled red dots denote symmetrically branched modes, empty dots: other modes. Green dots show out-of-plane modes of a doubly-clamped beam resonator with the same total length (l_{tot}).

stored by one segment is given by

$$\langle W^{(\text{tors})} \rangle_n = \frac{Ew_n h^3}{6(1+\nu)} \int_0^{l_n} dx_n (\tau'(x_n))^2, \quad (2.207)$$

where ν is Poisson's ratio. If the aspect ratio of the segment is high (which we assume in the following), the transition from τ_n to zero happens linearly and $\tau' = \tau_n/l_n$.

The quality factors of intrinsic loss-limited resonator modes are found by using 2.202. The energies involved are calculated by summing up the contributions from all the tree segments. The lossless “tension” energy is given by

$$\langle W^{(\text{nl})} \rangle = 2 \sum_{n=0}^N 2^n \sigma_n w_n h \int_0^{l_n} dx_n (u'_n(x_n))^2. \quad (2.208)$$

The lossy energy consists of three contributions

$$\langle W^{(\text{lin})} \rangle = \langle W^{(\text{bend,b})} \rangle + \langle W^{(\text{bend})} \rangle + \langle W^{(\text{tors})} \rangle. \quad (2.209)$$

The distributed bending energy is

$$\langle W^{(\text{bend})} \rangle = 2 \sum_{n=0}^N 2^n \frac{Ew_n h^3}{12} \int_0^{l_n} dx_n (u''_n(x_n))^2, \quad (2.210)$$

while the boundary bending is

$$\langle W^{(\text{bend,b})} \rangle = 2^N w_N h^2 \sqrt{\frac{E}{12}} \sqrt{\sigma_N} (u'_N(l_N - 0))^2, \quad (2.211)$$

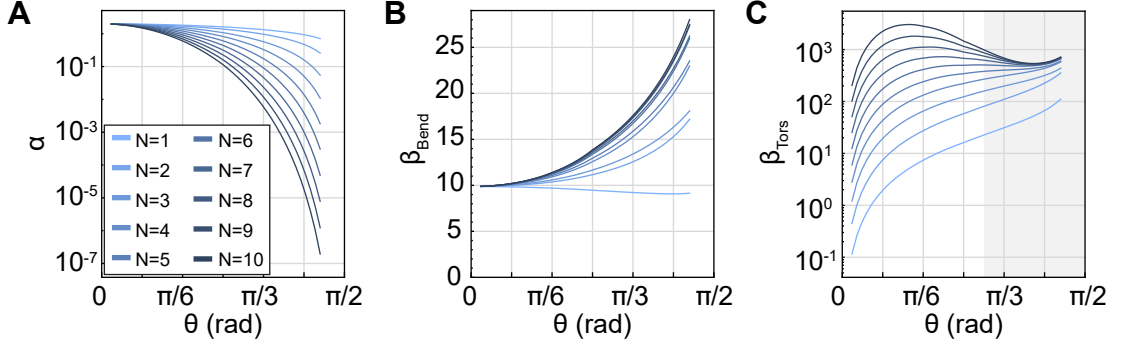


Figure 2.29: Loss coefficients for stress-preserving binary tree resonators with $r_l = r_{l,\text{crit}}(\theta)$ and different numbers of branchings N . A) boundary loss coefficient, B) distributed bending loss coefficient, C) distributed torsional loss coefficient, the region where β_{tors} converges with increasing N is shaded gray.

and the torsional contribution is

$$\langle W^{(\text{tors})} \rangle = 2 \sum_{n=1}^N 2^n \frac{E w_n h^3}{6(1+\nu)l_n} (u'_{n-1}(l_{n-1}) \sin(\theta))^2. \quad (2.212)$$

The loss coefficients in Eq. (2.202) are identified as

$$\alpha = \frac{\langle W^{(\text{bend,b})} \rangle}{\lambda \langle W^{(\text{nl})} \rangle}, \quad (2.213)$$

$$\beta = \frac{\langle W^{(\text{bend})} \rangle + \langle W^{(\text{tors})} \rangle}{\lambda^2 \langle W^{(\text{nl})} \rangle} = \beta_{\text{bend}} + \beta_{\text{tors}}, \quad (2.214)$$

Note that α and β are independent of λ , which in our case is defined as

$$\lambda = \frac{h}{l_{\text{tot}}} \sqrt{\frac{E}{12\sigma_0}}, \quad (2.215)$$

with l_{tot} being the total resonator size in the direction along the central segment. Given l_0 , r_l and θ one can find l_{tot} analytically, but the resulting expression is cumbersome.

Note that unlike the case of traditional membranes and beams, the definition of λ in our problem is a subtle question as fractal-like resonators do not have a single characteristic length scale and stress. Depending on our choice of l and σ , the boundary and distributed loss coefficients α and β would change, of course keeping the overall D_Q constant. Our definition of λ has the advantage that it ensures intuitive correspondence when the binary tree converges to a straight beam: if $\theta \rightarrow 0$ and $r_w \rightarrow 1/2$ then $\alpha \rightarrow 2$ and $\beta \rightarrow (m\pi)^2$, where m is the mode order.

The distribution of static stress in a binary tree resonator in general can be such that the stress is peaked either in the branch tips or in the trunk. For simplicity, we restrict our numeric analysis to the trees in which the static stress along the segments

is uniform. As follows from the balance of static forces (Eq. (2.205)), the condition $\sigma_{n+1} = \sigma_n$ is fulfilled (and the resonator is “stress-preserving”) if the width scaling ratio is set to $r_w = 1/(2 \cos(\theta))$. If a stress-preserving resonator is patterned from a film with isotropic initial pre-stress σ_{film} , the static stress in all segments is given by

$$\sigma_n = \sigma_{\text{film}}(1 - \nu). \quad (2.216)$$

The basic acoustic properties of binary tree resonators can be understood from an example. In Figure 2.27 and Figure 2.28 we present a simulation of the modes of a resonator made of high-stress stoichiometric silicon nitride film at room temperature (for parameters see [127]).

The fundamental resonator mode is shown in Figure 2.27A and Figure 2.27B. The reduction of mode amplitude gradient at each branch point can be observed from these figures, together with the fact that the gradient near the clamping points approaches zero. Note, that the apparent discontinuity of mode derivative in Figure 2.27B is due to the turns of the path following local x -axes, the real two-dimensional mode has no sharp bends at the branch points.

The calculated quality factors are presented in Figure 2.28, which shows that the Q of the fundamental mode is enhanced by about two orders in magnitude compared to a simple doubly-clamped beam of the same size. All low-frequency flexural modes experience similar Q enhancement, which gradually decreases as the acoustic wavelength becomes comparable to the length of the smallest segments.

Two methods were used to obtain the data in Figure 2.28, the theory presented in this work, which relies on the one-dimensional approximation of segment modes, and 2D finite-element method (FEM) simulation of a non-uniform plate under tension. The mode frequencies were found to agree better than within 1.5% between the two methods in the frequency range displayed in the figure. The agreement between the quality factors is at the same level for a few lower order modes, whereas higher order modes show higher discrepancy due to the onset of hybridization between bending and torsional modes, neglected in our theoretical analysis. The FEM simulation also provides information about all the acoustic modes supported by the structure, including non-symmetrically branched and in-plane modes. For clarity we do not show in-plane modes in Figure 2.28, as their quality factors are significantly lower compared to the out-of-plane modes, their density is about the same and the fundamental resonator mode never belongs to this family.

In order to obtain a more general insight into the properties of binary tree resonators, we systematically study the variation of boundary and distributed loss coefficients of the fundamental resonator mode. These loss coefficients are material- and scale-independent and are determined by the geometric parameters r_l , r_w , θ and N . One of the parameters, r_w , is fixed to satisfy the stress-preservation condition at given θ . Furthermore, we put $r_l = r_{l,\text{crit}}(\theta)$, where $r_{l,\text{crit}}$ is the value at which tip-to-tip self contact occurs in a fractal tree with infinite N , and there is no self-contact for finite N (see [164]). We sweep the remaining free parameters, θ and N , and present the results in Figure 2.29. It can be

seen that α is suppressed as θ increases, while β_{tors} , on the contrary, goes up. Therefore, the torsional lossy energy eventually becomes the main limitation for dissipation dilution as the boundary loss is suppressed. The exact parameters at which the distributed loss matches the boundary loss, and therefore the quality factor is maximized, depend on λ . When λ gets smaller, the optimum shifts towards larger θ or N as it takes a stronger boundary energy suppression to match the distributed contribution.

The data in Figure 2.29 helps us understand some properties of binary tree resonators in the fractal limit, when N goes to infinity. As N increases, the boundary loss coefficient α reduces to zero and the distributed bending loss coefficient β_{bend} converges to a finite value. The distributed torsion loss coefficient β_{tors} has more complex behavior with increasing N , it can either converge to a finite value or increase indefinitely. Which of the two scenarios is realized depends on the behavior of geometric series in Eq. (2.212), which can be shown to converge if $\cos(\theta) < \sqrt{r_l/(2r_w)}$. Correspondingly, depending on the behavior of β_{tors} , the Q of the fundamental mode of a fractal structure can either be finite and limited by the distributed energy loss or it can be zero (i.e. the Q would be low and determined by factors beyond the approximations of our theory). It is interesting to compare this conclusion to the case of membranes with self-similar boundaries, in which $Q \rightarrow 0$ was found to be the only possible scenario in the fractal limit [160].

2.6.2 Fractional spectral dimensionality

Self-similar structures do not have translational symmetry, but instead exhibit scale invariance. For this reason their densities of states can show signatures of non-integer dimensionality [165, 166], which were observed in proteins [167], silica aerogels and glasses [166]. Here we present a numeric evidence for fractional dimensionality in the vibrational mode densities of tensioned binary tree resonators.

Vibrational mode densities are convenient to characterize using the cumulative distribution function,

$$\text{CD}(\omega) = \sum_{n:\Omega_n \leq \omega} 1, \quad (2.217)$$

which gives the total number of modes below a given frequency, ω . It is easy to see that for a resonator cut out of a homogeneous medium in which sound waves have a dispersion relation $k \propto \omega$ the cumulative distribution of mode density is proportional to ω^d , where d is the dimension of the space. Hierarchical structures can also have a power law behavior of the low-frequency mode density, but for them the power is not necessarily integer. In this case,

$$\text{CD}(\omega) \propto \omega^{\tilde{d}}, \quad (2.218)$$

where \tilde{d} is by definition the spectral dimension of the structure [165, 166]. We find that the low-frequency spectra of binary tree resonators are consistent with Eq. (2.218) and non-integer \tilde{d} s.

We present in Figure 2.30 the cumulative distributions of out-of-plane modes of binary-tree resonators with $N = 5$ levels of hierarchy, the branching angle $\theta = \pi/2$,

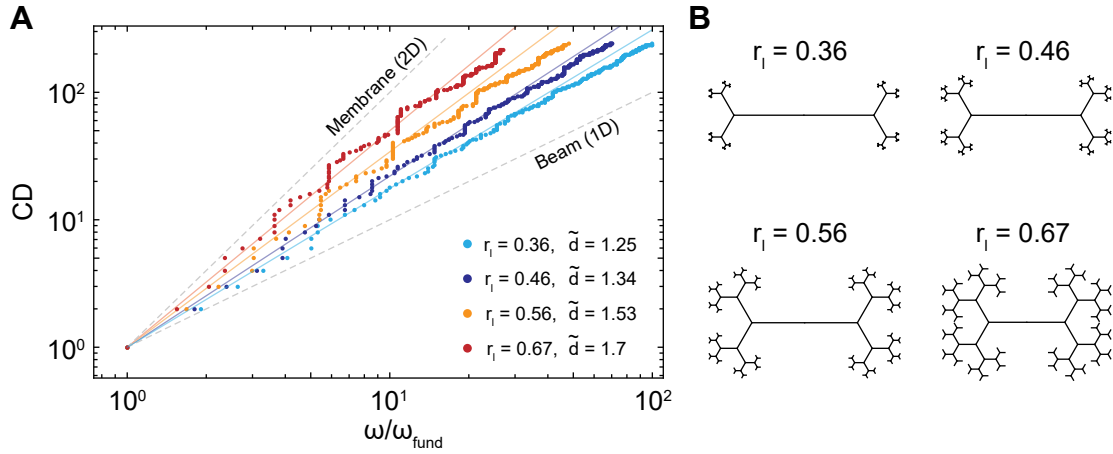


Figure 2.30: Spectral dimensions and geometries of binary tree resonators with $\theta = \pi/3$, $N = 5$ and different r_l . A) Cumulative distributions of out-of-plane modes found from 2D FEM simulation. The spectral dimensionalities \tilde{d} obtained from fits are indicated in the inset. B) Geometries of the resonators which spectra are presented in A.

and different length contraction ratios r_l . To obtain these distributions, we numerically calculate ≈ 230 lowest-frequency out-of-plane modes for each structure using COMSOL. The trees in the simulations are made of Si_3N_4 [127] and have the following spatial dimensions: $l_0 = 100 \mu\text{m}$, $w_0 = 100 \text{ nm}$, $h = 20 \text{ nm}$ (so that their fundamental mode frequencies are around 1 MHz). The branching angles are set to $\theta = \pi/2$ to make the resonators stress-preserving while maintaining the same widths for all segments. This allows us to keep torsional modes at high frequency and thus to distill the effect of self-similar geometry on the density of out-of-plane modes. In order to extract the spectral dimensions presented in Figure 2.30, we fit a power law to the low-frequency parts of the spectra (first 50 modes). All resulting dimensions are in the range of $1 < \tilde{d} < 2$, i.e. the range between the dimensions of a tensioned beam and a membrane. The numerical data also shows that the spectral dimension increases as r_l is increased, which is intuitively expected as a tree resonator with a larger r_l covers a larger portion of the plane.

2.6.3 Trampolines with branching tethers

Binary tree systems of branching strings (which are not necessarily self-similar) can be incorporated as building blocks in resonators geometries different from the fractal-like ones presented in Sec. 2.6.1. The underlying principle of flexural mode amplitude suppression by string branchings is even more general and can be also applied on its own. In Figure 2.31 we present finite element simulations of trampoline membrane resonators that make use of these ideas to enhance the quality factors of their fundamental modes beyond what has been reported in the literature so far.

Trampolines stand out among other high-stress thin-film resonators as they combine

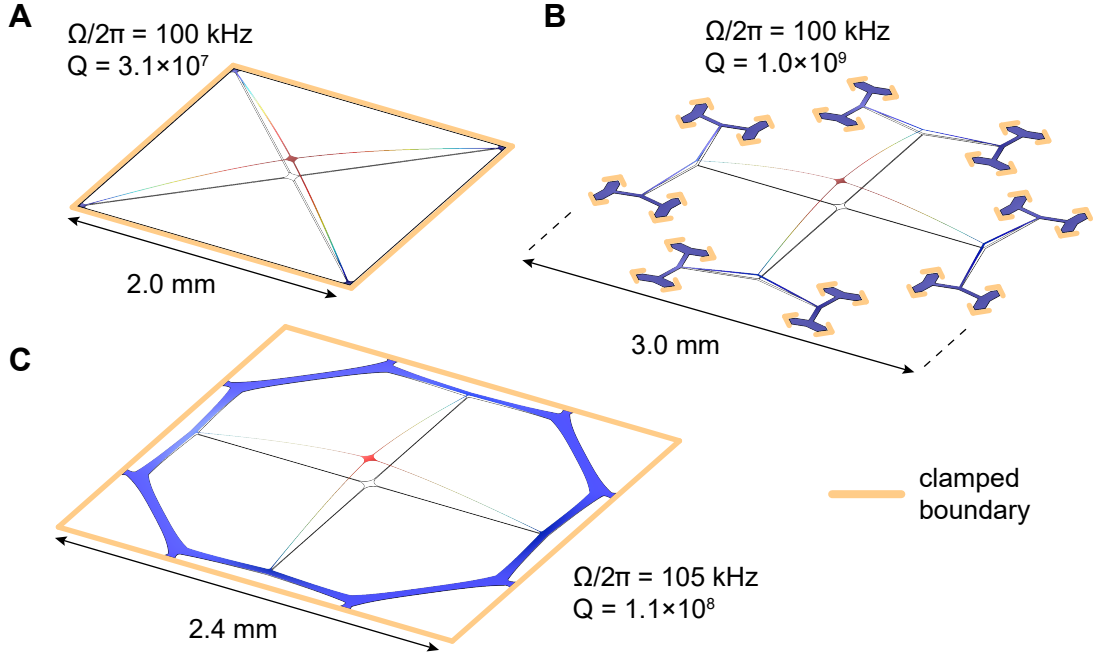


Figure 2.31: FEM simulations of fundamental modes of 20 nm-thick Si_3N_4 trampoline resonators. The dimensions are adjusted such that the fundamental mode frequency is equal to 100 kHz. The central pad size is $60 \times 60 \mu\text{m}$. Orange lines mark hard-clamped boundaries, all remaining boundaries are free. A) A simple trampoline. B) A trampoline with binary-tree tethers. C) A “steering wheel” trampoline.

low thermal noise, enabled primarily by their low fundamental mode frequency and low effective mass compared to unpatterned membranes, with compatibility with high-finesse Fabry-Perot cavities for optical readout [161]. State of the art silicon nitride trampoline resonators have mm-scale transverse size, quality factors up to 5×10^7 and typically operate at frequencies in the range of 50-150 kHz [161, 168]. The simulated fundamental mode of a simple trampoline resonator is shown in Figure 2.31A.

To show the enhancement of quality factors that can be gained by applying tether branching to trampoline devices, we present in Figure 2.31B and Figure 2.31C two trampoline designs with partially soft-clamped fundamental modes. In the simulations, we set the size of the central resonator pad to be $60 \times 60 \mu\text{m}$, the film thickness to be 20 nm, and the material parameters to be consistent with those of our standard silicon nitride [127]. To meaningfully compare between different designs, we adjust the transverse resonator size so that the fundamental mode frequencies are equal to 100 kHz. The quality factors of modes are simulated using COMSOL as described in Appendix A.2.

The design in Figure 2.31B is a straightforward application of the cascaded string branching to each of the trampoline tethers. The simulated quality factor of the fundamental resonator mode is similar to the quality factor of a self-similar binary tree string

resonator from Sec. 2.6.1 with the same size and number of branchings. The Q of the fundamental mode is predicted to be equal to 10^9 , about a factor of 30 beyond the Q of the simple structure shown in Figure 2.31A, and, in fact, higher than the Q of any mechanical nanoresonator demonstrated to date at room temperature.

The fabrication of structures similar to the one in Figure 2.31B, which is a work in progress in our lab, has multiple challenges. One of the challenges is that the clamped boundary of the trampoline in Figure 2.31B is rather complex. To be compatible with the fabrication process that uses a KOH undercut [169] the boundary is made in a way so that all clamped edges are oriented at a 90-degree angle with respect to one another. This allows one to orient all edges along the slow etching planes of silicon [141] and reduce the overhang of silicon nitride. The complexity of the boundary is one of the primary constraints on the number of branchings that seem realistic to implement practically.

In Figure 2.31C we present another resonator type, a “steering wheel”, which offers a less dramatic quality factor enhancement compared to the one shown in Figure 2.31B, but has a simpler rectangular clamped boundary. At the moment of writing, steering wheel trampoline membranes with quality factors in excess of 10^8 at 100 kHz were demonstrated in our laboratory, in excellent agreement with simulations.

The trampoline resonators in Figure 2.31B and C are composed of ribbon segments, most of which cannot be regarded as strings with negligible transverse size. This complicates the resonator design as wide ribbons with free side edges are prone to static buckling. Buckling makes fabricated devices non-planar and in this way can reduce their dissipation dilution by orders of magnitude. Typically, buckling effects can be avoided by making the structure stress-preserving (so that the centers of segment junctions do not displace upon film release) and by tapering the ribbon segments. The film buckling is discussed in more detail in Appendix A.3.

2.6.4 A pendulum with a self-similar suspension

Another type of resonator the quality factors of which could be improved by using binary tree systems of strings is the pendulum, which we discuss here as a hypothetical possibility. Dissipation dilution in pendula suspensions is similar to the dilution in planar structures clamped on all sides. As shown by González and Saulson [33], when a heavy point mass is suspended on a uniform wire, the Q of the pendulum mode is about twice as high as the Q of the fundamental violin mode. In this section, we show how the analysis of the previous section can apply to the pendulum mode of a mass hanging on a binary-tree suspension. Such a structure, shown in Figure 2.32, implements a soft-clamped pendulum mode, which has never been demonstrated to date. The soft-clamped pendulum experiences similar dissipation dilution to double-binary tree resonators presented previously if the branching configuration and the tension in the segments are the same.

The calculation of eigenmodes of a pendulum repeats the previously outlined procedure for multi-segment planar devices clamped on all sides, except that the boundary condition for the first string segment at $x_0 = 0$ is different. To formulate the new

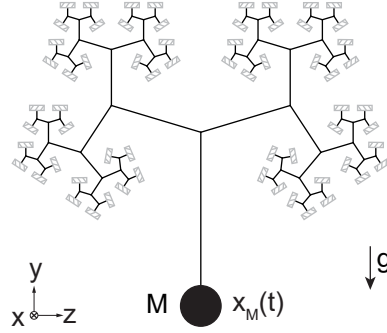


Figure 2.32: A binary tree used as suspension of mass M , the tree is supposed to be clamped at every tip of its branches. The mass motion described by the displacement $x_M(t)$ is perpendicular to the figure plane.

boundary conditions, we adopt the following simplifying assumptions:

1. The mass is a point mass. This means neglecting its angular dynamics and assuming that the mass rotation adiabatically follows the gradient of the string mode at the suspension point without applying any force moment.
2. The weight of the suspension strings can be neglected compared to the weight of the mass.

First notice that the complex amplitude of pendulum motion, \tilde{x}_M , must follow the trajectory of the suspension tip,

$$U_0(0) = \tilde{x}_M. \quad (2.219)$$

Additionally, the Newton's second law requires the acceleration of the mass to match the tension force exerted by the suspension, which can be expressed as

$$M\Omega^2\tilde{x}_M = -U'_0(0)\mathcal{T}_0, \quad (2.220)$$

where Ω is the resonance frequency and \mathcal{T}_0 is the tension of the first suspension segment. Combining Eq. (2.219) with Eq. (2.220) and using the fact that $\mathcal{T}_0 = Mg$, where g is the free fall acceleration, we find the boundary condition for the first suspension segment,

$$U'_0(0) = -\frac{\Omega^2}{g}U_0(0). \quad (2.221)$$

Recall that if the first string segment was hard clamped, it would obey $U_0(0) = 0$. The boundary condition allows one to find the eigenfrequencies and the deformation modes of the suspension, after which the diluted quality factors can be computed following the route outlined previously for resonators clamped on all sides.

2.7 Experimental characterization of high- Q mechanical resonators

The quality factors of mechanical resonators in our work are characterized using the ringdown technique, which is immune to mechanical frequency drifts. Such drifts happen at a slow time scale but lead to frequency changes much larger than the resonance linewidth, therefore making the resonance spectra appear inhomogeneously broadened. The setup is tailored to the characterization of slow decay times (some ringdowns taken are 10s of minutes long), although it is also capable of recording decays as short as 1 ms.

In our setup, shown in Figure 2.33, mechanical resonators are illuminated with a laser beam and the phase shift of the reflected light, proportional to the displacement of the resonator surface, is detected using homodyne interferometry. The homodyne output is supplied to a spectrum analyzer (Tektronix RSA 5103) for obtaining information about the mode frequencies from the spectrum of Brownian motion, and to an FPGA-based lock-in amplifier (Zurich Instruments UHFLI or MFLI) for selectively detecting the motion of one mode. After a mechanical mode of interest is identified, it is excited by finely sweeping the piezo drive frequency across the resonance, and its amplitude decay is monitored using the lock-in detector. The mechanical mode amplitude r is computed as

$$r = \sqrt{X^2 + Y^2}, \quad (2.222)$$

where X and Y are the quadratures demodulated by the lock-in. Sub-mm thick high-frequency piezos (from STEMiNC) were typically used for the excitation of vibrational modes. We found this method to be more efficient than the optical drive, implemented by amplitude-modulation of the probe laser light, especially for the thinnest (20 nm) samples.

In most of our experiments, samples were characterized in a high-vacuum chamber (pressure $10^{-8} - 10^{-6}$ mBar) at room temperature, using the light from a diode or Ti:Sa laser with a wavelength around 780 nm as a probe. An SEM-style vacuum loadlock and a translatable arm conveniently allowed chips to be swapped without exposing the main chamber to atmospheric pressure. In different experiments, we used lensed fiber-based or free-space schemes to illuminate samples and collect the reflected signals. These schemes are shown in Figure 2.33B and C.

In the first case, a lensed fiber (OZ Optics) with a working distance of around 12 μm and a spot diameter of 2.5 μm was guided inside the vacuum chamber via vacuum feedthrough. Both compression and connector-based feedthroughs were employed in several trials, and all performed satisfactorily. The lensed fiber was rigidly mounted inside the chamber by being pushed against a vertical v-groove and fixed in place with the help of UV-cured glue. Chips with beam samples were mounted on a three-axis stack of slip-stick piezo positioners (Attocube). The coupling area was imaged from the outside of the chamber using a tilted microscope with a working distance of a few centimeters. We found it to be more convenient to position the chip rather than the

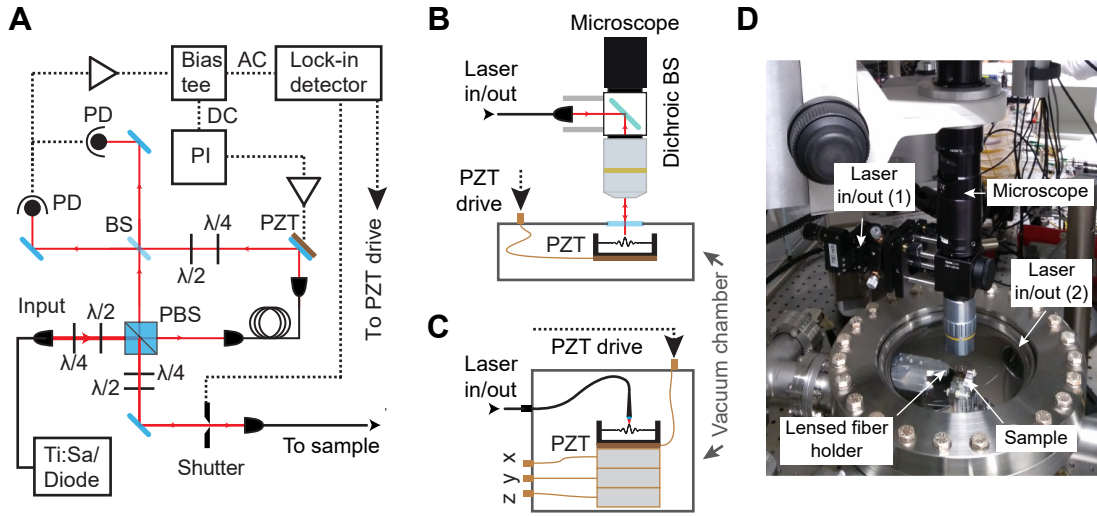


Figure 2.33: Schematic of a setup for mechanical quality factor characterization. A) Layout of the homodyne interferometer. B) Coupling to the sample from free space. The sample chip can stay fixed in this case. C) Coupling to the sample using a lensed fiber. In this case the chip is positioned using a three-stage nanopositioning system. D) Photograph of a sample chamber of a room-temperature ringdown setup, which has both lensed-fiber and free space coupling capabilities. Laser in/out 1 is for free space coupling, in/out 2 is for the lensed fiber.

lensed fiber, as during the positioning a visual reference has to be maintained in focus, and it was more difficult to locate the fiber tip on the microscope image rather than the resonator. The resolution of our imaging was not good enough to reliably position the laser spot on a sub-micron thick nanobeam, so the last stage of coupling had to rely on the optimization of the thermomechanical signal displayed by the spectrum analyzer. For efficient coupling, it was essential to obtain quick feedback in the signal display, and the real-time spectral analyzer (RSA) used in our work proved helpful. The typical reflection ratio that was achieved with the lensed fiber setup was about 0.5 % for 20nm-thick beams.

The lensed-fiber technique provided better signal-to-noise ratio for nanobeams than free space coupling. Using lensed fibers, we could observe the Brownian motion of nanobeam modes up to around 7 MHz frequency, spectra in Figure 2.18 show data close to the resolution limit of our setup. A major trade-off of this method is a time-consuming alignment. Moreover, in our setup during alignment samples were occasionally put in contact with the lensed fiber. While for beam samples this caused few problems—after detaching devices usually survived and showed no signs of degradation, touching a membrane with a lensed fiber would always lead to it breaking. Therefore, we found only the free-space technique to be suitable for the characterization of membranes.

In the free space setup, shown in Figure 2.33C, we used a Navitar microscope tube and an x10 objective to simultaneously image and illuminate the sample. A laser beam was added along the optical axis of the microscope using a fiber coupler and a dichroic

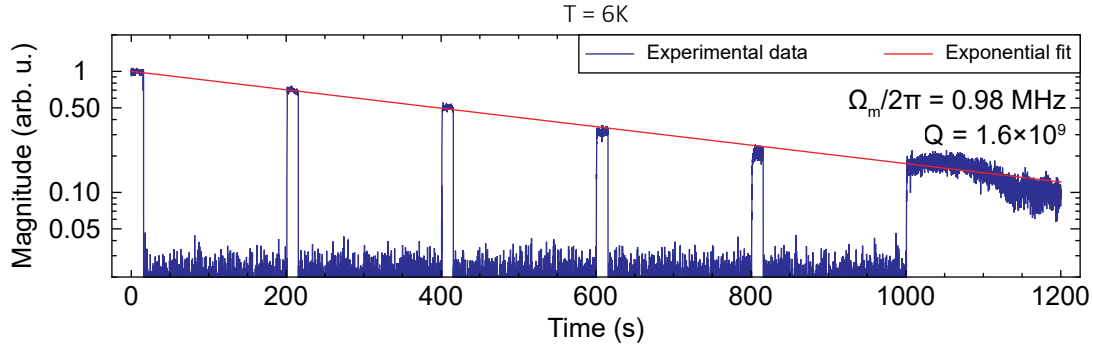


Figure 2.34: Gated ringdown measurement of a soft-clamped mode in a tapered PnC beam (geometry is presented in Sec. 2.5.2) made at 6 Kelvin temperature in a closed-cycle cryostat. The blue line shows experimental signal proportional to mechanical amplitude, red—exponential fit. The mode frequency and the quality factor are indicated in the inset. The sample was fabricated by Mohammad Bereyhi.

beamsplitter, reflecting above about 750 nm. The beam was aligned so that the reflection was coupled back into the fiber when the image was in focus. We typically obtained about 3% reflection efficiency from a 20nm-thick Si_3N_4 membrane. In the free-space coupling configuration no positioners for the sample chip are required, as the microscope already has all the necessary degrees of freedom. In our setup which has a loadlock, however, we still use Attocube positioners to move the chip between the loading and the measurement positions.

The modulation of the optical phase created by mechanical motion was read out using homodyne interferometry with shot-noise limited sensitivity. The path lengths of the signal and the local oscillator arms were balanced in length to mm precision to cancel the laser phase noise. Balancing was done by iteratively shortening the fiber in the local oscillator path using as an error signal the period of interference fringes obtained from scanning the laser frequency. The interferometer length was actively stabilized using a piezo-mounted mirror. The typical optical probe power in our setup was on the order of 1 mW, out of which only a few μW were collected back from the sample. The power in the local oscillator arm was also around 1 mW.

When characterizing mHz-scale mechanical damping rates in nanobeam resonators, we found that the bolometric dynamical backaction of probe light potentially can be an issue. The exact physical details of this backaction mechanism are somewhat obscure, but its overall effect is a renormalization of the mechanical damping rate when the resonator is continuously probed. It can make the mechanical damping rate to appear higher or lower than it actually is. For some modes with especially low damping rates (e.g. for MHz-frequency modes with $Q > 10^8$ or for low-frequency modes) we even observed self-excitation—the magnitude of motion slowly grew under steady laser illumination with no external piezo drive.

To measure the intrinsic energy relaxation rate of mechanical modes avoiding the

effect of bolometric backaction, we perform measurements in a gated way. The probe laser is switched on only for short periodically spaced intervals of time during the acquisition of ringdowns, and the rest of the time the oscillator evolves freely. Gating is implemented using an optical shutter, controlled by an auxiliary output of the lock-in, and synchronized with the ringdown acquisition trigger. An example gated ringdown is shown in Figure 2.34.

Aside from the room temperature experiments, we also implemented a cryogenic ringdown characterization setup. It has the same basic layout (shown in Figure 2.33A-B) as the room temperature setup, the two main differences are that the wavelength of the probe light is 1550 nm, and the sample plate inside the vacuum chamber is cooled to 5K. The cryostat is a closed-cycle system in which the cooling power is provided by a GM cryocooler. The cryocooler is vibrationally isolated from the sample chamber to enable interferometric measurements. For more details about the cryogenic system, see Appendix A.4.

Quantum correlations in position measurements

3.1 Introduction

Impressive advances have been made in recent experiments exploring the quantum properties of mechanical oscillators. In agreement with the rule of thumb that the smaller the object is, the less classical it is, the highest level of control over the quantum states is presently achieved for the vibrations of atomic ions confined in electromagnetic traps. For such vibrations, the preparation of phononic Fock states up to $n = 100$ and their superpositions was recently demonstrated [170]. Speaking about more macroscopic systems, significant progress has been made in controlling GHz-frequency acoustic modes in solid state resonators at millikelvin temperatures, performed by optical means or by piezoelectrically coupling mechanical modes to superconducting qubits. The latest results here include the preparation of single-phonon states [171], higher-order Fock states up to $n = 7$ [172], Fock state superpositions for small n [172, 173], entanglement between two remote oscillators [174], and the resolution of mechanical energy levels with a qubit [136]. In all these examples, the initialization of mechanical oscillator in the ground state has been essential. While for GHz frequencies such initialization requires dilution refrigeration, THz-frequency modes are in the ground state already at room temperature, which allowed the preparation of single-phonon states at ambient conditions [175, 176]. Pure, non-Gaussian quantum states of macroscopic mechanical resonators with sub-GHz frequencies have not been demonstrated so far, although there are continuing efforts ongoing in this challenging direction [177, 178].

Mechanical resonators with GHz frequencies are interesting from the perspective of quantum technologies—quantum computing, secure communication, and the transduction of quantum signals between microwave and optical frequencies. At the same time, resonators with much lower frequency and higher mass may be desirable for other purposes. This includes sensing applications, as well as experiments aiming to resolve some of the open questions in fundamental physics, including the detection of dark matter [179, 180], searching for fundamental sources of wavefunction collapse [181, 7, 182], or

corrections to canonical commutation relations in quantum mechanics [183, 184]. Most of the aforementioned problems have one aspect in common—they can be reduced in one or another way to the task of detecting a weak external force acting on the oscillator.

Mechanical oscillators used for force sensing (in the broad sense mentioned above) are typically too low-frequency to be cryogenically cooled to the ground state. Their laser- or measurement-based feedback cooling does not yield an improvement in force sensitivity, so they remain in a state with high thermal occupancy. This, however, does not mean that quantum mechanics is irrelevant to their description. Quantum effects manifest here as an unavoidable perturbation of the oscillator by measurements, which are performed in order to extract the force.

The theoretical understanding of force detection from the perspective of quantum measurement has shaped up in the second half of the 20th century with the works of Braginsky, Caves and others [1, 185, 16]. The early works were mostly motivated by a specific problem—the understanding of fundamental limitations on the sensitivity of gravitational wave detectors, which principle is to measure perturbations of space-time metric manifesting as tidal forces acting on test masses [186]. The results that were obtained, however, have broad generality and apply to a wide range of present-day experiments involving mechanical oscillators.

A force acting on the oscillator needs to be inferred in some way from the results of measurements performed on oscillator observables. Position is a canonical choice of such an observable, as it is by far the easiest to access in experiments. Quantum mechanics imposes limitations on the precision of continuous position monitoring. According to the uncertainty principle, if the position of an oscillator is observed, the uncertainty of its momentum increases, which means the oscillator evolution is affected by measurements made at prior times. This is a manifestation of the quantum backaction of measurements, which leads to the famous bound on position measurement error known as the standard quantum limit (SQL), first derived by Braginsky [1]. Although later proven to not be a fundamental limit, the SQL is still an important benchmark to assess the level of quantum error. In what follows, position and force measurements will sometimes be referred to interchangeably (where it does not cause confusion), on the basis that in the Fourier domain these quantities are simply proportional to one another. It is important, however, that position is the quantity that is observed directly.

Conceptually, there are very interesting alternative ways to detect forces with oscillators that do not rely on position measurements. Of particular interest are quantum non-demolition (QND) strategies, in which measurement backaction only affect the variable conjugated to the one measured, and thus never appears in the measurement record. In such a case, quantum mechanics imposes no restriction on the minimum error even when the measurement is continuous. QND strategies of force detection can be implemented by performing measurements of the oscillator speed [187], the quadratures of mechanical motion [16] (“backaction-evading” measurements), or the mechanical energy [1]. Experiments exploring these alternatives so far remain less advanced than those involving regular position coupling. The original concept of a speed meter has not been experimentally implemented to the best of our knowledge. Experiments probing

the oscillator energy, which is one of the oldest known methods of overcoming the SQL in force detection [1, 16], as well as other types of nonlinear measurements, remain at an early development stage. Backaction-evading measurements of oscillator quadratures were demonstrated [188, 189, 190], but not yet in the regime where they would actually yield sensitivity below the SQL¹. At the same time, it is presently known that the quantum error due to the measurement backaction in regular position measurements can in principle be largely eliminated with the help of variational readout strategy [191, 192, 193]. Similar to conventional QND measurements, it allows the erasure of quantum backaction from the measurement record, while the oscillator is still subjected to backaction. To date, variational measurement of oscillator position remains the only strategy that practically allowed to demonstrate force detection with sensitivity below the standard quantum limit [151]. Earlier works in which variational measurement were performed are [194, 195, 196].

After decades of theoretical discussions, preparations and preliminary experiments, gravitational waves were detected for the first time in 2015 [17]. During the observation run, quantum backaction of measurements was, although not directly evident, expected to contribute at the level of 10% into the total measurement noise [18]. Test masses in modern gravitational wave detectors are tens of centimeter in size and weight tens of kilogram [43]. Quantum backaction in position measurements of smaller, nano- and micrometer scale, mechanical oscillators have been observed by now in a variety of experiments, beginning with Ref. [20, 197, 189, 148, 198]. These experiments and their successors make use of conceptually the same interferometric position readout technique as gravitational wave interferometers. Here the oscillator modulates the frequency of an optical (or microwave) cavity, which is driven externally, and mechanical motion is read out as the modulation of light leaking out of the cavity. Classical and quantum aspects of interaction between the light and mechanical motion in this generic configuration have been extensively studied in the context of cavity optomechanics [19]. In an optomechanical interferometric position detector the imprecision is set in the by the vacuum fluctuations of optical field, in other words, by shot noise. The physical origin of measurement backaction here is the radiation pressure from the vacuum fluctuations of intracavity optical field, which drives the oscillator motion in a way similar to stochastic force. Quantum effects in position measurements are revealed when the magnitudes of forces from the thermal environment and from the measurement backaction are comparable, which corresponds to the onset of backaction-dominated regime [20].

While the existence of measurement backaction and a minimum bound on the system disturbance for a given imprecision has roots in quantum mechanics, their experimental manifestations might appear similar to an extra heating of the oscillator beyond equilibrium temperature. Indeed, an increase of phonon occupancy due to the measurement backaction was directly observed [20, 198, 199], although in practice it might be difficult to differentiate from photoheating by the absorption of optical photons. Quantum effects in position measurements can manifest more vividly in presence of correlations between sensing noise and measurement backaction. Such correlations exist under an

¹Without a correction for finite detection efficiency

appropriate choice of setup and are essential for implementing variational readout. Without correlations between imprecision and backaction, sensitivity in continuous position measurements cannot be better than the SQL. If the correlations are strong enough, they can directly prepare the measurement apparatus in a non-classical squeezed state [200, 201, 202, 203, 204].

In the following sections we present the demonstration of ponderomotive squeezing in a cryogenic environment and the observation of quantum correlations due to the measurement backaction at room temperature. The results are published in Ref. [202, 194, 123].

3.2 Linear continuous measurements

We begin by reviewing the theoretical foundations of continuous measurements, which help understanding how the information about quantum states reaches the classical eye of the observer. The concept of projective measurement appeared as early as the quantum theory itself. Their effect is collapsing the object wavefunction into one of the eigenstates of the measurement operator and at the same time providing the observer with information about which state it is. Weak measurements, which do not cause a complete collapse of the wavefunction, can be understood as a two-stage process [1, 3, 2]. The system first for a finite duration of time interacts with an ancillary quantum system, after which a projective measurement is performed on the ancilla. A repetition of this process approximates continuous measurement, where the system is free to evolve between the measurement operations. During such a process, a system which begins in a pure state always remains in a pure state, unless some information obtained from the measurements is lost. In the continuous limit, the object wavefunction evolves over the course of an ideal measurement process according to the stochastic Schroedinger equation [205]. If information obtained as a result of measurement is unavailable to the observer, measurements lead to decoherence. In such a case their effect is not very far from that of coupling the object to a thermal reservoir, although the fluctuation-dissipation theorem in general is not fulfilled for decoherence from measurements.

Practically, continuous measurements can be performed on a microscopic quantum system by weakly coupling it to a measurement apparatus (or “meter” [1]), which is a large reservoir-like but still completely quantum object. Information about the microscopic system is extracted by making projective (and usually destructive) measurements on the variables of meter, which can be done without directly disturbing the system of interest. In the experiments presented in this chapter the quantum system is a mechanical oscillator and the meter is propagating electromagnetic field at optical frequencies.

The intensity of the optical field is measured by photodetection, which converts propagating photons to bursts of photoelectrons. This process is close to an ideal projective measurement, setting aside photodetection inefficiency and classical electronic noises. An important aspect is that the intensity of propagating field commutes with itself at different times, which makes it a QND-type variable. Because of the absence of ob-

servable measurement backaction, such a variable behaves essentially classically under the photodetection process, which is an essential property that allows it to connect the classical and quantum worlds [15].

Although destructive for photons, photodetection does not directly affect the reduced state of mechanical oscillator², as after the optical field has interacted with the oscillator it propagates away from it and never meets it again.

3.2.1 Spectral densities of quantum operators and measurement records

The stochastic wavefunction (or density matrix) evolution approach provides an intuitive interpretation of continuous measurements, but it is not always easy to handle analytically. Alternatively and for us more conveniently, the interaction between the quantum system and the meter in the process of continuous measurement can be described within the framework of perturbation theory [1, 206]. Here the total Hamiltonian of the meter, system and their interaction is expressed as

$$\hat{H} = \hat{H}_{\text{sys}} + \hat{H}_{\text{meter}} + \hat{H}_{\text{int}}, \quad (3.1)$$

and the interaction term \hat{H}_{int} is adiabatically switched on in the remote past, so that in all present moments of time the interaction is stationary. At time t_0 before the interaction is switched on, the meter and the system are in a product state described by the density matrix $\hat{\rho}_0$, which is given by

$$\hat{\rho}_0 = \hat{\rho}_{\text{sys}}(t_0) \otimes \hat{\rho}_{\text{meter}}(t_0), \quad (3.2)$$

where $\hat{\rho}_{\text{sys}}(t_0)$ and $\hat{\rho}_{\text{meter}}(t_0)$ are known. Every operator $\hat{x}(t)$ on the joint Hilbert space of the system and the meter evolves under the full Hamiltonian \hat{H} according to the Heisenberg equations of motion as

$$\hat{x}(t) = e^{i\hat{H}(t-t_0)/\hbar} \hat{x}(t_0) e^{-i\hat{H}(t-t_0)/\hbar} \quad (3.3)$$

The expectation value of the operator is found as its trace over the total Hilbert space

$$\langle \hat{x}(t) \rangle \equiv \text{Tr}[\hat{x}(t)\hat{\rho}_0]. \quad (3.4)$$

Stationary linear continuous measurements (which are the only ones relevant to our experiments) are convenient to analyze in spectral domain. For every operator $\hat{x}(t)$ its Fourier transform $\hat{x}[\omega]$ is defined as

$$\hat{x}[\omega] = \frac{1}{\sqrt{T}} \int_{-T/2}^{T/2} \hat{x}(t) e^{i\omega t} dt, \quad (3.5)$$

²in a sense that the density matrix traced over all degrees of freedom other than the oscillator's does not change

where T must be regarded as a long time. For two operators, \hat{x} and \hat{y} , their cross-spectral density S_{xy} is defined as

$$S_{xy}[\omega] = \lim_{T \rightarrow \infty} \langle \hat{x}[\omega] \hat{y}[-\omega] \rangle. \quad (3.6)$$

In the following, the limit $T \rightarrow \infty$ will not be written explicitly but always implied. It can be checked that $\langle \hat{x}[\omega] \hat{y}[\omega'] \rangle = 0$ if $\omega' \neq -\omega$. Equivalently, S_{xy} can be obtained by Fourier-transforming the time domain correlation function

$$S_{xy}[\omega] = \int_{-\infty}^{\infty} \langle \hat{x}(t) \hat{y}(0) \rangle e^{i\omega t} dt. \quad (3.7)$$

Single-variable spectral density S_{xx} is obtained by putting $\hat{y} = \hat{x}$

$$S_{xx}[\omega] = \langle \hat{x}[\omega] \hat{x}[-\omega] \rangle. \quad (3.8)$$

Spectral densities introduced in this way characterize quantum operators, but do not necessarily directly correspond to the spectral content of measurement records. This can be seen already from the fact that for a Hermitian operator $\hat{x}(t)$ its Fourier transform $\hat{x}[\omega]$ is generally not Hermitian and hence does not correspond to an observable. As a consequence, the quantum spectral density, $S_{xx}[\omega]$, is not necessarily symmetric in frequency, unlike its classical counterpart. The relation between quantum spectral densities and the spectra of classical signals recorded in experiments depends on the measurement scheme. One could in principle conceive an experiment where asymmetric parts of quantum spectral densities would manifest³. At the same time, the fluctuations of classical signals and first order correlations between measurement records, obtained as a result of weak linear measurements, are related to the symmetrized spectra \bar{S}_{xy} defined by [23]

$$\bar{S}_{xy}[\omega] = \frac{1}{2}(S_{xy}[\omega] + S_{xy}[-\omega]^*). \quad (3.9)$$

This conclusion can be reached in a few, which include considering sequences of idealized discrete-time measurements [1], and Keldysh ordering in linear response theory [208]. Note that generally speaking symmetrized spectra only describe first-order correlations, while higher-order cumulants of measured signals may be related to more complex operator averages with highly non-classical features [209, 208].

To give one example how symmetrized spectra can emerge, suppose that we would like to estimate the spectral density of fluctuations of a Hermitian operator $\hat{y}(t)$ by measuring its cosine transform, defined as [23]

$$\hat{y}_{\cos, \omega} = \sqrt{\frac{2}{T}} \int_{-T/2}^{T/2} \hat{y}(t) \cos(\omega t) dt. \quad (3.10)$$

The cosine transform is a valid observable. Its fluctuations can (in principle) be measured, and the result will give the symmetrized spectrum,

$$\langle (\hat{y}_{\cos, \omega})^2 \rangle = \frac{1}{2}(S_{yy}[\omega] + S_{yy}[-\omega]) = \bar{S}_{yy}[\omega], \quad (3.11)$$

³see section "Quantum spectrum analyzers" in [23]

assuming that $\hat{y}(t)$ corresponds to a stationary process with zero mean.

It should be stressed that measuring the quantum cosine transform as defined by Eq. (3.10) is generally not equivalent to sampling the values of y and performing cosine transform on the record—continuous sampling is accompanied by measurement backaction if $\hat{y}(t)$ does not commute with itself at different times. Only in the case when the measured variable is QND-type [14], and does commute with itself at different times,

$$[\hat{y}(t), \hat{y}(t')] = 0, \quad (3.12)$$

the quantum spectrum of its fluctuations is already symmetric and can be directly obtained from the Fourier transform of the measurement record. Naturally, the use of either complex or cosine Fourier transform on the classical measurement record yields the same result.

3.2.2 Photodetection

The quadratures of the propagating optical field at a particular point in space are QND variables relevant to our work. The quadrature operators at different times correspond to different degrees of freedom and therefore naturally commute [182]. These operators are defined as follows: Suppose we have chosen a spatial mode of interest, which can be e.g. a guided mode of an optical fiber or a Gaussian beam mode in free space. Electric field \hat{E} at one point along the propagation direction of the mode is then given by

$$\hat{E}(t) = \hat{s}(t)e^{-i\omega_L t} + \hat{s}^\dagger(t)e^{i\omega_L t}, \quad (3.13)$$

where ω_L is the optical carrier frequency (the subscript derives from “laser”) and $\hat{s}(t)$ is an operator, describing the complex amplitude of the field. The normalization here, as conventional, is made such that $\langle \hat{s}^\dagger \hat{s} \rangle$ gives the average number of photons propagating over the mode cross section per unit time. The complex amplitude can be decomposed into the average and fluctuating parts as

$$\hat{s}(t) = \bar{s} + \delta\hat{s}(t), \quad (3.14)$$

where $\bar{s} = \langle \hat{s}(t) \rangle = \text{const}$ is real. The optical quadrature operator $\delta\hat{q}^\theta$ is defined as

$$\delta\hat{q}^\theta(t) = e^{-i\theta}\delta\hat{s}(t) + e^{i\theta}\delta\hat{s}^\dagger(t), \quad (3.15)$$

where θ is the quadrature angle. The self-commutation property of $\delta\hat{q}^\theta$ at different times can be verified explicitly. As a direct consequence of the definition of creation and annihilation operators in the spectral domain [207, 182], commutation relations for the complex amplitudes are given by

$$[\hat{s}(t), \hat{s}^\dagger(t')] = \delta(t - t'), \quad [\hat{s}(t), \hat{s}(t')] = [\hat{s}^\dagger(t), \hat{s}^\dagger(t')] = 0, \quad (3.16)$$

from which it follows that

$$[\delta\hat{q}^\theta(t), \delta\hat{q}^\theta(t')] = 0. \quad (3.17)$$

In our work, optical quadratures are the meter variables that carry information about the position of mechanical oscillator. Optical quadratures are projectively measured with the help of homodyne interferometry. In this measurement technique, the signal field is combined on a beam splitter with a local oscillator, which is in a strong coherent state of the same frequency as the signal carrier, and then converted to classical photocurrent on a photodetector. The phase of the local oscillator selects the detected quadrature angle. There are two configurations in which idealized homodyne detection does not add noise on top of the noise prescribed by the fluctuations (quantum or classical) of the signal field. The first configuration (single-port homodyning) uses a highly transmissive beam splitter, so that almost no signal is lost in reflection. In the second configuration (balanced homodyning) a symmetric beam splitter is used, both output channels are detected, and the final signal is obtained by subtracting the photocurrents. Balanced homodyne detection offers some practical advantages and hence is actually employed in our experiments (see Sec. 2.7 for details). At the same time, the theoretical analysis of balanced homodyning is technically more complex compared to the single-port case, while not conceptually different. For this reason we assume that single-port homodyning is used in order to illustrate how fluctuations of field quadratures are converted into the measured signal. In the single-port scheme the effect of local oscillator is simply to replace the mean field \bar{s} of the signal in Eq. (3.14) with a new value, $\bar{s}_h = |\bar{s}_h|e^{i\theta}$, so that the θ -quadrature of the signal is rotated to be the amplitude quadrature of the combined field. The photocurrent signal $I(t)$, produced by the combined field, can be found using the quantum theory of photodetection [207, 210, 211]. Up to the leading order in field fluctuations the correlation function of the photocurrent produced by an ideal detector with infinite bandwidth is given by [211]

$$\overline{I(t')I(t)} - \left(\overline{I(t)}\right)^2 = \langle \hat{s}^\dagger(t')\hat{s}^\dagger(t)\hat{s}(t)\hat{s}(t') \rangle + \langle \hat{s}^\dagger(t)\hat{s}(t) \rangle \delta(t-t') - \langle \hat{s}^\dagger(t)\hat{s}(t) \rangle^2 \approx |\bar{s}_h|^2 \langle \delta\hat{q}^\theta(t')\delta\hat{q}^\theta(t) \rangle. \quad (3.18)$$

The wide overline denotes averaging performed on the classical photocurrent record $I(t)$.

3.2.3 The mechanical oscillator

Our microscopic system of interest is a harmonic oscillator. We consider the measurement of its position, possibly with the goal of detecting some external force that may act on it. The system Hamiltonian in Eq. (3.1) is given by

$$\hat{H}_{\text{sys}} = \hbar\Omega_m \hat{b}^\dagger \hat{b} - \hat{x} \hat{F}_{\text{th}} + \hat{H}_{\text{B}}, \quad (3.19)$$

where Ω_m is the oscillator frequency and \hat{b} is the annihilation operator of the mechanical mode. Intrinsic dissipation of the oscillator is described by weak coupling to a thermal bath with Hamiltonian \hat{H}_{B} by means of the interaction term $-\hat{x}\hat{F}_{\text{th}}$. The bath is regarded as a part of the measured system, although it could have been separated. The amount of mechanical damping and fluctuations resulting from the bath can be obtained using usual methods, e.g. linear response theory [45] or the input-output framework [212].

It is convenient from the outset to normalize the oscillator coordinate x by the magnitude of zero point fluctuations,

$$x_{\text{zpf}} = \frac{\hbar}{2m\Omega_m}. \quad (3.20)$$

This is the same as defining $\hat{x} = \hat{b} + \hat{b}^\dagger$, so that the mean squared position fluctuations in the ground state $|0\rangle$ are equal to one,

$$\langle 0|\hat{x}^2|0\rangle = 1. \quad (3.21)$$

The linear response of the oscillator position to external forces is described using susceptibility χ_m , which in the frequency domain is given by

$$\chi_m[\omega] = \frac{1}{\hbar} \frac{2\Omega_m}{(\Omega_m^2 - \omega^2) - i\Omega_m^2\phi[\omega]}, \quad (3.22)$$

where ϕ is the loss angle. The asymmetric spectrum of position fluctuations in thermal equilibrium S_{xx}^{th} (Brownian motion) is given by the product of mechanical susceptibility and thermal force noise,

$$S_{xx}^{\text{th}}[\omega] = |\chi_m[\omega]|^2 S_{FF}^{\text{th}}[\omega]. \quad (3.23)$$

The spectrum of thermal force S_{FF}^{th} is proportional to the loss angle,

$$S_{FF}^{\text{th}}[\omega] = \hbar^2 \Omega_m \phi[\omega] (\Theta(-\omega)n_T(-\omega) + \Theta(\omega)(n_T(\omega) + 1)), \quad (3.24)$$

where $\Theta(\omega)$ is the Heaviside step function and n_T is the Bose distribution

$$n_T(\omega) = \frac{1}{e^{\hbar\omega/k_B T} - 1}. \quad (3.25)$$

The asymmetric part of the spectrum in Eq. (3.24) is responsible for zero-point fluctuations of mechanical position. The phonon occupancy in thermal equilibrium, including the zero-point contribution, is given by $\bar{n}_{\text{th}} = n_T(\Omega_m) + 1/2$. In our experiments, the equilibrium oscillator occupancy is always high, so that $\bar{n}_{\text{th}} \approx k_B T / (\hbar\Omega_m)$.

So far the general case of arbitrary frequency range was discussed. When only a narrow band around the mechanical resonance is of interest, some simplifications can be made in the mechanical response and noises. For frequencies $\omega \approx +\Omega_m$ the mechanical susceptibility can be approximated as

$$\chi_m[\omega] \approx \frac{1}{\hbar} \frac{1}{(\Omega_m - \omega) - i\Gamma_m/2}, \quad (3.26)$$

and the thermal force can be regarded as white noise with symmetrized spectral density given by

$$\bar{S}_{FF}^{\text{th}}[\omega] \approx \hbar^2 \Gamma_{\text{th}}. \quad (3.27)$$

Here Γ_{th} is the thermal decoherence rate,

$$\Gamma_{\text{th}} = \Gamma_m \bar{n}_{\text{th}}, \quad (3.28)$$

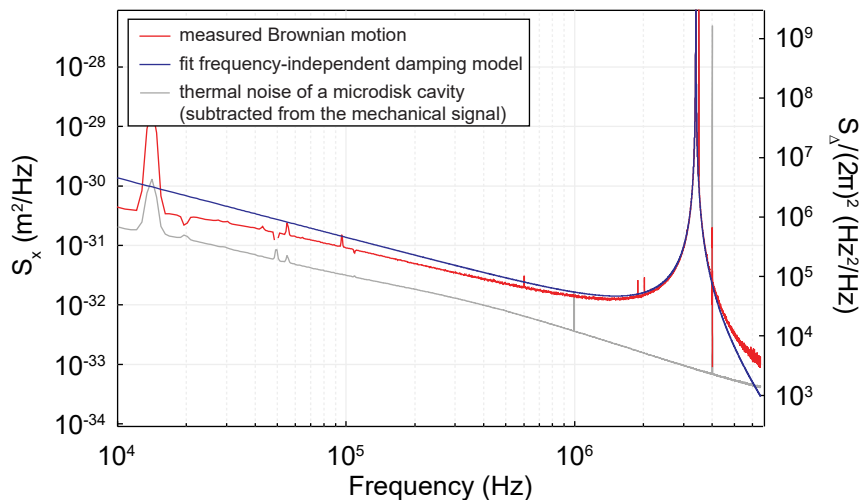


Figure 3.1: Broadband displacement spectrum of the fundamental mode of a Si_3N_4 nanobeam resonator. Red—experimental data with shot noise and microdisk thermal noise subtracted, blue—fit assuming frequency-independent damping, gray—thermal noise of a standalone microdisk optical cavity, which was the dominant extraneous noise in the measurement. The peak at 4 MHz corresponds to the phase modulation tone used to calibrate the measurement.

which is a characteristic rate at which quantum states of the oscillator decay due to the interaction with the environment [9]. As an example, at $\bar{n}_{\text{th}} \gg 1$, an oscillator initially prepared in the ground state heats up by one phonon over the time given by $1/\Gamma_{\text{th}}$. Whenever a transition from the narrowband spectra back to the full broadband form is desired, Γ_{th} can be formally replaced by the frequency-dependent expression $\Gamma_{\text{th}}(\omega) = \Omega_m \phi[\omega](n_T(\omega) + 1/2)$.

An experimental spectrum of Brownian motion for one of the oscillators used in our work is presented in Figure 3.1 where we plot it as one-sided spectral density $S_x = 2\bar{S}_{xx}$. The oscillator is the fundamental mode of a nanobeam mechanical resonator dispersively coupled to a microdisk optical cavity (see Sec. 3.4) and probed at room temperature [123]. At frequencies outside the immediate vicinity of the resonance, thermal force noise cannot be regarded as white, but instead has the scaling $\bar{S}_{FF}^{\text{th}}[\omega] \propto 1/\omega$.

3.2.4 General aspects of linear position measurements

Following the introduction of the microscopic system, we can now discuss the measurement process and quantum sensitivity limits that arise in it. Among these limits, the standard quantum limit was discovered first by Braginsky[213, 1] in the late 1960s, and later derived for interferometric measurements by Caves [185].

The position of a mechanical oscillator can be measured by coupling it to a meter by means of an interaction Hamiltonian of the type [1, 23]

$$\hat{H}_{\text{int}} = -\hat{x}\hat{F}, \quad (3.29)$$

where \hat{F} is a meter operator, which is yet to be specified. We are interested here in “linear” measurements, where the meter output is proportional to x (which is not guaranteed by only Eq. (3.29)). For a more precise definition of this type of measurements one may refer to [15] and [1].

Similarly to coupling to a thermal bath, coupling the oscillator to a position detector generally entails two effects—the modification of the force susceptibility χ_m and extra motion driven by the detector fluctuations. The modification of the susceptibility can be regarded as a consequence of coherent feedback imposed by the meter, where a part of the read out signal is excluded from the output and applied to drive the oscillator. Commonly, in such a situation the efficiency of position readout by an external observer is sub-optimal⁴, as a part of the signal is not available at the output, while the stochastic backaction force from the meter is not affected by feedback. In the following, we will concentrate on the case where the modification of oscillator susceptibility does not play a major role, and all (or almost all) the signal read out by the meter is available to the observer.

While one variable of the meter, F , is coupled to the oscillator, another variable, y , is monitored by the classical observer⁵. In order to obtain any linear response in the output channel, it is required that \hat{y} and \hat{F} do not commute [1, 182, 23]. The average output signal of a generic stationary linear detector is given by [1, 23]

$$\langle \hat{y}(t) \rangle = \langle \hat{y}(t_0) \rangle + \int_{t_0}^t \chi_{yF}(t-t') \langle \hat{x}(t') \rangle dt', \quad (3.30)$$

where

$$\chi_{yF}(\tau) = \frac{i}{\hbar} \Theta(\tau) \left\langle [\hat{y}(\tau), \hat{F}(0)] \right\rangle_0, \quad (3.31)$$

and $\langle \dots \rangle_0$ means the expectation for the uncoupled meter. For χ_{yF} to be non-zero, it is thus required that

$$[\hat{y}(t), \hat{F}(t')] \neq 0, \quad (3.32)$$

for at least some t and t' . The same linear response argument leads to the conclusion that if \hat{F} commutes with itself at different times, there is no coherent feedback from the meter.

In our experiments, the meter responds instantaneously to the oscillator motion, which implies⁶ $\chi_{yF}(\tau) = \delta_+(\tau)$. The scaling of \hat{y} here is chosen so that the measurement outcome directly gives unbiased estimation of instantaneous oscillator position,

$$\langle \hat{y}(t) \rangle = \langle \hat{x}(t) \rangle. \quad (3.33)$$

We are free to call the discrepancy between the actual position and the detected output “imprecision”,

$$\hat{z}(t) \equiv \hat{y}(t) - \hat{x}(t). \quad (3.34)$$

⁴see Ref. [206, 23] for a discussion of the case of cold damping

⁵Notations in this section widely follow the notations of Khalili et al. [214].

⁶ $\delta_+(\tau)$ is defined so that $\int_0^t \delta_+(\tau) f(\tau) d\tau = f(0)$ for $t > 0$.

In the absence of coupling to the oscillator $\hat{z} = \hat{y}$, which means that the imprecision operator \hat{z} represents intrinsic fluctuations of the meter.

Imprecision is not the only contribution to the total measurement error. The usual aim of position measurements is to detect the “true” motion of the oscillator, as it would be in the absence of coupling to the detector. This motion includes response to any external force, if the oscillator is used as a test body, quantum zero-point fluctuations, and thermal Brownian motion. At the same time, coupling to the detector inevitably introduces oscillator fluctuations driven by the quantum backaction. Due to the linearity of the problem, the total motion $\hat{x}(t)$ is simply the sum of two contributions,

$$\hat{x}(t) = \hat{x}_0(t) + \hat{x}_{\text{BA}}(t), \quad (3.35)$$

where \hat{x}_0 is the evolution in the absence of detector and \hat{x}_{BA} is the motion, driven by quantum backaction,

$$\hat{x}_{\text{BA}}(t) = \int_{t_0}^t dt' \chi_m(t-t') \hat{F}(t') dt'. \quad (3.36)$$

Overall, the meter output is given by

$$\hat{y}(t) = \hat{x}_0(t) + \hat{x}_{\text{BA}}(t) + \hat{z}(t), \quad (3.37)$$

we will regard $\hat{\varepsilon} = \hat{z} + \hat{x}_{\text{BA}}$ as the total position measurement error and be concerned with minimizing it.

Because of the non-trivial frequency dependence of the oscillator response, it is convenient to work in the frequency domain. When y is a QND observable, which is our case of practical interest, the quantum spectrum S_{yy} is symmetric in frequency and directly gives the spectrum of measurement outcomes. At the same time, the spectrum of oscillator motion, \hat{x}_0 , is asymmetric by the amount of zero-point fluctuations. In order to not appear in the total result, this asymmetry has to be precisely canceled by the spectrum of measurement error. This means that nontrivial quantum correlations exist between the measurement backaction and imprecision of the meter, which magnitude is equal to the oscillator zero-point motion. This fact has profound consequences—it explains why the standard quantum limit can be derived either by considering commutation relations for the mechanical oscillator or variables of the meter, and can lead to the conclusion that quantumness of the oscillator can be disregarded completely in the problem of force measurements [15]. It can also lead to an ambiguity of interpretation, as in the case of the asymmetry of power in the blue and red Raman scattering sidebands [215, 202]. After a debate, this asymmetry is regarded as either a consequence of the quantumness of mechanical oscillator, or backaction-imprecision correlations, depending on whether it is observed in photon counting or in heterodyne detection [214, 216].

The spectrum of the meter output is given by [214]

$$\bar{S}_{yy}[\omega] = \bar{S}_{xx}^0[\omega] + \underbrace{\bar{S}_{zz}[\omega] + 2\text{Re}(\chi_m^*[\omega]\bar{S}_{zF}[\omega]) + |\chi_m[\omega]|^2\bar{S}_{FF}^{\text{BA}}[\omega]}_{=\bar{S}_{\varepsilon\varepsilon}[\omega]}, \quad (3.38)$$

where the terms have natural correspondence to those in Eq. (3.37). We have symmetrized S_{yy} explicitly, such that we do not have to keep track of the asymmetric parts which do not contribute to the final answer. In the spectral domain, the optimum detection problem is solved by minimizing $\bar{S}_{\varepsilon\varepsilon}$ at a given frequency, while \bar{S}_{zz} , \bar{S}_{FF}^{BA} and \bar{S}_{zF} , are constrained by the laws of quantum mechanics.

Since \hat{z} and \hat{F} do not commute, their fluctuations cannot be arbitrarily small at the same time, similar to the position and momentum of a particle. The uncertainty relation that \hat{z} and \hat{F} satisfy in the general case is somewhat cumbersome and not reproduced here (for the full form see [1, 23]). The uncertainty relation, however, has a simple form under two assumptions: 1) there is no correlation between the quantum backaction and imprecision, 2) \hat{F} commutes with itself at different times. Then

$$\bar{S}_{zz}\bar{S}_{FF}^{\text{BA}} \geq \frac{\hbar^2}{4}. \quad (3.39)$$

Measurement apparatus that per given imprecision add only the minimum amount of quantum backaction, turning Eq. (3.39) into an equality, are called *quantum-limited*. An example of position detector that can be close to quantum-limited in practice is an optomechanical cavity, where the parametric modulation of cavity frequency by mechanical motion is read out from the output field.

Having a quantum-limited measurement apparatus is a prerequisite for performing optimal position measurements. The remaining step is to optimize the coupling strength between the meter and the oscillator, which simultaneously changes the amount of imprecision and backaction noises, so that the total error of position estimation is minimized. For uncorrelated z and F , the total spectral density of error obeys

$$\bar{S}_{\varepsilon\varepsilon}[\omega] \geq \hbar|\chi_m[\omega]|, \quad (3.40)$$

and the minimum allowed by Eq. (3.40) is known as the standard quantum limit (SQL) [1]. While the SQL is certainly a quantum bound on the error of continuous position measurements, it is not the ultimate bound. Without some of the assumptions made above about the measurement apparatus, errors below the SQL are possible.

One way to improve upon the SQL is to allow correlations between the variables z and F of the meter, which is the idea behind “variational measurements” proposed by Vyatchanin and Matsko [191, 192]. In the presence of correlations, the uncertainty relation for z and F is given by [1, 182]

$$\bar{S}_{zz}[\omega]\bar{S}_{FF}^{\text{BA}}[\omega] - |\bar{S}_{zF}[\omega]|^2 \geq \frac{\hbar^2}{4} + \hbar|\text{Im}(\bar{S}_{zF}[\omega])|, \quad (3.41)$$

and a quantum limit better than the SQL is obtained for the position measurement error,

$$\bar{S}_{\varepsilon\varepsilon}[\omega] \geq \hbar|\text{Im}(\chi_m[\omega])|. \quad (3.42)$$

We refer to the limit given by Eq. (3.42) as variational measurement limit, another name proposed recently is Dissipative Quantum Limit [217]. It coincides with the SQL

on mechanical resonance, where the susceptibility is purely imaginary and given by $\chi_m[\Omega_m] = 2i/(\hbar\Gamma_m)$, and progressively gets lower compared to the SQL as measurements become off-resonant or broadband. For a free mass probe ($\omega \gg \Omega_m$), the variational measurement strategy in principle allows to completely erase all signatures of quantum backaction from the measurement record.

In both the SQL and the variational quantum limit, the minimum residual error is not lower than \hbar times the imaginary part of mechanical susceptibility. For a stationary measurement that obtains information on both quadratures of the force, this seems to be the fundamental limit (Ref. [217] gives a general argument). By allowing the measurement to be non-stationary, one can engineer a situation when the variational limit is surpassed, but only at the expense of obtaining information about a single quadrature of the force. An example of such a scheme is the synodyne measurement, which was recently theoretically proposed in Ref. [218] and experimentally implemented in Ref. [219].

Although the standard quantum limit is not the ultimate limit, it is an important benchmark for the discussion of quantum limits on position measurements. One reason is that the SQL sensitivity can be approached with a moderately imperfect measurement apparatus, i.e. which is close to but not exactly quantum-limited, while sub-SQL strategies exploiting backaction-imprecision correlations are less robust. As an example, suppose that a part of the measured signal is discarded from the output of the meter. In optical measurements this can happen because of propagation losses of light and imperfect photodetection. The total losses are then quantified by the detection efficiency, η . For an imperfect meter in the absence of backaction-imprecision correlations we have $\bar{S}_{zz} \bar{S}_{FF}^{\text{BA}} = \hbar^2/(4\eta)$, where $\eta < 1$, and the minimum position estimation noise is given by

$$\bar{S}_{\varepsilon\varepsilon}[\omega] = \hbar \frac{|\chi_m[\omega]|}{\sqrt{\eta}}. \quad (3.43)$$

Such “finite detection efficiency SQL” is not very far from the actual SQL if the detection efficiency is reasonably high, $\eta \lesssim 1$. Under the same assumptions, the minimum noise obtained in the variational measurement scheme is given by

$$\bar{S}_{\varepsilon\varepsilon}[\omega] = \hbar \sqrt{\frac{(1-\eta)}{\eta} |\chi_m[\omega]|^2 + |\text{Im}(\chi_m[\omega])|^2}. \quad (3.44)$$

We see that even moderate detection losses bring the variational limit very close to the SQL. In order to improve upon the SQL by any amount using the variational strategy, one needs more than 50 % detection efficiency ($\eta > 1/2$), and in order to achieve an improvement by an order of magnitude, detection efficiency better than 99% is required. Achieving this is practically challenging, and position measurements of macroscopic oscillators with actual sub-SQL sensitivity (without detection efficiency correction) were demonstrated only very recently in Ref. [151]. As a side remark, physically the requirement for detector to be quantum-limited is the same as demanding that all the information read out about the oscillator by the meter is available to the observer [22, 23].

3.2.5 On the physical significance of SQL

Position sensitivity close to the standard quantum limit by now has been reached in numerous experiments (see references in [23] for some early examples). Achieving a low enough *imprecision* noise [220, 221] here is only half of the problem; the other half is keeping the product of imprecision and backaction of the overall measurement scheme close to the quantum limit (given by Eq. (3.39) and its generalizations). At the same time, reaching the SQL sensitivity does not guarantee that the quantum phenomena giving rise to this limit are readily apparent. The main reason is that the mechanical motion that one detects in the end includes the Brownian motion of the oscillator in thermal equilibrium. Although not as fundamentally random as vacuum fluctuations, Brownian motion is usually random for all practical purposes, and can be naturally regarded as another sensing error. The effect of quantum backaction in this case is a small additional heating of the oscillator, which is usually hard to discern unless the oscillator is in the ground state from the beginning, i.e. without any probe coupled to it. This conclusion especially concerns position measurements at frequencies near the mechanical resonance, where the Brownian noise is concentrated. For low-frequency mechanical oscillators their cryogenic cooling to the ground state would require very low temperatures (e.g. about 50 μK for a 1 MHz oscillator), and is typically impractical or even infeasible.

The importance of quantum limits at finite temperatures is higher in the broadband case, when the frequencies of interest are far from the mechanical resonance. Here the magnitude of Brownian motion can be, at least in principle, much lower than the minimum error set by the SQL, and the measurement backaction can play a bigger role. Historically, the standard quantum limit was first derived for the measurements on a free mass, which behaves similar to an oscillator at frequencies far higher than the resonance, $\omega \gg \Omega_m$.

Some aspects of the interplay between thermal and quantum noises in position detection are more transparent if the oscillator is regarded as a probe for the detection of external force. Many physical problems involving mechanical oscillators are either directly of this kind, or can be reduced to such. The spectrum of force $\bar{S}_{FF}^{\text{est}}$, estimated from the meter output, is simply proportional to the spectrum of estimated position,

$$\bar{S}_{FF}^{\text{est}}[\omega] = |\chi_m[\omega]|^{-2} \bar{S}_{yy}[\omega]. \quad (3.45)$$

The quantum limits for position detection directly translate into quantum limits for narrowband force estimation.

Thermal and zero-point fluctuations of the oscillator can be regarded as motion driven by the environmental force with spectral density \bar{S}_{FF}^{th} (see Eq. (3.24)). Any external force competes with the environmental contribution, so that \bar{S}_{FF}^{th} is the ultimate minimum measurement error, and there is no known way to overcome it. The imprecision and measurement backaction from the meter can add extra error on top of the thermal contribution. Quantum backaction is a broadband (usually white) force noise, while the imprecision equivalent force noise has frequency dispersion following the inverse oscilla-

tor response. The imprecision is minimum on mechanical resonance and increases with increasing the detuning $|\omega - \Omega_m|$. Correspondingly, the SQL for force estimation also increases with increasing the detuning, and eventually becomes higher than \bar{S}_{FF}^{th} . Still, the overall result is that the minimum error of force estimation always occurs on resonance, and is limited by thermal contribution, unless the oscillator is in the ground state. The conclusion about practical relevance of the SQL, however, depends on the problem. If the frequency band of interest is fixed, but there is freedom to choose the oscillator, one can benefit from making the resonance frequency low and reducing the thermal noise \bar{S}_{FF}^{th} in this way, until the SQL becomes a limitation. Hence, quantum limits can in principle be important for arbitrarily hot oscillators, as was originally envisioned when considering the problem of gravitational wave detection. Unlike modern gravitational wave detectors, which operate precisely in this broadband regime, smaller-scale optomechanical experiments more commonly can only access resonance phenomena. A notable exception from this rule is a series of recent optomechanical experiments with micro-mirrors [199, 204, 196], in which strong effects of quantum backaction were observed at room temperature.

3.2.6 An optomechanical cavity as a parametric position detector

The physical system that practically implements the position measurement apparatus in our work is an optomechanical cavity. The goal of this section is to establish connections between some of the abstract concepts introduced previously and their optomechanical implementation, and also to introduce remaining notations necessary to present the experimental data.

In our experiments presented further in this chapter, optical losses are chief among the imperfections preventing exactly quantum-limited operation (in terms of the backaction-imprecision product prescribed by Eq. (3.39)). For this reason, and also since they can qualitatively change predictions for the sensitivity of sub-SQL measurement schemes (Sec. 3.2.4), optical losses will be accounted for from the beginning. At the same time, extraneous classical noises of the optical field in our experiments were negligible, unless stated otherwise, and they will not be considered here.

An optomechanical cavity is convenient to analyze using input-output formalism and quantum Langevin equations, the foundations of which can be found elsewhere [212, 19] (also see Ref. [182] for some uncommon insights). Quantum Langevin equations are particularly useful for the description of radiation-pressure induced dynamical backaction of light on the mechanical oscillator. For our purposes, however, dynamical effects are not of primary importance, in particular since damping due to the meter must be small in order for it to perform quantum-limited position measurements [206, 24].

A key result of input-output theory is that the amplitude of the optical field just before the cavity, \hat{s}_{in} , is related to the amplitude after the cavity, \hat{s}_{out} , as

$$\hat{s}_{\text{out}}(t) = \hat{s}_{\text{in}}(t) - \sqrt{\kappa} \hat{a}(t). \quad (3.46)$$

Here \hat{a} is the annihilation operator of intracavity photons, and κ is the optical linewidth,

also equal to the photon energy decay rate. Both \hat{s}_{in} and \hat{s}_{out} are operators describing propagating fields, obeying the commutations relations given by Eq. (3.16). The dynamics of the intracavity field in the frame rotating with the drive laser frequency ω_L are given by

$$\frac{d}{dt}\hat{a} = i(\Delta + g_0\hat{x})\hat{a} - \kappa/2\hat{a} + \sqrt{\kappa}\hat{s}_{\text{in}}, \quad (3.47)$$

where $\Delta = \omega_L - \omega_{c,0}$ is the mean laser-cavity detuning, and g_0 is the single-photon optomechanical coupling rate. The oscillator position x is normalized to zero point fluctuations and given by $\hat{x} = \hat{b} + \hat{b}^\dagger$. The optomechanical coupling rate originates from the dependence of the cavity frequency on the position of the oscillator,

$$g_0 = -\partial\omega_c/\partial x. \quad (3.48)$$

In realistic optomechanical systems, the position that parametrizes the displacement field of mechanical mode is not unambiguously defined in general, unless it is if normalized to zero-point fluctuations. Whereas in some cases there is a natural choice of what to call the absolute mechanical coordinate, e.g. in Fabry-Perot resonators with movable mirrors it is the displacement of the mirror, in nanoresonators with complex shapes, like phoxonic crystals [134] or micro-disks and toroids [222, 223], the choice is less clear. Hence g_0 , a coupling constant which is unambiguously defined, is commonly used to characterize optomechanical systems even in the classical regime. This quantity is also convenient to experimentally calibrate—by comparing phase modulation due to Brownian motion (which in displacement units is $x_{\text{zpf}}\sqrt{\bar{n}_{\text{th}}}$) to a known phase-modulation reference tone [224].

An optomechanical cavity acts as a detector of the oscillator position that can approach quantum-limited performance in some parameter range. The conditions relevant to our experiments are the fast-cavity regime ($\kappa \gg \Omega_m$), laser locked on resonance ($\Delta = 0$), and RMS frequency fluctuations much smaller than the cavity linewidth ($g_0\sqrt{\langle x^2 \rangle} \ll \kappa$). Under these conditions the interaction between the cavity mode and the mechanical oscillator can be linearized by setting

$$\hat{s} = \bar{s} + \delta\hat{s}, \quad \hat{a} = \bar{a} + \delta\hat{a}, \quad (3.49)$$

and keeping only lowest-order fluctuation terms. We assume that the expectations of the propagating and intracavity fields, \bar{s} and \bar{a} , are made real by a proper choice of the reference phase. The linearized interaction Hamiltonian is given by

$$\hat{H}_{\text{int}} = -\hbar g(\delta\hat{a} + \delta\hat{a}^\dagger)\hat{x}, \quad (3.50)$$

where $g = g_0\bar{a}$ is the loaded optomechanical coupling. While the static component of the radiation pressure shifts the equilibrium mechanical coordinate, this shift does not affect the spectrum of x at finite frequencies, and is not explicitly distinguished to simplify the notations. Same applies to the static shift in the cavity frequency, which is assumed to be incorporated in the effective detuning Δ .

From the interaction Hamiltonian given by Eq. (3.50) one can identify the \hat{F} operator of the meter. The fast-cavity limit allows us to adiabatically eliminate the cavity mode, after which we find

$$\hat{F}(t) = \hbar\sqrt{\Gamma_{\text{BA}}}\delta\hat{q}_{\text{in}}(t), \quad (3.51)$$

where Γ_{BA} is the added oscillator decoherence rate due to the measurement backaction,

$$\Gamma_{\text{BA}} = 4g^2/\kappa. \quad (3.52)$$

The readout variable \hat{y} in our case is an appropriately normalized quadrature of the output field. After the elimination of cavity mode, the output field is given by

$$\delta\hat{s}_{\text{out}}(t) = -\delta\hat{s}'_{\text{in}}(t) - i\sqrt{\Gamma_{\text{meas}}}\hat{x}(t), \quad (3.53)$$

where Γ_{meas} is the measurement rate, and the modified input operator $\delta\hat{s}'_{\text{in}}$ accounts for optical losses (it will be explicitly given later). The measurement rate is defined as

$$\Gamma_{\text{meas}} = \eta \cdot 4g^2/\kappa, \quad (3.54)$$

where η is the overall detection efficiency, including intracavity and propagation optical losses, together with photodetection imperfection. While Γ_{meas} is indeed related to the rate at which information is obtained by the observer [23], for our purposes it can be regarded simply as a constant characterizing the coupling strength between the measurement apparatus and the oscillator. Importantly, in the case of perfect detection, corresponding to $\eta = 1$, the measurement rate equals the decoherence rate due to the measurement backaction, which is a generic signature of quantum-limited measurements [23].

Optical losses in the quantum case not only reduce the signal, but also introduce additional fluctuations, the magnitude of which can be found using the beamsplitter model of absorption. The modified input field $\delta\hat{s}'_{\text{in}}$ is given by

$$\hat{s}'_{\text{in}} = \sqrt{\eta}\hat{s}_{\text{in}} + \sqrt{1-\eta}\hat{s}_{\text{vac}}, \quad (3.55)$$

where \hat{s}_{vac} is the operator of an effective loss port, which field is in the vacuum state. While it is understandable that the cumulative effect of propagation losses in the output channel and the photodetection inefficiency can be described by a single beamsplitter, it is less straightforward to see that optical losses inside the cavity can be included in the same way. Although it does take a few steps to prove, it is indeed the case⁷.

Overall, the meter output \hat{y} is given by

$$\hat{y}(t) = -\hat{q}^\theta(t)/(2\sqrt{\Gamma_{\text{meas}}}\sin(\theta)), \quad (3.56)$$

where the choice of homodyne quadrature θ controls the level of backaction-imprecision correlations. The detection imprecision \hat{z} is found as

$$\hat{z} = \frac{\delta\hat{q}'_{\text{in}}\cot(\theta) + \delta\hat{p}'_{\text{in}}}{2\sqrt{\Gamma_{\text{meas}}}}. \quad (3.57)$$

⁷At least for an optomechanical system with dispersive coupling.

It can be checked now that the basic assumptions made in Sec. 3.2.4 about the meter are satisfied. Namely, both \hat{y} and \hat{F} commute with themselves at different times

$$[\hat{y}(t), \hat{y}(t')] = 0, \quad [\hat{F}(t), \hat{F}(t')] = 0, \quad (3.58)$$

which ensures, respectively, the classicality of the output and the absence of modification of the oscillator response. The mutual commutator is

$$[\hat{z}(t), \hat{F}(t')] = -i\hbar \delta_+(t - t'), \quad (3.59)$$

consistent with the instantaneous linear response χ_{yF} of the meter. The appearance of single-sided delta-function here is somewhat subtle, it can be traced to the requirement of causality [214], i.e. the fact that the cavity input is not affected by any operations performed on the output.

The calculation of output spectra requires the knowledge of meter state, which in the case of an optical cavity is fully characterized by the input field. In our case the input is a coherent state with no classical noises on top of the vacuum fluctuations,

$$\langle \delta \hat{s}_{\text{in}}^\dagger[\omega] \delta \hat{s}_{\text{in}}[-\omega] \rangle = 0, \quad \langle \delta \hat{s}_{\text{in}}[\omega] \delta \hat{s}_{\text{in}}^\dagger[-\omega] \rangle = 1, \quad (3.60)$$

from which it follows that

$$\langle \delta \hat{q}_{\text{in}}[\omega] \delta \hat{q}_{\text{in}}[-\omega] \rangle = 1, \quad \langle \delta \hat{q}_{\text{in}}[\omega] \delta \hat{p}_{\text{in}}[-\omega] \rangle = i. \quad (3.61)$$

Note that the correlations between the amplitude and phase quadrature of the vacuum field are not zero but purely imaginary, similar to the position and momentum of a harmonic oscillator. The spectra of imprecision and measurement backaction are given by

$$\bar{S}_{zz}[\omega] = \frac{\cot(\theta)^2 + 1}{4\Gamma_{\text{meas}}}, \quad (3.62)$$

$$\bar{S}_{FF}^{\text{BA}}[\omega] = \hbar^2 \Gamma_{\text{BA}}. \quad (3.63)$$

The backaction-imprecision correlations are easier to find in unsymmetrized form first,

$$S_{zF}[\omega] = \langle \hat{z}[\omega] \hat{F}[-\omega] \rangle = \frac{\hbar}{2} (\cot(\theta) - i). \quad (3.64)$$

The imaginary part of S_{zF} is canceled upon symmetrization. Finally, the spectrum of oscillator position fluctuations is given by

$$\bar{S}_{xx}[\omega] = \hbar^2 |\chi_m[\omega]|^2 \Gamma_{\text{dec}}, \quad (3.65)$$

where Γ_{dec} is the total decoherence rate, defined as a sum of the thermal contribution and the contribution from the measurement backaction,

$$\Gamma_{\text{dec}} = \Gamma_{\text{BA}} + \Gamma_{\text{th}}. \quad (3.66)$$

While for most our purposes Γ_{th} can be regarded as a constant, corresponding to narrowband approximation, the full frequency dispersion can be restored by replacing it with a frequency-dependent expression as explained in Sec. 3.2.3.

From the perspective of an external observer, who does not have access to the measurement record, Γ_{dec} plays the same role as thermal decoherence rate for an oscillator without meter. As will become evident in the following, the ratio of measurement and total decoherence rates,

$$\frac{\Gamma_{\text{meas}}}{\Gamma_{\text{dec}}} = \eta \frac{4g^2}{\kappa\Gamma_m \bar{n}_{\text{tot}}}, \quad (3.67)$$

ubiquitously appears as a measure of observability of quantum effects. Here \bar{n}_{tot} is the total oscillator phononic occupancy. The ratio of measurement and decoherence rates is closely related to quantum optomechanical cooperativity, the main difference being the presence of detection efficiency in Eq. (3.67), which is a signature of measurement-related problems.

3.3 Quantum correlations in variational homodyne measurements

The achievement of sub-SQL sensitivity in position measurements crucially requires non-zero correlations between the measurement backaction and imprecision, which in our case are represented by the variables F and z of the meter. Correlations between F and z do not require the meter to be prepared in a non-classical state, but rather reflect the choice of these variables such that they are not linearly independent (although the preparation of non-classical state would indeed work as an alternative way of obtaining correlations, as in the case of squeezed vacuum injection [225]). The core idea of the variational readout strategy is that a pre-existing admixture of F in the output channel, when properly selected, can cancel the backaction-driven motion x_{BA} from the measurement record, thus removing one source of error from the estimate of true position. Such a formulation makes it intuitive that imperfect detection efficiency strongly impacts the protocol—whenever F in the measurement record is contaminated by extra vacuum fluctuations introduced by the loss port, it is not perfectly correlated with the measurement backaction force that excited x_{BA} and thus cannot cancel it perfectly. Aside from the mere cancellation between the pre-existing admixture of F and x_{BA} , their “interference” in the output channel can reduce the total level of fluctuations below the vacuum level, which is a signature of squeezed state. Note that the generation of squeezing would require a different adjustment of z and F from that which minimizes the error in position detection.

Correlations induced between the oscillator motion and the imprecision noise of the meter can carry an amplified evidence of measurement backaction. In principle, there are schemes to measure these correlations with zero thermal noise background [226, 20, 227], which were originally proposed to unveil the measurement backaction in the presence of large Brownian motion, i.e. at $\Gamma_{\text{meas}}/\Gamma_{\text{dec}} \ll 1$. In practice, however, such

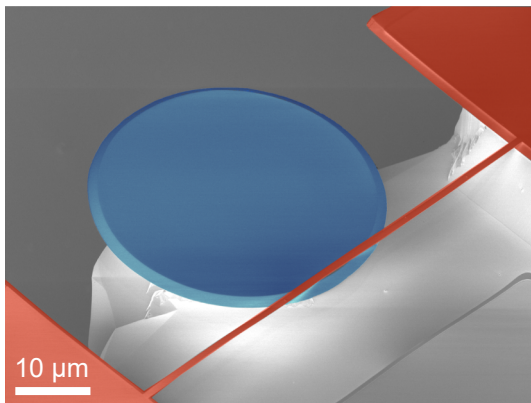


Figure 3.2: False-colored scanning electron microscope image of a monolithically integrated near-field optomechanical device. Red—silicon oxide, red—high-stress silicon nitride, gray—silicon (substrate). Image courtesy of Ryan Schilling.

schemes involve significant tradeoffs—high sensitivity to technical imperfections and long averaging times. Backaction-induced correlations in homodyne measurements have a magnitude that is on the order of $\sqrt{\Gamma_{\text{meas}}/\Gamma_{\text{dec}}}$. In the presence of high thermal noise, this value is much greater than the more typical $\Gamma_{\text{meas}}/\Gamma_{\text{dec}}$, which gives the amount of ponderomotive squeezing (see below) or the increase in phononic occupancy.

In this section we present various evidence for quantum correlations induced by the measurement backaction. Our experiments are performed with MHz-frequency mechanical oscillators at cryogenic (5 Kelvin) and room temperature (295 Kelvin), at which the thermal phononic occupancies are $\bar{n}_{\text{th}} \approx 3 \times 10^4$ and $\bar{n}_{\text{th}} \approx 2 \times 10^6$, respectively. At cryogenic temperature we can observe correlations strong enough to produce ponderomotive squeezing, whereas at room temperature, where thermal noise is two orders of magnitude higher, we can detect their presence and show their effect on the noise floor in force measurements.

The mechanical oscillators used in our experiments are fundamental modes of doubly-clamped high-stress nanobeam resonators, which are near-field coupled to microdisk optical cavities. One of our optomechanical devices is shown in Figure 3.2, for the description of fabrication process and for characterization data see [149], also more extended details are given the following Sec. 3.4. The typical parameters of these optomechanical devices are the following: optical linewidth $\kappa/(2\pi) = 0.8 - 3$ GHz, mechanical frequency $\Omega_m/(2\pi) = 3.4 - 4.4$ MHz, optomechanical vacuum coupling rate $g_0/(2\pi) = 20 - 60$ kHz, mechanical linewidth $\Gamma_m/(2\pi) \approx 15$ Hz at room temperature and $\Gamma_m/(2\pi) \approx 5$ Hz at 5K.

In all experiments we directly record photocurrent spectra obtained using the balanced homodyne detection of light exiting the optomechanical cavity. Photocurrent spectra are converted into spectra of optical quadrature fluctuations, S_{qq}^θ , by normalizing them to the shot noise, i.e. to the level of imprecision (vacuum) fluctuations of the meter beam. The shot noise level is a well established reference for optical signals in our

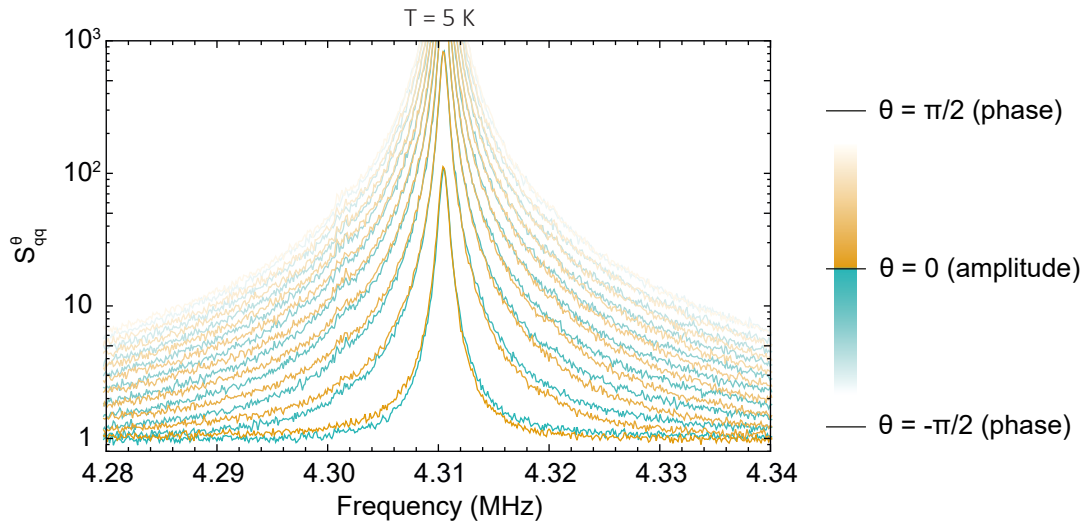


Figure 3.3: Spectra of position records obtained at different homodyne quadratures θ . Differences between spectra recorded at equal positive and negative detunings of θ from the amplitude quadrature originate from the measurement backaction.

experiments. In the balanced homodyne detection that we employ, it can be determined at sub-% level by blocking the signal beam. At the same time the determination of the measurement rate, which is needed to convert S_{qq}^θ to S_{yy} (see Sec. 3.2.6) requires an additional calibration, separate for each experimental run. For simplicity, we do not convert S_{qq}^θ to position units and give it directly when presenting experimental data.

3.3.1 Variational measurements

The concept of variational measurements was originally introduced by Vyatchanin and Matsko [191] and developed by Vyatchanin and Zubova [192, 193]. In early proposals it involved homodyne detection with time-dependent quadrature angle, or passing light through filter cavities [225]. Such complexity was mainly necessary in order to cancel quantum backaction in a wide frequency band, because of the frequency dependence of oscillator response. If only a narrow frequency band is of concern, a much more simple setting is sufficient, in which homodyne detection is performed at a fixed quadrature angle θ intermediate between amplitude and phase. In homodyne detection with fixed θ (such that $0 < |\theta| < \pi/2$), backaction and imprecision contributions to the measurement record interfere destructively or constructively, depending on the frequency. At every frequency the quadrature can be selected to optimally cancel backaction and imprecision contributions by their interference, which implements the variational measurement strategy. This narrowband variational homodyne detection was implemented in a few recent experiments [194, 195, 196, 151], and our work presented here was among the first.

Measurement backaction-induced quantum correlations in homodyne detection have

an imprint of mechanical susceptibility, and manifest as a Fano-looking asymmetry of otherwise Lorentzian shape of mechanical spectrum. Under the rotating wave approximation the spectrum of total (thermal noise and measurement backaction-driven) mechanical motion is given by

$$\bar{S}_{xx}[\omega] = \bar{S}_{xx}^{\text{BA}}[\omega] + \bar{S}_{xx}^0[\omega] = \frac{\Gamma_{\text{dec}}}{\Delta\omega_m^2 + (\Gamma_m/2)^2}, \quad (3.68)$$

where $\Delta\omega_m = \omega - \Omega_m$ is the frequency detuning from the mechanical resonance, and $\Gamma_{\text{dec}} = \Gamma_{\text{th}} + \Gamma_{\text{BA}}$ is the total decoherence time. It follows that $\bar{S}_{xx}[\Omega_m - \Delta\omega_m] = \bar{S}_{xx}[\Omega_m + \Delta\omega_m]$. In contrast, the correlation contribution to the meter output (see Eq. (3.38)) is given by

$$2\text{Re}(\chi_m^*[\omega]\bar{S}_{zF}[\omega]) = -\frac{\Delta\omega_m}{\Delta\omega_m^2 + (\Gamma_m/2)^2} \cot(\theta), \quad (3.69)$$

and is anti-symmetric in $\Delta\omega_m$. The sign and the magnitude of the correlation term depend on the quadrature angle; for homodyne quadratures of the same magnitude but opposite sign correlation contributions are opposite. We use this property in order to visualize the presence of measurement backaction-induced correlations in experimental homodyne spectra shown Figure 3.3. The data in this figure was obtained at cryogenic temperature (5K) under the condition $\Gamma_{\text{meas}}/\Gamma_{\text{dec}} \approx 0.02$ ⁽⁸⁾, where Γ_{dec} is dominated by thermal decoherence due to photoheating. The difference between spectra taken at opposite quadratures is indicative of the magnitude of backaction-imprecision correlations.

The symmetry properties of mechanical susceptibility help to extract backaction-imprecision correlations from experimental spectra even in the presence of large Brownian motion. We introduce a quantitative measure of correlations A as follows

$$A(\omega, \theta) \equiv \frac{\bar{S}_{yy}[\Omega_m + \Delta\omega_m] - \bar{S}_{yy}[\Omega_m - \Delta\omega_m]}{\bar{S}_{yy}[\Omega_m + \Delta\omega_m] + \bar{S}_{yy}[\Omega_m - \Delta\omega_m]} \underset{\text{RWA}}{\approx} \frac{2\Gamma_{\text{meas}}\text{Re}(\hbar\chi_m[\omega])\sin(2\theta)}{1 + 4\Gamma_{\text{meas}}\Gamma_{\text{dec}}|\hbar\chi_m[\omega]|^2\sin(\theta)^2}. \quad (3.70)$$

Although it might appear to be defined ad-hoc, this quantity has a simple scaling property which makes it practically very convenient. Namely, in a wide frequency range, the peak-to-peak variation of A over a full scan of θ directly gives the measurement-to-decoherence rate ratio. It can be shown that the variation of A , denoted as $\Delta A(\omega)$, is given by

$$\Delta A(\omega) = \max_{\theta}(A) - \min_{\theta}(A) = \frac{4\Gamma_{\text{meas}}|\text{Re}(\hbar\chi_m[\omega])|}{\sqrt{1 + 4\Gamma_{\text{meas}}\Gamma_{\text{dec}}|\hbar\chi_m[\omega]|^2}}, \quad (3.71)$$

where the optimization is conducted over $\theta \in [-\pi/2, \pi/2]$ at a fixed frequency ω . This result further simplifies to

$$\Delta A = 2\sqrt{\frac{\Gamma_{\text{meas}}}{\Gamma_{\text{dec}}}}, \quad (3.72)$$

⁸Calibrated from the magnitude of ponderomotive squeezing, see further.

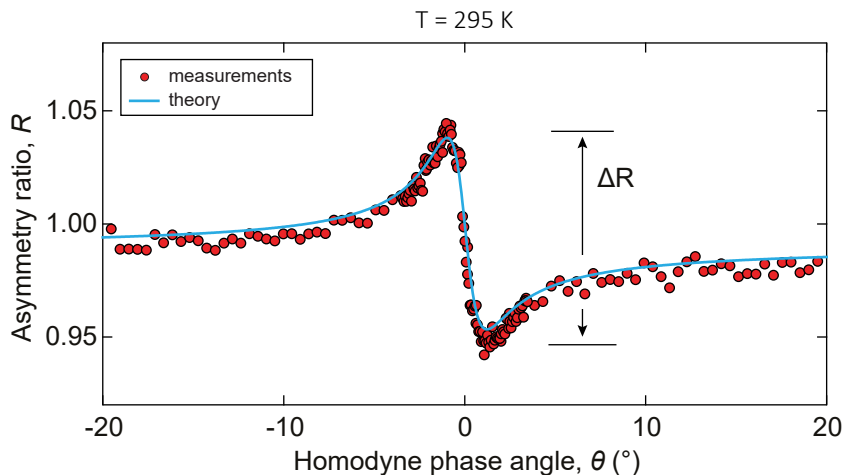


Figure 3.4: Asymmetry ratio as a function of homodyne quadrature.

for any frequency satisfying

$$\Gamma_m/2 \ll |\Delta\omega_m| \ll 2\sqrt{\Gamma_{\text{meas}}\Gamma_{\text{dec}}}. \quad (3.73)$$

Because of the frequency- and quadrature- independence of the extremum value ΔA , it can be alternatively obtained from the variation of A over ω at a fixed quadrature θ . The measurement to decoherence rate ratio can be inferred in this way from a single spectrum.

Our experiments operate in the regime $\Gamma_{\text{meas}}/\Gamma_{\text{dec}} \ll 1$, where we approximate A using the asymmetry ratio R , defined as

$$R(\omega, \theta) \equiv \frac{\bar{S}_{qq}^\theta[\Omega_m + \Delta\omega_m]}{\bar{S}_{qq}^\theta[\Omega_m - \Delta\omega_m]} \approx 1 + 2A(\omega, \theta). \quad (3.74)$$

The variation of R over the quadrature scan, $\Delta R \approx 2\Delta A$, is also universal as long as the measurement rate is not too large.

An example experimental variation of asymmetry ratio R over the scan of quadrature angle is shown in Figure 3.4, where the measurement is performed on a room-temperature mechanical oscillator at $\Gamma_{\text{meas}}/\Gamma_{\text{dec}} \approx 5 \times 10^{-4}$. The scaling of peak-to-peak magnitude of ΔR with measurement rate is shown in Figure 3.5. Different data points at the same measurement rates in Figure 3.5 correspond to different choices of ω within the range defined by Eq. (3.73), which are ideally expected to produce identical ΔR . Overall the experimental data is in a very good agreement with the theoretical prediction, which does not involve fitting parameters.

The absolute magnitudes of correlations observed in our experiments, as well as their scaling with oscillator-detector coupling controlling the measurement rate, matches the expectation for the quantum backaction of the meter. Hypothetically, coupling an

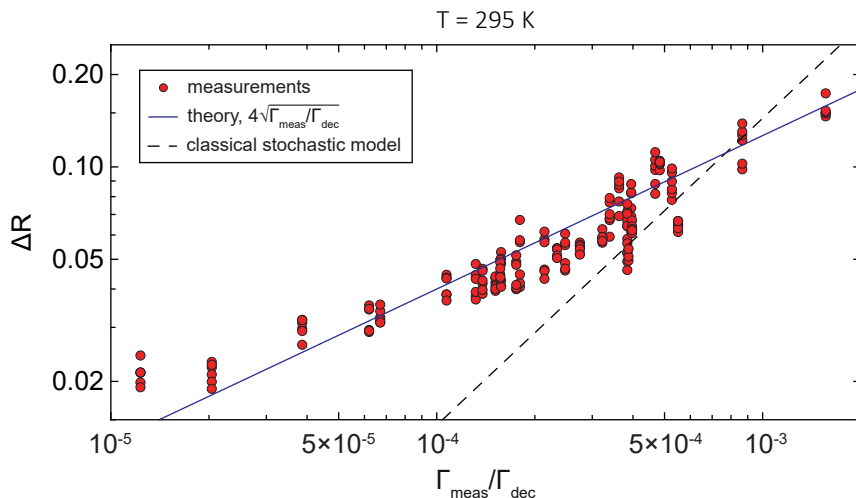


Figure 3.5: The scaling of the visibility of quantum measurement-induced correlations with measurement rate, controlled by the input laser power. The absolute laser powers used in these experiments are in the range of 3 – 300 μW .

oscillator to a classically noisy meter, in which the fluctuations of F are above the quantum minimum, could also produce correlations between the mechanical motion and the imprecision noise. Classical correlations in the meter output would look qualitatively similar to quantum, but their magnitude would be arbitrary, and their scaling with oscillator-detector coupling would be markedly different. We show this discrepancy by fitting the experimental data with a model where the detected correlations are produced by classical fluctuations in the meter variables. This fit is shown by the dashed line in Figure 3.5 and is clearly at odds with experimental data. In our case, where the meter is an optical field, the difference between classical and quantum scaling can be explained by the fact that the vacuum fluctuations of coherent light are independent of the optical power, while classical fluctuations are proportional to the power.

We finally comment on the metrological gain due to backaction-imprecision correlations. The variational strategy reaching the minimum position measurement error allowed by Eq. (3.44) can be implemented as follows. At a given frequency, the overall error $\bar{S}_{\varepsilon\varepsilon}$ is minimized by choosing the optimum detection quadrature,

$$\cot(\theta_{\text{opt}}) = -2\Gamma_{\text{meas}}\text{Re}(\hbar\chi_m[\omega]), \quad (3.75)$$

and setting the measurement rate to the optimum value,

$$\Gamma_{\text{meas}}^{\text{opt}} = 1/2 \cdot (|\hbar\chi_m[\omega]|(1-\eta)/\eta + \text{Im}(\hbar\chi_m[\omega])^2)^{-1/2}. \quad (3.76)$$

Different choices of frequency require different θ and Γ_{meas} . At detunings much greater than the mechanical linewidth, the minimum error is essentially limited by the detection efficiency, and not by the imaginary part of χ_m

$$\bar{S}_{\varepsilon\varepsilon}[\omega] \approx \sqrt{\frac{1-\eta}{\eta}} |\hbar\chi_m[\omega]|. \quad (3.77)$$

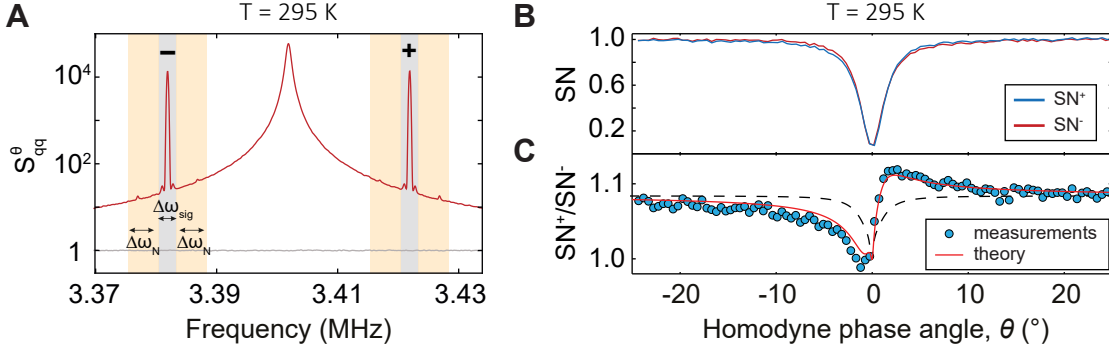


Figure 3.6: Signal-to-noise ratio in force measurements in the presence of quantum backaction. (A) Position spectrum of mechanical motion, showing the Brownian peak in the center and two peaks corresponding to driven motion. The integration bands shown in gray and orange were used for in signal to noise estimation in B and C. (B) The variation of the signal to noise ratio, normalized to that at the phase quadrature, over quadrature scan. (C) Dots show ratios of experimentally measured SN^+ and SN^- . Red solid line—theory, black dashed line—a model with no imprecision-backaction correlations.

In our experimental setup, the optimum measurement rate $\Gamma_{\text{meas}}^{\text{opt}}$ can be reached in a wide frequency band around the mechanical resonance, so that one could expect some metrological advantage for position estimation in this range. The value of detection efficiency typical in our experiments is 25 % (including the cavity factor), which means that the variational strategy can in principle improve upon the finite detection efficiency SQL by 15 %. However, this metrological advantage could not be independently verified, as the absolute position estimation error was much smaller than the magnitude of Brownian motion in the frequency band accessible in our experiment. A sensitivity improvement offered by variational measurements can be sizable compared to Brownian motion only in backaction-dominated regime, which our experiments did not access.

3.3.2 Narrowband external force detection

The cancellation of quantum noises due to backaction-imprecision correlations can improve sensitivity in the detection of external forces, applied to the oscillator. Such an improvement was demonstrated in our experiments, although not at a level sufficiently high to outperform the classically optimum measurement strategy. For proof-of-the-principle demonstration of the effect of quantum correlations on signal-to-noise ratio (SN), we apply an external force to our oscillator using the radiation pressure of an auxiliary laser. The auxiliary laser is coupled the optomechanical cavity and amplitude-modulated using a bichromatic RF signal, the two frequencies of which are equally far detuned from the mechanical resonance to the low and high-frequency sides. A spectrum of mechanical motion in the presence of external drive is shown in Figure 3.6A, it contains the usual Lorentzian peak corresponding to Brownian motion and two resolution-bandwidth limited driven peaks marked as “+” and “-”.

For a classical signal with force spectral density S_{FF}^{sig} , the signal-to-noise ratio of its estimation from the position measurement record is given by

$$\text{SN}[\omega] = \frac{S_{FF}^{\text{sig}}[\omega]}{|\chi_m[\omega]|^{-2}\bar{S}_{\varepsilon\varepsilon}[\omega] + \bar{S}_{FF}^{\text{th}}[\omega]}. \quad (3.78)$$

Here $\bar{S}_{\varepsilon\varepsilon}$ is the quantum contribution to the measurement error and \bar{S}_{FF}^{th} is the thermal contribution including the oscillator zero-point motion. In our experiment, the noise can be estimated at a small offset from the force frequency, as shown in Figure 3.6A.

Signal-to-noise ratios for the positively and negatively detuned drives are denoted by SN^+ and SN^- , respectively, and their variation with quadrature angle is shown in Figure 3.6B. SN values here are normalized to the ones obtained at phase quadrature, which is the optimum quadrature choice in the classical case with no measurement backaction. In this measurement, $\Gamma_{\text{meas}}/\Gamma_{\text{dec}} \approx 5 \times 10^{-4}$. Although SN^+ and SN^- in Figure 3.6B are very close, it is clear their difference changes sign when passing over the amplitude quadrature, $\theta = 0$, which is a signature that the noise level is affected by correlations between the measurement backaction and imprecision. In Figure 3.6C we visualize this difference by plotting the ratio of SN^+ and SN^- . For a comparison to the classical case, in the same figure as a dashed black line we plot a model which does account for imprecision-backaction correlations. As the quantum error in our experiments is much smaller than the thermal force, \bar{S}_{FF}^{th} , quantum correlations do not bring an observable improvement in force sensitivity, which would manifest as SN ratios in Figure 3.6B going above unity.

3.3.3 Ponderomotive squeezing

Aside from providing an advantage in position estimation, correlations between the measurement backaction and imprecision can directly create non-classical states in the meter output. In experiments at cryogenic temperatures we observe that the fluctuations of meter optical field are reduced below the vacuum level, meaning that the field is in a squeezed state. Experimental data demonstrating this is shown in Figure 3.7 for $\Gamma_{\text{meas}}/\Gamma_{\text{dec}} \approx 2 \times 10^{-2}$. As it is physically a consequence of nonlinearity induced by radiation pressure, squeezing generated in optomechanical cavities like ours is referred to as ponderomotive squeezing.

In order to show how measurement backaction can lead to squeezed states, we consider the spectrum of the output optical field quadrature, given by

$$\bar{S}_{qq}^{\theta}[\omega] = 1 + 2\Gamma_{\text{meas}}\text{Re}(\hbar\chi_m[\omega])\sin(2\theta) + 4\Gamma_{\text{meas}}\Gamma_{\text{dec}}|\hbar\chi_m[\omega]|^2\sin(\theta)^2. \quad (3.79)$$

Here the noise level set by vacuum fluctuations is 1, and the backaction-imprecision correlation term can be negative and can reduce the overall \bar{S}_{qq}^{θ} below this level. At each frequency, the detection quadrature θ can be chosen to minimize \bar{S}_{qq}^{θ} . At the optimum angle θ_{opt} , such that

$$\text{tg}(2\theta_{\text{opt}}) = -\frac{\text{Re}(\hbar\chi_m[\omega])}{\Gamma_{\text{dec}}|\hbar\chi_m[\omega]|^2}, \quad (3.80)$$

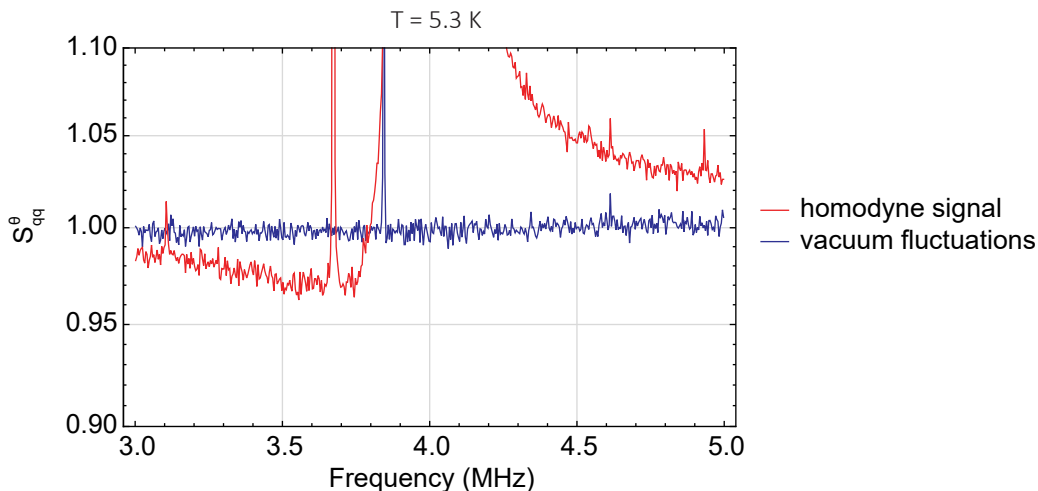


Figure 3.7: Spectrum of homodyne signal showing ponderomotive squeezing at frequencies $\lesssim 3.8$ MHz, where the signal fluctuations are below the vacuum level.

the minimum level of fluctuations is attained, given by

$$\bar{S}_{qq}^\theta = 1 - \frac{\Gamma_{\text{meas}}}{\Gamma_{\text{dec}}} \left| \frac{\text{Re}(\chi_m[\omega])}{\chi_m[\omega]} \right|^2. \quad (3.81)$$

Here it was assumed for simplicity that $\theta_{\text{opt}} \ll 1$, which turns out to be the optimum regime giving the lowest \bar{S}_{qq}^θ . At frequencies away from the mechanical resonance, $|\omega - \Omega_m| \gg \Gamma_m/2$, the mechanical susceptibility χ_m is purely real. In this case how far \bar{S}_{qq}^θ is reduced below the vacuum level is simply determined by the ratio of measurement and total decoherence rates,

$$\bar{S}_{qq}^\theta = 1 - \frac{\Gamma_{\text{meas}}}{\Gamma_{\text{dec}}}. \quad (3.82)$$

Arbitrarily high degree of ponderomotive squeezing is theoretically possible according to Eq. (3.82) in the limit $\Gamma_{\text{meas}} \rightarrow \Gamma_{\text{dec}}$, in other words when $\Gamma_{\text{meas}} \gg \Gamma_{\text{th}}$ and $\eta \rightarrow 1$. Practically, however, ponderomotive squeezing demonstrated to date remains modest compared to the squeezing generated with nonlinear crystals. It is limited by thermal noises in optomechanical cavities, the difficulty of optimizing their intracavity optical losses, and in many cases by photoheating. The best ponderomotively squeezed light reported to date had fluctuations -2.4 dB below the vacuum level [203], which is considerably higher than in the best squeezed light generated with optical parametric amplifiers, where the residual fluctuations can be as low as -15 dB with respect to the vacuum level [228].

Because of the frequency dispersion of the oscillator response, ponderomotive squeezing has strong frequency dependence. An alternative way to describe this effect is by saying that narrowband photons exiting the cavity at frequencies $\omega_L + \omega$ and $\omega_L - \omega$ are

in two-mode squeezed states [182]. In order to verify the two-mode squeezing in experiment, one would need to implement a very narrowband optical filter, which is usually impractical, so the frequency-dependent squeezing language is commonly adopted in optomechanics.

3.3.4 Main experimental limitations

Effects related to the measurement backaction in position measurements can be reliably observed only when the experimental apparatus sufficiently closely approximates the idealized meter considered in the theory in Sec. 3.2. Here we mention some main practical nonidealities in our experiments, which are overall quite typical for optomechanics and interferometric position measurements in general.

One challenge, which has been mentioned already, is reaching high detection efficiency η . Optical losses from absorption inside the cavity or in the propagating output field result in the deviation of measurement apparatus from quantum-limited [23] by raising the measurement-to-backaction rate ratio above unity,

$$\Gamma_{\text{meas}}/\Gamma_{\text{BA}} = \eta. \quad (3.83)$$

Whereas in ideal variational measurements the optimum choice of detection quadrature is a genuinely quantum problem, whenever the detection efficiency is small, the optimum choice converges to that of the classical case—detection at the phase quadrature—which minimizes the imprecision noise only. In our experiments the typical detection efficiency is $\eta \approx 0.25$ where half of the loss is contributed by optical absorption and scattering inside the microdisk cavity, and half by the combined propagation losses and photodetection efficiency.

Classical noises in the optical field is another key challenge. Similar to detection losses, they make the backaction-imprecision product of the measurement apparatus higher than the quantum limit, however their exact effect is more complex to predict and depends in their physical origin. Phase noise of the optical field in excess of vacuum fluctuations simply increases the measurement imprecision. Classical amplitude noise can have more severe consequences—it can potentially lead to correlations similar to imprecision-backaction correlations, thus creating a loophole for misinterpretation of experimental results. Indeed, the origin of backaction-imprecision correlations can be traced to the interference of amplitude and phase fluctuations of light. While in the quantum case the optical phase has an imprint of mechanical motion driven by the amplitude vacuum fluctuations of the optical field, classical amplitude fluctuations would have a similar signature. One difference, however, is that in the quantum case the magnitude of backaction-imprecision correlations is always the same as zero-point motion, while classical noises can produce correlation of arbitrary scale, which moreover are dependent on the optical power. Practically, it is important to make sure in the experiment that any classical amplitude fluctuations are sufficiently below the vacuum level.

Classical optical noises can be of two origins—from the inside and from the outside of the optomechanical cavity. Noises before the cavity in our case predominantly come from the laser source. In principle, they can be suppressed by the use of filtering cavities and/or wideband locking to a stable frequency reference, although it might be technically challenging. In the majority of experiments presented in this section, we used a titanium-sapphire laser in which classical noises were sufficiently low with no extra filtering, simply because the resonance frequencies of our mechanical resonators (3.4 – 4.4 MHz) were much higher than the frequency of relaxation oscillations of the laser (≈ 350 kHz).

Optical noises of intracavity origin constitute a more difficult challenge, as there is usually no way of separating them from the light modulation created by the oscillator motion. A fundamental and practically most important class of intracavity noises has its origin in the thermodynamic fluctuations of cavity parameters in thermal equilibrium. It includes thermorefractive noise [40, 229], frequency noise due to the Brownian motion of highly damped microdisk modes, and possibly other contributions. At some point in our experiments, we also observed that the tapered fiber used for the input coupling of light could add extra noise, apparently, due to the modulation of coupling rate by thermal vibrations (see SI of [194] for more details). In this case because of the dissipative type of the coupling, an optical quadrature between phase and amplitude was modulated by thermal noise, which was especially detrimental in the quadrature scan experiment, where signals from quadratures close to the amplitude were of primary interest. Overall, the requirement to operate in the regime of low enough input optical power, where the thermal cavity noises are negligible compared to the optical vacuum fluctuations, was one of the key aspects limiting the achievable measurement-to-decoherence rate ratio in our experiments at room temperature.

At cryogenic temperatures, another key limitation in our experiments was photoheating. The absorption of optical power increases the temperature of mechanical bath, which in steady state manifests as a maximum achievable measurement-to-decoherence rate ratio below one (typically not exceeding 0.2 in our case). Although the consequence of photoheating might appear similar to the limitation in Eq. (3.83), the analogy would not be very far reaching. While the effect of imperfect measurement-to-decoherence rate ratio is instantaneous, photoheating can be circumvented by making fast pulsed measurements, which was demonstrated in Ref. [171, 174], where the measurements are made faster than the absorbed optical power redistributes between the resonator degrees of freedom.

3.4 Experiments with near-field optomechanical cavities

Experimental data presented in Sec. 3.3 was obtained using on-chip optomechanical cavities, each of which consisted of a silicon oxide microdisk and a silicon nitride nanobeam placed in the near field of the microdisk whispering gallery modes (WGM). The geometry of a typical device is shown in Figure 3.8. In this section, we present details of experiments with such devices, with the aim of illustrating the way in which the data

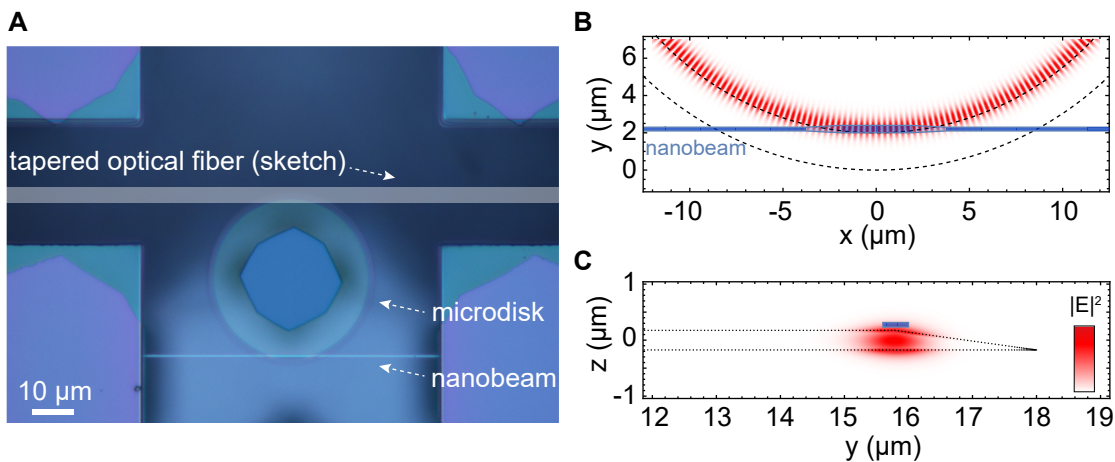


Figure 3.8: (A) Microscope image of a near-field coupled optomechanical device (not from the vacuum experimental setup), with a sketch added on top showing the position of the tapered optical fiber during experiments. (B-C) Red—electrical field distribution in a whispering gallery mode of the disk, obtained from finite element simulation. Dashed contour—the boundaries of the microdisk. Blue—nanobeam.

in Sec. 3.3 was obtained rather than exhaustively covering the subject. We focus on the operation at room temperature. For the operation of the He3 cryogenic setup, see the theses of former students, Stefan Weis [230] and Vivishek Sudhir [231] in particular. For additional information about the room temperature setup, see the thesis of Hendrik Schütz [232]. All integrated optomechanical devices were fabricated by Ryan Schilling, whose thesis covers them thoroughly [233].

Integrated near-field optomechanical transducers are probed by coupling light into a whispering gallery mode of the microdisk using a tapered fiber with a sub-micron waist size. Tapers are made by locally melting cuts of 780 HP single-mode optical fiber in hydrogen flame and elongating them at a constant speed using two linear translation stages (Newport MFA-CC). While taper pulling is not a very well reproducible process, for our experiments we selected tapers with transmission efficiency better than 95 %. After a taper is pulled, it is tensioned close to the breaking limit and attached to a holder using small amounts of UV-curable glue (Norland Optical Adhesive 81). Tensioning is necessary to efficiently couple to WGMs in vacuum using slip-stick positioners, which create a substantial amount of vibration on each step. Tension is checked on a separate setup by bringing the taper in contact with a microtoroid on a dummy chip and pulling it away until it is unstuck. The distance at which the unsticking happens serves as an indicator of tension.

For performing optomechanics experiments, a chip with near-field samples is mounted inside a vacuum chamber on top of a stack of Attocube positioners providing three translational degrees of freedom. A holder with a tapered fiber is mounted in a stationary position inside the chamber and the taper waist is imaged using an outside microscope. In this configuration, a selected sample can be positioned to touch the taper at the edge

of the microdisk. The sample during an experiment looks similar to what is shown in Figure 3.8A, the main difference being that the imaging resolution in the actual setup is not as good as in the picture, for which a high-resolution microscope image was taken separately. Optical coupling rate is inferred from the transmission drop when the laser is swept across one of the optical resonances. A high coupling selectivity can be achieved for one family of WGM resonances, so that the transmission level away from the coupled resonances is unaffected by the fiber touching the disk.

Standalone silicon oxide microdisks defined using ebeam lithography can host WGM modes with intrinsic optical linewidths down to 10 MHz [149], but the linewidths of the same disks integrated with nanobeams are more commonly in the GHz range. Overwhelming this level of optical loss with extrinsic taper coupling is challenging. Our experiments typically operate under “critical coupling” condition [234], i.e. when the extrinsic optical damping due to the light escape to the tapered fiber, κ_{ext} , matches the intrinsic optical loss rate, κ_0 ,

$$\kappa_{\text{ext}} = \kappa_0. \quad (3.84)$$

This corresponds to the light escape ratio $\eta_c = 1/2$ and makes the primary contribution to the overall detection inefficiency in our experiments. Operation at critical coupling, however, has one advantage. The output signal from the cavity has zero carrier, which facilitates quantum-limited balanced homodyne detection as the amplitude of the local oscillator can be easily made much larger than the amplitude of the signal. Operating deeply in the regime of strong local oscillator is also required to reliably calibrate the shot noise level with a sub-percent error.

3.4.1 Setup for the detection of measurement backaction-imprecision correlations at room temperature

The layout of the experimental setup used for the detection of backaction-imprecision correlations at room temperature [194] is shown in Figure 3.9. In this work, the sample was placed in a high vacuum chamber, at a pressure below $\sim 10^{-6}$ mbar. Light is coupled in and out of the microdisk cavity using a tapered optical fiber, the position of the sample is adjusted using piezo actuators to achieve critical coupling.

The cavity is probed on resonance using a *meter* laser beam, which is subsequently detected in a balanced homodyne scheme. Additionally, the oscillator is feedback cooled using an auxiliary *feedback* beam for the purpose of reducing thermal intermodulation noise around the mechanical resonance frequency. Two lasers were employed in the experiment – a TiSa laser (MSquared Solstis) with wavelength centered around 780 nm as the meter beam, and an auxiliary 850 nm external cavity diode laser (NewFocus Velocity) as the feedback beam. Both beams are combined before the cavity and separated after it using dichroic beamsplitters. The feedback beam is detected on an avalanche photodetector (APD), while the meter beam is fed into a length- and power-balanced homodyne detector. A small portion of the meter beam—stray reflection from the dichroic beam-splitter—is directed onto an APD.

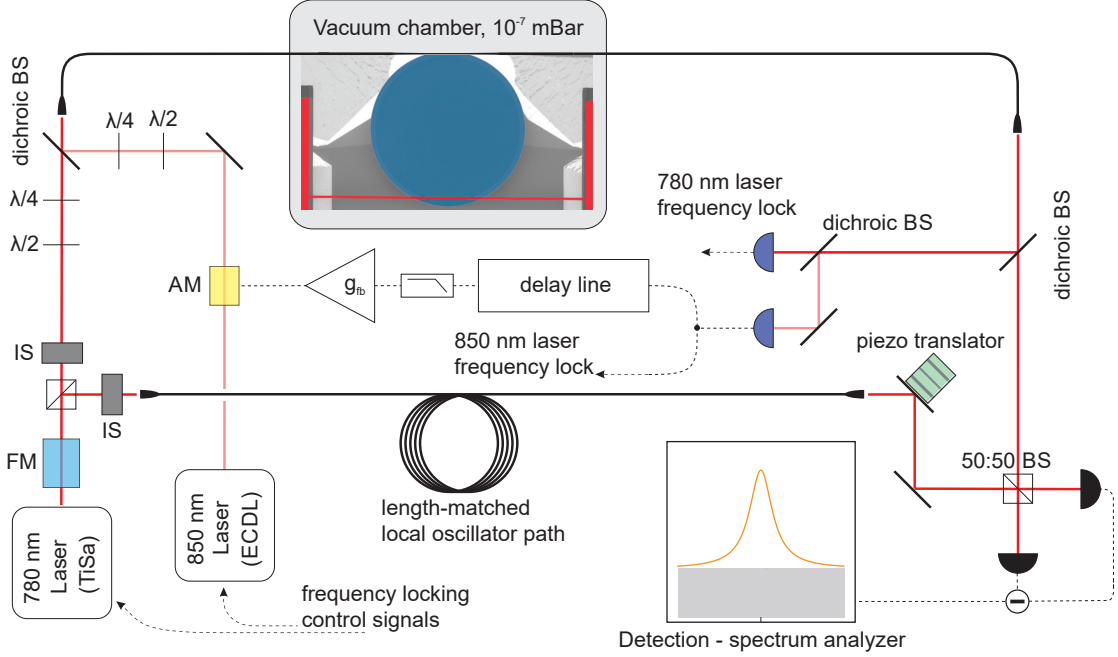


Figure 3.9: Schematic of the room temperature experimental setup. Abbreviations: AM – amplitude modulator, FM – frequency modulator, BS – beam splitter, IS – intensity stabilizer.

Both lasers are actively locked to their independent cavity resonances using the APD signal. For the meter beam, a lock on cavity resonance ($|\Delta| \lesssim 0.1 \cdot \kappa$) is implemented using the Pound-Drever-Hall technique. For the feedback beam, a part of the APD signal is used directly to implement a side-of-the-line lock red-detuned from cavity resonance.

The other part of the feedback beam APD signal is used to perform moderate feedback cooling of the mechanical oscillator from the equilibrium phononic occupancy $\bar{n} = 1.8 \cdot 10^6$ to $\bar{n} \approx 10^4$. For this purpose, the photosignal is amplified, low-pass filtered and phase-shifted, before using it to amplitude modulate the same laser. As in conventional cold damping [235], the phase-shift in the feedback loop is adjusted to synthesise an out-of-phase radiation pressure force that damps the mechanical oscillator. At a nominal feedback laser power of $5 \mu\text{W}$, a damping rate of about 1 kHz is realized. The associated increase in the mechanical decoherence rate due to injected imprecision noise was estimated to be below 5%.

The path length difference of the homodyne interferometer is actively stabilized using a two-branch piezo translation system. Demodulation of the homodyne signal at the PDH modulation frequency also produced interference fringes suitable for locking the homodyne angle near the amplitude quadrature (i.e. $\theta = 0$). The residual homodyne angle fluctuations could be estimated $\theta_{\text{RMS}} \lesssim 1^\circ \approx 0.017 \text{ rad}$, inferred from the suppression of thermomechanical signal-to-noise ratio on amplitude quadrature of $\approx 10^{-4}$ compared to the phase quadrature. An offset DC voltage is applied to the homodyne error signal to deterministically choose the detection quadrature. Since the feedback cooling

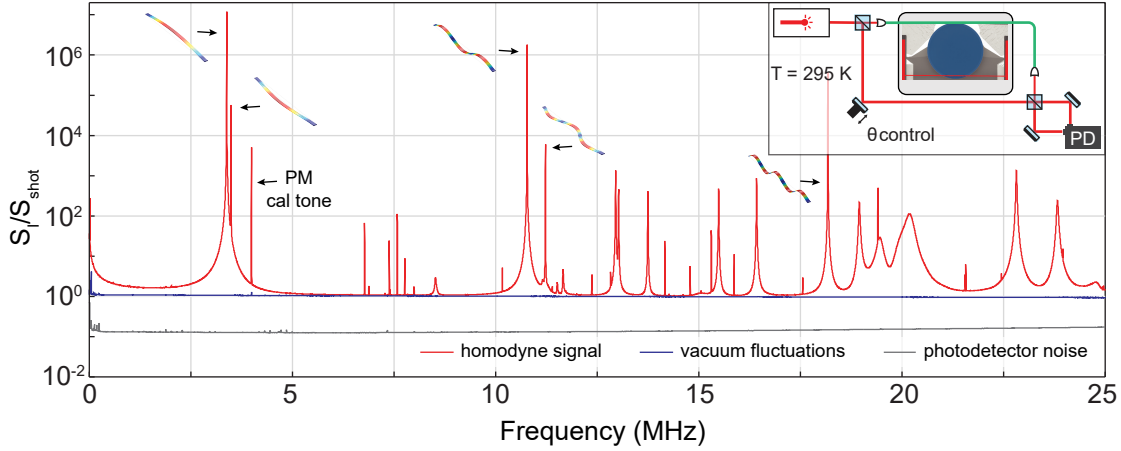


Figure 3.10: Broadband noise as read out by the homodyne interferometer. A few lowest-order flexural modes of the nanobeam are identified in the spectrum. The measurement setup is sketched in the inset.

exclusively relies on the auxiliary diode laser, the homodyne measurements on the 780 nm meter beam are completely out-of-loop and does not contain electronically-induced correlations.

The near-field optomechanical sample used in our room-temperature experiment [194] consisted of a 80 nm thick Si_3N_4 nanomechanical resonator placed in the near field of a microdisk. The diameter of the microdisk is equal to $40 \mu\text{m}$, thickness $\sim 350 \text{ nm}$, and it has a gently sloping sidewall of $\sim 10^\circ$. The mechanical resonator is $70 \mu\text{m}$ long and consists of a narrow (200 nm) beam with a wider (400 nm) rectangular defect at the center which tapers linearly into the thin beam, as shown in Figure 3.8B and C. The purpose of the defect is to increase the vacuum optomechanical coupling rate, g_0 . The defect length is $5 \mu\text{m}$, which exhibits an effective mass only 11% larger than that of a standard 200 nm wide beam. According to the finite element simulation, $m_{\text{eff}} = 1.94 \text{ pg}$. The device was fabricated by a monolithic wafer-scale process that utilizes a sacrificial layer to define a $\sim 50 \text{ nm}$ gap between the microdisk and nanobeam, as detailed in [149]. Similar devices also were used for the cryogenic experiments [148, 202].

The vacuum optomechanical coupling rate of the described sample is $g_0 \approx 2\pi \cdot 60 \text{ kHz}$ for the fundamental, $\Omega_m = 2\pi \cdot 3.4 \text{ MHz}$ flexural beam mode. In conjunction with the high room temperature mechanical quality factor, $Q_m \approx 3 \cdot 10^5$ (giving a damping rate of $\Gamma_m = \Omega_m/Q_m \approx 2\pi \cdot 12 \text{ Hz}$), and a critically coupled cavity decay rate of $\kappa \approx 2\pi \cdot 4.5 \text{ GHz}$, a near-unity single photon cooperativity of $C_0 = 4g_0^2/\kappa\Gamma_m \approx 0.27$ is attained. Importantly, the near-field optomechanical cavity operates in the fast cavity regime, i.e. $\kappa \gg \Omega_m$.

3.4.2 Broadband correlations

Integrated near-field optomechanical transducers provide access to broadband phenomena which are not limited to the spectral vicinity of the mechanical resonance. A broadband spectrum of displacement fluctuation read out from the near-field sample described in the previous section 3.4.1 is shown in Figure 3.10. At frequencies below approximately 6 MHz, the displacement signal is dominated by the Brownian motion of the fundamental out-of-plane nanobeam mode, aside from a small spectral region around the fundamental in-plane mode. Above 6 MHz the spectrum is more crowded, although higher-order out-of-plane nanobeam modes still provide the largest contribution to the signal and are clearly identifiable. The remaining noise peaks belong to other mechanical resonances of the integrated transducer and have low quality factors.

The clear spectrum at low frequencies enabled the measurement of wideband frequency dispersion of the thermal force noise acting on the fundamental mechanical mode reported in [123]. We observed that the spectral density of thermal force noise at low frequencies increases $\propto 1/\omega$, which is consistent with a frequency-independent loss angle and is common for structurally damped solid-state resonators (i.e. losses in which are limited by internal friction). This behavior of loss angle, in particular, means that the thermal noise acting on the oscillator is manifestly non-Markovian, in contrast to the case of viscous damping with friction force proportional to velocity. Broadband frequency dispersion of Brownian motion was measured for the first time in experiments with macroscopic masses suspended on silica wires [236, 237] at the end of the 1990s. For nanomechanical resonators, similar results came only more recently. Aside from our work, broadband thermal noise measurements were reported for silicon phononic crystals [200] and GaAs cantilevers [199].

In variational measurements performed with integrated near-field devices signatures of correlations between the radiation pressure shot noise and the measurement imprecision can be observed in a frequency band on the order of the mechanical resonance frequency. Recall that in our implementation of variational measurements, we simply sweep the homodyne quadrature angle θ so that at every angle in the vicinity of amplitude quadrature, $\theta = 0$, the measurement backaction is optimally canceled at one frequency. Reversing the sign of the homodyne angle reverses the sign of quantum correlations. The contrast between reduced/enhanced noise levels for signals taken at two opposite quadratures can be observed in the data presented in Figure 3.11A. Quantum correlations induced by the measurement backaction are clearly visible in the band between one and six MHz, below which the amplitude noise of the Ti:Sa laser becomes non-negligible, and above which the mechanical spectrum is not single-mode any more. The visibility of measurement backaction-induced correlations at low frequencies is lower because of the $1/\omega$ behavior of the thermal noise, specific to mechanical oscillators with frequency-independent damping. Figure 3.11B shows the application of the asymmetry ratio measure introduced in Sec. 3.3.1 to extract the magnitude of correlations. As the offset from the mechanical resonance increases, the deviation of thermal noise from white and the mechanical susceptibility from that prescribed by the rotating wave

approximation become more apparent, which manifests in $R(\theta)$ acquiring a component symmetric in θ . Despite the asymmetry ratio analysis not being as transparent as in the near-resonant case, its result is still well described by the full theoretical model taking into account the broadband behavior of thermal noise and oscillator dispersion.

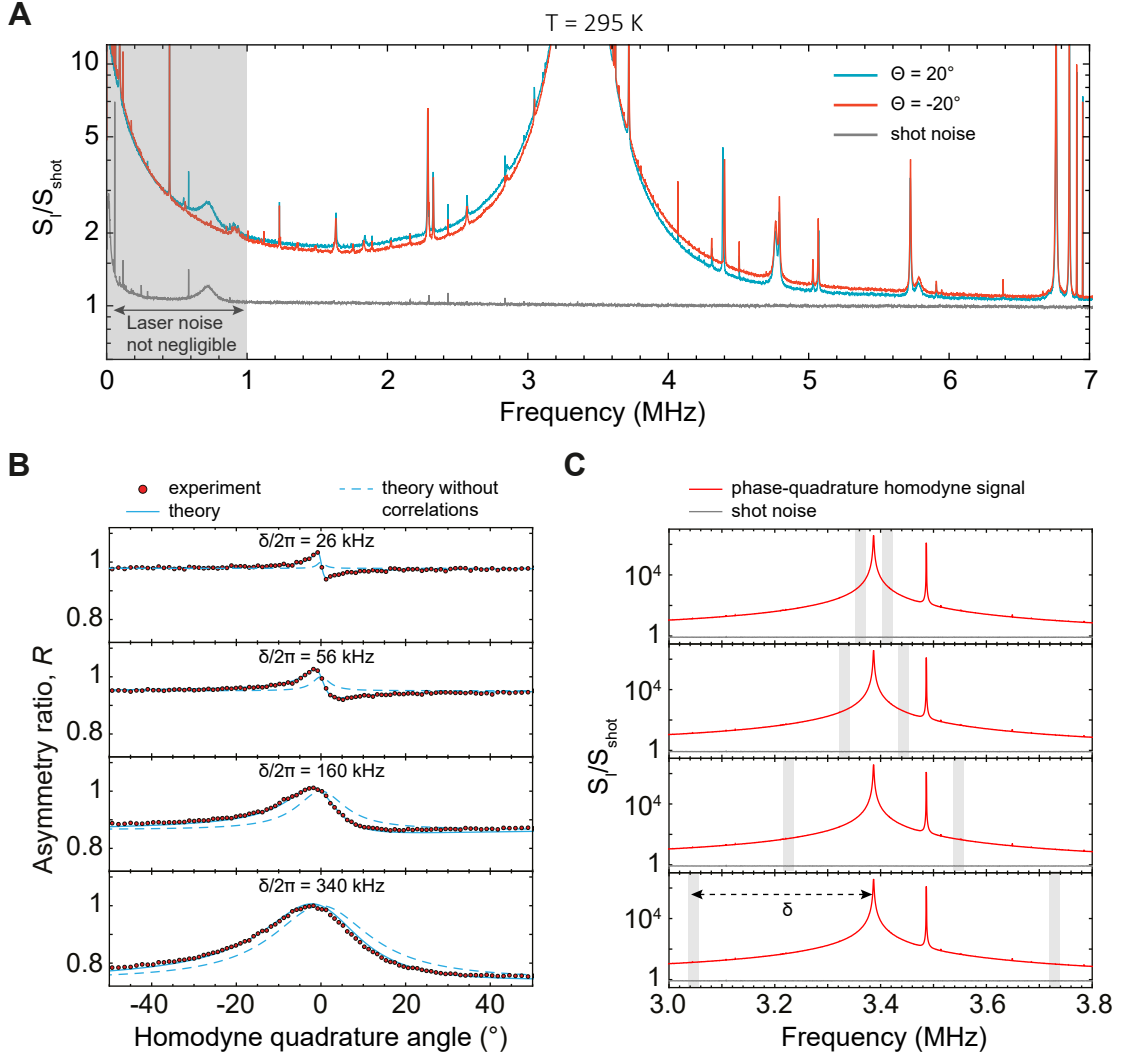


Figure 3.11: Broadband quantum backaction-imprecision correlations in homodyne detection at room temperature. A) Homodyne spectra taken at two opposite quadratures showing signatures of quantum correlations over a 5 MHz band. θ is the homodyne quadrature angle. The data was taken at $P_{\text{in}} = 315 \mu\text{W}$. B) Illustration of the variation of the experimental asymmetry ratio $R(\theta)$ for different offsets δ at fixed integration bandwidth equal to 20 kHz. Solid and dashed red curves show theoretical predictions accounting and not accounting for the quantum backaction-imprecision correlations. C) Plots show the integration bands used for calculation of the $R(\theta)$ on the left (shaded gray regions). Red is a mechanical spectrum and blue is the local oscillator trace showing the shot noise level. The data was taken at $P_{\text{in}} = 200 \mu\text{W}$.

Nonlinear measurements and thermal intermodulation noise

4.1 Introduction

Interferometric position detectors achieve unprecedented sensitivity by using the optical wavelength as a reference for mechanical displacements. A simple model of an interferometric detector is shown in Figure 4.1. Here, the phase shift of the probe light, reflected from the test mass M , is proportional to the displacement x of the mass. The phase shift is linear in x ; however, it is not measured directly but needs to be inferred from an interference pattern. This is commonly accomplished with the help of homodyne detection (as shown in Figure 4.1B), where the signal field with the complex amplitude s_{out} is combined with a local oscillator s_{LO} on a beamsplitter and then photodetected. The differential photocurrent is given by

$$I \propto |s_{\text{out}}s_{\text{LO}}| \cos(\phi - \phi_0), \quad (4.1)$$

where ϕ_0 is the local oscillator phase, $\phi = -4\pi x/\lambda$ is the probe phase and λ is the wavelength of the optical field. The photocurrent given by Eq. (4.1) is periodic in x , and hence the position measurement is inherently nonlinear. Only when the displacement of the mass is small compared to the optical wavelength can the homodyne photocurrent be linearized. In this case, the linear measurement sensitivity is maximized at $\phi_0 = \pi/2$. Even for small displacements, however, the local oscillator phase can be chosen such that the leading contribution to the photocurrent is due to the mechanical displacement squared, x^2 , and hence the measurement is nonlinear. In our phase convention this is accomplished by setting $\phi_0 = 0$, so that $I \propto (1 - 8\pi^2(x/\lambda)^2)$.

Optical cavities are commonly employed to improve the sensitivity of interferometric measurements. Cavities make the probe field interact with the test object multiple times, the number of which is given by the cavity finesse \mathcal{F} . The spatial scale of interference pattern for light reflected from a cavity on resonance is reduced from λ to λ/\mathcal{F} . Correspondingly, the linear transduction of displacements is enhanced by the factor \mathcal{F} , and quadratic by the factor \mathcal{F}^2 . This makes the nonlinearity of interferometric measurements more pronounced when high-finesse cavities are employed. The nonlinearity of

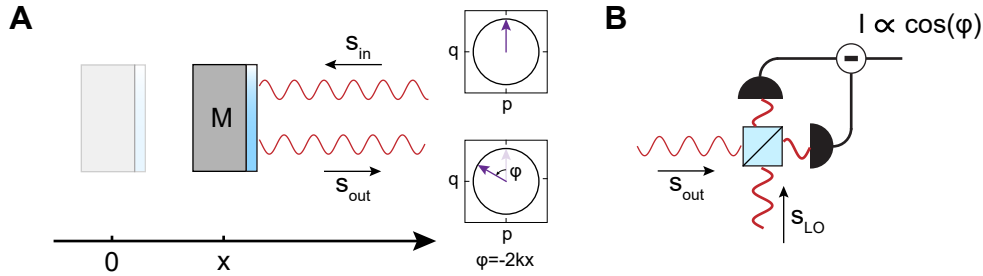


Figure 4.1: Interferometric position measurements are nonlinear for large displacements, or if the reference phase is specifically chosen. A) Phase shift of probe light, reflected from a test body. The two insets show the complex amplitude of light before and after the interaction in terms of phase (p) and amplitude (q) quadratures. B) Homodyne detection of phase shift with local oscillator phase set so that $d\phi/dx = 0$ produces photocurrent which leading contribution is quadratic in x .

oscillator position transduction by a cavity is illustrated in Figure 4.2A for the case of resonant laser drive.

Nonlinear measurements of oscillator position have been a long-standing subject of theoretical research as they potentially allow the creation of complex quantum states and measurements at sub-SQL sensitivity. In quantum systems consisting of bosonic modes with linear couplings, which are subject to linear measurements and feedback, and which are all initially prepared in Gaussian states, the states always remain Gaussian over their evolution. Experiments presented in Chapter 3 fall into this category. In this case while states can become squeezed and non-classical, their Wigner function is always positive, and thus their dynamics still bears some resemblance to a classical stochastic process (see [206, 182] for discussion). Quantum mechanics here mainly supplies power spectral densities to the noises. Nonlinear measurements or non-Gaussian initial states can be used to circumvent this limitation.

Interferometric nonlinearity was recognized as a resource for quantum measurements in Ref. [238] as early as in 1995, but after that received almost no further attention for more than a decade. In this historic example, it was proposed that quantum non-demolition measurements of oscillator phase can be realized using a high-finesse Fabry-Perot cavity parametrically coupled to an oscillator in a typical optomechanical setting. It is instructive to review this simple scheme. The cavity was assumed to be resonant with a laser probe when the oscillator is at rest (at $x = 0$). When the oscillator is highly excited, so that it shifts the cavity frequency by much more than one optical linewidth at its deflection maximum, every time the oscillator passes through $x = 0$ it creates a short spike in cavity transmission. At all other times the cavity transmission is zero. While the information about mechanical position is extracted at every half a period, providing a measurement of the oscillation phase, the quantum backaction that acts during the time when the light is resonant only affects the oscillation amplitude. This scheme has some common aspects with stroboscopic measurements [14], but here the timing of the effective “measurement pulses” is entirely set by the oscillator.

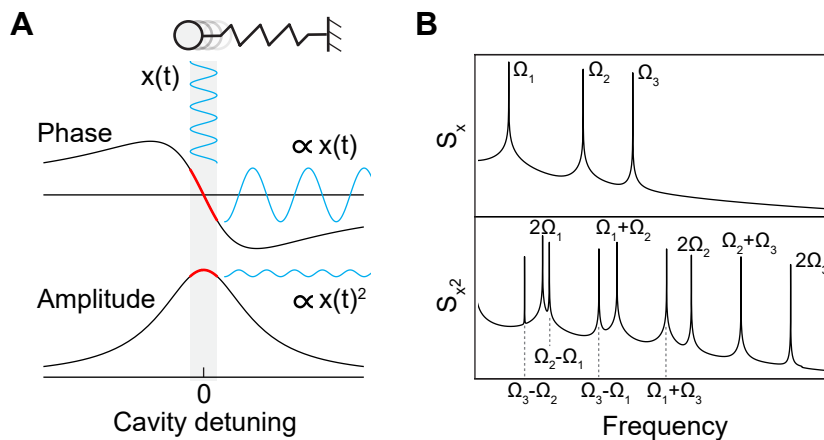


Figure 4.2: Nonlinear frequency transduction by a cavity. A) Transduction of the oscillator’s motion to the phase (upper panel) and amplitude (lower panel) quadratures of resonant intracavity light. B) Spectra of linear (upper panel) and quadratic (lower panel) position fluctuations of a multimode resonator, showing the emergence of wideband noise.

A wider interest in nonlinear measurements has been fueled by the prospects of performing quantum non-demolition detection of oscillator energy [1]. One possible way of accomplishing this task is directly coupling a meter to the mechanical displacement squared [239, 240]. When the meter is an optical cavity driven by a propagating field [23], the interaction Hamiltonian for quadratic readout is given by

$$\hat{H}_{\text{int}} = -\hbar G_2 \hat{x}^2 \hat{n}_c / 2, \quad (4.2)$$

where $G_2 = -\partial^2 \omega_c / \partial x^2$ is the coupling constant, ω_c is the cavity frequency, and \hat{n}_c is the intracavity photon number. The QND criterion (see Sec. 4.4 of [1]) is readily satisfied in this case, as the measured quantity, x^2 , is an integral of free oscillator motion and it commutes with the interaction Hamiltonian in Eq. (4.2). Quadratic measurements of this kind can be used for the observation of phononic jumps [239, 240], phononic shot noise [209], and the creation of mechanical squeezed states [241]. While considerable efforts have been dedicated to realizing nonlinear optomechanical coupling described by Eq. (4.2), achievable coupling rates remain modest [242, 243], and the corresponding experiments have so far been deeply in the classical regime. Some of the challenges here will become clear from the rest of the discussion.

Quadratic position measurements with parametric cavity detectors need to be analyzed taking into account the output leakage of intracavity field. Coupling the cavity mode to a propagating field is fundamentally required in order to provide detectable signal to the observer and for the cavity to be externally driven. Results of the Hamiltonian analysis of a closed cavity-oscillator system can be highly misleading, as illustrated by the example of a membrane-in-the-middle (MIM) system, schematically shown in Figure 4.3. It was noted by Thompson et al. [84] that the quadratic Hamiltonian given by Eq. (4.2) can be realized in a membrane-in-the-middle system if the membrane is

positioned symmetrically between the cavity mirrors so that its motion does not shift the optical mode frequencies to the first order in x . However, it was later found out by Miao et al. [244] that the leakage of light through the cavity mirrors leads to a linear modulation of the output field via the mechanism known as dissipative coupling. The linear signal proportional to the mechanical position is accompanied by quantum back-action, and hence this scheme does not realize a QND measurement. Although it was clarified later in Ref. [245] that a perfectly one-sided membrane-in-the-middle cavity is free from dissipative coupling, even a small mirror loss would still make the realization of this scheme extremely challenging.

Accounting for propagating optical modes naturally brings the question of interferometric nonlinearity, which is another effect not fully revealed when the optical cavity is treated as a closed system (although the position-squared coupling in a MIM system has the same interferometric origin). As will be shown in Sec. 4.2.3, the overall magnitude of the interferometric nonlinearity in a MIM cavity can be \mathcal{F} times larger than the maximum magnitude of quadratic coupling. This fact was first pointed out by Vanner [246] in the work which revived the interest in nonlinear measurements with linear coupling. Considering the open cavity as a meter, nonlinear signals produced by linear coupling can be understood as an effect beyond the linear response regime. As the meter sensitivity is increased, which in the case of an optical cavity can be accomplished by increasing its finesse, eventually measurements enter the regime where information is still obtained gradually, but the first order perturbation theory [206] is not sufficient to describe the measurement process [247]. Such measurements were experimentally demonstrated in [248, 249], yet in the classical domain. It was experimentally confirmed in [248], that under quite typical conditions the nonlinearity of the cavity as a meter is orders of magnitude stronger than the nonlinearity due to quadratic coupling. It was also recognized that interferometric nonlinearity crucially requires the cavity to be coupled to the propagating field, and does not have an equivalent in a closed system of a mechanical oscillator coupled to an isolated optical mode [250].

The relatively strong transduction nonlinearity of interferometric measurements does not necessarily make them QND, as such measurements are typically accompanied by linear quantum backaction. This can be qualitatively understood by considering for example the scheme presented in Ref. [246]. Here the amplitude quadrature of light reflected from an optomechanical cavity and quadratically modulated by mechanical motion is detected, as a result of which the mechanical oscillator is conditionally prepared in a non-Gaussian state. This scheme also measures the amplitude quadrature of the input optical field, on top of which mechanical modulation is added, because of which after each measurement the resonator receives a random “kick” from the backaction of the meter. In order to use such nonlinear measurements for verifiable non-classical state preparation, it was proposed to perform the measurement and verification stroboscopically [246], or to implement measurement-based feedback [248].

As was mentioned earlier, experimental progress towards performing nonlinear quantum measurements of the oscillator position remains modest to date. The practical difficulty of engineering a strong nonlinearity of measurements and the presence of li-

near quantum backaction in some settings are two parts of the problem. Another part is that performing nonlinear measurements on a single oscillator mode requires a highly selective coupling to this mode. Most of the present-day micromechanical resonators used in quantum optomechanics experiments are multimode systems. The effective displacement x measured in this case is a sum of many normal mode contributions x_n ,

$$x(t) = \sum_n x_n(t). \quad (4.3)$$

In the linear measurement case they can be separated in the spectral domain if x_n correspond to high- Q modes at different frequencies. The separation is never perfect, however, as the spectrum of motion of each mode spans the entire frequency axis. In the non-linear case, the separation of modes quickly becomes a formidable task as the number of modes is increased. E.g., if a quadratic measurement is performed on a multimode system, the measurement signal is contributed by all the mixing products of different modes,

$$x(t)^2 = \sum_{n,m} x_n(t)x_m(t), \quad (4.4)$$

all of which, although peaked, have non-zero spectral density at all frequencies. Example spectra of $x(t)$ and $x(t)^2$ for a measurement setup where three modes contribute to x are illustrated in Figure 4.2B. It is particularly important for the following that the spectral density of quadratic signal is not limited to the peaks at the sum and the difference frequencies of the modes. For the reason above, in a multimode system at high temperature at which all the modes are far from their ground states, measurement nonlinearity creates a large amount of broadband thermal noise.

In this chapter, which is largely based on our work reported in Ref. [44], we describe the operation of a membrane in the middle optomechanical setup and experimentally show that the nonlinear modulation of the optical field by thermal frequency fluctuations can manifest as a broadband added noise in detection. We refer to this noise as *thermal intermodulation noise* (TIN), since it mixes different Fourier components of cavity frequency fluctuations. This noise dominates when the linearly transduced thermal fluctuations are small, such as when detecting the intensity of near-resonant optical probe. As it is the leading-order contribution, TIN is not necessarily negligible even when the nonlinearity of cavity transduction is small.

We experimentally observe and study TIN in a membrane-in-the-middle (MIM) optomechanical system [84, 85]—a promising platform for room temperature quantum optomechanical experiments [199, 251]—and find excellent agreement with our developed theoretical model. Using a Si_3N_4 membrane resonator hosting a high- Q and low mass soft-clamped mode [36, 152], we operate at a nominal quantum cooperativity of unity, i.e. in the regime where the linear measurement quantum backaction (arising from radiation pressure quantum fluctuations) is expected to overwhelm the thermal motion. This regime is required for a range of quantum enhanced measurement protocols [192, 194, 195], or generation of optical squeezed states [200, 201]. Yet, the nonlinearity of our cavity prevents the observation of quantum correlations between the field quadratures,

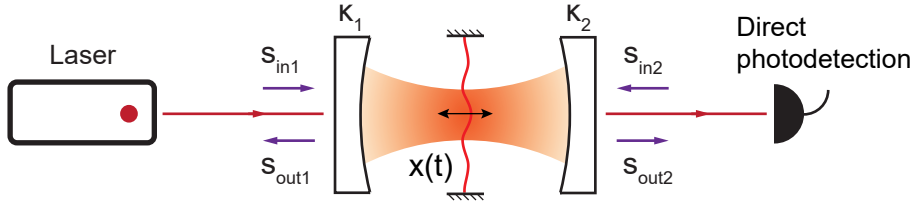


Figure 4.3: Schematic of a membrane-in-the-middle optomechanical system with optical input and output fields marked by violet arrows.

and manifests itself in TIN significantly above the shot noise (i.e. quantum noise) level. Since TIN is a coherent effect, it only requires the knowledge of spectrum of cavity frequency fluctuations to be modeled, and our experimental data is well matched by a model with no free parameters.

We show that for a particular “magic” detuning from the cavity TIN is fully canceled in direct detection, and propose a more general cancellation scheme suitable for arbitrary detuning. Our observations, while made for an optomechanical system, are broadly applicable, irrespective of the underlying thermal noise source. Thermal intermodulation noise can be of relevance to any cavity based measurement schemes at finite temperature.

4.2 Thermal intermodulation noise in a membrane in the middle cavity

4.2.1 Membrane in the middle cavity

Membrane-in-the-middle is a highly successful optomechanical scheme which enabled the first observation of quantum backaction in oscillator position measurements [20] and a number of other quantum experiments since then [201, 252, 195, 253, 203, 150, 151, 178]. A key advantage of the MIM scheme is that it can combine one of the highest- Q mechanical resonators developed to date with high-finesse optical cavities. Additionally, the spatial separation of optically reflective surfaces from the mechanical mode make photoheating in MIM much less problematic than in other optomechanical systems. MIM cavities can show no signs of photoheating even when operated at millikelvin temperatures inside a dilution refrigerator [195].

While all quantum experiments performed to date with MIM cavities operated at cryogenic temperatures, it is also a promising setting for room-temperature quantum optomechanics [194, 227, 199] because of the high achievable cooperativity and a low level of extrinsic thermal frequency noises in Fabry-Perot cavities. High cooperativity, however, achieved with the help of high cavity finesse is also accompanied by high transduction nonlinearity of the cavity, which leads to strong thermal intermodulation noise.

In this section we introduce a few facts about membrane in the middle cavities which

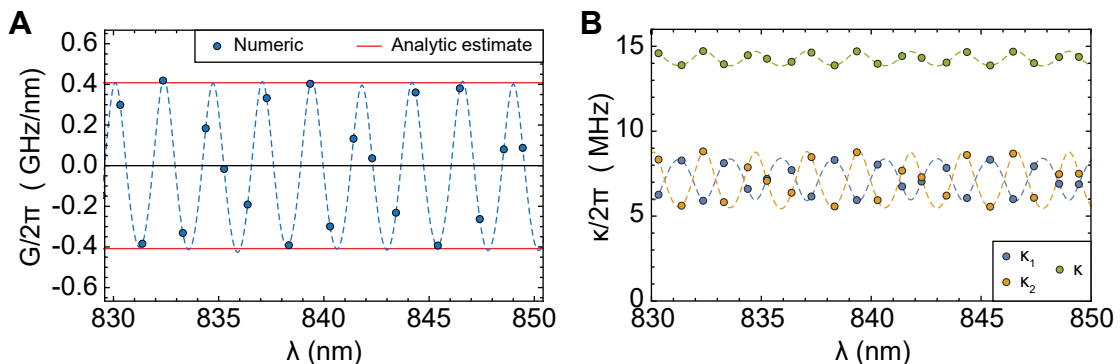


Figure 4.4: Theoretical optomechanical frequency pull factors and linewidths for the resonances of a MIM cavity with $l_c = 350 \mu\text{m}$, $\Delta l = 25 \mu\text{m}$, $\mathcal{F} = 3 \times 10^4$, membrane thickness $h = 20 \text{ nm}$. Dots correspond to numerically calculated cavity resonances, dashed lines are guides to the eye. A) Wavelength dependence of optomechanical frequency pull factor G . B) Blue and orange dots and lines show the wavelength dependence of external output coupling rates through the first and the second cavity mirrors, κ_1 and κ_2 , respectively. Green is the total cavity linewidth, $\kappa = \kappa_1 + \kappa_2$.

are necessary for the following discussion and the presentation of the experimental results. A comprehensive overview of MIM theory can be found elsewhere (e.g. see [254]). A MIM cavity, shown in Figure 4.3, consists of a thin silicon nitride membrane placed between two high-reflectivity mirrors so that the membrane motion along the cavity axis can modulate the optical resonance frequency. When referring to membrane displacement x we will mean the longitudinal displacement of the membrane center, if necessary averaged over transverse profile of the cavity waist [255, 254]. Membrane motion along the cavity axis modulates the frequencies of optical cavity modes, ω_c , in quasi-periodic fashion [84]; for small displacement the modulation is linear. The magnitude and the sign of the optomechanical frequency pull factor,

$$G = -\partial\omega_c/\partial x, \quad (4.5)$$

is sensitive to membrane displacements at the scale of optical wavelength. Even without precisely knowing the membrane position, however, it is possible to give a typical highest number for the expected optomechanical coupling rate,

$$|G| = 2r \frac{\omega_c}{l_c}, \quad (4.6)$$

where l_c is the total cavity length and r is the membrane reflectivity in terms of the field amplitude ($r = 0.2 - 0.5$ in our experiments). Deviations from the estimate given by Eq. (4.6) are only possible if the membrane reflectivity is close to one and the membrane is positioned close to one of the cavity ends [254, 256], which is not a regime relevant to the experiments in this thesis.

In Figure 4.4 we present the results of numerical calculations of resonance positions, optomechanical couplings and optical linewidths of a MIM cavity with parameters typical

for our experiments: cavity length $l_c = 350 \mu\text{m}$, membrane displacement from the cavity center $\Delta l = 25 \mu\text{m}$, empty cavity finesse $\mathcal{F} = 3 \times 10^4$ with both mirrors being equal, membrane thickness $h = 20 \text{ nm}$. This cavity geometry also corresponds to the one shown in Figure 4.5 of the experimental section. The theoretical mean free spectral range of such cavity is 1.08 nm. It can be seen from the figures that the optomechanical coupling rates and the optical linewidths follow a pattern which is periodic with wavelength. The discreteness of resonances, however, can make experimentally obtained coupling rates appear to vary irregularly with wavelength. In any case, for a cavity with fixed membrane position one can practically always identify a resonance with coupling rate close to the maximum value given by Eq. (4.6). The variation of optical linewidth with wavelength, shown in Figure 4.4B, is not particularly pronounced in this example where the membrane is close to the cavity center. Shifting the membrane close to one of the cavity sides would increase the magnitude of oscillatory patterns in Figure 4.4B, and can even make a cavity with identical mirrors substantially asymmetric in terms of decay rates through the two mirrors. The predicted variation of extrinsic coupling rates shown Figure 4.4B was not directly observed in our experiments, as small tilt misalignments of membrane usually added extra optical losses, and only selected optical resonances had linewidths close to those of an empty Fabry-Perot cavity (see further for the data).

In order to evaluate the performance of the membrane-in-the-middle scheme from the perspective of linear quantum optomechanics, we calculate the “critical” input power required to reach quantum cooperativity, C_q [19], equal to one and thus the radiation pressure shot noise dominated regime. This metric is directly relevant when measurements are limited by extrinsic classical noises. While optomechanical coupling is parametrically enhanced by the laser drive and can be made very large in state-of-the-art optomechanical systems, classical laser noises and extraneous thermal noises in the cavity are a common practical limitation. The attainability of the quantum regime of the linear optomechanical interaction requires the classical laser and cavity noises to be lower than shot noise at the critical power. Low critical power means lower level of classical noises relative to shot noise. For a resonance of a membrane-in-the-middle cavity which maximizes optomechanical coupling to the value prescribed by Eq. (4.6), the critical input power P_{crit} to reach $C_q = 1$ is found as

$$P_{\text{crit}} = \frac{\pi c}{32\hbar} \frac{\lambda_c}{\mathcal{F}^2} \frac{S_{FF}^{\text{th}}}{4r^2}. \quad (4.7)$$

Here c is the speed of light, λ_c is the optical resonance wavelength, and S_{FF}^{th} is the spectral density of thermal force noise acting on the selected mode of the membrane and evaluated on mechanical resonance.

Another convenient aspect of the critical power given by Eq. (4.7) is the fact that it does not directly depend on the cavity length, l_c . Given a choice of cavity mirrors, the separation at which they are installed does not affect P_{crit} . This is in contrast to many other common figures of merit, such as vacuum optomechanical coupling g_0 and single-photon cooperativity C_0 [19], both of which scale $\propto 1/l_c$, and are higher for shorter cavities. In a MIM system, this enhancement does not necessarily directly provide an

4.2 Thermal intermodulation noise in a membrane in the middle cavity

Design	l (mm)	h (nm)	$\Omega_m/(2\pi)$ (Hz)	Q	m_{eff} (ng)	$\sqrt{S_{FF}^{\text{eff}}}$ at 295 K (aN/ $\sqrt{\text{Hz}}$)
Soft-clamped (design from [150])	2.3	20	1.4×10^6	5.8×10^7	4.5	180
Soft-clamped (low m_{eff})	2.3	20	1.5×10^6	5.8×10^7	1.1	90
Trampoline [161]	3	80	41×10^3	$4.5 \cdot 10^7$	1	6

Table 4.1: Thermal force noises scaled by the membrane reflectivity for a few representative silicon nitride membrane designs at room temperature. The parameters of soft-clamped membranes are taken from our simulations, parameters for the trampoline membrane are experimental values from the cited reference. l is the membrane length, h is the thickness. The membrane reflectivity is assume to be $r = 0.21$ at 20 nm and $r = 0.57$ at 80 nm ([254]).

practical advantage, as for shorter cavities the transduction of thermal frequency fluctuations is also higher, and maintaining a given number of intracavity photons requires a higher input photon flux. The cavity length, although, does control the sideband resolution factor Ω_m/κ , and hence the efficiency of sideband amplification and cooling. All experiments in this chapter operate in the fast-cavity regime $\Omega_m/\kappa \ll 1$. Finally, we note for reference that to date the most successful experiments operated with MIM cavities with mm-scale lengths [20, 150].

A reduction of critical input power in MIM system can be accomplished by improving on its optical and mechanical components. On the optics side, changing the operational wavelength from near infrared (which is presently standard) to the blue part of the visible spectrum would improve P_{crit} only by little, and likely would be accompanied by tradeoffs like an increase in optical losses and absorption. The best optical finesse of Bragg mirrors, $\mathcal{F} \lesssim 10^6$ [257], seems to change little over the past two decades. Also, same as reducing the cavity length, improving the cavity finesse does not improve the ratio of mechanical signal to mirror noise, which is a major practical limitation. Towards the goal of reducing the mirror noise, crystalline coatings with low material dissipation are being developed [258].

A way to improve the parameters of MIM system which has not been exhausted so far is engineering a better membrane resonator, with modes that have higher Q and lower effective mass for a given reflectivity. The properties of membrane resonator in Eq. (4.7) are represented by the thermal noise spectral density and the membrane reflectivity. It is convenient to aggregate them into an “effective” force noise S_{FF}^{eff} , given by

$$S_{FF}^{\text{eff}} = \frac{S_{FF}^{\text{th}}}{4r^2} = \frac{2k_B T m_{\text{eff}} \Gamma_m}{4r^2}. \quad (4.8)$$

This can be seen as a result of re-defining the effective mass of mechanical mode to be consistent with a new coordinate, $y = 2rx$, which represents not the physical displacement but rather the change in the roundtrip optical path produced by it. For relatively thick membranes with thicknesses in the range of 50-100 nm $S_{FF}^{\text{eff}} \approx S_{FF}^{\text{th}}$, while for thin-

ner membranes S_{FF}^{eff} can be significantly larger than S_{FF}^{th} . In Table. 4.2.1, we present the calculations of effective thermal force noises for a few membrane geometries with parameters taken from the literature and from our work. Note that for the fundamental mode of trampoline membrane [161] the thermal noise level is particularly low because of its low frequency. The downside here, however, is that classical laser noises of solid-state lasers (like Ti:Sa) are also high at these frequencies. In contrast, laser noises can be practically negligible with no filtering at frequencies above 1 MHz, at which soft-clamped localized modes can be created in phononic crystal membranes. In Table. 4.2.1, we list the results of simulations for two phononic crystal membrane designs, the one reported by Rossi et. al. [150] and the one that was described in Sec. 2.5.4. These designs have localized modes with essentially identical frequencies and quality factors, but the effective mass of our design is four times lower. Note that in Ref. [150] $Q = 10^9$, was experimentally obtained, which is more than an order of magnitude higher than the value indicated in Table. 4.2.1. This discrepancy is due to the combination of temperature difference (intrinsic losses are lower at cryogenic temperature than at the room temperature that we assume), frequency difference (the Q of a soft-clamped mode is $\propto 1/\Omega_m^2$), and, possibly, difference in the material parameters compared to what we assumed in simulations.

The thermal noises presented in Table. 4.2.1 can be converted to the critical power needed to reach $C_q = 1$ with the help of the following formula,

$$P_{\text{crit}} = 0.24 (\mu\text{W}) \times \frac{\lambda_c}{850 (\text{nm})} \times \left(\frac{10^4}{\mathcal{F}} \times \frac{\sqrt{S_{FF}^{\text{eff}}} (\text{aN}/\sqrt{\text{Hz}})}{10 (\text{aN}/\sqrt{\text{Hz}})} \right)^2. \quad (4.9)$$

Using the state-of-the-art soft-clamped membranes listed in Table. 4.2.1 in combination with moderately high-finesse optical cavities ($\mathcal{F} = 3 \cdot 10^4$), $C_q = 1$ is predicted to be reachable with input powers below 10 μW . Both classical phase and amplitude noises of our Ti:Sa laser (Sirah Matisse) are below the shot noise for this power. The extrinsic thermal noise due to the cavity mirrors is more problematic, but it does not manifest if one detects the amplitude quadrature of the outcoupled light, which is, for example, required for the observation of ponderomotive squeezing. It can be concluded therefore that membrane-in-the-middle scheme is promising for quantum optomechanics even at room temperature. While pursuing this goal, we observed that the nonlinear transduction of thermal fluctuations of the membrane becomes a key practical limitation, this phenomenon will be explored in details in the remainder of this section.

4.2.2 Theory of thermal intermodulation noise

In this section we present the theory of thermal intermodulation noise with the assumption that the cavity frequency fluctuations are slow compared to the optical decay rate. We assume the classical regime and concentrate on the lowest-order, i.e. quadratic, nonlinearity of the cavity detuning transduction. We consider (as in our experimental setup, also as shown in Figure 4.3) an optical cavity with two ports, which is driven by a laser coupled to port one. The output from port two is directly detected on a

photodiode. In the classical regime, i.e. neglecting vacuum fluctuations, the complex amplitude of the intracavity optical field, a , and the output field $s_{\text{out},2}$ can be found from the input-output relations

$$\frac{da(t)}{dt} = \left(i\Delta(t) - \frac{\kappa}{2} \right) a(t) + \sqrt{\kappa_1} s_{\text{in},1}, \quad (4.10)$$

$$s_{\text{out},2}(t) = -\sqrt{\kappa_2} a(t), \quad (4.11)$$

where $s_{\text{in},1}$ is the constant coherent drive amplitude, $\Delta(t) = \omega_L - \omega_c(t)$ is the laser detuning from the cavity resonance, modulated by the cavity frequency noise, and $\kappa_{1,2}$ are the external coupling rates of ports one and two ($\kappa_1 = \kappa_2$ in our case) and $\kappa = \kappa_1 + \kappa_2$. In the fast cavity limit, when the optical field adiabatically follows $\Delta(t)$, the intracavity field is found as

$$a(t) = 2\sqrt{\frac{\eta_1}{\kappa}} L(\nu(t)) s_{\text{in},1}, \quad (4.12)$$

where we introduced for brevity the normalized detuning $\nu = 2\Delta/\kappa$, the cavity decay ratios $\eta_{1,2} = \kappa_{1,2}/\kappa$ and Lorentzian susceptibility

$$L(\nu) = \frac{1}{1 - i\nu}. \quad (4.13)$$

Expanding L in Eq. (4.12) over small detuning fluctuations $\delta\nu$ around the mean value ν_0 up to second order we find the intracavity field as

$$a = 2\sqrt{\frac{\eta_1}{\kappa}} L(\nu_0) (1 + iL(\nu_0)\delta\nu - L(\nu_0)^2\delta\nu^2) s_{\text{in},1}. \quad (4.14)$$

According to Eq. (4.14), the intracavity field is modulated by the cavity frequency excursion, $\delta\nu$, and the frequency excursions squared, $\delta\nu^2$. If $\delta\nu(t)$ is a stationary Gaussian noise process, like typical thermal noises, the linear and quadratic contributions are uncorrelated (despite clearly not being independent). This is due to the fact that odd-order correlations vanish for Gaussian noise,

$$\langle \delta\nu(t)^2 \delta\nu(t + \tau) \rangle = 0, \quad (4.15)$$

where $\langle \dots \rangle$ is the time average, for an arbitrary time delay τ . Next, we consider the photodetected signal, which, up to a conversion factor, equals the intensity of the output light and is found to be

$$I(t) = |s_{\text{out},2}(t)|^2 \propto |L(\nu_0)|^2 \left(1 - \frac{2\nu_0}{1 + \nu_0^2} \delta\nu(t) + \frac{3\nu_0^2 - 1}{(1 + \nu_0^2)^2} \delta\nu(t)^2 \right). \quad (4.16)$$

Notice that $\delta\nu(t)$ and $\delta\nu(t)^2$ can be distinguished by their detuning dependence. The linearly transduced fluctuations vanish on resonance ($\nu_0 = 0$), where $\partial L/\partial\nu = 0$. Similarly, when $\partial^2 L/\partial\nu^2 = 0$, the quadratic frequency fluctuations vanish, and thus also the thermal intermodulation noise. We refer to the corresponding detuning values,

$$\nu_0 = \pm 1/\sqrt{3}, \quad (4.17)$$

as “magic”. In the following experiments, we will make measurements at $\nu_0 = -1/\sqrt{3}$ and $\nu_0 = 0$ to independently characterize the spectra of $\delta\nu(t)$ and $\delta\nu(t)^2$, respectively.

The total spectrum¹ of the detected signal, $I(t)$, is an incoherent sum of the linear term given by,

$$S_{\nu\nu}[\omega] = \int_{-\infty}^{\infty} \langle \delta\nu(t)\delta\nu(t+\tau) \rangle e^{i\omega\tau} d\tau, \quad (4.18)$$

and the quadratic term, which for Gaussian noise can be found using Wick’s theorem [259]

$$\langle \delta\nu(t)^2 \delta\nu(t+\tau)^2 \rangle = \langle \delta\nu(t)^2 \rangle^2 + 2\langle \delta\nu(t)\delta\nu(t+\tau) \rangle^2, \quad (4.19)$$

as

$$S_{\nu\nu}^{(2)}[\omega] = \int_{-\infty}^{\infty} \langle \delta\nu(t)^2 \delta\nu(t+\tau)^2 \rangle e^{i\omega\tau} d\tau = 2\pi \langle \delta\nu^2 \rangle^2 \delta[\omega] + 2 \times \frac{1}{2\pi} \int_{-\infty}^{\infty} S_{\nu\nu}[\omega'] S_{\nu\nu}[\omega - \omega'] d\omega', \quad (4.20)$$

where $\delta[\omega]$ is the Dirac delta function.

In an optomechanical cavity, the dominant source of cavity frequency fluctuations is the Brownian motion of mechanical modes coupled to the cavity,

$$\delta\nu(t) = 2\frac{G}{\kappa}x(t), \quad (4.21)$$

where $G = -\partial\omega_c/\partial x$ is the linear optomechanical coupling constant, and x is the total resonator displacement, i.e. the sum of independent contributions x_n of different mechanical modes, averaged over the cavity mode waist (see more details in [44]). It is the finite cavity waist width that is the dominant factor preventing the coupling of high-frequency membrane modes to the cavity and thus proving a high-frequency cutoff for $\delta\nu(t)$. The spectrum of the Brownian frequency noise is then found to be

$$S_{\nu\nu}[\omega] = \left(\frac{2G}{\kappa}\right)^2 \sum_n S_{xx,n}[\omega], \quad (4.22)$$

where $S_{xx,n}[\omega]$ are the displacement spectra of individual mechanical modes (see [44] for explicit expressions). The thermomechanical frequency noise given by Eq. (4.22) produces TIN which contains peaks at sums and differences of mechanical resonance frequencies and a broadband background due to the off-resonant components of thermal noise, as illustrated in Figure 4.2B. The magnitude of the intermodulation noise is related to the quadratic spectrum of the total mechanical displacement, $S_{xx}^{(2)}$, as

$$S_{\nu\nu}^{(2)} = (2G/\kappa)^4 S_{xx}^{(2)}. \quad (4.23)$$

¹In this chapter, we use two-sided spectral densities, denoted as $S_{xx}[\omega]$, in theoretical derivations and one-sided spectral densities, denoted as $S_x[\omega] = 2S_{xx}[\omega]$ for $\omega > 0$, for the presentation of experimental data.

A reservation needs to be made: the theory presented above is only strictly applicable to an optomechanical cavity when the input power is sufficiently low, such that the driving of mechanical motion by radiation pressure fluctuations created by the intermodulation noise is negligible; otherwise the fluctuations of $x(t)$ and $\delta\nu(t)$ may deviate from purely Gaussian and correlations exist between $\delta\nu(t)$ and $\delta\nu(t)^2$. On a practical level, this reservation has minor significance for our experiment. Also, the presence of linear dynamical backaction of radiation pressure does not change the results of this section but does modify S_{xx} .

4.2.3 Quadratic transduction and quadratic coupling in MIM system

In this section we compare the magnitudes of nonlinear coupling and nonlinear transduction in membrane-in-the-middle cavity. It is helpful to clarify terminology first. One way to understand the operation of cavity-assisted measurements of oscillator position is the following. For an isolated cavity, an oscillator displacement x produces a shift of the resonance frequency $\Delta\omega_c$, which is linear or quadratic in x depending on the kind of function $\omega_c(x)$. When $\Delta\omega_c(x)$ is not linear in x , we speak about nonlinear coupling. In order for the cavity frequency shift $\Delta\omega_c$ to be measurable, the cavity needs to be coupled to a propagating field. When the cavity frequency excursion $\Delta\omega_c$ is small compared to the optical linewidth, it is typically transduced linearly to the modulation of propagating field (e.g., for the phase of light reflected off the cavity on resonance one has $\Delta\phi \sim \Delta\omega_c/\kappa \ll 1$). Whenever it happens that the linear transduction is zero, as when detecting the amplitude quadrature of light reflected on cavity resonance, or when the cavity frequency excursions are large compared to the linewidth, the propagating field is modulated non-linearly by the excursions of cavity frequency. In this case we speak about nonlinear transduction of cavity frequency fluctuations, or, more precisely, nonlinear transduction of laser-cavity detuning.

Nonlinear cavity transduction can produce signals quadratic in mechanic displacement which are orders of magnitude stronger than previously experimentally demonstrated quadratic coupling arising from $\partial^2\omega_c/\partial x^2$ terms [248]. Below we derive the classical dynamics of the optical field in an optomechanical cavity taking into account terms that are quadratic in displacement. We show that in a membrane-in-the-middle cavity, the quadratic signals originating from nonlinear transduction are $r\mathcal{F}$ larger than the signals due to the nonlinear optomechanical coupling, $\partial^2\omega_c/\partial x^2$.

The fluctuations of ν due to the mechanical displacement are given by

$$\delta\nu(t) \approx 2\frac{G}{\kappa}x(t) + \frac{G_2}{\kappa}x(t)^2, \quad (4.24)$$

where $G = -\partial\omega_c/\partial x$ and $G_2 = -\partial^2\omega_c/\partial x^2$ are the linear and quadratic optomechanical coupling, respectively, and the total displacement x consists of partial contributions of different modes x_n

$$x(t) = \sum_n x_n(t). \quad (4.25)$$

For a resonant laser probe we can find the intracavity field as

$$a(t) \approx 2\sqrt{\frac{\eta_1}{\kappa}}(1 - i\nu(t) - \nu(t)^2)s_{\text{in},1} = 2\sqrt{\frac{\eta_1}{\kappa}} \left(1 - 2i\frac{G}{\kappa}x(t) - \left(\left(2\frac{G}{\kappa}\right)^2 + i\frac{G_2}{\kappa} \right) x(t)^2 \right) s_{\text{in},1}. \quad (4.26)$$

It is instructive to compare the magnitudes of the two contributions to the prefactor of $x(t)^2$. The typical value for G (assuming the membrane is not very close to one of the mirrors) is

$$G \sim 2r\frac{\omega_c}{l_c}, \quad (4.27)$$

while the typical value for G_2 is [84]

$$G_2 \sim 4\frac{r\omega_c^2}{cl_c}, \quad (4.28)$$

where c is the speed of light, r is the membrane reflectivity and l_c is the cavity length. The ratio of the two contributions is evaluated as

$$\left(2\frac{G}{\kappa}\right)^2 \bigg/ \left(\frac{G_2}{\kappa}\right) \sim \mathcal{F}r. \quad (4.29)$$

As the cavity finesse \mathcal{F} is typically large, on the order of 10^3 to 10^5 , and the membrane reflectivity r is between 0.1 and 0.5, we conclude that linear optomechanical coupling needs to be extremely well suppressed in order for the quadratic coupling G_2 to be observable.

4.3 Experimental observation and characterization of TIN

4.3.1 Setup, cavity assembly and alignment

Experiments with a membrane in the middle systems begin with cavity assembly. In our case, the cavity is made by directly clamping a membrane chip between two supermirrors. All supermirrors used in our work have identical coatings: 29 Ta₂O₅/SiO₂ bilayers, with nominal transmission equal to 100 ppm at the reflectivity band center, 850 nm. The high-reflectivity mirror coatings were deposited by the company FiveNine Optics on superpolished quartz substrates. Each mirror also has an anti-reflection coating on the opposite side. We experimentally characterized finesse as high as 3.6×10^4 in a Fabry-Perot cavity made of two such mirrors without a membrane. The assembled cavity (shown in Figure 4.5A) is mounted vertically, mostly to facilitate membrane handling and its transverse alignment with respect to the cavity mode. We use a concave mirror with the radius of curvature equal 5 cm at the top and a flat mirror at the bottom of the cavity. The assembly is fixed by one top clamp (as shown in Figure 4.5B) and does

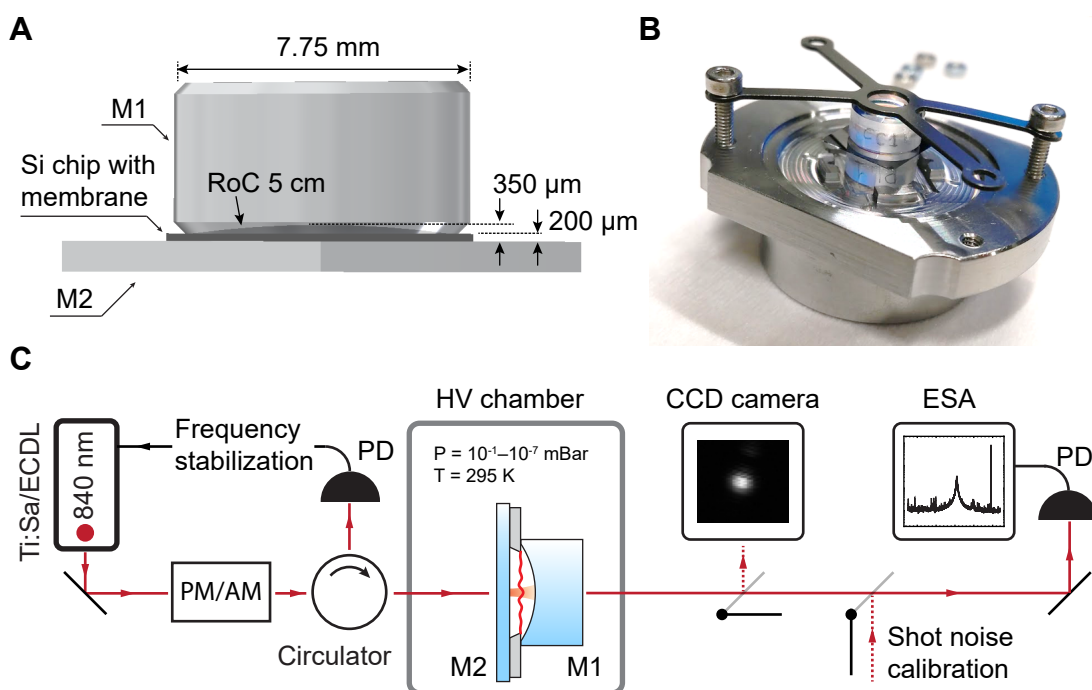


Figure 4.5: A) To-scale rendering of a membrane-in-the-middle cavity with a flat mirror chip as bottom mirror (M2). B) Photo of a clamped MIM assembly with a circular bottom mirror. In the photo two out of four clamping screws are not present, while normally all four are used. C) Experimental setup in which TIN is studied consisting of a membrane-in-the-middle opto-mechanical system. PD: photo diode. PM/AM: Phase/amplitude modulator. ESA: Electronic spectrum analyzer.

not use any glue. To verify mirror finesse or to measure the cavity frequency noise due to the thermal fluctuation in the mirrors (dominated by their Brownian motion), the cavity can be assembled with a spacer chip or by directly placing one mirror on top of another.

Even a small membrane tilt with respect to the cavity axis can lead to excess optical losses. The direction of optical axis in our cavities is defined by the flat bottom mirror (perpendicular to its surface), so it is important that the membrane is parallel to the mirror surface. In our assembly scheme, there is no deterministic control over tilt once the components are put together, and it relies on the surfaces of the mirror and the membrane chip to be clean. If necessary (which is usually the case), these surfaces are cleaned prior to the assembly using lint-free cleanroom q-tips and acetone or methanol as solvent. For cleaning the supermirrors, FirstContact polymer is another option. Cleaning the bottom part of the membrane chip is a tricky part and requires some manual dexterity, as the membrane can be easily broken at this stage. In our experience, over numerous cavity assemblies there were accidents that led to membrane breaking. After some of the accidents the residues of membranes could not be entirely removed from

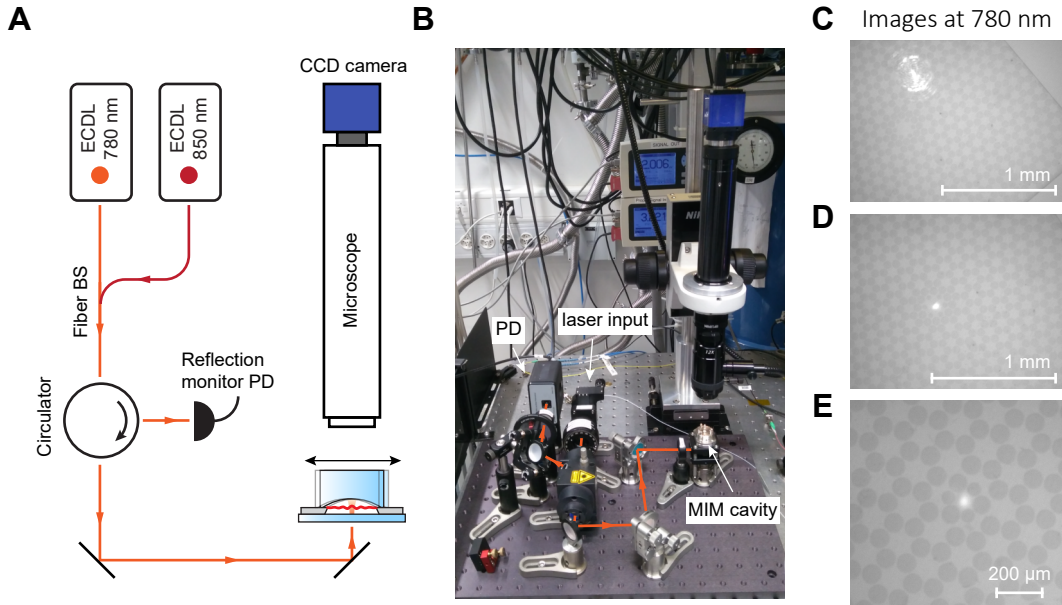


Figure 4.6: MIM transverse alignment setup. A) Optical layout. B) Photo of the actual setup. C-E show the microscope camera images when the cavity is illuminated from the bottom using a 780 nm tunable diode laser. C) A High-order optical mode which center is off the PnC membrane defect—this is a typical picture in the beginning of the alignment. D-E) TEM_{00} mode centered with the defects of PnC membranes.

the mirror surfaces. We did not observe, however, this leading to a degradation of the cavity finesse. Most likely this is because of the small size of the cavity mode waist, which means that even a small area of clean mirror surface is enough to maintain high finesse.

The total length of our cavity is around $350 \mu\text{m}$, and cavity beam waist for the TEM_{00} mode is about $35 \mu\text{m}$. While the nominal cavity length is well defined by the thickness of the chip and the radius of curvature of the top mirror, the lengths of practical assemblies showed some variation, which manifested as a variation of the mean free spectral range². This could be due to imperfect chip flatness and cleanliness of the surfaces.

The Rayleigh length of the cavity mode in our case is much longer than the cavity length. We did not observe excess optical losses due to the membrane not being positioned perfectly at the cavity waist (which coincides with the flat bottom mirror).

Despite all our precautions, the insertion of a membrane into the cavity resulted in excess loss for most of the optical resonances. Nevertheless, for some resonances, the optical quality factors were reduced by only 10%. A typical variation of optical loss with wavelength for a cavity with unpatterned membrane is shown in Figure 4.7.

Experiments with patterned membranes (trampolines and PnCs hosting soft-clamped

²The optical resonances in a MIM cavity are not equidistant, but their average separation is still well defined.

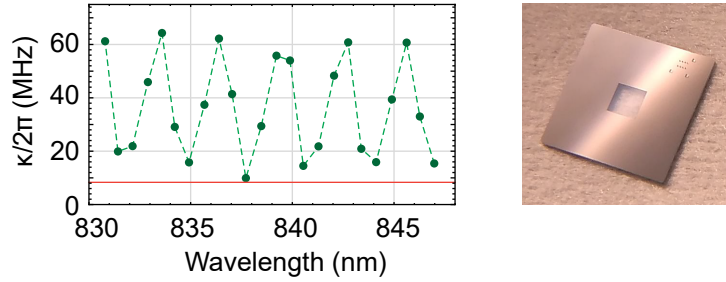


Figure 4.7: Optical linewidths of MIM cavity. Green points—measured linewidths of different optical resonances of MIM cavity with a $2\text{mm} \times 2\text{mm} \times 20\text{nm}$ unpatterned membrane, the dashed line is a guide to eye. Orange line—linewidth of an empty cavity with the same length.

modes) require precise transverse alignment of the cavity. The membrane center, which can be as small as $100 \mu\text{m}$ needs to coincide with the cavity waist. A difficulty in such alignment is that the position of the cavity mode is a priori unknown, as it is not marked by any visual references and depends on the mirror tilt (a small tilt of the top mirror shifts the cavity axis but does not lead to any optical losses). At the same time, inserting a patterned membrane in a Fabry-Perot cavity with $\mathcal{F} \sim 3 \times 10^4$ at a position not centered with the cavity axis easily introduces enough optical loss to prevent the observation of any optical resonances. Without observing resonances, there is no feedback for further adjustment of the membrane position. To circumvent this issue, we perform the transverse cavity alignment in a separate setup, shown in Figure 4.6. In this setup, the light of a 780 nm diode laser is coupled to the cavity and the membrane is imaged through the top mirror using a microscope. At 780 nm , the finesse of our cavity is below 100, so that even a severe misalignment of the membrane does not preclude the observation of optical modes. To make the membrane center and cavity axis coincide, the top mirror is moved by hand or using tweezers, while the assembly is gently clamped. The chip remains fixed in its place if the contact with the bottom mirror is good. Once the cavity mode is positioned, the top clamp is tightened stronger by iteratively and uniformly adjusting all four clamping screws. Here a balance should be maintained—too strong tightening can break the membrane chip, while a loose cavity is susceptible to acoustic vibrations and may preclude laser locking. After the cavity is aligned, high- Q optical resonances with low transverse order can be observed with 840 nm light coupled to the cavity. It was experimentally verified that the spatial location of the TEM_{00} cavity mode is the same at 780 nm and 840 nm , which is an expected outcome.

After the cavity is assembled and aligned, it is manually transferred with the holder (shown in Figure 4.5B) to the vacuum chamber of the main setup (shown in Figure 4.5C). While the main setup also has a camera for imaging the membrane and the optical mode, the resolution here is not sufficient for membrane alignment. The camera is mainly used to verify that a TEM_{00} mode is excited, and it can also facilitate the cavity coupling. Without using the camera and a flashlight to see the position of the excitation beam, coupling to a MIM cavity with a patterned membrane might be challenging, since high

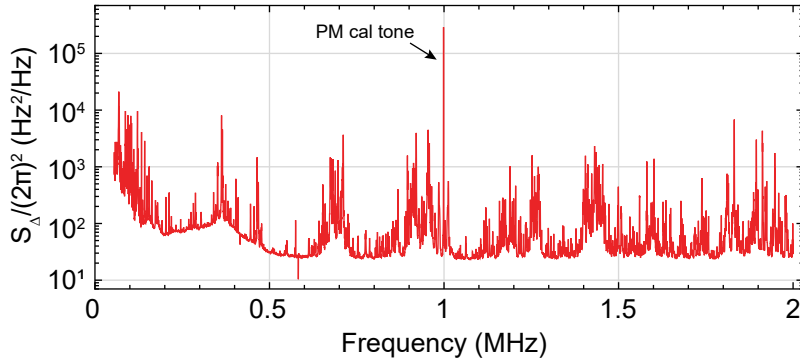


Figure 4.8: Spectrum of thermal detuning fluctuations due to the substrate noise, measured for a Fabry-Perot cavity without membrane.

order optical modes are too strongly damped to show up in transmission, and a low transverse order ($\sim 0 - 3$) mode needs to be found from the beginning.

The main experimental setup, as shown in Figure 4.5C, comprises a membrane-in-the-middle cavity, situated in a vacuum chamber at room temperature and probed using a Ti:Sa or a tunable external cavity diode laser. The laser wavelength is around 840 nm, close to the maximum reflectivity wavelength of the mirrors. A Ti:Sa laser was used in all the thermal noise measurements, whereas a diode laser was used for characterization of optical linewidths. The measurement signal was generated by direct detection of the light transmitted through the cavity on an avalanche photodiode. The reflected light, separated using a circulator, was used for Pound-Drever-Hall (PDH) locking of the Ti:Sa frequency. The one-sided spectra of signals were detected in transmission and calibrated either as relative intensity noise (RIN) or as effective cavity detuning fluctuations, S_{Δ} , with the help of calibration tones applied to the amplitude or phase quadratures of the laser, respectively. Optomechanical vacuum coupling rates, g_0 , were measured using frequency noise calibration as described in Ref. [224]. In order to calibrate the shot noise level in this scheme, we measure the power of signal beam first, and then direct a reference beam with the same power on the detection. Note that the mode imaging and shot noise calibration do not operate at the same time as measurements, the corresponding paths are engaged/disengaged with the help of flip mirrors.

In all noise measurements presented in the following, the classical intensity noise of the Ti:Sa laser was more than an order of magnitude below the resonant RIN of MIM cavities for frequencies above 100 kHz. The classical frequency noise of the laser is below $1 \text{ Hz}^2/\text{Hz}$ for frequencies above 100 kHz (see the supplementary information of [194] and [44]), which is at least an order of magnitude below the thermal detuning noise of an empty Fabry-Perot cavity (assembled using a silicon chip without a membrane as a spacer) as shown in Figure 4.8. Additionally, we did not observe any significant effect of the laser lock performance on the magnitude of TIN, which indicates that the nonlinear up-conversion of detuning noise from low frequencies (below 100 kHz), where the laser noise is largest, contributes negligibly to the TIN in our cavities.

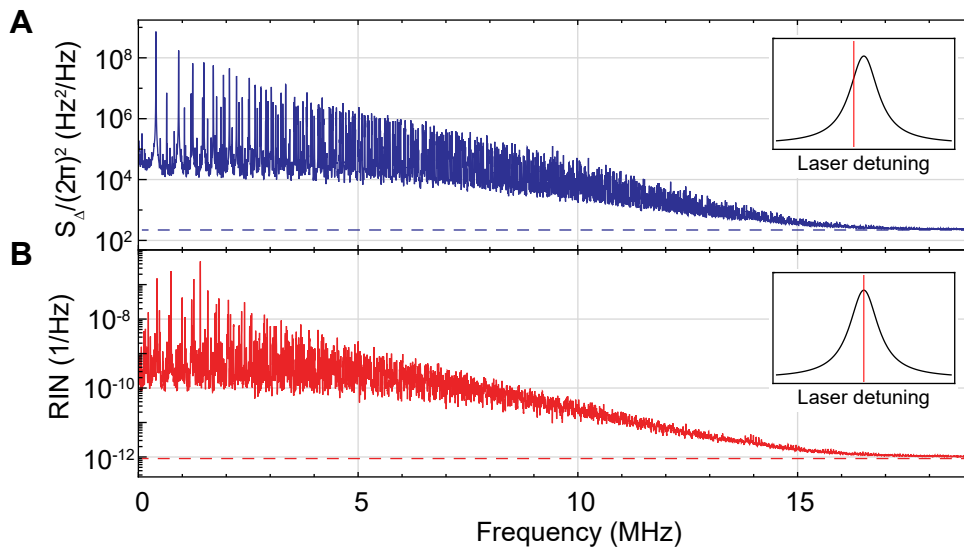


Figure 4.9: Spectra of resonant and off-resonant thermal noise in the transmitted signal. Solid lines represent experimental data, dashed lines—the estimated levels of shot noise. A) Detuning noise of a MIM cavity with a 1 mm square membrane, $\kappa/2\pi = 26.6$ MHz and $g_0/2\pi = 330$ Hz for the fundamental mode, measured at the laser detuning $2\Delta/\kappa \approx -1/\sqrt{3}$. B) Resonant RIN measured under the same conditions as in (A) but at $\Delta = 0$.

4.3.2 Square membranes

In this section, we characterize the TIN in cavities with 20 nm-thick uniform square membranes of different sizes. The optomechanical cooperativity was kept low in order to eliminate dynamical backaction of the light. For this purpose the residual pressure in the vacuum chamber was kept high, 0.22 ± 0.03 mBar, such that the quality factors of the fundamental modes of the membranes were limited by gas damping to $Q \sim 10^3$. The reflection signals of two resonances of a MIM cavity with a $2\text{mm} \times 2\text{mm}$ membrane are presented in Figure 4.11B. The resonances have similar optical linewidths (about 15 MHz) but their optomechanical coupling is different by a factor of ten. The resonance with high coupling ($g_0/2\pi = 150$ Hz) shows clear signatures of thermal noise. For this resonance the total r.m.s. thermal frequency fluctuations are expected to be around 2 MHz, which is still well below the cavity linewidth, $\kappa/2\pi = 16$ MHz.

Thermal fluctuations of the reflection signal are clearly observed in the right panel of Figure 4.11B even when the laser is resonant with the cavity. This is not expected in linear optomechanics, where the mechanical motion only modulates the phase of a resonant laser probe. Typical spectra of the detected noise are shown in Figure 4.9 for a cavity with a different, $1\text{mm} \times 1\text{mm}$, square membrane. With the laser detuned from the cavity resonance close to the “magic” detuning, $\nu_0 \approx -1/\sqrt{3}$, the transmission signal is dominated by the Brownian motion of membrane modes transduced by the cavity (shown in Figure 4.9A), in agreement with the prediction of linear optomechanics. The magnitude of thermomechanical noise is gradually reduced at high frequencies due to

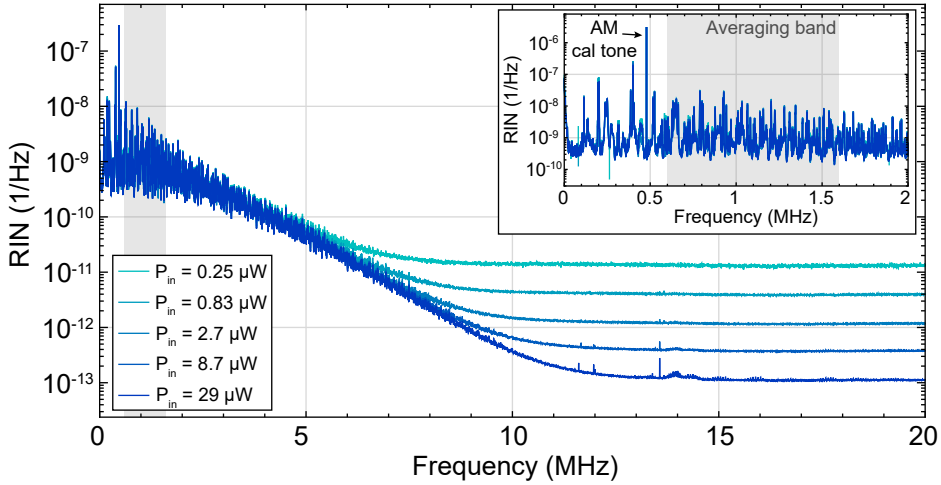


Figure 4.10: Spectra of resonant relative intensity noise for a 2 mm square unpatterned membrane (resonance wavelength 837.7 nm, $g_0/2\pi = 84$ Hz, $\kappa/2\pi = 9.9$ MHz) at different input powers. The inset shows the same plot zoomed in at low frequencies. The RIN levels plotted in Figure 4.11 are averaged over the frequency range shaded gray.

the averaging of membrane mode profiles [255, 254] over the cavity waist, until it meets shot noise at around 15 MHz. With the laser on resonance (Figure 4.9B), from linear optomechanics it is expected that the output signal is shot noise limited. However, the experimental signal contains a large amount of thermal noise—at an input power of $5 \mu\text{W}$ the classical RIN exceeds the shot noise level by about 25 dB at MHz frequencies. The spectrum of the resonant RIN is different from the spectrum of detuning fluctuations, owing to the nonlinear origin of the noise. At high frequency, the RIN level approaches shot noise, as verified by the optical power dependence presented in Figure 4.10.

An unambiguous proof of the intermodulation origin of the resonant intensity noise is obtained by examining the scaling of the noise level with G/κ . In thermal equilibrium, the spectral density of frequency fluctuations, $\delta\nu(t)$, created by a particular membrane is proportional to $(G/\kappa)^2$, and therefore the spectral density of intermodulation noise is expected to be proportional to $(G/\kappa)^4$. We confirm this scaling by measuring the resonant intensity noise for different optical resonances of a cavity with a $2\text{mm} \times 2\text{mm}$ membrane and present in Figure 4.11A the average noise magnitude as a function of g_0/κ , where g_0 is the optomechanical coupling of the fundamental mechanical mode. By performing a sweep of the input laser power on one of the resonances of the same cavity we show (see Figure 4.10) that the resonant intensity noise level is power-independent and therefore the noise is not related to radiation pressure effects.

The TIN observed in our experiments agrees well with our theoretical model. By calculating the spectrum of total membrane fluctuations according to Eq. (4.22) and applying the convolution formula from Eq. (4.20), we can accurately reproduce the observed noise. In Figure 4.12, we compare the measured detuning and intensity noise

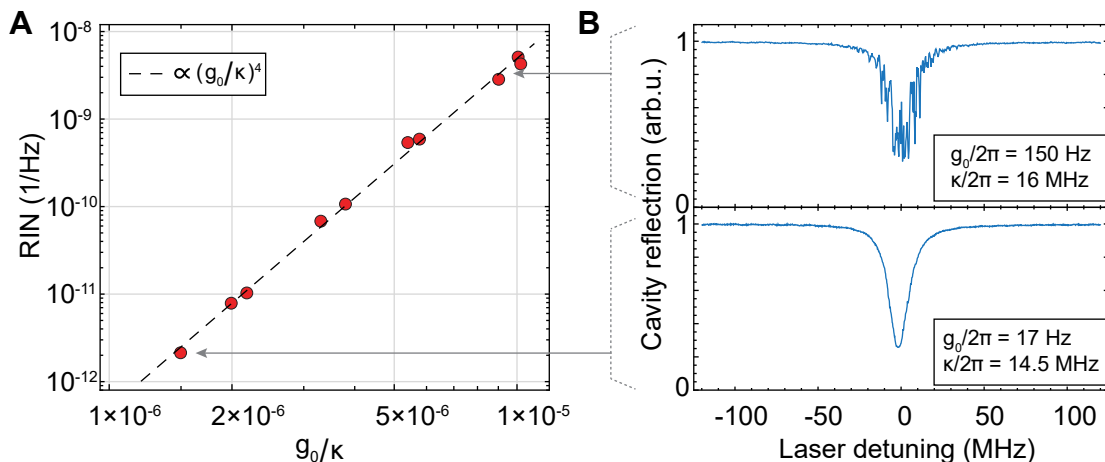


Figure 4.11: TIN measurements for a membrane-in-the-middle cavity with a 2 mm square membrane. A) Dependence of the average RIN in a 0.6 – 1.6 MHz band on g_0/κ . B) Cavity reflection signal as the laser is scanned over two resonances, with low (bottom) and high (top) optomechanical coupling.

spectra with the theoretical model. Here, we assume that the damping rates of all the membrane modes are identical, as the experiment is operated in the gas-damping-dominated regime. While this model is not detailed enough to reproduce all the noise features, it accurately reproduces the overall magnitude and the broadband envelope of the intermodulation noise observed in the experiment.

We would like to mention two potential confounding effects: *laser frequency noise* and *dissipative coupling*. The intensity noise of the laser was below 10^{-12} Hz^{-1} for frequencies above 100 kHz and therefore negligible in all resonant RIN measurements. In the same frequency range, the frequency noise of the laser is below $1 \text{ Hz}^2/\text{Hz}$, which is, again, much lower than the thermomechanical noise. As dissipative coupling leads to the modulation of optical linewidth by mechanical position, it could also potentially explain intensity noise in a resonant optical field. Although dissipative coupling is generally present in MIM cavities (see e.g. [254]), the magnitude of this noise is expected to be orders of magnitude below that measured in our experiments. Moreover, dissipative coupling cannot explain the observed scaling of resonant RIN ($\propto (G/\kappa)^4$) and the absence of correlation between the RIN level and the excess optical loss added by the membrane.

4.3.3 PnC membranes with soft-clamped modes

Localized soft-clamped defect modes in stressed phononic crystal (PnC) resonators can have quality factors in excess of 10^8 at room temperature due to enhanced dissipation dilution [36, 32]. Owing to their high Q and low effective mass, which result in low thermal force noise, $S_{FF}^{\text{th}} = 2k_B T m_{\text{eff}} \Gamma_m$, these modes are promising for quantum optomechanics experiments [150]. The phononic bandgap spectrally isolates soft-clamped

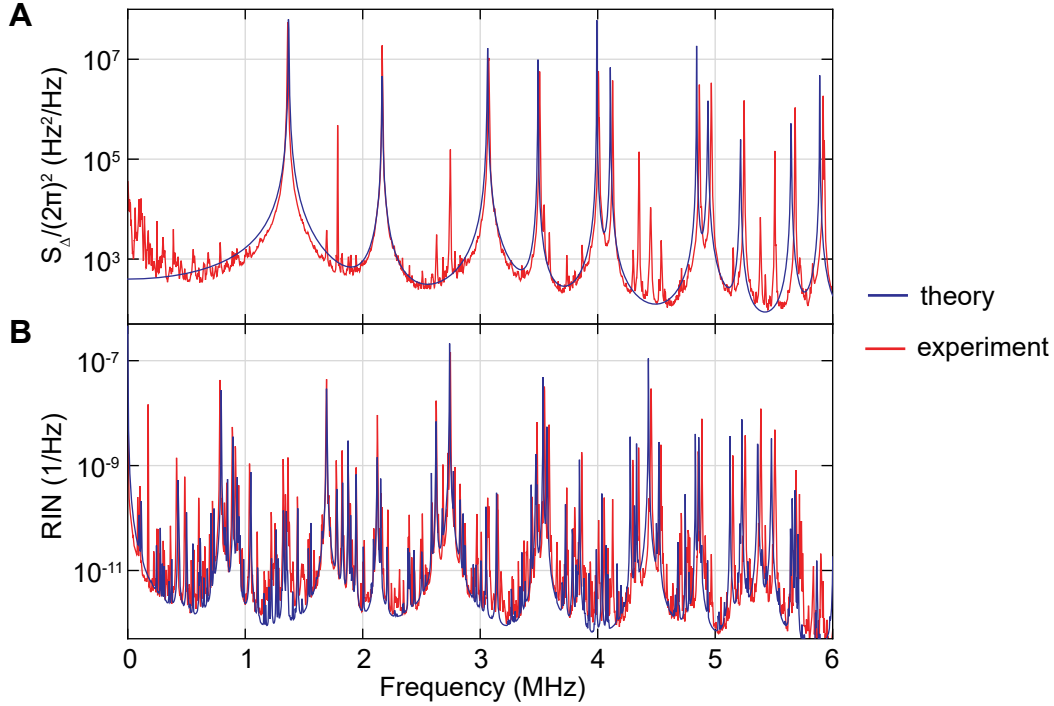


Figure 4.12: Comparison of theoretical and experimental frequency and resonant intensity noises. A) Detuning fluctuation and B) relative intensity noise spectra produced by the modes of a 20-nm thick, $0.3\text{mm} \times 0.3\text{mm}$, rectangular, Si_3N_4 membrane. Red shows experimental data and blue is the theoretical prediction.

modes from the thermomechanical noise created by the rest of the membrane spectrum. Nevertheless, when a PnC membrane is incorporated in a MIM cavity the entire multitude of membrane modes contributes to the TIN even within bandgap frequencies, as TIN is produced by a nonlinear process.

The measurements with PnC membrane presented in this section were made using the setup shown in Figure 4.5C, the vacuum pressure was kept below 5×10^{-7} mBar in order to eliminate gas damping. The insertion of a PnC membrane in a MIM cavity typically resulted in a somewhat larger excess optical loss than the insertion of a rectangular membrane. The excess optical loss was estimated to be 300 ppm per roundtrip for the cavity resonance in Figure 4.13, and 150 ppm for the resonance in Figure 4.14.

Figure 4.13 shows the spectrum of light transmitted through a resonance of membrane-in-the-middle cavity with $g_0/2\pi = 0.9$ kHz for the soft-clamped mode, $\kappa/2\pi = 34$ MHz and $C_0 = 2.5$. The noise at bandgap frequencies is dominated by TIN, which exceeds the shot noise by four orders of magnitude. The spectrum also shows a dispersive feature in the middle of the bandgap, which is a signature of classical correlations due to the intracavity TIN exciting the localized mechanical mode. The mechanical resonator in this case is a 2 mm square PnC membrane with the patterning described in Sec. 2.5.4, made

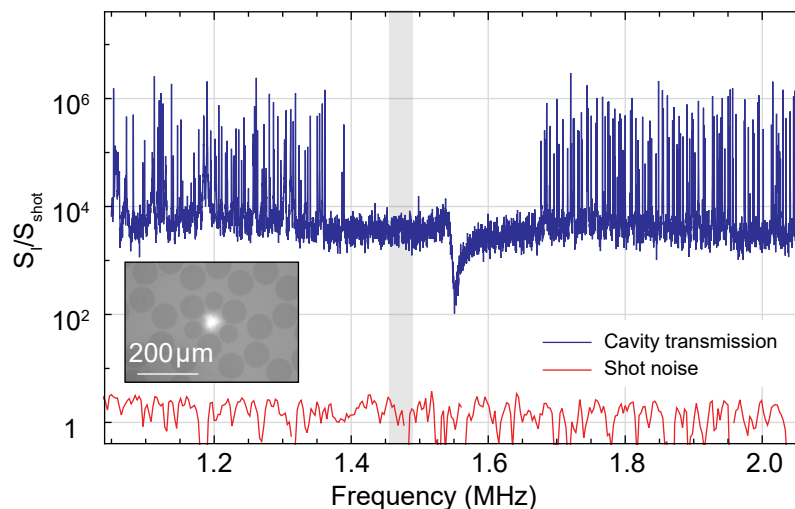


Figure 4.13: Measurement of the frequency spectrum of thermal optomechanical intermodulation noise with a phononic crystal membrane. Blue—photocurrent noise spectrum detected with the cavity-laser detuning set to $2\Delta/\kappa \approx -0.3$, red—shot noise level. The shaded region shows the noise averaging band for the plot in b. The inset shows an optical cavity mode (imaged at $\lambda \approx 780$ nm) overlapping with the PnC membrane defect.

of 40 nm-thick Si_3N_4 . The membrane has a single soft-clamped mode with $Q = 4.1 \times 10^7$ at 1.55 MHz, as characterized immediately before inserting the membrane in the cavity assembly. The input power in the measurement was $100 \mu\text{W}$ after correcting for spatial mode matching, which corresponds to a nominal $C_q \approx 1$. The shot noise level was calibrated in a separate measurement by directing an independent laser beam on the detector.

We next present in Figure 4.14 the dependence of the bandgap noise level on the laser detuning, measured on a different optical resonance of the same MIM cavity and at lower input power. In this measurement $g_0/2\pi = 360$ Hz for the localized mode, $\kappa/2\pi = 24.8$ MHz and the input power was $30 \mu\text{W}$. For performing the detuning sweep, the offset of the laser frequency from the cavity resonance was controlled by and inferred from the locking set point. For detunings greater than $2\Delta/\kappa \approx 0.5$, where the PDH error flips sign, side of the line locking was used instead of PDH. The bandgap noise was averaged over a 35 kHz band indicated in Figure 4.13. The measurement shows that the in-bandgap excess noise is dominated by TIN at all detunings except for the immediate vicinity of the “magic” detuning $\nu_0 = -1/\sqrt{3}$. Around $\nu_0 = -1/\sqrt{3}$ the excess noise is consistent with the substrate noise of an empty cavity. Figure 4.15 shows an overlap of the detuning fluctuations spectra taken for an empty cavity and a cavity with PnC membrane at magic detuning, which shows an almost perfect coincidence of the extraneous noise levels. The uncertainty of the empty cavity noise indicated in Figure 4.14 by a band comes from the fine structure of the noise peaks, which makes the exact level dependent on the selection of integration band.

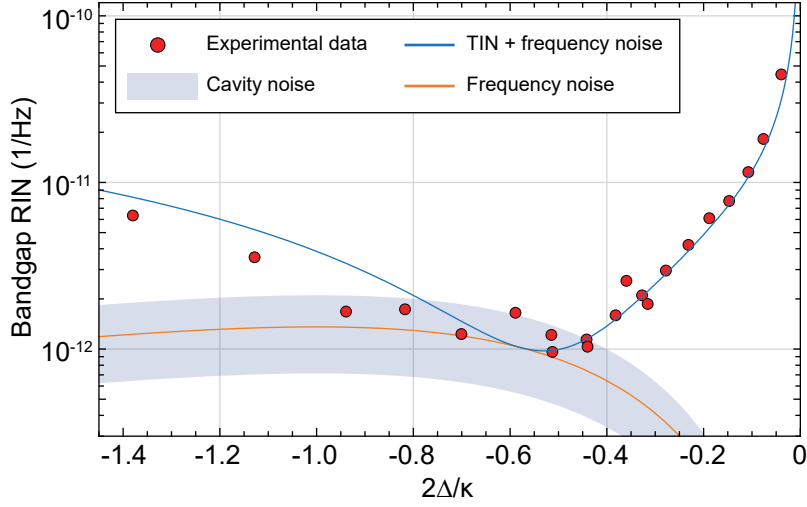


Figure 4.14: Measurement of the detuning dependence of thermal optomechanical intermodulation noise with a phononic crystal membrane. Variation of the relative intensity noise at bandgap frequencies with cavity-laser detuning. Red circles are experimental measurements, blue line—fit, orange line—cavity phase noise inferred from the fit, shaded blue region—independently calibrated cavity noise, with uncertainty from the selection of the averaging band.

The total noise level in Figure 4.14 is well fitted by our model that includes both $S_{\nu\nu}$ and $S_{\nu\nu}^{(2)}$ contributions to the detected signal and accounts for the radiation pressure cooling (full details of the model are given in Ref. [44]).

Finally, we notice that the intensity of the detected light in our measurement is proportional to the intensity of the intracavity field. Therefore, the suppression of TIN at magic detuning necessarily implies the suppression of the corresponding radiation pressure noise, which can lead to classical heating of the mechanical oscillator and thereby limit the true quantum cooperativity.

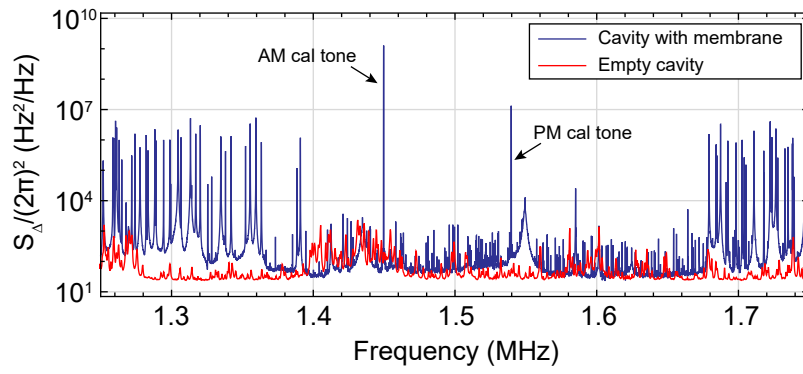


Figure 4.15: Substrate noise overlapped with a trace from detuning sweep presented in Figure 4.14 corresponding to $2\Delta/\kappa = -0.51$.

Summary and outlook

To conclude, we covered several efforts, experimental and theoretical, united by the common goal of observing the quantum behavior of low-frequency macroscopic mechanical oscillators at high temperatures ($kT/(\hbar\Omega_m) \gg 1$). Such oscillators are naturally very classical objects, in part because their thermal environments usually set a high minimum rate of decoherence for quantum states, and in part because the oscillator dynamics in the quantum and classical cases can be very similar. Unlike electromagnetically trapped ions or optically levitated nanoparticles, modes of solid-state mechanical resonators cannot be completely decoupled from their thermal bath because a part of the bath is made by other internal degrees of freedom within the resonator itself. The strain-mediated coupling of acoustic modes to internal degrees of freedom leads to intrinsic mechanical losses, minimizing which is a key step towards controlling these modes in the quantum regime.

Leveraging the reduction of intrinsic dissipation in the presence of static stress, known as dissipation dilution, was instrumental to the advancements recently made in quantum experiments with mechanical microresonators. While the basic limitations of this technique were understood early on (a decade ago, since the idea is relatively young), only within the last couple of years new insights allowed to access its full potential. Engineering dissipation dilution in resonators under given constraints seems far from being exhausted and may lead to new breakthroughs. It is surprising to an extent, that while the structural mechanics of thin films has been studied for more than a hundred years, acoustic vibrations of stressed patterned plates, and, in particular, their dissipation properties attracted little attention till now. It is well possible that ideas from new fields like topology, metamaterials, and kirigami can enable low-loss mechanical resonators with unprecedented properties.

Measurements operate in the quantum regime only when all non-fundamental sources of error are carefully eliminated. In principle, mechanical decoherence even at a high temperature can be counteracted by performing measurements faster than the decoherence rate. In practice, however, the absolute resolution required to reach this regime can be so high that even a small experimental imperfection will readily lead to a prohibitively large classical error. In our experiments with integrated near-field coupled

optomechanical cavities, the measurement rate remained significantly below the mechanical decoherence rate limited by the onset of thermal intracavity noises and the low finesse of the optical cavity. Incorporating record-high Q nanobeam resonators in the near-field scheme would bridge the gap, but the fabrication challenges on this route have still not been overcome.

In our membrane-in-the-middle experiment, the parameter range is more promising for reaching the quantum regime of oscillator measurements even at room temperature. However, we found that the deviation of the interferometric measurement scheme from purely linear is a significant source of classical error, in addition to the thermal noise of the cavity mirrors. The ability to perform nonlinear measurements can be highly desirable, as in principle can be used to create non-Gaussian states, which preparation for sub-GHz frequency mechanical oscillators remains an enticing but elusive goal. In our experiments, however, the transduction nonlinearity of interferometric measurements was a key challenge. Avoiding thermal intermodulation, either by selectively coupling to only one mechanical oscillator or by devising measurement schemes which would be free of second-order nonlinearity, will be important for future quantum measurement experiments. Our results showed that thermal intermodulation noise, although complex, is predictable and can be reliably modeled.

Appendices

A.1 Elastic energy and dissipation in a geometrically non-linear body

In this appendix, we present some details that were skipped in the main text and introduce the elastic energy and the intrinsic dissipation in the presence of geometrically nonlinear strain. Geometrically nonlinear deformations are treated in the framework of the theory of large deformation. Although the usage of this theory might appear to be at odds with the end goal, which is to understand the properties of acoustic modes with infinitesimally small amplitudes, it is justified by the fact that the total deformations (static plus dynamic) in our problem are finite.

We follow the notation of Ref. [94] and describe the deformation as a time-dependent mapping between the material coordinates X^a and the spatial coordinates $x^i(X^a, t)$. We always choose the spatial frame to be Cartesian, while the material coordinate system can be curvilinear as a consequence of the deformations, which explains the need to differentiate between lower and upper indices of tensors. We denote indices in different frames by letters from different parts of the Latin alphabet— $a, b, c\dots$ correspond to indices in the material frame and $i, j, k\dots$ correspond to indices in the spatial frame. Transformations of the components of tensors between the frames is done using the distortion tensor,

$$x_a^i \equiv \frac{\partial x^i}{\partial X^a}, \quad (\text{A.1})$$

and its inverse,

$$X_i^a \equiv \frac{\partial X^a}{\partial x^i}. \quad (\text{A.2})$$

The metric tensor in the material frame is denoted as g_{ab} . By definition, the strain ϵ_{ab} is the deviation of the metric in the material frame from the Kronecker tensor,

$$\epsilon_{ab} \equiv \frac{1}{2}(g_{ab} - \delta_{ab}). \quad (\text{A.3})$$

Given our choice of the spatial frame, the metric tensor here is constant and equal to the Kronecker tensor, $g_{ij} = \delta_{ij}$.

Forces acting inside a continuous body (which is not assumed to be elastic at this stage) are described by a symmetric stress tensor σ^{ij} . The force df^i acting on a small surface element is given by

$$df^i = \sigma^{ij} ds_j. \quad (\text{A.4})$$

The surface element here is characterized by the vector ds_j , which length is equal to the area and direction is perpendicular to the surface, and summation over repeated indices is assumed. The force acting on a unit element of volume is found using the divergence theorem as

$$f^i = \frac{\partial \sigma^{ij}}{\partial x^j}. \quad (\text{A.5})$$

This expression for the divergence uses the fact that the spatial frame is Cartesian.

The work $\delta\mathcal{W}$ performed by intrinsic forces on the entire body per an interval of time dt is found as

$$\frac{\delta\mathcal{W}}{dt} = - \int f^i v_i dV, \quad (\text{A.6})$$

where $v_i = \partial x_i / \partial t$ is the speed of motion of the material elements and $\int \dots dV$ denotes the integration over the body volume in the spatial frame. Integrating by parts and using the symmetry of the stress tensor, we find

$$\frac{\delta\mathcal{W}}{dt} = \int \sigma^{ij} \frac{\partial v_i}{\partial x_j} dV = \int \sigma^{ij} \mathcal{V}_{ij} dV, \quad (\text{A.7})$$

where \mathcal{V}_{ij} is the rate of strain change tensor,

$$\mathcal{V}_{ij} = \frac{1}{2} \left(\frac{\partial v_i}{\partial x^j} + \frac{\partial v_j}{\partial x^i} \right). \quad (\text{A.8})$$

In the material frame, the rate of strain change is simply given by

$$\mathcal{V}_{ab} = \frac{\partial}{\partial t} \epsilon_{ab}, \quad (\text{A.9})$$

whereas in the spatial frame $\mathcal{V}_{ij} \neq \frac{\partial}{\partial t} \epsilon_{ij}$ and Eq. (A.8) should be used directly instead.

In the process of deformation, intrinsic body forces perform work. This work either dissipates externally supplied¹ energy or stores it as elastic energy of deformations inside the material. Since the work is related to the rate of strain change, which has a simple expression in the material frame, it is convenient to use this frame to derive expressions for the stored and dissipated energies. When energy is dissipated by body forces, their work is always negative, and the dissipation power is given by

$$P^{(\text{diss})} = - \frac{\delta\mathcal{W}}{dt} = - \int \sigma^{ab} \frac{\partial}{\partial t} \epsilon_{ab} dV. \quad (\text{A.10})$$

This justifies the way intrinsic dissipation was introduced in Sec. 2.3.4. When the body forces are conservative, one can introduce elastic energy, $W^{(\text{el})}$. It is convenient to do so by considering deformation in the quasi-static limit, when the kinetic energy is negligible, so that all the work is done at the expense of elastic energy change,

$$\frac{dW^{(\text{el})}}{dt} = \int \sigma^{ab} \frac{\partial}{\partial t} \epsilon_{ab} dV. \quad (\text{A.11})$$

In order to advance further, we need to make an assumption regarding the dependence of internal stresses on strains (i.e. to introduce constitutive relations). If the material is physically linear [94], the stress is related to the strain as

$$\sigma^{ab} = \frac{\rho_0}{\rho} C^{abcd} \epsilon_{cd}, \quad (\text{A.12})$$

¹Or converted from another form of energy.

where C^{abcd} are material constants, which may experience spatial variation inside the body but do not depend on strain, and ρ_0/ρ is the ratio of densities of the undeformed and deformed bodies. The elastic energy of a physically linear elastic material is given by

$$W^{(\text{el})} = \frac{1}{2} \int C^{abcd} \epsilon_{ab} \epsilon_{cd} d\mathring{V} = \frac{1}{2} \int \sigma^{ab} \epsilon_{ab} d\mathring{V}, \quad (\text{A.13})$$

where we introduced the element of undeformed body volume, $d\mathring{V} = \rho_0 dV/\rho$. In Eq. (A.13) the juggling of indices is done using the metric in the undeformed state, \mathring{g}_{ab} .

In the main text, we do not distinguish between the deformed and the undeformed body volumes and put $d\mathring{V} \approx dV$, which is justified as long as the total deformations are small ($\epsilon_{ab} \ll 1$). The same applies to the volume integral in the expression for the dissipated power in Eq. (A.10).

The equations governing the dynamics of acoustic vibrations can be found from the variation of action [94]. The first step in this procedure is expressing the Lagrangian function

$$\mathcal{L} = W^{(\text{kin})} - W^{(\text{el})}, \quad (\text{A.14})$$

in terms of acoustic deformations and their spatial and temporal derivatives. Here the kinetic energy $W^{(\text{kin})}$ is given by

$$W^{(\text{kin})} = \int \frac{\rho v^i v_i}{2} dV. \quad (\text{A.15})$$

We are interested in infinitesimal dynamical deformations on top of finite static deformations, so that the overall deformation field is given by

$$x^i(X^a, t) = \bar{x}^i(X^a) + u^i(X^a, t). \quad (\text{A.16})$$

The time-dependent field $u^i(X^a, t)$ describes acoustic vibrations,

$$u^i(X^a, t) = U^i(X^a) e^{-\Omega t} + \text{c.c.} \quad (\text{A.17})$$

A similar decomposition into the static and dynamic parts applies to the stress and strain,

$$\epsilon_{ab}(X^a, t) = \bar{\epsilon}_{ab}(X^a) + \Delta\epsilon_{ab}(X^a, t), \quad (\text{A.18})$$

$$\sigma_{ab}(X^a, t) = \bar{\sigma}_{ab}(X^a) + \Delta\sigma_{ab}(X^a, t). \quad (\text{A.19})$$

The elastic energy, referred to a unit volume of the undeformed body, is given by

$$w = \frac{1}{2} \bar{\sigma}^{ab} \bar{\epsilon}_{ab} + \bar{\sigma}^{ab} \Delta\epsilon_{ab} + \frac{1}{2} \Delta\sigma^{ab} \Delta\epsilon_{ab}, \quad (\text{A.20})$$

which was obtained using the identity $\bar{\epsilon}^{ab} \Delta\sigma_{ab} = \bar{\sigma}^{ab} \Delta\epsilon_{ab}$. Both parts of the dynamic energy, the one proportional to $\bar{\sigma}^{ab} \Delta\epsilon_{ab}$ and the one proportional to $\Delta\sigma^{ab} \Delta\epsilon_{ab}$, contribute to the quadratic potential for vibrational modes. Overall, the Lagrangian function is given by

$$\mathcal{L} = \int \left(\frac{1}{2} \rho_0 v^a v_a - \bar{\sigma}^{ab} \Delta\epsilon_{ab} - \frac{1}{2} \Delta\sigma^{ab} \Delta\epsilon_{ab} \right) d\mathring{V}, \quad (\text{A.21})$$

where $d\overset{\circ}{V}$ is the integration in the undeformed material frame and ρ_0 is the local density in the absence of deformations.

To derive the elastodynamics equations in the main text we used the Lagrangian given by Eq. (A.21) and assumed that the metric tensor is unity, $g_{ab} = \delta_{ab}$, which ultimately made it unnecessary to distinguish between the upper and lower indices. For the elastic energy terms, this does not correspond to any approximation as their indices are moved by the metric of the undeformed state we are free to set $\overset{\circ}{g}_{ab} = \delta_{ab}$ by choosing the undeformed material frame to coincide with the spatial Cartesian frame. For the kinetic energy term, setting $g_{ab} \approx \delta_{ab}$ can introduce a relative error of the order of $\bar{\epsilon}_{ab}$, which is negligible for small static strains ($\bar{\epsilon}_{ab} \ll 1$).

The transformation of the rate of strain change from the material to the spatial frame. From the definition of the strain and the strain change rate tensors it follows that,

$$\mathcal{V}_{ab} = \frac{\partial}{\partial t} \epsilon_{ab} = \frac{1}{2} g_{ij} \left(x_a^i \frac{\partial x_b^j}{\partial t} + x_b^j \frac{\partial x_a^i}{\partial t} \right). \quad (\text{A.22})$$

Using the fact that in the Cartesian spatial frame $g_{ij} = \delta_{ij}$ and also that,

$$\frac{\partial}{\partial t} x_a^i = \frac{\partial v^i}{\partial X^a} = x_a^k \frac{\partial v^i}{\partial x^k}, \quad (\text{A.23})$$

we find

$$\mathcal{V}_{ab} = \frac{1}{2} x_a^i x_b^k \left(\frac{\partial v_i}{\partial x^k} + \frac{\partial v_k}{\partial x_i} \right), \quad (\text{A.24})$$

and finally,

$$V_{ij} = X_i^a X_j^b \mathcal{V}_{ab} = \frac{1}{2} \left(\frac{\partial v_i}{\partial x^j} + \frac{\partial v_j}{\partial x_i} \right). \quad (\text{A.25})$$

A.2 FEM simulation of dissipation dilution in patterned membranes

For practical simulations of dissipation dilution of flexural modes in patterned membranes we use pre-stressed frequency domain analysis in COMSOL shell interface. Shell simulations are substantially more time-efficient than simulations in full three dimensions. Moreover, we observed that the results of three dimensional analysis were not always reliable for structures with extreme aspect ratios. Dilution factors obtained from numeric simulations of uniform beams with rectangular cross-section with $l/h \gtrsim 5 \times 10^3$ deviated from analytical values by up to 20%. Shell simulations did not show such discrepancy for all aspect ratios considered in our work. The simulation procedure outlined below was developed and benchmarked in collaboration with Alberto Beccari.

The pre-stressed analysis consists of two simulation stages. During the first stage, the original homogeneous distribution of static stress (or strain) in the material is “relaxed” to a new equilibrium configuration that satisfies the boundary conditions on the free edges. This may be physically interpreted as simulating the suspension of a pre-stressed film. During the second stage, the eigenfrequencies and mode shapes are computed. The option “include geometric nonlinearity” must be on during this step to include tension energy. In order to obtain reliable deformation profiles around clamped boundaries, the narrow region close to the boundary needs to be densely meshed at the scale below $\lambda l = h\sqrt{E/(12\bar{\sigma})}$. In our case this was accomplished using swept meshing. After the solution is found, dissipation dilution factors are calculated based on the two-dimensional formulas from Sec. 2.4.1 as

$$D_Q = \rho\Omega^2/k^{(\text{lin})}. \quad (\text{A.26})$$

We use the kinetic energy to find the total spring constant (as described in Sec. 2.3.6), which simplifies the procedure as it does not require cross-coupling of the static and dynamic solutions. We also tried computing the nonlinear dilution energy directly from its definition (Eq. (2.90) in Sec. 2.3.6), and verified that this approach gives the same result.

For consistency, we calculate dissipation dilution using explicit formulas for the energies that use only on the deformation profiles and eigenfrequencies of the modes. This approach avoids relying on complex functionality of the simulation software, which is heavily version-dependent and was not always backward-compatible in our experience. We define the bending energy and kinetic energies as integral boundary probes under the component-level definition node, so that these quantities are computed with the model. Quality factors are computed as derived values in post-processing (under the “results” node).

Below we reproduce expression that can be directly copy-pasted to COMSOL. The bending energy (`bend_energy`) is given by:

```
shell.E*h_mbr^3*((dtang(dtang(w,x),x)+dtang(dtang(w,y),y))^2+
2*(1-shell.nu)*(dtang(dtang(w,x),y))^2-
```

```
dtang(dtang(w,x),x)*dtang(dtang(w,y),y))/(12*(1-shell.nu^2))
```

Note that the Gaussian curvature term (the last two lines in the expression above) must be retained unless all edges of the membrane are clamped. The kinetic energy (`kin_energy`) is given by:

```
h_mbr*shell.rho*shell.omega^2*shell.disp^2
```

and the quality factors are found as:

```
Qint*kin_energy/bend_energy
```

The expressions above use standard built-in symbols, including the Young's modulus `shell.E` and the Poisson's ratio `shell.nu`, and also two user-defined parameters, the membrane thickness `h_mbr` and the intrinsic quality factor of the film `Qint`.

Finally, we comment on an alternative way to calculate quality factors, which is implemented by adding an imaginary component to the Young's modulus and substituting in the material properties $E \rightarrow E(1 - i\phi)$, where $\phi = 1/Q_{\text{int}}$ is the loss angle of the film. Vibrational eigenfrequencies found in this case by the FEM solver are complex, and the ratios of their real and imaginary parts can be expected to directly give diluted quality factors. While this simple procedure works in some cases, it can also fail to give the right result. This is not entirely surprising, as finding the eigenmodes of a medium with complex Young's modulus is not always straightforward to physically justify, and in any case, this needs to be done with great care. Overall we find introducing complex Young's modulus to be a less reliable approach than the perturbative way of computing quality factors outlined above.

A.3 Buckling of thin-film structures

A thin-film mechanical resonator can have high dissipation dilution only as long as it remains planar. Any buckling effects, which are quite common in structures made of suspended thin films, need to be avoided. We could identify two different static buckling mechanisms that affected the devices employed in our works. The first one is related to compressive stress, and the second one, as we conjecture, to the transverse inhomogeneity of the film.

The stress distribution of a suspended patterned film can have regions where the local stress is compressive in some directions even if the film was uniformly biaxially tensioned prior to suspension. The two-dimensional static stress tensor $\bar{\sigma}_{ij}$, which describes the equilibrium stress in the film, can be diagonalized at any spatial point by an appropriate rotation of the coordinate axes,

$$\bar{\sigma}_{ij} = \begin{bmatrix} \sigma_{p1} & 0 \\ 0 & \sigma_{p2} \end{bmatrix}, \quad (\text{A.27})$$

where $i, j = x, y$ and σ_{p1} and σ_{p2} are the two principal stresses. A direction in which the stress is compressive exists if one of the principal stresses is less than zero.

In an infinitely thin membrane, a locally compressive principal stress results in exponential growth of the amplitudes of acoustic modes propagating in this direction. This leads to static buckling instability, i.e. a situation where a non-planar configuration of the membrane is energetically favorable. In membranes with finite thicknesses, instabilities occur only when threshold compressive stress is exceeded, the value of which depends on the thickness. In our work, we did not observe buckling of silicon nitride films thicker than 50 nm for any of the resonator designs that were explored. In contrast, for some of the 20 nm-thick devices buckling was a major issue.

One example of static buckling that we faced is shown in Figure A.1A. The picture shows the area around one of the clamping points of a 20 nm-thick steering wheel trampoline membrane, similar to the ones described in Sec. 2.6.3. On the segment enclosed by the yellow dash-dotted circle there is a stripe pattern, which is the result of buckling instability triggered by compressive stress in the direction perpendicular to the segment. The fact that this segment does have significant compressive stress (down to -30 MPa) is evident from the FEM simulation presented in Figure A.1B. This situation can be avoided if the widths of the resonator segments are adjusted so that the junctions do not displace upon film suspension, which is the same as fulfilling the “stress preservation” condition discussed in Sec. 2.6.1. Note that the simulation in Figure A.1B also predicts other regions of compressive principal stress, where, apparently, it is not high enough to trigger instabilities. These regions can be eliminated by tapering membrane segments as shown in Figure A.1E.

Buckling due to transverse compressive stress, according to our understanding, also limited the aspect ratios of unit cells in the tapered PnC beams described in Sec. 2.5.2. Figure A.1C shows a dark-field microscope image of a 20 nm-thick silicon nitride PnC beam where the unit cell buckling manifests as a blurring of the wide segment edges,

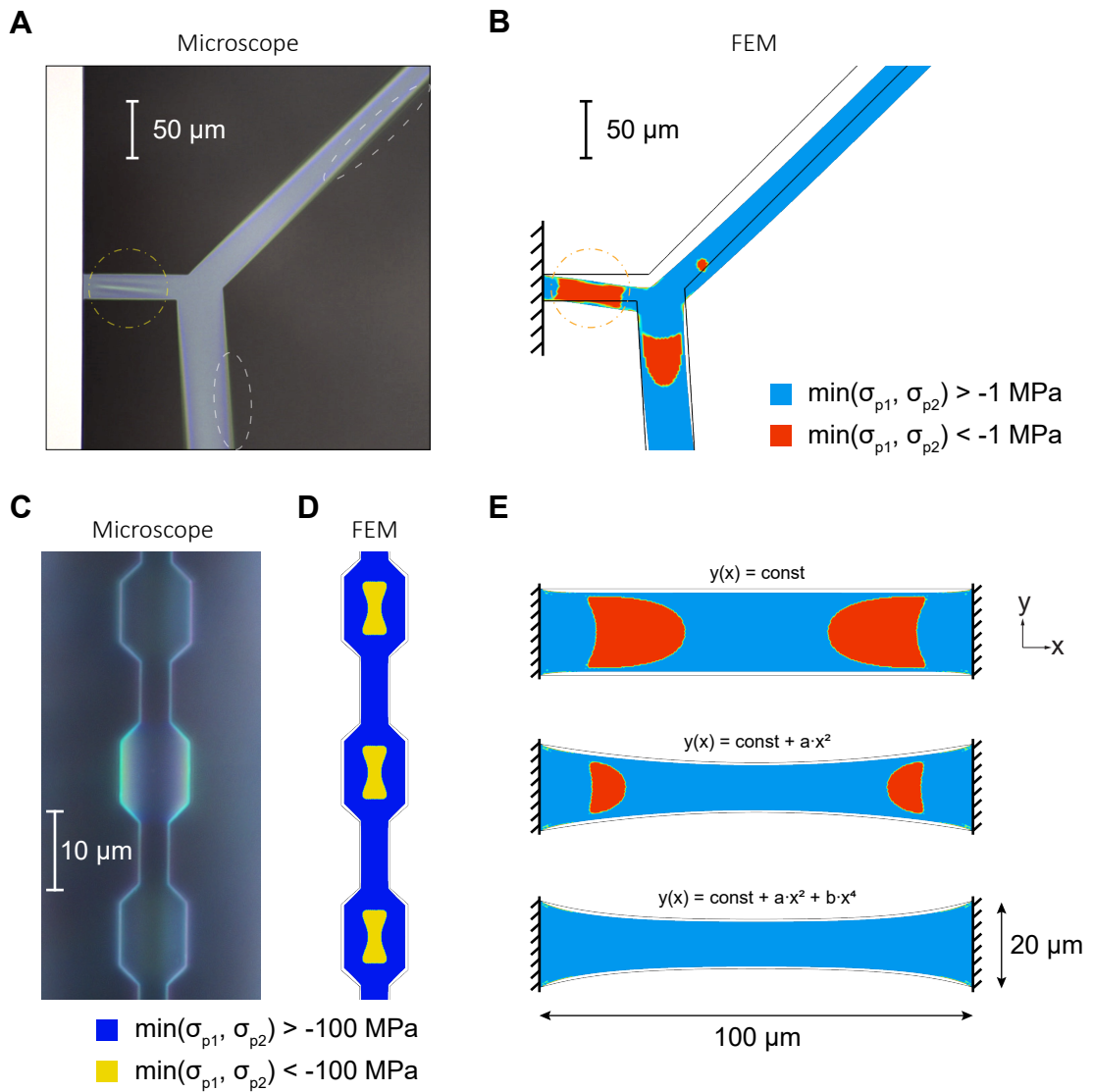


Figure A.1: Static deformation-induced compressive stress and buckling in suspended 20 nm-thick silicon nitride resonators. Panels B, D and E show FEM simulations of compressive stress and static film deformations; here black contours show undeformed geometries and the deformation magnitudes are amplified by a factor of 20. A) Microscope image of a segment of a steering wheel trampoline membrane (courtesy of Alberto Beccari). The yellow and white contours enclose regions where the film is deformed out of the figure plane. B) FEM simulation of the region shown in A. C) Microscope image (dark-field) of a PnC beam segment which is buckled in the transverse direction. D) Finite-element simulation of the segment in C which shows the existence of regions of strong compressive principal stress. E) Simulations of doubly clamped ribbons that show the elimination of compressive principal stress regions by tapering. $y(x)$ are the functions defining the free ribbon edges.

which occurs as the edges go out of the microscope's focus. We conjecture that the different colors of the unit cells imaged in dark field are caused by buckling in opposite directions. The FEM simulation presented in Figure A.1C confirms that the structure has a strong, up to -200 MPa, compressive stress in the transverse direction.

We also observed out-of-plane deformations of structures which were not so readily explained by compressive principal stress. Such deformations can be seen in Figure A.1A, where the edges of long segments (e.g. inside the regions enclosed in the white dashed ellipses) are out of focus, which indicates that the ribbons are deformed out of plane. We conjecture that this can be a consequence of the non-homogeneity of the film along the vertical direction. It is expected that this deformation can also be removed by increasing the film thickness or by engineering stress so that it is tensile in all directions. Indirect evidence in favor of this is that we did not observe such deformations in steering wheel resonators with segments tapered as shown in Figure A.1E.

A.4 Closed-cycle low-vibration cryogenic setup

Cryogenic experiments with mechanical resonators are attractive for a number of reasons. First of all, thermal noises are reduced at low temperatures, including extraneous noises in optical cavities, which can prevent quantum-limited position readout, and the thermal force noises acting on mechanical modes, which result in the decoherence of mechanical states. Second, material dissipation is also improved at cryogenic temperatures (though not always monotonously with lowering the temperature), which further reduces mechanical decoherence. For our silicon nitride devices, we typically observed moderate improvements in quality factors, about a factor of three, between the room temperature and 6K. In other cases, as for resonators made of crystalline materials, improvements can be larger. Finally, experiments with low damping rate thin-film mechanical resonators require a high-vacuum environment, which borders with UHV for the current state-of-the-art devices. Such an environment can be conveniently created by the cryopumping of sample chamber parts cooled to 5K, as this temperature is below the freezing point of atmospheric gases.

Our cryogenic setup is shown in Figure A.2. The cooling power is provided by a GM cryocooler (Sumitomo) driven by its own helium compressor. Vibrations, created by the pulsed operation of closed-cycle cryocoolers, is a notorious challenge for combining them with setups requiring interferometric stability. Vibration isolation is therefore required, which in our case relies on two mechanisms. The first one is a proprietary “Stinger” system of delivering the cooling power from the cryocooler to the sample space. This is done by recirculating helium gas inside a closed line so that the gas is pre-cooled to 7 Kelvin around the cryocooler, and then around the sample holder, it passes through a thin capillary and delivers the cooling power utilizing the Joule-Thompson process. The helium gas flow line is flexible and therefore efficiently decouples the sample chamber from the vibrations of the cryocooler. The second isolation mechanism is more standard. It consists of a Helium gas-gap isolation stage, so that the cooling Stinger line is not attached to the cryocooler directly, and transmits even fewer vibrations to the sample chamber.

The cryostat vacuum chamber, shown in Figure A.2B, was designed in collaboration with the supplier company (ColdEdge) and is similar to the vacuum chambers of our room-temperature setups. It allows continuous operation at 5K temperature with the residual pressure, as detected by a vacuum gauge mounted on the chamber, around 5×10^{-9} mBar. We note that the vacuum level is not necessarily reliably determined by the gauge, but the true value is more likely to be lower than higher.

The helium flow valves, the cryocooler and the recirculator of the cryostat can be remotely controlled from a PC. For convenience, we implemented a custom driver for the valve control manifold, which can be found on GitHub and on the local group server. A GUI-based MATLAB program for the remote control of the cryostat was implemented as a part of the data acquisition system.

At the moment of writing, the cryogenic setup is mostly used for the characterization of high-stress crystalline mechanical resonators, which are not covered in this thesis.

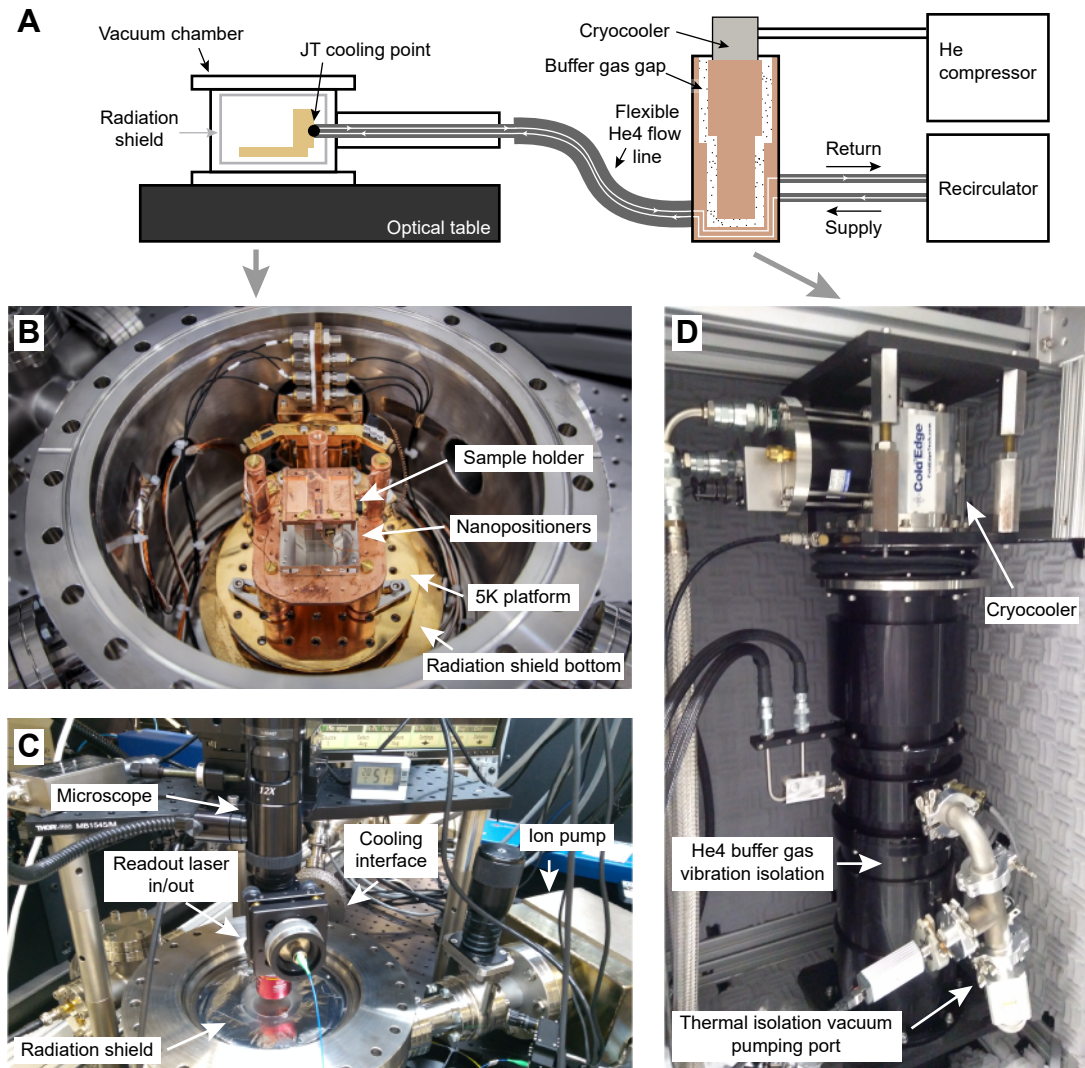


Figure A.2: Schematic and photographs of the closed-cycle low-vibration cryogenic setup. A) Conceptual layout of the setup. JT: Joule-Thompson. B) Sample space inside the vacuum chamber, with the radiation shield removed. C) Cryostat with the vacuum chamber closed. The microscope and the other optics above the chamber are parts of a free-space mechanical quality characterization setup (the layout is described in Sec. 2.7). D) Cryocooler with the buffer gas-gap vibration isolation.

While the essential optical layout is the same, it operates at a different wavelength—1550 nm, and uses an optical drive with a weak 780 nm light beam.

A.5 Scalable data acquisition framework

Present-day physics experiments record very nearly all measurement data in one or another digital form. Organizing digital data acquisition and storage for sophisticated experiments can involve a good deal of programming. Correspondingly, common software engineering problems such as code reusability, scalability, and version control cannot be ignored. This leads to the evolution of small-scale experiment-specific scientific software into more systematic frameworks. Whereas there is no sharp transition here, the usual signature of a software framework is that it can automate experimental routines while having the flexibility to be transferred between different setups to be continuously adapted to new experimental goals and hardware changes without extensive reprogramming. Several data acquisition and instrument control frameworks that emerged in recent years are open-source python-based projects, including Qudi [260], QTLab [261] (which is used by the superconducting circuit optomechanics team at LPQM), and QCoDeS [262]. There is also at least one commercial solution, Labber [263]. Numerous other projects that serve the same goals certainly exist within the scientific community, but most of them are either less developed or not given wide publicity by their creators.

The flexibility of measurement software frameworks is achieved with the help of abstractions that decouple different functionalities and separate the software into building blocks. The blocks can be modified independently and combined with one another to fit the needs of a particular experiment. The blocks are commonly (but not necessarily) implemented as software classes, meaning the usage of an object-orient approach.

Over the course of this thesis the author together with Nils Engelsen developed a MATLAB-based data acquisition and analysis framework to facilitate our experimental activity. The code is freely available from GitHub² and is supplemented by some documentation. The structure of our software inherits several features from the predecessor LabVIEW-based system developed by Dalziel Wilson, and also uses many conceptual solutions common with the python-based projects cited above.

The main motivation behind our software system was to automate, and to make a graphical interface for, the following tasks:

1. Recording data from a variety of physical instruments and saving it in a human-readable format with metadata that contains the state of all other instruments at the time of acquisition.
2. On-the-fly fitting and calibration of measurement traces, in most of the cases to extract mechanical and optical quality factors, vacuum optomechanical coupling rates and classical noise levels.
3. Continuous logging of setup parameters (usually vacuum pressure and cryogenic temperature) and the browsing of existing logs.

At the moment of writing, the part of the software responsible for these tasks have been extensively employed in our experiments for about two years, and proved its practical utility. The software is currently utilized on four measurement setups.

²<https://github.com/engelsen/Instrument-control/wiki>

The implementation details of our software system can be found in the wiki of the git repository. One core abstraction that it uses is the “instrument” class, instances of which are responsible for maintaining communication each with one physical device. The concept of instrument class in fact appears in all python-based data acquisition frameworks cited above. In our case instrument objects also acquire data, perform pre-processing on it, and make the data available in a standardized format for further analysis and saving. While modern physical instruments can contain hundreds of hardware settings, all of them are rarely relevant to one experiment. In our implementation, the function of an instrument class is also to define a relevant subset of settings and provide easy access to them. Another key element of our software framework is a plotter app (see Figure A.3B), which function is to receive data traces acquired by instrument objects and makes them available for interactive analysis using connected sub-apps.

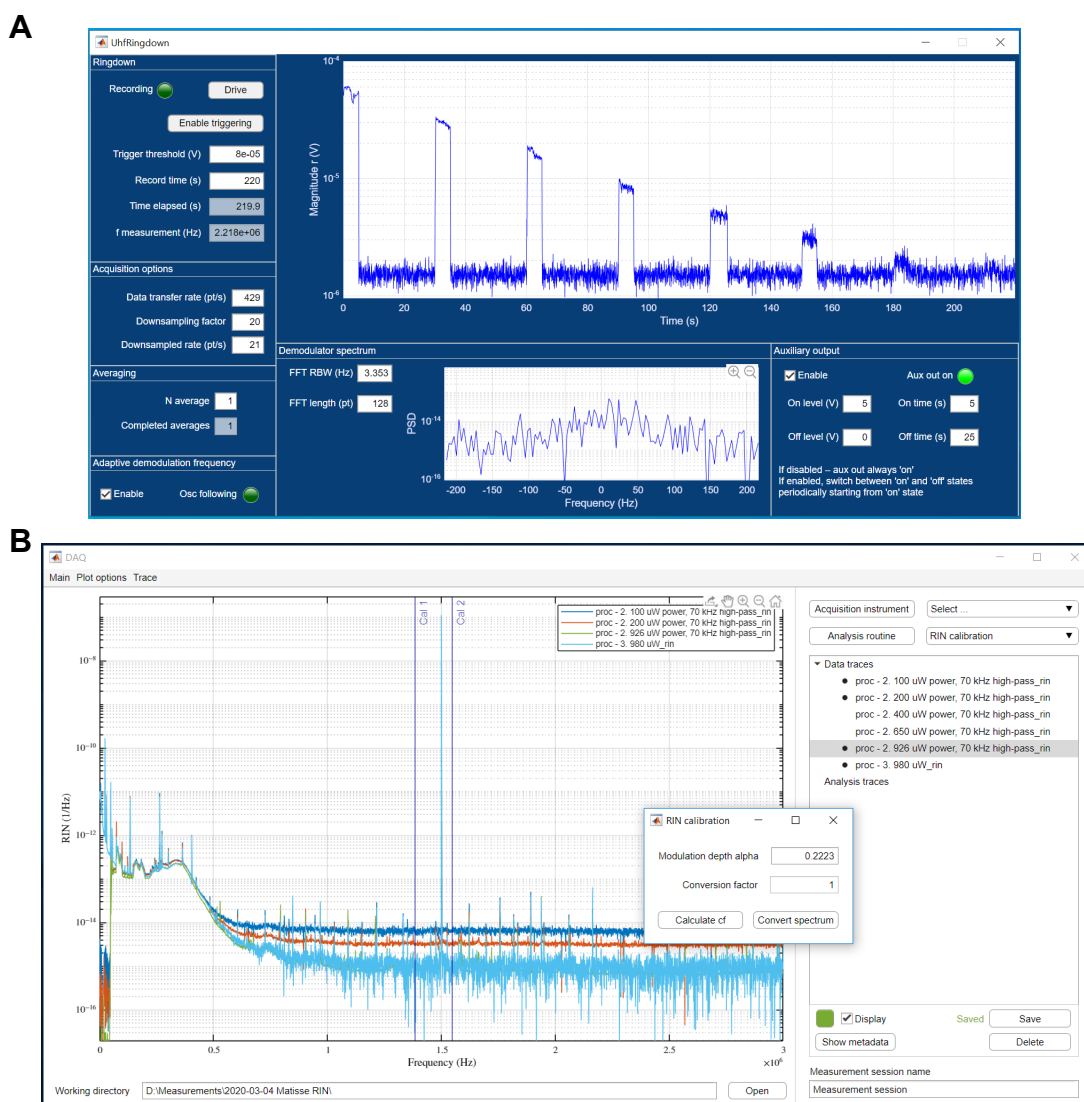


Figure A.3: Screenshots of the data acquisition software. A) Mechanical ringdown spectroscopy program. B) The plotter app with the RIN calibration routine.

Bibliography

- [1] V. B. Braginsky, F. Y. Khalili, and K. S. Thorne. *Quantum Measurement*. 1 edition. Cambridge England ; New York, NY, USA: Cambridge University Press, Sept. 1992.
- [2] C. M. Caves. “Quantum mechanics of measurements distributed in time. A path-integral formulation”. In: *Physical Review D* 33 (6) (Mar. 15, 1986), pp. 1643–1665.
- [3] W. H. Zurek. “Decoherence, einselection, and the quantum origins of the classical”. In: *Reviews of Modern Physics* 75 (3) (May 22, 2003), pp. 715–775.
- [4] N. Gisin. “Collapse. What else?”. In: *arXiv:1701.08300 [quant-ph]* (Jan. 2017). arXiv: 1701.08300.
- [5] S. L. Adler and A. Bassi. “Is Quantum Theory Exact?”. In: *Science* 325 (5938) (July 17, 2009), pp. 275–276.
- [6] S. Bose, K. Jacobs, and P. L. Knight. “Scheme to probe the decoherence of a macroscopic object”. In: *Physical Review A* 59 (5) (May 1999), pp. 3204–3210.
- [7] A. Vinante et al. “Improved Noninterferometric Test of Collapse Models Using Ultracold Cantilevers”. In: *Physical Review Letters* 119 (11) (Sept. 2017), p. 110401.
- [8] A. Pontin et al. “An ultra-narrow line width levitated nano-oscillator for testing dissipative wavefunction collapse”. In: *arXiv:1907.06046 [quant-ph]* (July 2019). arXiv: 1907.06046.
- [9] W. H. Zurek. “Decoherence and the Transition from Quantum to Classical”. In: *Physics Today* 44 (10) (1991), p. 36.
- [10] T. Sauter et al. “Observation of Quantum Jumps”. In: *Physical Review Letters* 57 (14) (Oct. 6, 1986).
- [11] J. C. Bergquist et al. “Observation of Quantum Jumps in a Single Atom”. In: *Physical Review Letters* 57 (14) (Oct. 6, 1986), pp. 1699–1702.
- [12] S. Gleyzes et al. “Quantum jumps of light recording the birth and death of a photon in a cavity”. In: *Nature* 446 (7133) (Mar. 2007), pp. 297–300.
- [13] C. Guerlin et al. “Progressive field-state collapse and quantum non-demolition photon counting”. In: *Nature* 448 (7156) (Aug. 2007), pp. 889–893.
- [14] V. B. Braginsky, Y. I. Vorontsov, and K. S. Thorne. “Quantum Nondemolition Measurements”. In: *Science* 209 (4456) (Aug. 1, 1980), pp. 547–557.
- [15] V. B. Braginsky et al. “Noise in gravitational-wave detectors and other classical-force measurements is not influenced by test-mass quantization”. In: *Physical Review D* 67 (8) (Apr. 7, 2003), p. 082001.

BIBLIOGRAPHY

- [16] C. M. Caves et al. “On the measurement of a weak classical force coupled to a quantum-mechanical oscillator. I. Issues of principle”. In: *Reviews of Modern Physics* 52 (2) (Apr. 1, 1980), pp. 341–392.
- [17] LIGO Scientific Collaboration and Virgo Collaboration et al. “Observation of Gravitational Waves from a Binary Black Hole Merger”. In: *Physical Review Letters* 116 (6) (Feb. 2016), p. 061102.
- [18] LSC Instrument Authors et al. “Quantum correlation measurements in interferometric gravitational-wave detectors”. In: *Physical Review A* 95 (4) (Apr. 21, 2017), p. 043831.
- [19] M. Aspelmeyer, T. J. Kippenberg, and F. Marquardt. “Cavity optomechanics”. In: *Reviews of Modern Physics* 86 (4) (Dec. 30, 2014), pp. 1391–1452.
- [20] T. P. Purdy, R. W. Peterson, and C. A. Regal. “Observation of Radiation Pressure Shot Noise on a Macroscopic Object”. In: *Science* 339 (6121) (Feb. 15, 2013), pp. 801–804.
- [21] M. H. Devoret and R. J. Schoelkopf. “Amplifying quantum signals with the single-electron transistor”. In: *Nature* 406 (6799) (Aug. 2000), pp. 1039–1046.
- [22] A. A. Clerk, S. M. Girvin, and A. D. Stone. “Quantum-limited measurement and information in mesoscopic detectors”. In: *Physical Review B* 67 (16) (Apr. 28, 2003), p. 165324.
- [23] A. A. Clerk et al. “Introduction to quantum noise, measurement, and amplification”. In: *Reviews of Modern Physics* 82 (2) (Apr. 15, 2010), pp. 1155–1208.
- [24] D. Mozyrsky and I. Martin. “Quantum-Classical Transition Induced by Electrical Measurement”. In: *Physical Review Letters* 89 (1) (June 13, 2002), p. 018301.
- [25] V. B. Braginsky, V. P. Mitrofanov, and V. I. Panov. *Systems with Small Dissipation*. University of Chicago Press, 1985.
- [26] A. Ageev et al. “Very high quality factor measured in annealed fused silica”. In: *Classical and Quantum Gravity* 21 (16) (Aug. 2004). arXiv: gr-qc/0403105, pp. 3887–3892.
- [27] W. A. Phillips. “Two-level states in glasses”. In: *Reports on Progress in Physics* 50 (12) (Dec. 1987), pp. 1657–1708.
- [28] A. L. Kimball and D. E. Lovell. “Internal Friction in Solids”. In: *Physical Review* 30 (6) (Dec. 1, 1927), pp. 948–959.
- [29] A. S. Nowick and B. S. Berry. *Anelastic relaxation in crystalline solids*. 1-st. Vol. 11. Academic Press, 1972. 694 pp.
- [30] P. R. Saulson. “Thermal noise in mechanical experiments”. In: *Physical Review D* 42 (8) (Oct. 1990), pp. 2437–2445.
- [31] G. S. MacCabe et al. “Phononic bandgap nano-acoustic cavity with ultralong phonon lifetime”. In: *arXiv:1901.04129 [cond-mat, physics:quant-ph]* (Jan. 2019). arXiv: 1901.04129.
- [32] A. H. Ghadimi et al. “Elastic strain engineering for ultralow mechanical dissipation”. In: *Science* 360 (6390) (May 2018), pp. 764–768.
- [33] G. I. González and P. R. Saulson. “Brownian motion of a mass suspended by an anelastic wire”. In: *The Journal of the Acoustical Society of America* 96 (1) (July 1994), pp. 207–212.

-
- [34] S. A. Fedorov et al. “Generalized dissipation dilution in strained mechanical resonators”. In: *Physical Review B* 99 (5) (Feb. 28, 2019), p. 054107.
- [35] Q. P. Unterreithmeier, T. Faust, and J. P. Kotthaus. “Damping of Nanomechanical Resonators”. In: *Physical Review Letters* 105 (2) (July 2010), p. 027205.
- [36] Y. Tsaturyan et al. “Ultracoherent nanomechanical resonators via soft clamping and dissipation dilution”. In: *Nature Nanotechnology* 12 (8) (Aug. 2017), p. 776.
- [37] M. J. Breyhi et al. “Clamp-Tapering Increases the Quality Factor of Stressed Nanobeams”. In: *Nano Letters* 19 (4) (Apr. 10, 2019), pp. 2329–2333.
- [38] P. Sadeghi et al. “Influence of clamp-widening on the quality factor of nanomechanical silicon nitride resonators”. In: *Journal of Applied Physics* 126 (16) (Oct. 24, 2019), p. 165108.
- [39] S. A. Fedorov et al. “Fractal-like Mechanical Resonators with a Soft-Clamped Fundamental Mode”. In: *Physical Review Letters* 124 (2) (Jan. 16, 2020), p. 025502.
- [40] V. B. Braginsky, M. L. Gorodetsky, and S. P. Vyatchanin. “Thermo-refractive noise in gravitational wave antennae”. In: *Physics Letters A* 271 (5) (July 10, 2000), pp. 303–307.
- [41] V. B. Braginsky, M. L. Gorodetsky, and S. P. Vyatchanin. “Thermodynamical fluctuations and photo-thermal shot noise in gravitational wave antennae”. In: *Physics Letters A* 264 (1) (Dec. 13, 1999), pp. 1–10.
- [42] M. L. Gorodetsky. “Thermal noises and noise compensation in high-reflection multilayer coating”. In: *Physics Letters A* 372 (46) (Nov. 17, 2008), pp. 6813–6822.
- [43] T. L. S. Collaboration et al. “Advanced LIGO”. In: *Classical and Quantum Gravity* 32 (7) (2015), p. 074001.
- [44] S. A. Fedorov et al. “Thermal intermodulation noise in cavity-based measurements”. In: *arXiv:2004.05700 [physics, physics:quant-ph]* (May 14, 2020). arXiv: 2004.05700.
- [45] R. Kubo. “The fluctuation-dissipation theorem”. In: *Reports on Progress in Physics* 29 (1) (1966), p. 255.
- [46] M. Poggio and C. L. Degen. “Force-detected nuclear magnetic resonance: recent advances and future challenges”. In: *Nanotechnology* 21 (34) (July 2010), p. 342001.
- [47] A. N. Cleland. *Foundations of Nanomechanics: From Solid-State Theory to Device Applications*. Advanced Texts in Physics. Berlin Heidelberg: Springer-Verlag, 2003.
- [48] J. Q. Broughton et al. “Direct atomistic simulation of quartz crystal oscillators: Bulk properties and nanoscale devices”. In: *Physical Review B* 56 (2) (July 1, 1997), pp. 611–618.
- [49] R. Hamdan, J. P. Trinastic, and H. P. Cheng. “Molecular dynamics study of the mechanical loss in amorphous pure and doped silica”. In: *The Journal of Chemical Physics* 141 (5) (Aug. 1, 2014), p. 054501.
- [50] S. S. Verbridge et al. “Size and frequency dependent gas damping of nanomechanical resonators”. In: *Applied Physics Letters* 93 (1) (July 2008), p. 013101.

BIBLIOGRAPHY

- [51] M. J. Martin et al. “Damping Models for Microcantilevers, Bridges, and Torsional Resonators in the Free-Molecular-Flow Regime”. In: *Journal of Microelectromechanical Systems* 17 (2) (Apr. 2008), pp. 503–511.
- [52] M. Bao and H. Yang. “Squeeze film air damping in MEMS”. In: *Sensors and Actuators A: Physical*. 25th Anniversary of Sensors and Actuators A: Physical 136 (1) (May 2007), pp. 3–27.
- [53] J. Chan et al. “Optimized optomechanical crystal cavity with acoustic radiation shield”. In: *Applied Physics Letters* 101 (8) (Aug. 2012), p. 081115.
- [54] A. H. Ghadimi, D. J. Wilson, and T. J. Kippenberg. “Radiation and Internal Loss Engineering of High-Stress Silicon Nitride Nanobeams”. In: *Nano Letters* 17 (6) (Mar. 31, 2017), pp. 3501–3505.
- [55] I. Wilson-Rae et al. “High-Q Nanomechanics via Destructive Interference of Elastic Waves”. In: *Physical Review Letters* 106 (4) (Jan. 27, 2011), p. 047205.
- [56] G. D. Cole et al. “Phonon-tunnelling dissipation in mechanical resonators”. In: *Nature Communications* 2 (Mar. 2011), p. 231.
- [57] Y. Tsaturyan et al. “Demonstration of suppressed phonon tunneling losses in phononic bandgap shielded membrane resonators for high-Q optomechanics”. In: *Optics Express* 22 (6) (Mar. 2014), pp. 6810–6821.
- [58] R. Lifshitz and M. L. Roukes. “Thermoelastic damping in micro- and nanomechanical systems”. In: *Physical Review B* 61 (8) (Feb. 15, 2000), pp. 5600–5609.
- [59] A. A. Kiselev and G. J. Iafrate. “Phonon dynamics and phonon assisted losses in Euler-Bernoulli nanobeams”. In: *Physical Review B* 77 (20) (May 30, 2008), p. 205436.
- [60] K. Kunal and N. R. Aluru. “Akhiezer damping in nanostructures”. In: *Physical Review B* 84 (24) (Dec. 30, 2011), p. 245450.
- [61] M. Imboden and P. Mohanty. “Dissipation in nanoelectromechanical systems”. In: *Physics Reports*. Dissipation in nano-electromechanical systems 534 (3) (Jan. 20, 2014), pp. 89–146.
- [62] Y. Tao et al. “Permanent reduction of dissipation in nanomechanical Si resonators by chemical surface protection”. In: *Nanotechnology* 26 (46) (2015), p. 465501.
- [63] S. Mouaziz et al. “Combined Al-protection and HF-vapor release process for ultrathin single crystal silicon cantilevers”. In: *Microelectronic Engineering*. Micro- and Nano-Engineering MNE 2005 83 (4) (Apr. 1, 2006), pp. 1306–1308.
- [64] L. G. Villanueva and S. Schmid. “Evidence of Surface Loss as Ubiquitous Limiting Damping Mechanism in SiN Micro- and Nanomechanical Resonators”. In: *Physical Review Letters* 113 (22) (Nov. 25, 2014), p. 227201.
- [65] G. González. “Suspensions thermal noise in the LIGO gravitational wave detector”. In: *Classical and Quantum Gravity* 17 (21) (2000), p. 4409.
- [66] G. Cagnoli et al. “Damping dilution factor for a pendulum in an interferometric gravitational waves detector”. In: *Physics Letters A* 272 (1) (July 2000), pp. 39–45.
- [67] S. S. Verbridge et al. “High quality factor resonance at room temperature with nanostrings under high tensile stress”. In: *Journal of Applied Physics* 99 (12) (June 15, 2006), p. 124304.

- [68] B. M. Zwickl et al. “High quality mechanical and optical properties of commercial silicon nitride membranes”. In: *Applied Physics Letters* 92 (10) (Mar. 10, 2008), p. 103125.
- [69] P.-L. Yu, T. P. Purdy, and C. A. Regal. “Control of Material Damping in High- Q Membrane Microresonators”. In: *Physical Review Letters* 108 (8) (Feb. 2012), p. 083603.
- [70] L. D. Landau and E. M. Lifshitz. *Theory of elasticity*. London Pergamon Press, 1970.
- [71] K. Y. Fong, W. H. P. Pernice, and H. X. Tang. “Frequency and phase noise of ultrahigh Q silicon nitride nanomechanical resonators”. In: *Physical Review B* 85 (16) (Apr. 27, 2012), p. 161410.
- [72] C. Coullais, D. Sounas, and A. Alù. “Static non-reciprocity in mechanical metamaterials”. In: *Nature* 542 (7642) (Feb. 2017), pp. 461–464.
- [73] C.-C. Nguyen, L. Katehi, and G. Rebeiz. “Micromachined devices for wireless communications”. In: *Proceedings of the IEEE* 86 (8) (Aug. 1998). Conference Name: Proceedings of the IEEE, pp. 1756–1768.
- [74] G. Binnig, C. F. Quate, and C. Gerber. “Atomic Force Microscope”. In: *Physical Review Letters* 56 (9) (Mar. 3, 1986), pp. 930–933.
- [75] D. Rugar et al. “Single spin detection by magnetic resonance force microscopy”. In: *Nature* 430 (6997) (July 2004), pp. 329–332.
- [76] Y. T. Yang et al. “Zeptogram-Scale Nanomechanical Mass Sensing”. In: *Nano Letters* 6 (4) (Apr. 1, 2006), pp. 583–586.
- [77] A. G. Krause et al. “A high-resolution microchip optomechanical accelerometer”. In: *Nature Photonics* 6 (11) (Nov. 2012), pp. 768–772.
- [78] D. Garcia-Sanchez et al. “Casimir Force and In Situ Surface Potential Measurements on Nanomembranes”. In: *Physical Review Letters* 109 (2) (July 9, 2012), p. 027202.
- [79] R. Fischer et al. “Spin detection with a micromechanical trampoline: towards magnetic resonance microscopy harnessing cavity optomechanics”. In: *New Journal of Physics* 21 (4) (Apr. 2019), p. 043049.
- [80] D. Halg et al. “Membrane-based scanning force microscopy”. In: *arXiv:2006.06238 [cond-mat, physics:physics]* (June 11, 2020). arXiv: 2006.06238.
- [81] G. D. Cole et al. “Tensile-strained $\text{In}_x\text{Ga}_{1-x}\text{P}$ membranes for cavity optomechanics”. In: *Applied Physics Letters* 104 (20) (May 19, 2014), p. 201908.
- [82] A. Moridi et al. “Residual stresses in thin film systems: Effects of lattice mismatch, thermal mismatch and interface dislocations”. In: *International Journal of Solids and Structures* 50 (22) (Oct. 15, 2013), pp. 3562–3569.
- [83] D. R. Southworth et al. “Stress and Silicon Nitride: A Crack in the Universal Dissipation of Glasses”. In: *Physical Review Letters* 102 (22) (June 5, 2009), p. 225503.
- [84] J. D. Thompson et al. “Strong dispersive coupling of a high-finesse cavity to a micromechanical membrane”. In: *Nature* 452 (7183) (Mar. 6, 2008), pp. 72–75.
- [85] D. J. Wilson et al. “Cavity Optomechanics with Stoichiometric SiN Films”. In: *Physical Review Letters* 103 (20) (Nov. 13, 2009), p. 207204.

BIBLIOGRAPHY

- [86] R. A. Minamisawa et al. “Top-down fabricated silicon nanowires under tensile elastic strain up to 4.5%”. In: *Nature Communications* 3 (Oct. 2, 2012), p. 1096.
- [87] T. Corbitt et al. “Optical Dilution and Feedback Cooling of a Gram-Scale Oscillator to 6.9 mK”. In: *Physical Review Letters* 99 (16) (Oct. 18, 2007), p. 160801.
- [88] K.-K. Ni et al. “Enhancement of Mechanical Q Factors by Optical Trapping”. In: *Physical Review Letters* 108 (21) (May 21, 2012), p. 214302.
- [89] J. M. Pate et al. “Casimir spring and dilution in macroscopic cavity optomechanics”. In: *arXiv:2004.05983 [cond-mat, physics:physics, physics:quant-ph]* (Apr. 6, 2020). arXiv: 2004.05983.
- [90] G. Steele. Private communication.
- [91] Y. L. Huang and P. R. Saulson. “Dissipation mechanisms in pendulums and their implications for gravitational wave interferometers”. In: *Review of Scientific Instruments* 69 (2) (Feb. 1, 1998), pp. 544–553.
- [92] A. Cumming et al. “Finite element modelling of the mechanical loss of silica suspension fibres for advanced gravitational wave detectors”. In: *Classical and Quantum Gravity* 26 (21) (Oct. 2009), p. 215012.
- [93] Y. Michimura and K. Komori. “Quantum sensing with milligram scale optomechanical systems”. In: *arXiv:2003.13906 [astro-ph, physics:physics, physics:quant-ph]* (Mar. 30, 2020). arXiv: 2003.13906.
- [94] V. Berdichevsky. *Variational Principles of Continuum Mechanics: I. Fundamentals*. Interaction of Mechanics and Mathematics. Berlin Heidelberg: Springer-Verlag, 2009.
- [95] R. L. Edwards, G. Coles, and W. N. Sharpe. “Comparison of tensile and bulge tests for thin-film silicon nitride”. In: *Experimental Mechanics* 44 (1) (Feb. 1, 2004), pp. 49–54.
- [96] O. M. Jadaan et al. “Probabilistic Weibull behavior and mechanical properties of MEMS brittle materials”. In: *Journal of Materials Science* 38 (20) (Oct. 1, 2003), pp. 4087–4113.
- [97] S. Bertolazzi, J. Brivio, and A. Kis. “Stretching and Breaking of Ultrathin MoS₂”. In: *ACS Nano* 5 (12) (Dec. 27, 2011), pp. 9703–9709.
- [98] K. Cao et al. “Elastic straining of free-standing monolayer graphene”. In: *Nature Communications* 11 (1) (Jan. 15, 2020), pp. 1–7.
- [99] L. Boltzmann. “Zur Theorie der elastischen Nachwirkung”. In: *Annalen der Physik* 241 (11) (1878), pp. 430–432.
- [100] C. Zener. “Internal Friction in Solids. I. Theory of Internal Friction in Reeds”. In: *Physical Review* 52 (3) (Aug. 1, 1937), pp. 230–235.
- [101] R. Vacher, E. Courtens, and M. Foret. “Anharmonic versus relaxational sound damping in glasses. II. Vitreous silica”. In: *Physical Review B* 72 (21) (Dec. 9, 2005), p. 214205.
- [102] B. D. Coleman and W. Noll. “Foundations of Linear Viscoelasticity”. In: *Reviews of Modern Physics* 33 (2) (Apr. 1, 1961), pp. 239–249.
- [103] R. N. Kleiman, G. Agnolet, and D. J. Bishop. “Two-level systems observed in the mechanical properties of single-crystal silicon at low temperatures”. In: *Physical Review Letters* 59 (18) (Nov. 2, 1987), pp. 2079–2082.

-
- [104] R. W. Keyes. “Two-level systems in the mechanical properties of silicon at low temperatures”. In: *Physical Review Letters* 62 (11) (Mar. 13, 1989), pp. 1324–1324.
- [105] L. Knopoff. “Q”. In: *Reviews of Geophysics* 2 (4) (1964), pp. 625–660.
- [106] R. O. Pohl, X. Liu, and E. Thompson. “Low-temperature thermal conductivity and acoustic attenuation in amorphous solids”. In: *Reviews of Modern Physics* 74 (4) (Oct. 30, 2002), pp. 991–1013.
- [107] G. Cagnoli and P. A. Willems. “Effects of nonlinear thermoelastic damping in highly stressed fibers”. In: *Physical Review B* 65 (17) (Apr. 24, 2002), p. 174111.
- [108] Y. Huang and P. R. Saulson. “A method for measuring the dependence of internal friction on strain”. In: *Review of Scientific Instruments* 65 (6) (June 1, 1994), pp. 2102–2106.
- [109] J. Harms and C. M. Mow-Lowry. “Suspension-thermal noise in spring–antispring systems for future gravitational-wave detectors”. In: *Classical and Quantum Gravity* 35 (2) (Dec. 2017), p. 025008.
- [110] A. V. Cumming et al. “Design and development of the advanced LIGO monolithic fused silica suspension”. In: *Classical and Quantum Gravity* 29 (3) (Jan. 2012), p. 035003.
- [111] T. Zabel et al. “Top-down method to introduce ultra-high elastic strain”. In: *Journal of Materials Research* 32 (4) (Feb. 2017), pp. 726–736.
- [112] T. Capelle et al. “Polarimetric analysis of stress anisotropy in nanomechanical silicon nitride resonators”. In: *Applied Physics Letters* 110 (18) (May 1, 2017), p. 181106.
- [113] S. Timoshenko. *Theory of elasticity*. Google-Books-ID: HSfto8If1moC. McGraw-Hill, 1987. 596 pp.
- [114] A. C. Stevenson. “Complex potentials in two-dimensional elasticity”. In: *Proc. R. Soc. Lond. A* 184 (997) (Aug. 21, 1945), pp. 129–179.
- [115] M. P. D. Carmo. *Differential Geometry of Curves and Surfaces*. Englewood Cliffs, N.J: Prentice-Hall, Feb. 11, 1976. 503 pp.
- [116] M. Deserno. “Fluid lipid membranes: From differential geometry to curvature stresses”. In: *Chemistry and Physics of Lipids*. Membrane mechanochemistry: From the molecular to the cellular scale 185 (Jan. 1, 2015), pp. 11–45.
- [117] Zhu Cheng and DiMaggio Frank L. “Contribution of Gaussian Curvature to Strain Energy of Plates”. In: *Journal of Engineering Mechanics* 115 (7) (July 1, 1989), pp. 1434–1440.
- [118] L. Catalini, Y. Tsaturyan, and A. Schliesser. “Soft-Clamped Phononic Dimers for Mechanical Sensing and Transduction”. In: *Physical Review Applied* 14 (1) (July 15, 2020), p. 014041.
- [119] T. Faust et al. “Signatures of two-level defects in the temperature-dependent damping of nanomechanical silicon nitride resonators”. In: *Physical Review B* 89 (10) (Mar. 10, 2014), p. 100102.
- [120] P. Mohanty et al. “Intrinsic dissipation in high-frequency micromechanical resonators”. In: *Physical Review B* 66 (8) (Aug. 20, 2002), p. 085416.

BIBLIOGRAPHY

- [121] M. Hamoumi et al. “Microscopic Nanomechanical Dissipation in Gallium Arsenide Resonators”. In: *Physical Review Letters* 120 (22) (May 29, 2018), p. 223601.
- [122] A. M. Gretarsson and G. M. Harry. “Dissipation of mechanical energy in fused silica fibers”. In: *Review of Scientific Instruments* 70 (10) (Sept. 29, 1999), pp. 4081–4087.
- [123] S. A. Fedorov et al. “Evidence for structural damping in a high-stress silicon nitride nanobeam and its implications for quantum optomechanics”. In: *Physics Letters A. Special Issue in memory of Professor V.B. Braginsky* 382 (33) (Aug. 25, 2018), pp. 2251–2255.
- [124] A. M. Gretarsson and P. R. Saulson. “Monitoring the thermal and nonthermal excitation of fibers”. In: *Review of Scientific Instruments* 76 (5) (May 1, 2005), p. 054502.
- [125] J. Guo, R. Norte, and S. Gröblacher. “Feedback Cooling of a Room Temperature Mechanical Oscillator close to its Motional Ground State”. In: *Physical Review Letters* 123 (22) (Nov. 27, 2019), p. 223602.
- [126] S. A. Fedorov. *Mathematica package for calculation of Q factors of strained non-uniform beams*. June 23, 2018.
- [127] In our simulations of Si₃N₄ resonators we assumed the following material parameters, consistent with silicon nitride films produced at CMi (EPFL Center of MicroNanotechnology) and studied at room temperature: film deposition stress $\sigma_{\text{film}} = 1.14$ GPa, Young’s modulus $E = 250$ GPa, Poisson’s ratio $\nu = 0.23$, density $\rho = 3100$ kg/m³, intrinsic loss angle $1/\phi_{\text{film}} = 1.4 \times 10^3$ at 20 nm and $\phi_{\text{film}} \propto h$ for thickness $h < 100$ nm.
- [128] A. Kaushik, H. Kahn, and A. H. Heuer. “Wafer-level mechanical characterization of silicon nitride MEMS”. In: *Journal of Microelectromechanical Systems* 14 (2) (Apr. 2005), pp. 359–367.
- [129] U. Dürig, O. Züger, and A. Stalder. “Interaction force detection in scanning probe microscopy: Methods and applications”. In: *Journal of Applied Physics* 72 (5) (Sept. 1, 1992), pp. 1778–1798.
- [130] D. Ramos et al. “Detection of bacteria based on the thermomechanical noise of a nanomechanical resonator: origin of the response and detection limits”. In: *Nanotechnology* 19 (3) (Dec. 2007), p. 035503.
- [131] E. Gavartin, P. Verlot, and T. J. Kippenberg. “Stabilization of a linear nanomechanical oscillator to its thermodynamic limit”. In: *Nature Communications* 4 (Dec. 11, 2013), p. 2860.
- [132] R. Martínez-Sala et al. “Sound attenuation by sculpture”. In: *Nature* 378 (6554) (Nov. 1995), pp. 241–241.
- [133] R. H. Olsson III and I. El-Kady. “Microfabricated phononic crystal devices and applications”. In: *Measurement Science and Technology* 20 (1) (Nov. 2008), p. 012002.
- [134] M. Eichenfield et al. “Optomechanical crystals”. In: *Nature* 462 (7269) (Nov. 2009), pp. 78–82.
- [135] M. Kalaei et al. “Quantum electromechanics of a hypersonic crystal”. In: *Nature Nanotechnology* 14 (4) (Apr. 2019), pp. 334–339.

-
- [136] P. Arrangoiz-Arriola et al. “Resolving the energy levels of a nanomechanical oscillator”. In: *Nature* 571 (7766) (July 2019), pp. 537–540.
- [137] G. Ma, M. Xiao, and C. T. Chan. “Topological phases in acoustic and mechanical systems”. In: *Nature Reviews Physics* 1 (4) (Apr. 2019), pp. 281–294.
- [138] C. Brendel et al. “Snowflake phononic topological insulator at the nanoscale”. In: *Physical Review B* 97 (2) (Jan. 18, 2018), p. 020102.
- [139] M. Serra-Garcia et al. “Observation of a phononic quadrupole topological insulator”. In: *Nature* 555 (7696) (Mar. 2018), pp. 342–345.
- [140] Y. Lai et al. “Genetically designed L3 photonic crystal nanocavities with measured quality factor exceeding one million”. In: *Applied Physics Letters* 104 (24) (June 16, 2014), p. 241101.
- [141] R. Groth and M. J. Breyhi. “Fabrication of high-aspect ratio Si₃N₄ nanobeam resonators”. In: *Nanofab-net* (2020).
- [142] J. Li, Z. Shan, and E. Ma. “Elastic strain engineering for unprecedented materials properties”. In: *MRS Bulletin* 39 (2) (Feb. 2014), pp. 108–114.
- [143] J. Feng et al. “Strain-engineered artificial atom as a broad-spectrum solar energy funnel”. In: *Nat. Phot.* 6 (12) (2012), pp. 866–872.
- [144] P. Chidambaram et al. “Fundamentals of silicon material properties for successful exploitation of strain engineering in modern CMOS manufacturing”. In: *IEEE Transactions on Electron Devices* 53 (5) (2006), pp. 944–964.
- [145] D. Yu, J. Feng, and J. Hone. “Elastically strained nanowires and atomic sheets”. In: *MRS Bulletin* 39 (2) (2014), pp. 157–162.
- [146] A. Castellanos-Gomez et al. “Local Strain Engineering in Atomically Thin MoS₂”. In: *Nano Letters* 13 (11) (Nov. 13, 2013), pp. 5361–5366.
- [147] M. Poggio et al. “Feedback Cooling of a Cantilever’s Fundamental Mode below 5 mK”. In: *Physical Review Letters* 99 (1) (July 2, 2007), p. 017201.
- [148] D. J. Wilson et al. “Measurement-based control of a mechanical oscillator at its thermal decoherence rate”. In: *Nature* 524 (7565) (Aug. 20, 2015), pp. 325–329.
- [149] R. Schilling et al. “Near-Field Integration of a SiN Nanobeam and a SiO₂ Microcavity for Heisenberg-Limited Displacement Sensing”. In: *Physical Review Applied* 5 (5) (May 26, 2016), p. 054019.
- [150] M. Rossi et al. “Measurement-based quantum control of mechanical motion”. In: *Nature* 563 (7729) (Nov. 2018), p. 53.
- [151] D. Mason et al. “Continuous force and displacement measurement below the standard quantum limit”. In: *Nature Physics* 15 (8) (Aug. 2019), pp. 745–749.
- [152] C. Reetz et al. “Analysis of Membrane Phononic Crystals with Wide Band Gaps and Low-Mass Defects”. In: *Physical Review Applied* 12 (4) (Oct. 14, 2019), p. 044027.
- [153] D. S. Sukhdeo et al. “Bandgap-customizable germanium using lithographically determined biaxial tensile strain for silicon-compatible optoelectronics”. In: *Optics Express* 23 (13) (), pp. 16740–16749.
- [154] B. Mandelbrot. “How Long Is the Coast of Britain? Statistical Self-Similarity and Fractional Dimension”. In: *Science* 156 (3775) (May 5, 1967), pp. 636–638.

BIBLIOGRAPHY

- [155] H. Choi, M. Heuck, and D. Englund. “Self-Similar Nanocavity Design with Ultrasmall Mode Volume for Single-Photon Nonlinearities”. In: *Physical Review Letters* 118 (22) (May 30, 2017), p. 223605.
- [156] R. Lakes. “Materials with structural hierarchy”. In: *Nature* 361 (6412) (Feb. 1993), p. 511.
- [157] D. Rayneau-Kirkhope, Y. Mao, and R. Farr. “Ultralight Fractal Structures from Hollow Tubes”. In: *Physical Review Letters* 109 (20) (Nov. 16, 2012), p. 204301.
- [158] S. Alexander and R. Orbach. “Density of states on fractals : « fractons »”. In: *Journal de Physique Lettres* 43 (17) (Sept. 1, 1982), pp. 625–631.
- [159] B. Sapoval, T. Gobron, and A. Margolina. “Vibrations of fractal drums”. In: *Physical Review Letters* 67 (21) (Nov. 18, 1991), pp. 2974–2977.
- [160] B. Sapoval, O. Haeberlé, and S. Russ. “Acoustical properties of irregular and fractal cavities”. In: *The Journal of the Acoustical Society of America* 102 (4) (Oct. 1, 1997), pp. 2014–2019.
- [161] C. Reinhardt et al. “Ultralow-Noise SiN Trampoline Resonators for Sensing and Optomechanics”. In: *Physical Review X* 6 (2) (Apr. 1, 2016), p. 021001.
- [162] T. Corbitt et al. “Measurement of radiation-pressure-induced optomechanical dynamics in a suspended Fabry-Perot cavity”. In: *Physical Review A* 74 (2) (Aug. 15, 2006), p. 021802.
- [163] T. Bodiya et al. “Sub-hertz optomechanically induced transparency with a kilogram-scale mechanical oscillator”. In: *Physical Review A* 100 (1) (July 29, 2019), p. 013853.
- [164] B. B. Mandelbrot and M. Frame. “The Canopy and Shortest Path in a Self-Contacting Fractal Tree”. In: *The Mathematical Intelligencer* 21 (2) (Mar. 1, 1999), pp. 18–27.
- [165] R. Rammal. “Spectrum of harmonic excitations on fractals”. In: *Journal de Physique* 45 (2) (1984), pp. 191–206.
- [166] T. Nakayama, K. Yakubo, and R. L. Orbach. “Dynamical properties of fractal networks: Scaling, numerical simulations, and physical realizations”. In: *Reviews of Modern Physics* 66 (2) (Apr. 1, 1994), pp. 381–443.
- [167] H. J. Stapleton et al. “Fractal Form of Proteins”. In: *Physical Review Letters* 45 (17) (Oct. 27, 1980), pp. 1456–1459.
- [168] C. M. Pluchar et al. “Towards cavity-free ground-state cooling of an acoustic-frequency silicon nitride membrane”. In: *Applied Optics* 59 (22) (Aug. 1, 2020), G107–G111.
- [169] A. Beccari. “High aspect ratio Si₃N₄ nanomembranes”. In: *Nanofab-net* (2020).
- [170] K. C. McCormick et al. “Quantum-enhanced sensing of a single-ion mechanical oscillator”. In: *Nature* 572 (7767) (Aug. 2019), pp. 86–90.
- [171] S. Hong et al. “Hanbury Brown and Twiss interferometry of single phonons from an optomechanical resonator”. In: *Science* (Sept. 21, 2017).
- [172] Y. Chu et al. “Creation and control of multi-phonon Fock states in a bulk acoustic-wave resonator”. In: *Nature* 563 (7733) (Nov. 2018), pp. 666–670.
- [173] K. J. Satzinger et al. “Quantum control of surface acoustic-wave phonons”. In: *Nature* 563 (7733) (Nov. 2018), pp. 661–665.

-
- [174] R. Riedinger et al. “Remote quantum entanglement between two micromechanical oscillators”. In: *Nature* 556 (7702) (Apr. 2018), pp. 473–477.
- [175] M. D. Anderson et al. “Two-Color Pump-Probe Measurement of Photonic Quantum Correlations Mediated by a Single Phonon”. In: *Physical Review Letters* 120 (23) (June 5, 2018), p. 233601.
- [176] S. T. Velez et al. “Preparation and Decay of a Single Quantum of Vibration at Ambient Conditions”. In: *Physical Review X* 9 (4) (Oct. 7, 2019), p. 041007.
- [177] X. Ma et al. “Nonclassical energy squeezing of a macroscopic mechanical oscillator”. In: *arXiv:2005.04260 [cond-mat, physics:quant-ph]* (May 8, 2020). arXiv: 2005.04260.
- [178] I. Galinskiy et al. “Phonon counting thermometry of an ultracoherent membrane resonator near its motional ground state”. In: *Optica* 7 (6) (June 20, 2020), pp. 718–725.
- [179] A. Arvanitaki, S. Dimopoulos, and K. Van Tilburg. “Sound of Dark Matter: Searching for Light Scalars with Resonant-Mass Detectors”. In: *Physical Review Letters* 116 (3) (Jan. 22, 2016), p. 031102.
- [180] J. Manley et al. “Searching for Scalar Dark Matter with Compact Mechanical Resonators”. In: *Physical Review Letters* 124 (15) (Apr. 16, 2020), p. 151301.
- [181] W. Marshall et al. “Towards Quantum Superpositions of a Mirror”. In: *Physical Review Letters* 91 (13) (Sept. 23, 2003), p. 130401.
- [182] Y. Chen. “Macroscopic quantum mechanics: theory and experimental concepts of optomechanics”. In: *Journal of Physics B: Atomic, Molecular and Optical Physics* 46 (10) (May 2013), p. 104001.
- [183] I. Pikovski et al. “Probing Planck-scale physics with quantum optics”. In: *Nature Physics* 8 (5) (May 2012), pp. 393–397.
- [184] M. Bawaj et al. “Probing deformed commutators with macroscopic harmonic oscillators”. In: *Nature Communications* 6 (1) (June 19, 2015), p. 7503.
- [185] C. M. Caves. “Quantum-Mechanical Radiation-Pressure Fluctuations in an Interferometer”. In: *Physical Review Letters* 45 (2) (July 14, 1980), pp. 75–79.
- [186] B. P. Abbott et al. “LIGO: the Laser Interferometer Gravitational-Wave Observatory”. In: *Reports on Progress in Physics* 72 (7) (June 2009), p. 076901.
- [187] V. B. Braginsky and F. J. Khalili. “Gravitational wave antenna with QND speed meter”. In: *Physics Letters A* 147 (5) (July 16, 1990), pp. 251–256.
- [188] J. B. Hertzberg et al. “Back-action-evading measurements of nanomechanical motion”. In: *Nature Physics* 6 (3) (Mar. 2010), pp. 213–217.
- [189] J. Suh et al. “Mechanically detecting and avoiding the quantum fluctuations of a microwave field”. In: *Science* 344 (6189) (June 13, 2014), pp. 1262–1265.
- [190] I. Shomroni et al. “Optical backaction-evading measurement of a mechanical oscillator”. In: *Nature Communications* 10 (1) (May 7, 2019), p. 2086.
- [191] S. P. Vyatchanin and A. B. Matsko. “Quantum limit on force measurements”. In: *JETP* 77 (Aug. 1993), p. 218.
- [192] S. P. Vyatchanin and E. A. Zubova. “Quantum variation measurement of a force”. In: *Physics Letters A* 201 (4) (May 29, 1995), pp. 269–274.

BIBLIOGRAPHY

- [193] S. P. Vyatchanin. “The estimation of signal force parameters in quantum variation measurement”. In: *Physics Letters A* 239 (4) (Mar. 9, 1998), pp. 201–208.
- [194] V. Sudhir et al. “Quantum Correlations of Light from a Room-Temperature Mechanical Oscillator”. In: *Physical Review X* 7 (3) (Sept. 26, 2017), p. 031055.
- [195] N. S. Kampel et al. “Improving Broadband Displacement Detection with Quantum Correlations”. In: *Physical Review X* 7 (2) (Apr. 18, 2017), p. 021008.
- [196] J. Cripe et al. “Quantum Backaction Cancellation in the Audio Band”. In: *Physical Review X* 10 (3) (Sept. 23, 2020), p. 031065.
- [197] S. Schreppler et al. “Optically measuring force near the standard quantum limit”. In: *Science* 344 (6191) (June 27, 2014), pp. 1486–1489.
- [198] J. D. Teufel, F. Lecocq, and R. W. Simmonds. “Overwhelming Thermomechanical Motion with Microwave Radiation Pressure Shot Noise”. In: *Physical Review Letters* 116 (1) (Jan. 6, 2016), p. 013602.
- [199] J. Cripe et al. “Measurement of quantum back action in the audio band at room temperature”. In: *Nature* 568 (7752) (Apr. 2019), pp. 364–367.
- [200] A. H. Safavi-Naeini et al. “Squeezed light from a silicon micromechanical resonator”. In: *Nature* 500 (7461) (Aug. 8, 2013), pp. 185–189.
- [201] T. P. Purdy et al. “Strong Optomechanical Squeezing of Light”. In: *Physical Review X* 3 (3) (Sept. 3, 2013).
- [202] V. Sudhir et al. “Appearance and Disappearance of Quantum Correlations in Measurement-Based Feedback Control of a Mechanical Oscillator”. In: *Physical Review X* 7 (1) (Jan. 6, 2017), p. 011001.
- [203] W. H. P. Nielsen et al. “Multimode optomechanical system in the quantum regime”. In: *Proceedings of the National Academy of Sciences* 114 (1) (Jan. 3, 2017), pp. 62–66.
- [204] N. Aggarwal et al. “Room-temperature optomechanical squeezing”. In: *Nature Physics* 16 (7) (July 2020), pp. 784–788.
- [205] K. Jacobs and D. A. Steck. “A straightforward introduction to continuous quantum measurement”. In: *Contemporary Physics* 47 (5) (Sept. 1, 2006), pp. 279–303.
- [206] A. A. Clerk. “Quantum-limited position detection and amplification: A linear response perspective”. In: *Physical Review B* 70 (24) (Dec. 7, 2004), p. 245306.
- [207] R. J. Glauber. “The Quantum Theory of Optical Coherence”. In: *Physical Review* 130 (6) (June 15, 1963), pp. 2529–2539.
- [208] A. A. Clerk. “Full counting statistics of energy fluctuations in a driven quantum resonator”. In: *Physical Review A* 84 (4) (Oct. 14, 2011), p. 043824.
- [209] A. A. Clerk, F. Marquardt, and J. G. E. Harris. “Quantum Measurement of Phonon Shot Noise”. In: *Physical Review Letters* 104 (21) (May 27, 2010), p. 213603.
- [210] P. L. Kelley and W. H. Kleiner. “Theory of Electromagnetic Field Measurement and Photoelectron Counting”. In: *Physical Review* 136 (2) (Oct. 19, 1964), A316–A334.
- [211] H. J. Carmichael. *Statistical Methods in Quantum Optics 2: Non-Classical Fields*. Theoretical and Mathematical Physics, Statistical Methods in Quantum Optics. Section 9.3.3. Berlin Heidelberg: Springer-Verlag, 2008.

-
- [212] C. W. Gardiner and M. J. Collett. “Input and output in damped quantum systems: Quantum stochastic differential equations and the master equation”. In: *Physical Review A* 31 (6) (June 1, 1985), pp. 3761–3774.
- [213] V. B. Braginsky. “Classical and Quantum Restrictions on the Detection of Weak Disturbances of a Macroscopic Oscillator”. In: *Journal of Experimental and Theoretical Physics* 26 (Apr. 1968), p. 831.
- [214] F. Y. Khalili et al. “Quantum back-action in measurements of zero-point mechanical oscillations”. In: *Physical Review A* 86 (3) (Sept. 25, 2012), p. 033840.
- [215] A. H. Safavi-Naeini et al. “Observation of Quantum Motion of a Nanomechanical Resonator”. In: *Physical Review Letters* 108 (3) (Jan. 17, 2012), p. 033602.
- [216] A. J. Weinstein et al. “Observation and Interpretation of Motional Sideband Asymmetry in a Quantum Electromechanical Device”. In: *Physical Review X* 4 (4) (Oct. 7, 2014), p. 041003.
- [217] F. Y. Khalili and E. Zeuthen. “Quantum limits for stationary force sensing”. In: *arXiv:2011.14716 [quant-ph]* (Nov. 2020). arXiv: 2011.14716.
- [218] L. F. Buchmann et al. “Complex Squeezing and Force Measurement Beyond the Standard Quantum Limit”. In: *Physical Review Letters* 117 (3) (July 12, 2016), p. 030801.
- [219] C. F. Ockeloen-Korppi et al. “Revealing Hidden Quantum Correlations in an Electromechanical Measurement”. In: *Physical Review Letters* 121 (24) (Dec. 14, 2018), p. 243601.
- [220] J. D. Teufel et al. “Nanomechanical motion measured with an imprecision below that at the standard quantum limit”. In: *Nature Nanotechnology* 4 (12) (Dec. 2009), pp. 820–823.
- [221] G. Anetsberger et al. “Measuring nanomechanical motion with an imprecision below the standard quantum limit”. In: *Physical Review A* 82 (6) (Dec. 29, 2010), p. 061804.
- [222] T. J. Kippenberg et al. “Analysis of Radiation-Pressure Induced Mechanical Oscillation of an Optical Microcavity”. In: *Physical Review Letters* 95 (3) (July 12, 2005), p. 033901.
- [223] L. Ding et al. “High Frequency GaAs Nano-Optomechanical Disk Resonator”. In: *Physical Review Letters* 105 (26) (Dec. 23, 2010), p. 263903.
- [224] M. L. Gorodetsky et al. “Determination of the vacuum optomechanical coupling rate using frequency noise calibration”. In: *Optics Express* 18 (22) (Oct. 25, 2010), pp. 23236–23246.
- [225] H. J. Kimble et al. “Conversion of conventional gravitational-wave interferometers into quantum nondemolition interferometers by modifying their input and/or output optics”. In: *Physical Review D* 65 (2) (Dec. 26, 2001), p. 022002.
- [226] P. Verlot et al. “Scheme to Probe Optomechanical Correlations between Two Optical Beams Down to the Quantum Level”. In: *Physical Review Letters* 102 (10) (Mar. 10, 2009), p. 103601.
- [227] T. P. Purdy et al. “Quantum correlations from a room-temperature optomechanical cavity”. In: *Science* 356 (6344) (June 23, 2017), pp. 1265–1268.

BIBLIOGRAPHY

- [228] H. Vahlbruch et al. “Detection of 15 dB Squeezed States of Light and their Application for the Absolute Calibration of Photoelectric Quantum Efficiency”. In: *Physical Review Letters* 117 (11) (Sept. 6, 2016), p. 110801.
- [229] M. L. Gorodetsky and I. S. Grudinin. “Fundamental thermal fluctuations in microspheres”. In: *JOSA B* 21 (4) (Apr. 1, 2004), pp. 697–705.
- [230] S. A. Weis. “Cavity-Optomechanics with Silica Microtoroids Quantum-Coherent Coupling and Optomechanically Induced Transparency”. In: (2012). Place: Lausanne, Publisher: EPFL, p. 176.
- [231] V. Sudhir. *Quantum Limits on Measurement and Control of a Mechanical Oscillator*. Springer Theses. Springer International Publishing, 2018.
- [232] H. Schütz. “Quantum optomechanics at room temperature”. In: (2017). Place: Lausanne, Publisher: EPFL, p. 175.
- [233] R. D. Schilling. “Development of a monolithic near-field optomechanical system”. In: (2018). Place: Lausanne, Publisher: EPFL, p. 219.
- [234] S. M. Spillane et al. “Ideality in a Fiber-Taper-Coupled Microresonator System for Application to Cavity Quantum Electrodynamics”. In: *Physical Review Letters* 91 (4) (July 22, 2003), p. 043902.
- [235] P. F. Cohadon, A. Heidmann, and M. Pinard. “Cooling of a Mirror by Radiation Pressure”. In: *Physical Review Letters* 83 (16) (Oct. 18, 1999), pp. 3174–3177.
- [236] G. I. González and P. R. Saulson. “Brownian motion of a torsion pendulum with internal friction”. In: *Physics Letters A* 201 (1) (May 15, 1995), pp. 12–18.
- [237] M. Kajima et al. “Wide-band measurement of mechanical thermal noise using a laser interferometer”. In: *Physics Letters A* 263 (1) (Nov. 22, 1999), pp. 21–26.
- [238] V. B. Braginsky, F. Y. Khalili, and A. A. Kulaga. “Quantum-non-demolition measurement of the phase”. In: *Physics Letters A* 202 (1) (June 12, 1995), pp. 1–6.
- [239] I. Martin and W. H. Zurek. “Measurement of Energy Eigenstates by a Slow Detector”. In: *Physical Review Letters* 98 (12) (Mar. 23, 2007), p. 120401.
- [240] A. A. Gangat, T. M. Stace, and G. J. Milburn. “Phonon number quantum jumps in an optomechanical system”. In: *New Journal of Physics* 13 (4) (2011), p. 043024.
- [241] A. Nunnenkamp et al. “Cooling and squeezing via quadratic optomechanical coupling”. In: *Physical Review A* 82 (2) (Aug. 31, 2010), p. 021806.
- [242] T. P. Purdy et al. “Tunable Cavity Optomechanics with Ultracold Atoms”. In: *Physical Review Letters* 105 (13) (Sept. 22, 2010), p. 133602.
- [243] T. K. Paraíso et al. “Position-Squared Coupling in a Tunable Photonic Crystal Optomechanical Cavity”. In: *Physical Review X* 5 (4) (Nov. 12, 2015), p. 041024.
- [244] H. Miao et al. “Standard Quantum Limit for Probing Mechanical Energy Quantization”. In: *Physical Review Letters* 103 (10) (Sept. 2, 2009), p. 100402.
- [245] Y. Yanay, J. C. Sankey, and A. A. Clerk. “Quantum backaction and noise interference in asymmetric two-cavity optomechanical systems”. In: *Physical Review A* 93 (6) (June 8, 2016), p. 063809.
- [246] M. R. Vanner. “Selective Linear or Quadratic Optomechanical Coupling via Measurement”. In: *Physical Review X* 1 (2) (Nov. 28, 2011).

-
- [247] M.-A. Lemonde, N. Didier, and A. A. Clerk. “Nonlinear Interaction Effects in a Strongly Driven Optomechanical Cavity”. In: *Physical Review Letters* 111 (5) (Aug. 2, 2013), p. 053602.
- [248] G. A. Brawley et al. “Nonlinear optomechanical measurement of mechanical motion”. In: *Nature Communications* 7 (1) (Mar. 21, 2016), p. 10988.
- [249] R. Leijssen et al. “Nonlinear cavity optomechanics with nanomechanical thermal fluctuations”. In: *Nature Communications* 8 (1) (July 7, 2017), pp. 1–10.
- [250] A. B. Matsko and S. P. Vyatchanin. “Electromagnetic-continuum-induced nonlinearity”. In: *Physical Review A* 97 (5) (May 17, 2018), p. 053824.
- [251] M. J. Yap et al. “Broadband reduction of quantum radiation pressure noise via squeezed light injection”. In: *Nature Photonics* (Oct. 7, 2019), pp. 1–5.
- [252] M. Underwood et al. “Measurement of the motional sidebands of a nanogram-scale oscillator in the quantum regime”. In: *Physical Review A* 92 (6) (Dec. 2, 2015), p. 061801.
- [253] C. B. Møller et al. “Quantum back-action-evading measurement of motion in a negative mass reference frame”. In: *Nature* 547 (7662) (July 13, 2017), pp. 191–195.
- [254] D. J. Wilson. “Cavity optomechanics with high-stress silicon nitride films”. PhD thesis. California Institute of Technology, June 15, 2012.
- [255] Y. Zhao et al. “Suppression of extraneous thermal noise in cavity optomechanics”. In: *Optics Express* 20 (4) (Feb. 13, 2012), pp. 3586–3612.
- [256] V. Dumont et al. “Flexure-tuned membrane-at-the-edge optomechanical system”. In: *Optics Express* 27 (18) (Sept. 2, 2019), pp. 25731–25748.
- [257] C. J. Hood, H. J. Kimble, and J. Ye. “Characterization of high-finesse mirrors: Loss, phase shifts, and mode structure in an optical cavity”. In: *Physical Review A* 64 (3) (Aug. 13, 2001), p. 033804.
- [258] G. D. Cole et al. “Tenfold reduction of Brownian noise in high-reflectivity optical coatings”. In: *Nature Photonics* 7 (8) (Aug. 2013), pp. 644–650.
- [259] C. W. Gardiner. *Handbook of Stochastic Methods*. 2nd edition. section 2.8.1. Berlin: Springer, Jan. 1985.
- [260] J. M. Binder et al. “Qudi: A modular python suite for experiment control and data processing”. In: *SoftwareX* 6 (Jan. 1, 2017), pp. 85–90.
- [261] R. Heeres. QTLab measurement environment.
URL: <http://qtlab.sourceforge.net>.
Git repository: <https://github.com/heeres/qtlab>.
- [262] QCoDeS data acquisition framework.
URL: <https://qcodes.github.io/Qcodes>.
- [263] Labber—software for instrument control and measurement automation.
URL: <https://labber.org>.

BIBLIOGRAPHY

Curriculum Vitae

PERSONAL DETAILS

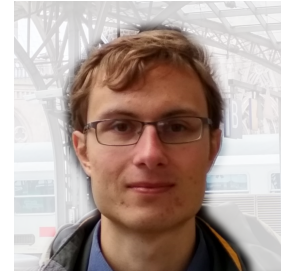
Date of birth: 25 May 1992

☎ +41-76-42-95204

✉ fedorov.s.a@outlook.com

ORCID: 0000-0003-4606-0546

Laboratory of Photonics and
Quantum Measurements
PH D3 345
EPFL Station 3
CH-1015 Lausanne
Switzerland



EDUCATION

- Sep 2015 – present | Ph.D. in Physics, Swiss Federal Institute of Technology in Lausanne (EPFL), Switzerland
Thesis: *Mechanical resonators with high dissipation dilution in precision and quantum measurements.*
Advisor: Prof. Tobias J. Kippenberg
Anticipated defense date: 19/11/2020
- Sep 2013 – Jul 2015 | Master of Science, Department of General and Applied Physics, Moscow Institute of Physics and Technology (MIPT), Russia
Thesis: *A femtosecond optical frequency comb in near-infrared range.*
Diploma with honors
Defense date: 30/06/2015
- Sep 2009 – Jul 2013 | Bachelor of Science, Department of General and Applied Physics, Moscow Institute of Physics and Technology (MIPT), Russia
Thesis: *Dynamics of exciton-trionic systems in quantum wells in the presence of excess charge carriers*
Diploma with honors
Defense date: 25/06/2013

EMPLOYMENT HISTORY

- Sep 2015 – present | **Graduate Researcher**, *Laboratory of Photonics and Quantum Measurements, Swiss Federal Institute of Technology in Lausanne (EPFL), Switzerland*
Detected quantum correlations in position measurements of mesoscopic mechanical oscillators. Developed theory and simulation codes for the calculation of dissipation dilution in soft-clamped mechanical resonators. Built optical setups and characterized mechanical and optical resonators. Set up a low-vibration closed-cycle cryogenic station for optomechanics experiments. Characterized thermal noises in optical resonators.
Advisor: Prof. Tobias J. Kippenberg
- Sep 2013 – Jul 2015 | **Undergraduate Researcher**, *Lebedev Physical Institute, Russia*
Conducted precision saturation absorption spectroscopy of Thulium atoms. Designed and implemented a self-referenced frequency comb for optical frequency metrology. Calculated atomic polarizability for the implementation of an optical atomic clock.
Advisor: Prof. Nikolay Kolachevsky
- Sep 2013 – Jul 2015 | **Undergraduate Researcher**, *Department of Theoretical Physics, Moscow Institute of Physics and Technology, Russia*
Developed theory and Fortran code for the stochastic simulation of single-electron transistors with ferroelectric tunnel barriers.
Advisor: Prof. Nikolay Chtchelkatchev

TEACHING EXPERIENCE

- Feb 2016 – **Graduate Teaching Assistant** in Statistical Physics IV class at EPFL.
Jul 2019 Advanced statistical physics course taught by Prof. Tobias Kippenberg, attended by master and doctoral students from EPFL
Developed exercises for the course, conducted exercise session, graded homeworks and supervised final exams.
- Sep 2016 – **Graduate Teaching Assistant** in Lasers: theory and modern applications class at EPFL.
Jan 2019 Physics course taught by Prof. Christophe Moser and Prof. Tobias Kippenberg, Attended by master and doctoral students from EPFL.
Developed exercises for the course, conducted exercise session, graded homeworks and supervised final exams.

LANGUAGES

Russian (native), English (C2), French (A2).

List of publications

- [1] **S. A. Fedorov***, A. Beccari*, A. Arabmoheghi, D. J. Wilson, N. J. Engelsen, and T. J. Kippenberg. Thermal intermodulation noise in cavity-based measurements. *arXiv:2004.05700 [physics, physics:quant-ph]*, **2020**. Accepted to publication at *Optica*.
URL: <http://arxiv.org/abs/2004.05700>
*Indicates equal contributor.
- [2] **S. A. Fedorov**, A. Beccari, N. J. Engelsen, and T. J. Kippenberg. Fractal-like Mechanical Resonators with a Soft-Clamped Fundamental Mode. *Physical Review Letters*, 124(2):025502, **2020**.
DOI: [10.1103/PhysRevLett.124.025502](https://doi.org/10.1103/PhysRevLett.124.025502).
- [3] A. K. Tagantsev and **S. A. Fedorov**. Quantum-Limited Measurements Using an Optical Cavity with Modulated Intrinsic Loss. *Physical Review Letters*, 123(4):043602, **2019**.
DOI: [10.1103/PhysRevLett.123.043602](https://doi.org/10.1103/PhysRevLett.123.043602).
- [4] **S. A. Fedorov**, N. J. Engelsen, A. H. Ghadimi, M. J. Breyhi, R. Schilling, D. J. Wilson, and T. J. Kippenberg. Generalized dissipation dilution in strained mechanical resonators. *Physical Review B*, 99(5):054107, **2019**.
DOI: [10.1103/PhysRevB.99.054107](https://doi.org/10.1103/PhysRevB.99.054107).
- [5] M. J. Breyhi, A. Beccari, **S. A. Fedorov**, A. H. Ghadimi, R. Schilling, D. J. Wilson, N. J. Engelsen, and T. J. Kippenberg. Clamp-Tapering Increases the Quality Factor of Stressed Nanobeams. *Nano Letters*, 19(4):2329–2333, **2019**.
DOI: [10.1021/acs.nanolett.8b04942](https://doi.org/10.1021/acs.nanolett.8b04942).
- [6] A. H. Ghadimi*, **S. A. Fedorov***, N. J. Engelsen*, M. J. Breyhi, R. Schilling, D. J. Wilson, and T. J. Kippenberg. Elastic strain engineering for ultralow mechanical dissipation. *en. Science*, 360(6390):764–768, **2018**.
DOI: [10.1126/science.aar6939](https://doi.org/10.1126/science.aar6939).
*Indicates equal contributor.
- [7] **S. A. Fedorov**, V. Sudhir, R. Schilling, H. Schütz, D. J. Wilson, and T. J. Kippenberg. Evidence for structural damping in a high-stress silicon nitride nanobeam and its implications for quantum optomechanics. *Physics Letters A. Special Issue in memory of Professor V.B. Braginsky*, 382(33):2251–2255, **2018**.
DOI: [10.1016/j.physleta.2017.05.046](https://doi.org/10.1016/j.physleta.2017.05.046).
- [8] V. Sudhir*, R. Schilling*, **S. A. Fedorov***, H. Schütz*, D. J. Wilson, and T. J. Kippenberg. Quantum Correlations of Light from a Room-Temperature Mechanical Oscillator. *Physical Review X*, 7(3):031055, **2017**.
DOI: [10.1103/PhysRevX.7.031055](https://doi.org/10.1103/PhysRevX.7.031055).
*Indicates equal contributor.
- [9] V. Sudhir, D. J. Wilson, R. Schilling, H. Schütz, **S. A. Fedorov**, A. H. Ghadimi, A. Nunnenkamp, and T. J. Kippenberg. Appearance and Disappearance of Quantum Correlations in Measurement-Based Feedback Control of a Mechanical Oscillator. *Physical Review X*, 7(1):011001, **2017**.
DOI: [10.1103/PhysRevX.7.011001](https://doi.org/10.1103/PhysRevX.7.011001).